Pt (II) complexes-based assays for small biomolecules detection in aqueous media

Zur Erlangung des akademischen Grades einer

DOKTORIN DER NATURWISSENSCHAFTEN

(Dr. rer. nat.)

von der KIT-Fakultät für Chemie und Biowissenschaften des Karlsruher Instituts für Technologie (KIT)

Karlsruher Institut für Technologie

genehmigte

DISSERTATION

von

M.Sc. Rui Kang

1. Referentin: Prof. Anne S. Ulrich

2. Korreferentin: Prof. Luisa De Cola

Tag der mündlichen Prüfung: 18. Juli 2022

Die vorliegende Arbeit wurde in der Zeit von 5. Oktober 2018 bis 01. Juni 2022 am Institut für Nanotechnologie (INT) auf dem Campus Nord des Karlsruher Instituts für Technologie (KIT) unter der Leitung von Dr. Frank Biedermann, Prof. Luisa De Cola und Prof. Anne S. Ulrich angefertigt. Die Arbeit wurde von den China Scholarship Council (CSC) und der Deutsche Forschungsgesellschaft (DFG) gefördert.

The present work was realized between October 5, 2018 and June 1, 2022 at the Institute of Nanotechnology (INT) on the Campus North of Karlsruhe Institute of Technology (KIT) under the supervision of Dr. Frank Biedermann, Prof. Luisa De Cola, and Prof. Anne S. Ulrich. The work was funded by the China Scholarship Council (CSC) and Deutsche Forschungsgesellschaft (DFG).

Declaration

I hereby declare that:

1. This work was done wholly while in candidature for a research degree at KIT.
2. The whole thesis was written by me, and no other sources other than the specified were used.
3. The rules for ensuring the good scientific practice of the Karlsruhe Institute of Technology (KIT) have been used, and the submission and archiving of the primary data, in accordance with section A(6) of the rules for ensuring the good scientific practice of KIT, has been ensured.
4. The electronic version of the work is consistent with the written version.
5. Where I have consulted the published work of others, this is always clearly attributed.
6. I have acknowledged all main sources of help.
7. Where the thesis is based on work done by myself jointly with others, I have made clear exactly what was done by others and what I have contributed myself.
8. Furthermore, I declare that I did not undertake any previous doctoral studies, and I am currently not enrolled in any other ongoing doctoral procedure.

Rui Kang

Deklaration

Ich erkläre:

1. Diese Arbeit wurde vollständig während der Kandidatur für ein Forschungsstudium am KIT durchgeführt.
2. Die gesamte Arbeit wurde von mir verfasst und es wurden keine anderen Quellen als die angegebenen verwendet.
3. Es wurden Maßnahmen zur Sicherstellung einer guten wissenschaftlichen Praxis des Karlsruher Instituts für Technologie (KIT) angewendet und die Übermittlung und Archivierung der Primärdaten gemäß Abschnitt A(6) der Regeln zur Sicherstellung einer guten wissenschaftlichen Praxis des KIT sichergestellt.
4. Die elektronische Fassung des Werkes entspricht der schriftlichen Fassung.
5. Im Fall, dass ich die veröffentlichten Arbeiten anderer konsultiert habe, wird dies immer eindeutig zugeordnet.
6. Ich habe alle wichtigen Hilfsquellen zur Kenntnis genommen.
7. Wenn die Arbeit auf Arbeiten basiert, die ich gemeinsam mit anderen geleistet habe, habe ich kenntlich gemacht, was von anderen geleistet wurde und was ich selbst beigesteuert habe.
8. Des Weiteren erkläre ich, dass ich kein vorheriges Promotionsstudium absolviert habe und mich derzeit nicht in einem anderen laufenden Promotionsverfahren befinde.

Rui Kang

Table of contents

Abstract

Supramolecular principles such as self-assembly, stimuli-responsiveness, and adaptiveness are widely utilized concepts for developing advanced functional materials. Particularly, they have also significantly impacted analytical science development. In the last two decades, countless supramolecular binders, molecular probes, and chemosensors combined with innovative assays have led to a revolution in molecular sensing and medical diagnostics. Nevertheless, most of these molecular sensing systems are still suffering from either low-binding affinity or low-selectivity or decomposition in complex media such as biofluids, which are the main obstacles limiting their further practical applications. Therefore, the development of new molecular sensing systems that can reach practical requirements is still one of the frontiers in supramolecular chemistry. So far, traditional chromatography-based techniques, *e.g.*, HPLC-MS, are often used for molecular sensing, which are reliable but usually time- and cost-intensive, difficult to do parallel analysis, and require trained personnel. Spectroscopic method-based chemosensors and probes may thus become more suitable for practical applications because of cost-effectiveness, ease of handling, and high-throughput screening ability.

Herein, the self-assembling probe (SAP)-based molecular sensing concept is described. By combining molecular reactions and supramolecular interactions, both the high-selective and the high-binding affinity are achieved for the identification and quantification of analytes by utilizing SAP.

Beginning with fundamental photophysical knowledge in luminescence, a general introduction of this thesis is given in **Chapter 1**. As primary candidates for constructing the self-assembling probes (SAPs), transition metal complexes, particularly platinum(II) complexes, are briefly reviewed, including their basic photophysics and applications. In addition, current molecular sensing concepts are introduced and discussed, providing the essential background for the proposed sensing concept in the following text.

Small-emitting water-soluble fluorophores are in demand in many application fields, such as fluorescent labels in *in-vivo* research, indicator dyes in molecular sensing systems, and test cases for theoretical computation studies. In this context, a size-record breaking green-emissive fluorophore 3-hydroxy-isonicotinic aldehyde (HINA, 128 g/mol, λ_{ex} = 525 nm) is investigated in **Chapter 2**. Furthermore, HINA also serves as the model case for demonstrating problems that molecular probes face, and it functions as a suitable indicator moiety in the construction of the SAPs.

In **Chapter 3**, the self-assembling probe (SAP)-based molecular sensing concept is described, where time- and spectra-resolved information is observed for the distinction and quantification of target analytes. Due to the combination of the supramolecular and molecular interactions, thirteen tested structural similar analytes can be distinguished by merely using one probe, which overcame the low-selectivity problem of other current molecular sensing concepts. In addition, the potential application of SAPs in human biofluids is explored.

As an extension of **Chapter 3**, **Chapter 4** explores the mechanism of the high-selective SAP systems, which is essentially the supramolecular self-assembling of the SAP-analyte conjugates driven by the non-covalent interactions between the adjacent molecules. Therefore, the SAP concept was also applied for chirality sensing as the chiral analyte created a chiral environment and enhanced the chiral signal of the SAP-analyte conjugate.

Finally, the conclusion of this thesis is given in **Chapter 5**. Outlook and suggestions regarding the further investigation of the SAP concepts are included as well.

Kurzzusammenfassung/Abstract in German

Supramolekulare Prinzipien wie Selbstorganisation, Stimulierbarkeit und Anpassungsfähigkeit sind weit verbreitete Konzepte für die Entwicklung fortschrittlicher Funktionsmaterialien, wobei sie insbesondere die Entwicklung der Analytik erheblich beeinflusst haben. In den letzten zwei Jahrzehnten haben zahllose supramolekulare Binder, molekulare Sonden und Chemosensoren in Verbindung mit innovativen Assays zu einer Revolution in der molekularen Sensorik und medizinischen Diagnostik geführt. Dennoch leiden die meisten dieser molekularen Sensorsysteme an zu geringen Bindungsaffinitäten oder -selektivitäten oder ihrer Zersetzung in komplexen Medien wie beispielsweise biologische Flüssigkeiten, wodurch ihre praktischen Anwendungen stark einschränkt wird. Die Entwicklung neuer molekularer Sensorsysteme, welche den praktischen Anforderungen gerecht werden können, ist daher nach wie vor eine der wichtigsten Aufgaben der supramolekularen Chemie. Im Vergleich zu traditionellen, auf Chromatographie basierenden molekularen Sensing-Strategien, welche zuverlässig, aber in der Regel zeit- und kostenintensiv sind, sowie keine parallele Analyse ermöglichen und zudem eingewiesenes Fachpersonal erfordern, könnten sich spektroskopische Chemosensor- und Sonden-basierte Methoden besser für praktische Anwendungen eignen aufgrund ihrer Kosteneffizienz, einfachen Handhabung und der Möglichkeit zu Highthroughput Screenings.

In dieser Arbeit wird das Konzept der selbstorganisierenden Sonde (SAP) auf der Basis von molekularen Sensoren beschrieben. Durch die Kombination von molekularen Reaktionen und supramolekularen Wechselwirkungen werden sowohl eine hohe Selektivität als auch eine hohe Bindungsaffinität für die Identifizierung und Quantifizierung von Analyten durch den Einsatz der SAP erreicht.

In **Kapitel 1** wird eine allgemeine Einführung dieser Arbeit gegeben, die einen Überblick über die grundlegenden, photophysikalischen Kenntnissen der Lumineszenz gibt. Zunächst werden Übergangsmetallkomplexe, insbesondere Platin(II)-Komplexe, als Hauptkandidaten für die Konstruktion der selbstorganisierenden Sonden (SAPs) kurz beschrieben, einschließlich ihrer grundlegenden photophysikalichen Prinzipien sowie ihrer Anwendungen. Darüber hinaus werden aktuelle molekulare Sensorkonzepte vorgestellt und diskutiert, welche den wesentlichen Hintergrund für das im folgenden Kapitalen vorgeschlagene Sensorkonzept bilden.

In vielen Anwendungsbereichen besteht eine Nachfrage an kleine, emittierende, und wasserlösliche Fluorophore für den Einsatz beispielsweise als Fluoreszenzmarker in der *in vivo*-Forschung, als Indikatorfarbstoffe in molekularen Sensorsystemen und als Testkandidaten für theoretische Berechnungsstudien. In diesem Zusammenhang wird in **Kapitel 2** das größenrekordbrechende, grün-emittierende Fluorophor 3-Hydroxy-Isopicotin-Aldehyd (HINA, 128 g/mol, λ_{ex} = 525 nm) genauer untersucht. Darüber hinaus dient HINA als Modellfall zur Demonstration von Problemen, mit denen molekulare Sonden konfrontiert sind, und es fungiert als geeigneter Indikatorrest bei der Konstruktion der SAPs.

In **Kapitel 3** wird das auf selbstorganisierenden Sonden (SAP) basierende molekulare Sensing-Konzept beschrieben, bei dem die zeitlich- und spektralaufgelösten Informationen zur Unterscheidung und Quantifizierung der Zielanalyten verwendet werden. Durch die Kombination von supramolekularen und molekularen Wechselwirkungen können dreizehn getestete strukturell ähnliche Analyten mit nur einer Sonde unterschieden werden, wodurch das Problem der geringen Selektivität anderer aktueller molekularer Sensorikkonzepte überwunden wird. Darüber hinaus wird die potenzielle Anwendung der SAPs in menschlichen Bioflüssigkeiten erforscht.

Als Ergänzung zu **Kapitel 3** wird der Mechanismus der hochselektiven SAP-Systeme in **Kapitel 4** erforscht. Dieser beruht im Wesentlichen auf der supramolekularen Polymerisation der SAP-Analyt-Konjugate, welchedurch die nicht-kovalenten Wechselwirkungen zwischen den benachbarten Molekülen angetrieben wird. Zusätzlich wurde das SAP-Konzept auch für die Chiralitätserkennung eingesetzt, da der chirale Analyt die chirale Polymerisation des SAP-Analyt-Konjugats auslöst.

Schließlich wirdok das Fazit dieser Arbeit in **Kapitel 5** gegeben und ein Ausblick und Vorschläge zur weiteren Erforschung des SAP-Konzepts andiskutiert.

1 General introduction

1.1 Fundamental concept of luminescence

The term luminescence is defined as the spontaneous emission of radiation from an electronically excited state species or a vibrationally excited species that are not in thermal equilibrium with its environment. Therefore, luminescence is also considered a cold light as the temperature does not increase during the luminescence process.[1] Different types of luminescence are classified according to their excitation mode. For instance, the well-explored photoluminescence that consists of fluorescence and phosphorescence (or delayed fluorescence) is initiated by the absorption of light (photons).[2-3] Luminescent compounds, also known as luminophores, can be divided into three different types: *i*) inorganic compounds such as lanthanide ions (*e.g.*, Eu^{3+}, Tb^{3+}), semiconductor nanocrystals (*e.g.*, CdSe), and uranyl ion (UO_2^+); *ii*) pure organic compounds such as aromatic hydrocarbons (*e.g.*, naphthalene, anthracene, pyrene, perylene) and derivatives, dyes (fluorescein, rhodamine) and polyenes; *iii*) organometallic compounds such as ruthenium complexes, copper complexes, platinum complexes and complexes with lanthanide ions or fluorogenic chelating agents.[3]

Luminescence is an important property and has been wildly applied in the construction of advanced materials, for example, semiconductors and organic light-emitting diodes (OLEDs) materials.[4-5] Photoluminescence, one of the particular cases of luminescence, is attractive in the sensing field. Thus, photoluminescence is also the main interest of this thesis due to its high sensitivity, ease of monitoring, and fast response properties.[3, 6-9] Before elaborating on the applications of photoluminescence, the fundamental concepts of the photoluminescence process are introduced in this chapter.

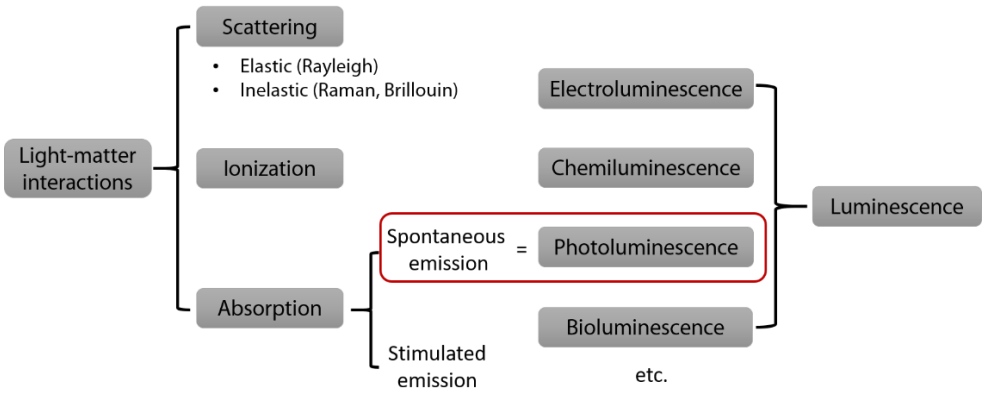

Figure 1.1. The position of photoluminescence in the framework of the light-matter interaction.

Generally, molecules are usually present in their energetic lowest state, the ground state (S_0). After the absorption of the photons, the molecule reaches an electronically excited state. Then the excited molecule undergoes a de-excitation process that accompanies the spontaneous emission of photons, called photoluminescence (**Figure 1.1**). The spontaneous emission is classified as fluorescence, phosphorescence, or delayed fluorescence according to their different pathways of returning to the ground state by releasing photons. The possible pathways for the excitation and relaxation process include absorption, internal conversion (IC), fluorescence, phosphorescence, intersystem crossing (ISC), and delayed fluorescence. The detailed information is shown in the following Perrin-Jablonski diagram and briefly explained in the following.

Absorption

Upon the absorption of photons, the ground state molecules are brought to the excited state in higher energy levels, *e.g.*, S_1 and S_2. Electronic transitions can occur in the spectra range of ultraviolet (UV), visible (vis), and near-infrared (IR).[3, 10]

In order to understand the electronic transition, here the molecular orbital (MO) theory is briefly introduced.[11] There are several types of molecular orbitals, including σ orbitals and *p* orbitals formed from atomic orbitals. For instance, σ orbitals can be formed either from two *s* atomic orbitals, one *s* and one *p* atomic orbitals, or two *p* atomic orbitals with a collinear axis of symmetry. The molecular bond is formed by the overlay of two molecular orbitals: the molecular σ orbitals correspond to the σ bond, and molecular *p* orbitals result in the π bond. After absorbing a photon of proper energy, one of the π electrons can promote to an antibonding orbital called π^* orbital, and the corresponding transition is named $\pi \rightarrow \pi^*$. The transitions of σ electrons correspond to $\sigma \rightarrow \sigma^*$ and $\sigma \rightarrow \pi^*$, which are usually not considered due to the required higher energy (far UV range). Apart from those, the orbitals occupied by nonbonding electrons are called *n* orbitals. Promoting a nonbonding electron to an antibonding orbital is possible, and the transition is named $n \rightarrow \pi^*$. **Figure 1.2** shows a molecular orbital diagram of formaldehyde.

After being exciting by light, one of the nonbonding electrons located on the highest occupied molecular orbitals (HOMO) promotes to the lowest unoccupied molecular orbital (LUMO), corresponding to the $n \rightarrow \pi^*$ transition. Then, the molecule reaches to the excited state. According to the spin direction of these two electrons, two different excited states are possible.

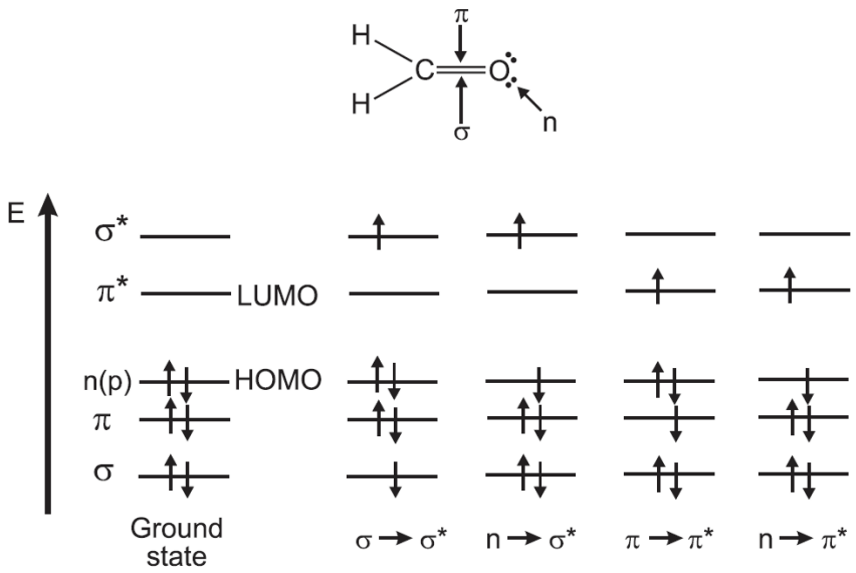

Figure 1.2. Energy levels of molecule orbitals for formaldehyde molecule and the possible electronic transitions. HOMO: highest occupied molecular orbitals, LUMO: lowest unoccupied molecular orbitals. Reprint with permission from ref [3]. © 2012 Willey.

If the spin of those two electrons, one in the *n* orbitals and the other in π^* orbitals, is in the opposite direction, it refers to a singlet excited state (**Figure 1.3**). On the contrary, if they are in the same spin direction, the excited state is a triplet state (**Figure 1.3**). In other words, the absorption can be understood by the rearrangement of the electron density of the molecules induced by the absorption of the photons.[3]

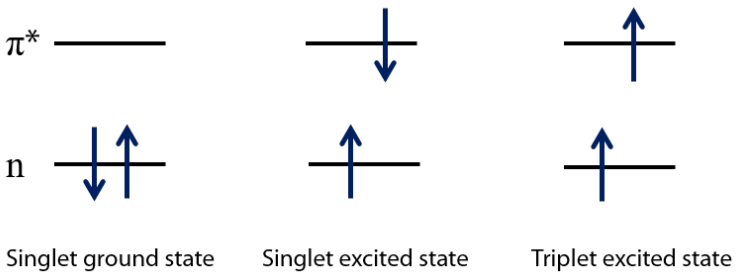

Figure 1.3. Electron configurations for singlet ground state, singlet excited state, and triplet excited state.

The absorption spectrum reflects the relationship between the absorption strength (absorbance or optical density) of the molecules and the wavelength of the incident light. Lambert-Beer's law[12] shows the direct correlation between the absorption intensity (A), the concentration of the molecule (c), the pathlength of the light (d), and the extinction coefficient (ε):

$$A = \lg(\frac{I_0}{I_1}) = c * d * \varepsilon \qquad \textbf{Eq. 1.1}$$

In the equation, I_0 refers to the intensity of the incident light, I_1 refers to the intensity of the transmitted light. The extinction coefficient (ε) is a material constant representing the probability of the electronic transition.

After absorption, the molecules in the excited state will relax to their ground state *via* different pathways, which can be classified into two major groups depending on whether photons emit during the de-excitation (de-active) process. Non-radiative transitions that mean no photon emitting include vibrational relaxation (VR), internal conversion (IC), and intersystem crossing (ISC). The de-excitation process accompanying the emission of photons is called radiative transition, including fluorescence and phosphorescence. All of these processes are considered and illustrated in the Perrin-Jablonski diagram below (**Figure 1.4**).[3, 13]

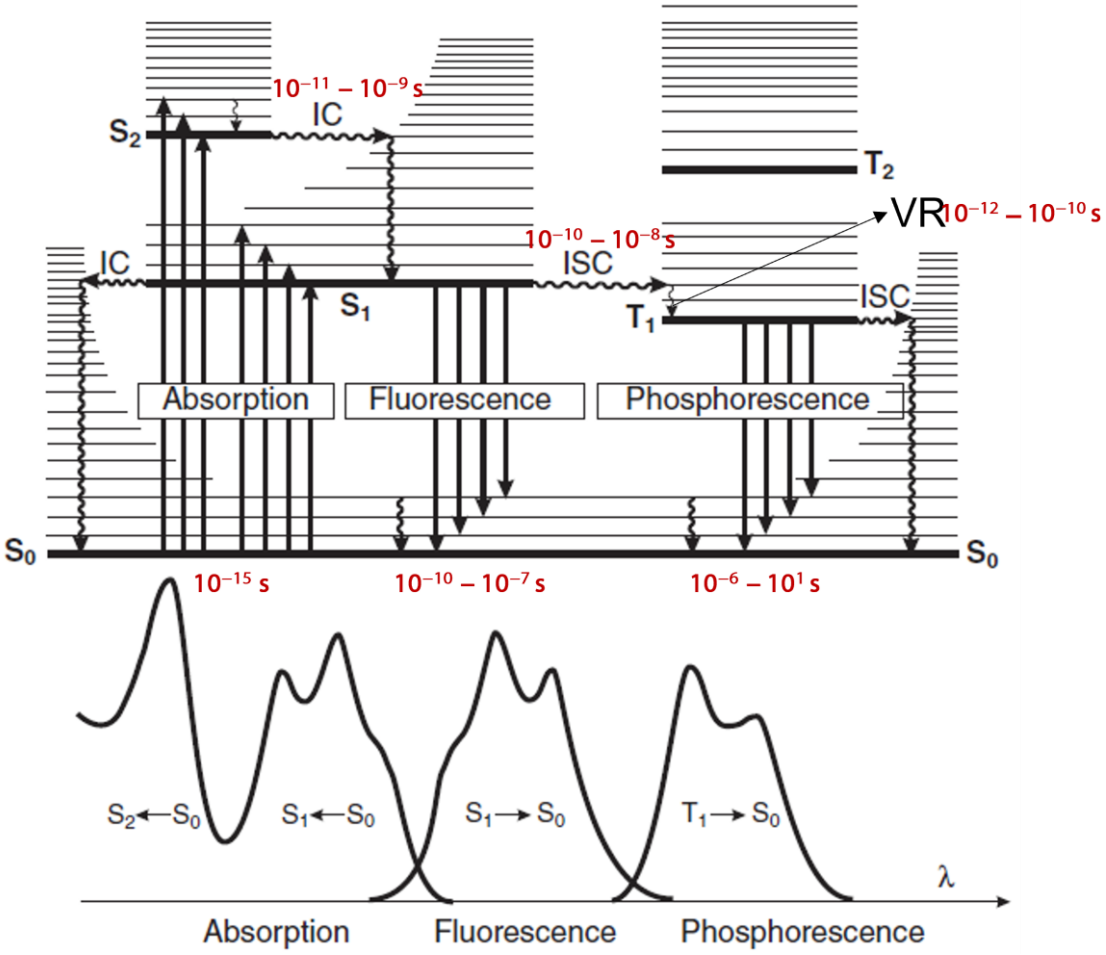

Figure 1.4. Illustration of Perrin-Jablonski diagram and the relevant position of the absorption, fluorescence, and phosphorescence spectrum. The characteristic time of each transition process is labeled in red. The straight arrows represent radiative processes. The up-arrows correspond to the absorption process while the down-arrows correspond to the emission processes, and the wavy arrows represent non-radiative ones. In the diagram, S_0, S_1, and S_2 represent the singlet ground state, first and second electronic excited states, respectively. T_1 represents the excited triplet state. Adapted with permission from ref [3]. © 2012 Willey.

The Perrin-Jablonski diagram shows that S_0, S_1, and S_2 represent the singlet ground state, first, and second electronic excited states, respectively. T_1 and T_2 represent the first and second electronic triplet excited states, respectively. At each electronic energy state, the molecules can exist in several vibrational energy levels, depicted as 0, 1, 2, and 3. Besides, several processes caused by the interactions between molecules are excluded in this diagram, such as quenching, energy transfer, excimer formation, and solvation.

Non-radiative transition

As shown in the Perrin-Jablonski diagram (**Figure 1.4**), the relaxation of electrons from a higher vibrational level to their low vibrational levels in the same electronic state is termed vibrational relaxation (VR). Vibrational relaxation is a rapid process with an average lifetime of $< 10^{-12}$ s. Internal conversion (IC) is another non-radiative relaxation in which the electron in the ground vibrational levels of the higher energy electronic state directly passes into a high vibrational level of a lower energy electronic state of the same spin state, for instance, $S_2 \rightarrow S_1$ transition. In other words, internal conversion can be understood as the vibrational relaxation in different electronic energy states. Therefore, a molecule in an excited state can return to the ground state without emitting photons by combining vibrational relaxation and internal conversion. The term intersystem crossing (ISC) is the relaxation of electrons from a higher energy electronic excited state to a lower energy state with an opposite spin direction, for instance, the $S_1 \rightarrow T_1$ transition (**Figure 1.4**). In principle, the transition from singlet state to triplet state is forbidden (spin selection rule),[14] but can be made possible by the spin-orbit coupling (SOC). The amount of the intersystem crossing depends on the singlet and triplet states involved. For example, if the transition $S_1 \rightarrow S_0$ is of $n \rightarrow \pi^*$, the intersystem crossing is often efficient.[3]

Radiative transition

Unlike non-radiative transition, radiation transition refers to the one in which the release of the energy occurs by emitting photons when an excited molecule returns to the ground state. Two processes are mainly included: one is fluorescence emission, and the other is phosphorescence.

Fluorescence

The emission of a photon from the excited singlet state to the ground state ($S_1 \rightarrow S_0$) is called fluorescence, and the technique used to characterize this phenomenon is fluorescence spectroscopy. Fluorescence emission competes with non-radiative pathways either to the ground state or to the lowest excited triplet state *via* internal conversion and intersystem crossing. Due to the energy loss of the vibrational relaxation in the excited state, the

fluorescence emission spectrum is located at longer wavelengths (lower energy) than the absorption spectrum, although the 0→0 transition in the first approximation is the same for both processes. Furthermore, the differences between the vibrational levels are similar in the ground and excited states, so the fluorescence emission spectrum ($S_1 \rightarrow S_0$) is often a mirror imaging of the first absorption band ($S_0 \rightarrow S_1$), which is the "mirror image" rule.[15] The energy gap (expressed in wavenumbers) between the maximum of the first absorption band and the maximum fluorescence is called the Stokes shift.[3, 13]

Noteworthy, the emission of a photon occurs in the same time scale as the absorption, 10^{-15} s, but excited molecules can stay in the S_1 state for a comparably much longer time, in picoseconds to nanoseconds time scales, before emitting a photon or undergoing another non-radiative process. This time that reflects the average lifetime of the molecules in S_1 excited state is called the excited-state lifetime.

Phosphorescence

Apart from fluorescence, after absorbing a photon, the excited electron first relaxes to the triplet excited state *via* ISC, then releases the energy (photon) and returns to the singlet ground state. The emission during this process-or the energy between this excited triplet state and the single ground state-is defined as phosphorescence. In brief, the transition in different energy states is $T_1 \rightarrow S_0$ for phosphorescence emission, while that for fluorescence emission is $S_1 \rightarrow S_0$. As mentioned above, the transition from a triplet state to a singlet state is actually "spin-forbidden," but it can be observed if the spin-orbit coupling consists. It is worth mentioning that the presence of heavy atoms with a large atomic number, *e.g.*, Br, Pb, Pt, increases the spin-orbit coupling (SOC) possibility of the molecule and thus favors phosphorescence emission.

Compared to fluorescence, the process of phosphorescence emission is much less likely to occur and is much slower, in a time range of 10^{-6}-10^{1} s. Because of the slow process, the possibility of energy loss through collisions with solvent molecules and heat loss increases. Therefore, phosphorescence measurement often requires a low temperature and(or) a rigid medium to minimize the molecule motion. Under these conditions, the lifetime of phosphorescence can be up to seconds, even minutes or more, which means phosphorescence emission may be visible for some time after removing the excitation light source.

Since the energy of the lowest vibrational level of the triplet state (T_1) is lower than that of the singlet state, the phosphorescence spectrum is located at a longer wavelength range than the fluorescence spectrum, see **Figure 1.4**.

Lifetime (τ) and quantum yield (Φ) are the important characteristic parameters for luminophores and are associated with the rate constants of the de-excitation process mentioned above (**Eq. 1.2-1.3**).[3, 13] For instance, fluorescence quantum yield is the ratio of the number of the emitted photons to the number of the absorbed photons, reflecting the efficiency of the radiative transition of a fluorophore.

$$\tau_s = \frac{1}{k_r^s + k_{nr}^s} \quad \textbf{Eq. 1.2}$$

$$\Phi_f = \frac{k_r^s}{k_r^s + k_{nr}^s} = k_r^s \, \tau_s \quad \textbf{Eq. 1.3}$$

k_r^s denotes the rate constant of the radiative transition from the excited singlet state to the ground singlet state, while k_{nr}^s represents the non-radiative state.

Delayed fluorescence, another mechanism in the de-excitation process, is rarely observed compared to phosphorescence.[3] In short, after relaxation to a triplet state ($S_1 \rightarrow T_1$), the excited-photon can return to the singlet excited state *via* internal conversion driven by a thermal activation ($T_1 \rightarrow S_1$), then the emission of the $S_1 \rightarrow S_0$ transition is called delayed fluorescence. This fluorescence emission is thermally activated, and thus the efficiency increases with the increasing temperature.

1.2 Transition metal complexes

1.2.1 General introduction of transition metal complexes

Organometallic compounds are one of the major groups of luminophores. In particular, the transition metal complexes (TMCs) have been attractive for a long time due to their remarkable photophysical and electrochemical properties.[16-23] Apart from the metallic characteristics of the *d*-block elements, such as malleability and ductility, the particular electronic configurations provide rich photophysical properties compared to the main group elements.[24-27] Firstly, the partly unoccupied *d* orbitals of the elements allow for the additional electronic transition (*d*→*d* transition) after absorbing photons, enabling the light absorption of the complexes covering the whole visible range. Secondly, as mentioned before, heavy atoms can enhance the spin-orbital coupling (SOC) to promote the intersystem crossing process of the excited photons, resulting in the $S_1 \rightarrow T_1$ transition. Room temperature phosphorescence and long excited lifetime thus can be observed with many of the transition metal complexes. Thirdly, the energy gap between the transition elements' potential oxidation states is relatively small, causing various oxidation states. Therefore, transition metal complexes, particularly the d^6, d^8, and d^{10} transition metals, such as Ru(II), Os(II), Ir(III), Pd(II), Pt(II), Ag(I), Cu(I), and Zn(II), have been widely applied

in organic light-emitting diodes (OLEDs),[28-31] dye-sensitized solar cells (DSSCs),[32-34] light-emitting electrochemical cells (LEECs),[35-38] photosynthesis and photocatalysis,[39-40] luminescence echinochromes materials,[41-42] non-linear optical (NLO) materials,[43] spin-cross over (SCO) materials,[44-45] sensing[9, 46] and bio-relevant application such as bio-imaging,[47] drug delivery, and diagnostics.[48-49]

Electronic transitions occur after the absorption of photons, and the complex laying in the ground state is then brought to the excited state. However, the electronic transition for transition metal complexes is not as simple as for the pure organic molecules. Before introducing the electronic transition, a brief description of the molecular orbitals for the metal complexes is needed. Firstly, there are five different types of *d* orbitals in transition metals. Three of them, namely d_{xy}, d_{xz}, and d_{yz}, have their lobes directed between the Cartesian axes, while the other two, namely d_{z^2} and $d_{x^2-y^2}$, are directed along these axes (**Figure 1.5**a). The ligand field theory is an expansion of crystal field theory, which assumes the transition metal center is positively charged while the ligand displays negative charges in the complex. These five *d* orbitals are not energetic degenerated and split into groups depending on the geometry of the metal complex that originated from the arrangement and the nature of the ligand. For instance, the *d* orbitals in an octahedral geometry metal complex split into the stabilization t_{2g} set that includes d_{xy}, d_{xz} ,and d_{yz} orbitals, and the destabilization e_g set that includes d_{z^2} and $d_{x^2-y^2}$ orbitals (**Figure 1.5**b). The energy between these two different orbital sets is termed as Δ_{oct} and can be evaluated from the electronic absorption spectroscopic data.

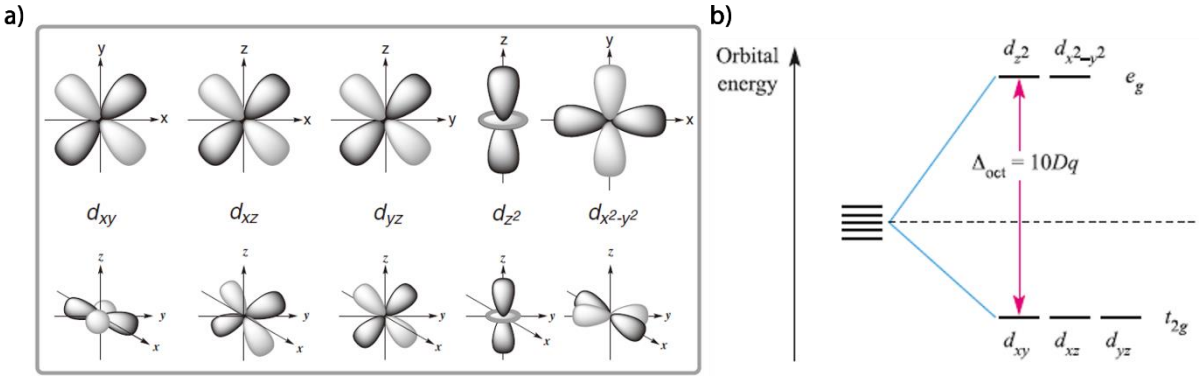

Figure 1.5. a) Illustration of five *d* orbitals of transition metals, each of them is represented in two different views. b) Splitting of the *d* orbitals in an octahedral crystal field. Adapted with permission from ref[50]. © 2012 Pearson Education Limited.

According to the molecular orbital (MO) theory that considers covalent interactions between the metal center and ligands, several MOs can be generated for the metal complex (ground state) and classified according to their predominant atomic orbital contributions, including: *i*) bonding,

ligand-centered $\sigma_{L,}$ and π_L orbitals; *ii*) essentially nonbonding, metal-centered π_M orbitals of e_g symmetry; *iii*) antibonding, metal-centered π_M* orbitals of e_g symmetry; *iv*) antibonding ligand-centered π_L* orbitals, and *v*) antibonding metal-centered σ_M* orbitals.[51] **Figure 1.6** shows the MO diagram for an octahedral transition metal complex in which the σ_L and π_L orbitals are fully occupied while *n* electrons reside in the π_M and π_M* orbitals.

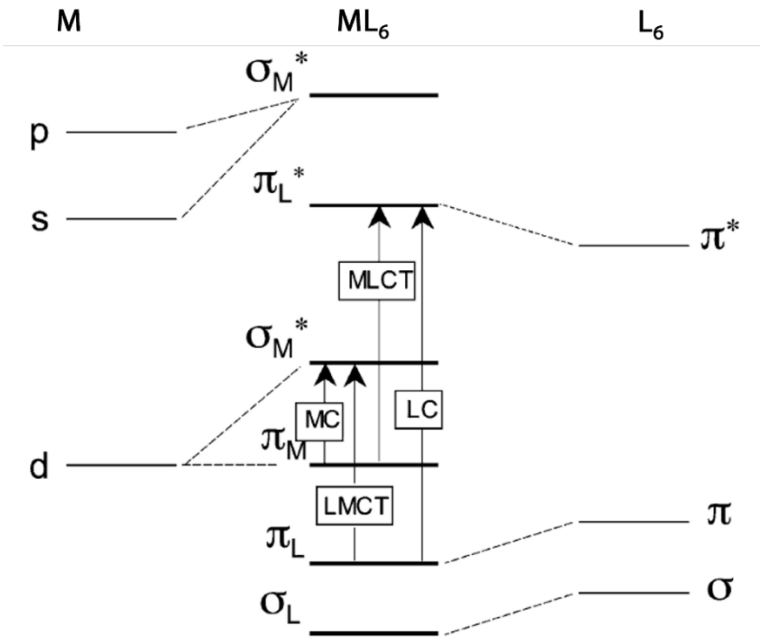

Figure 1.6. Illustration of the molecular orbitals diagram for an octahedral transition metal complex. The arrows indicate the possible electronic transitions based on the localized MO configuration. Adapted with permission from ref [51]. © 2007 Springer.

After being excited by light, one electron from the occupied orbitals promotes to the unoccupied orbitals, and several electronic transitions can occur. According to the contributions of the molecular orbitals, these transitions can be classified mainly as: ligand-centered transition (LC), metal-centered transition (MC), metal-to-ligand charge transfer transition (MLCT), and ligand-to-metal charge transfer transition (LMCT). The relative energy position of the generated excited electronic configuration depends on the nature of the ligands and the metal centers, and therefore different tunable photophysical and electrochemical properties can be observed by the variation of the ligands and metal centers.[52]

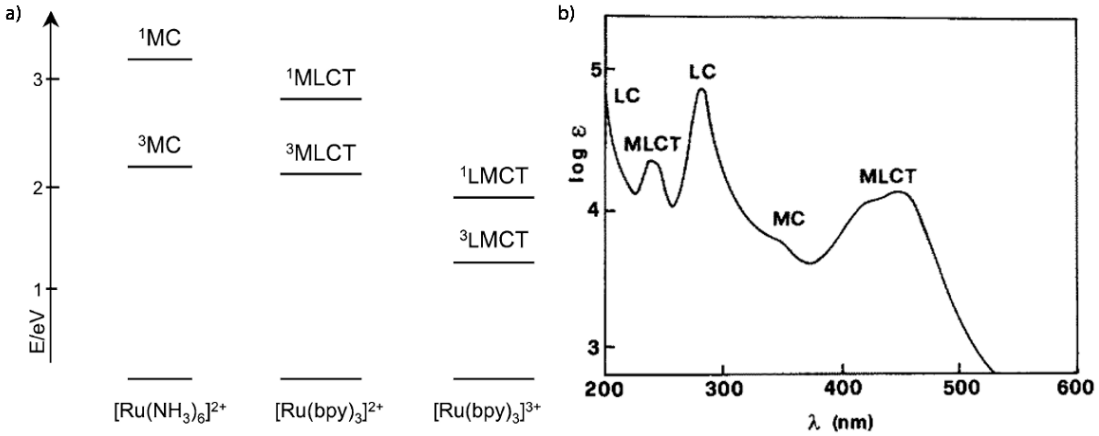

Figure 1.7. a) Illustration of energy level diagrams for $[Ru(NH_3)_6]^{2+}$, $[Ru(bpy)_3]^{2+}$, and $[Ru(bpy)_3]^{3+}$. b) Absorption spectrum of $[Ru(bpy)_3]^{2+}$ in aqueous solution at room temperature. Reprinted with permission from ref [51]. © 2007 Springer.

1.2.2 Photophysics of platinum(II) complexes

The platinum element lies in the third row of the *d*-block transition metals and adopts a d^8 electronic configuration in its oxidized state +2, which makes it prefer to form a square planar geometry complex in the strong ligand field (**Figure 1.8**a).[50, 53] This square conformation is responsible for many key features that characterize the absorption, luminescence, and other excited states properties of the Pt(II) complexes.[53-55]

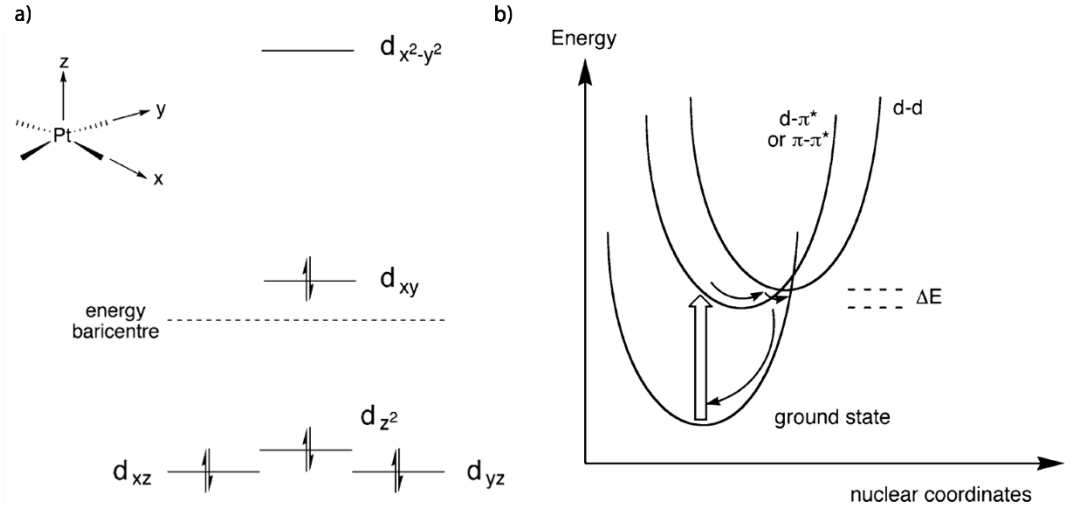

Figure 1.8. a) Illustration of the *d* orbital splitting of the square planar geometry Pt(II) complexes. b) Harmonic potentials illustrating the ground and excited states of a Pt(II)-complex. The non-emissive *d-d* states are thermally accessible from other (emissive) states such as MLCT or LC. Reprinted with permission from ref [53]. © 2007 Springer.

As shown in **Figure 1.8**a, the $d_{x^2-y^2}$ orbital is highly antibonding. If this orbital is populated after the absorption of photons, the molecule will undergo a distortion upon the formation of the *d*→*d* transition, and the Pt-L bond lengths increase. This is not a favorable case for the

luminescence since the thermal accessibility of the isoenergetic crossing point where non-radiative relaxation (internal conversion or intersystem crossing) from the excited states to the ground state can occur. This is why those Pt(II) complexes with a simple inorganic ligand, such as $[PtCl_4]^{2+}$, are always not emissive at room temperature. However, LC and MLCT excited states can be formed by introducing conjugate aromatic ligands, which can partly solve this problem. Pt(II) complexes can thus have a strong emissive only with a large ΔE value (**Figure 1.8**b).

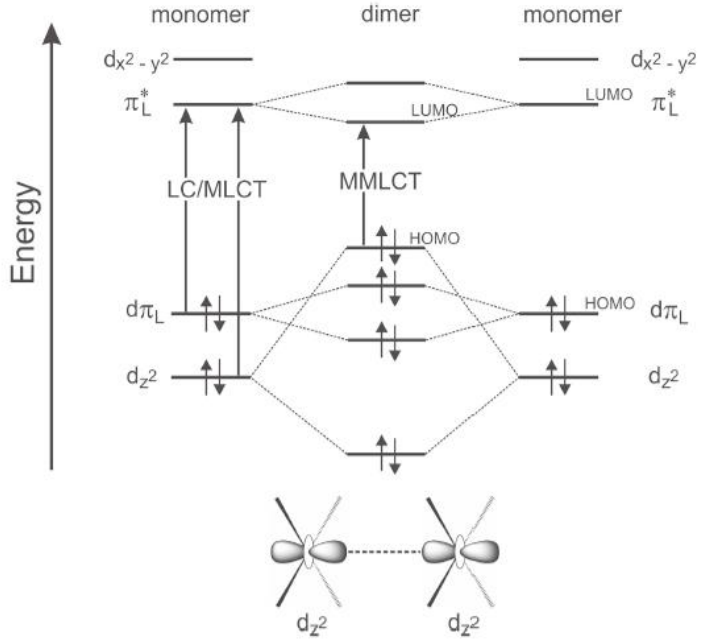

Figure 1.9. Illustration of simplified molecular orbital (MO) diagram of two interacting platinum(II) complexes at their ground states. The diagram shows the intermolecular d_{z^2} orbitals overlap and its influence on the energy of the MO levels. Reprinted with permission from ref[54]. © 2015 The Chemical Society of Japan.

Unlike other transition metal complexes, the flat square planar geometry of Pt(II) complexes allows the intimate interactions with other molecules, *i.e.*, intermolecular stacking or dimerization in the ground state and the excimer formation in the excited states.[53-54] In the ground state of the complex, the fully occupied d_{z^2} orbitals in the metal center usually do not react with ligands and are prone to interact with the surrounding species, such as the solvent molecules or the neighboring platinum complex. In the latter case, the energy of the highest occupied metal-based molecular orbitals is increased compared to that of the isolated molecules so that the lowest-energy electronic transitions are shifted to lower energies compared to the LC or MLCT energy gap. This leads to a switchover of the lowest-energy excited state (**Figure 1.9**). A new excited state between these two Pt(II)-complex molecules is formed caused by the metal-metal-to-ligand charge transfer (MMLCT). For those complexes with planar aromatic

ligands, π-π interactions between ligands of the neighboring molecules are also possible, and this charge transfer is termed ligand-metal-metal charge transfer (LMMCT). It is worth noting that these kinds of CT transitions strongly depend on the metal-metal distance and orientation, and the typical distance of the intermolecular interaction is 3 - 3.5 Å.[53]

1.2.3 Applications of Pt(II) complexes

1.2.3.1 Supramolecular assembly

Supramolecular chemistry is a powerful tool for creating large functional complex architectures because of its self-organization properties. The main driving forces for self-assembling (or self-organization) are the dynamic interactions, including non-covalent interactions (*e.g.*, electrostatic hydrogen bonding, π-π stacking, Van der Waals force, metal-metal interactions) and covalent interactions (dynamic covalent bonding), between the smaller and discrete entities in the supramolecular systems. Owning to the Pt···Pt and π-π interaction, the square planar Pt(II) complex has been employed as an efficient motif in the bottom-up approach toward the preparation and development of novel molecular materials in the last decades.[19, 54, 56-60] In this subchapter, several examples are given.

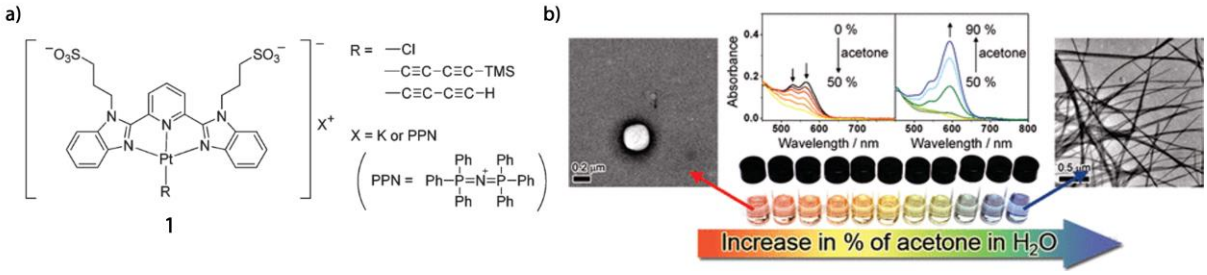

Figure 1.10. a) Chemical structures of the amphiphilic anionic platinum(II) bzimpy complexes. b) The changes in the color, absorption spectra, and the morphology of the solutions of the complexes with the increase of acetone in the water-acetone mixture solvent. Reprinted with permission from ref [61]. © 2011 American Chemistry Society.

Due to the weak and non-covalent nature of the Pt···Pt interaction, the so-formed assemblies are generally very sensitive to the microenvironment, such as temperature, solvent composition, and pH.[55, 61-64] Because the microenvironment changes directly affect the distance and orientation of the metal centers, it consequently varies the spectroscopic properties and nanostructures of the complexes. For instance, Yam's group reported a series of alkynylplatinum(II) complexes bearing an amphiphilic anionic bzimpy moiety as the terdentate ligand (**Figure 1.10**, compound **1**).[61] These complexes have shown interesting aggregation-partial disaggregation-aggregation processes and a morphological transformation from vesicles to nanofibers associated with spectroscopic changes in terms of absorption and emission.

As shown in **Figure 1.10**b, when the ratio of acetone to water is lower than 1 (≤ 50 % acetone), the red absorption centered at 532 nm and 564 nm dropped in with the increase of the acetone content, resulting in the yellow-colored solution once the acetone is up to 50 %. It indicates a partial disaggregation of the complex, and therefore, the Pt···Pt and π-π interactions were disrupted. On a further increase of acetone, the yellow solution gradually changed to blue, and the new absorption bands at 542 nm and 594 nm appeared, which indicated a second aggregation state with stronger Pt···Pt and π-π interactions formed. In general, with the increase of the acetone percentage in the aqueous solution, the solution changed from red (100 % water) to yellow (50 % acetone) to blue (90 % acetone), which were attributed to the variations of the low-lying MMLCT absorption bands. More interestingly, the aggregation processes of such complexes can be easily tuned by the ligand structure. For example, the presented bulky trimethylsilyl group in the ligand PPN can prevent the formation of the second aggregation state. Furthermore, as demonstrated by the scanning electronic microscopy (SEM) and transmission electron microscopy (TEM), the aggregation-partial disaggregation-aggregation process was accompanied by a morphological transition of the aggregation structures from vesicles (high water content) to long fibers (high acetone content). More systematic studies can be found in the reports from the Yam group.[65-66]

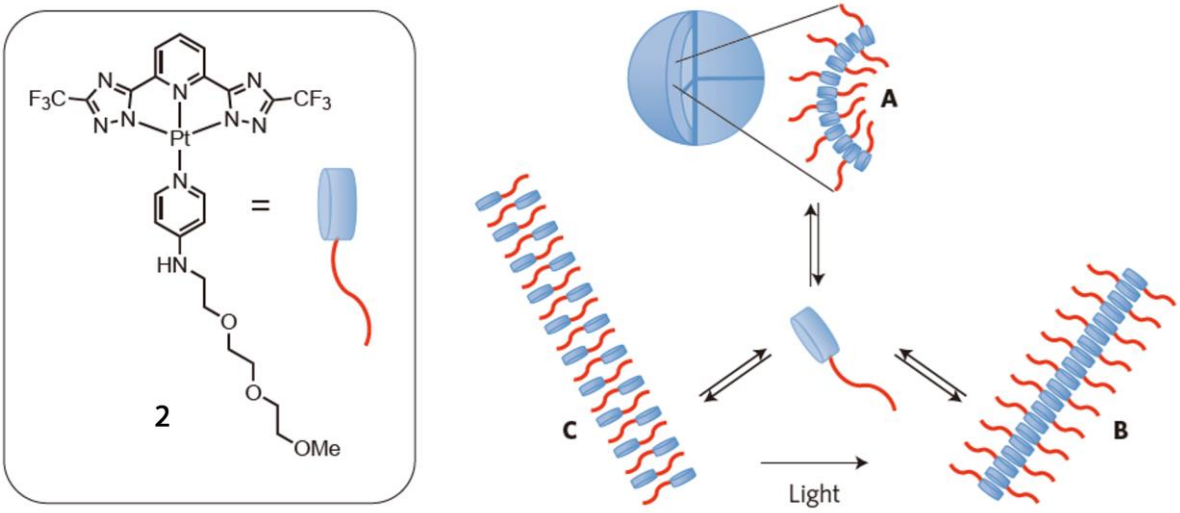

Figure 1.11. Illustration of the different supramolecular self-assembling pathways of the Pt(II) complex **2**. The initial flash injection of **2** in the mixture of dioxane and water gives exclusively the nanoparticles **A**, which over time, or upon the increase of the amount of organic solvent, convert into **C**. The formation of **C** passes through the second metastable state of **B**. The conversation from **C** to **B** could also be possible by using laser light irradiation. Reprinted with permission from ref [67]. © 2016 Springer Nature Limited.

In order to explore the pathways of self-assembling, a class of terdentate dianionic bis(tetrazolate)-pyridine ligand-based amphiphilic Pt(II) complexes were demonstrated by De Cola and coworkers to gain an in-depth understanding of how the highly organized aggregated

with well-defined sized, shapes and properties were formed.[68] In their studies, three assembled species of the complex **2** (**Figure 1.11**) featured completely different photophysical properties and morphology structures were observed and visually monitored by the confocal laser scanning microscope in real-time. Due to the simultaneous presence of a hydrophobic ligand and a hydrophilic triethylene glycol pendant, the complex **2** was predicted to form aggregates under certain conditions, *e.g.*, different components of water-organic mixture solvents. Upon a flash injection of the 1,4-dioxane solution of **2** in water, a metastable state species (assembly **A**) that displayed a strong orange phosphorescence ($\lambda_{max,em}$ = 615 nm) with a long-lived excited lifetime (646 ns) was observed. Such luminescence properties resulted from the establishment of the Pt···Pt metallophilic interactions between neighboring molecules of **1**, owing to the fast (kinetically controlled) formation of the emitting nanoparticles (**Figure 1.11**).

Surprisingly, assembly **A** interconverts over a significantly long period (a couple of weeks) into an alternative aggregated **C**, a thermodynamically stable isoform of **A**. This process was accompanied by the changes in morphological appearance from particles (**A**) to micrometer-long fibers and the changes in photophysical properties. The conversion from **A** to **C** is a slow, thermodynamically controlled process and is highly dependent on the ratio of dioxane/water. The increase of organic solvent content can speed this conversion process up. Moreover, the author demonstrated that this high quantum yield and longer excited lifetime properties of the assembly **C** are not caused by the Pt···Pt and π-π interaction between the adjacent complex molecules but result from an increased rigidity and the shielding of the oxygen quenching exerted by the packing into fiber structures.

Involved by the depth exploration of supramolecular polymerization pathway studies,[69-72] De Cola's group investigated that the formation of assembly **C** process a nucleation elongation mechanism upon addition of complex **2**. Furthermore, the third isoform (assembly **B**) was found during the photophysical studies, and its formation is also a solvent-dependent process. In fact, it was pointed out that assembly **B** was a transient species formed after **A** but then gradually transmitted to **C**, indicating that **B** is a kinetically metastable state. Interestingly, the transition from assembly **C** to **B** was also a possible dynamic process, and it was controlled by laser excitation. The formation of all the assemblies (**A**, **B**, and **C**) and their transitions can be easily monitored by the confocal microscope, which provides clear, direct visual evidence for the controlled assembly and disassembly process.

More recently, the follow-up studies were reported by the same group where not only process-dependent confocal microscope images but also the crystal structures for each assembly state

were characterized.[73] Along with molecular simulation demonstration, the self-assembling process of Pt(II) complexes was evidenced directly both in the experiment and theoretical calculations, which brought an in-depth understanding of the supramolecular polymerization pathways and provided chemists a closer step to the controlled complex supramolecular systems design.[67] In fact, these studies also bring new perspectives to transition metal complexes researchers. More studies were found in the Fernández's group,[74-77] the Wang's group,[78] and the Che's group,[79] which offer a bridge from the fundamental (in)organic chemistry to the supramolecular adaptive chemistry.[80-81]

Owning to the unique Pt···Pt and π-π non-covalent interactions and chemical reactivities, Pt(II) complexes are one of the ideal candidates for the construction of the functional supramolecular assemblies in dimensions varying from 1D (*e.g.*, particles, fibers) to 2D (sheets).[82] With the introduction of the constitutional dynamic chemistry (CDC) concept, it is even possible to create more complicated 3D assembly structures, *e.g.*, molecular cages and molecular machine-like motors.[83-86]

1.2.3.2 Molecular sensing

According to the ligand field theory, the MOs of metal complexes can be rearranged by the change of ligands, and thus a variety of electronic transitions can be observed once the molecules absorb photons. In particularly, Pt···Pt and π-π non-covalent interactions between two adjacent Pt(II) complex molecules, which are originated from the square planar geometry, further enrich the electronic configurations by the formation of MMLCT and LMMCT transition energy bands. As a result, various photophysical properties such as tunable emission bands, long-live excited lifetime, and high quantum yield are often observed with Pt(II) complexes. Therefore, these complexes could be utilized as an optical reporter to reflect the changes of either structures or microenvironments. This high stimuli-responsive functionality offers Pt(II) complexes the capability of serving as an ideal candidate in the artificial receptors design.[87-88]

In general, the design of Pt(II) complex-based probes mainly focuses on two pathways, directly and indirectly sensing. In the former case, the target analyte directly coordinates to the Pt metal center to form the Pt-analyte conjugate that serves as the reporter for analyte detection owning to the analyte-induced photophysical properties changes of the conjugate. Such design is suitable for those analytes with reactive groups that can bind to the metal center, *e.g.*, thiols, pyridines, and amines.[87-88]

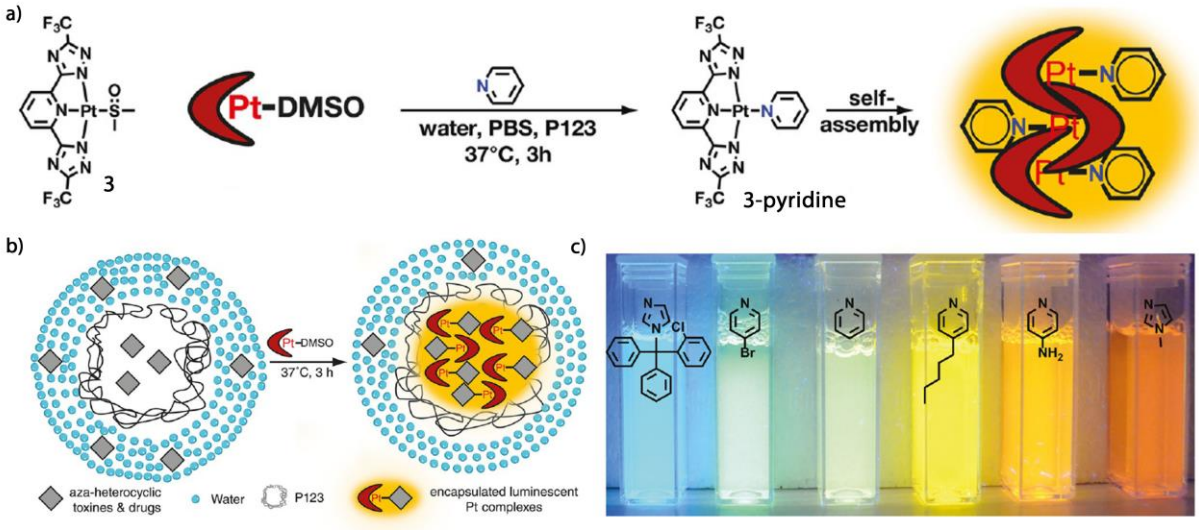

Figure 1.12. a) Chemical structure of the reaction of probe **3** with the represented analyte pyridine. b) Schematic representation of the reaction of aza-heterocyclic analytes with **3** in water containing PEG-PPG-PEG (P123) surfactant. The formed complexes self-assemble into highly luminescent species. c) Photographs of the different luminescent species formed from the reaction of the probe with several represented analytes. Adapted with permission from ref [88]. © 2017 Wiley.

Sinn *et al*. showcased a Pt(II) complex-based reactive phosphorescent probe **3** that can achieve the differential detection of aza-heterocyclic drugs and toxins through the coordination interactions between the probe and target analytes in aqueous media.[88] In their study, 52 different pyridines, imidazoles, and triazoles were investigated out of 23, which formed strongly emissive aggregates upon the coordination with **3**. The emission color of the **3**-analyte conjugates variations from blue to red because of the variety of low-energy MMLCT bands formed by different ligands (**Figure 1.12**). Gathering all the information, including different emission and kinetics features from all the analytes, 23 different Pt-complexing analytes can be clearly distinguished by the principal components analysis (PCA). Some of them were already distinguishable from their different emission colors by the naked eyes. Therefore, probe **3** can serve as an emissive label for aza-heterocyclic drugs and toxins.

In the other scenario, the target analyte does not directly bind to the metal center but to a bridging moiety. For instance, dipicolylamine (DPA) that combines the target analyte with Pt(II) complex is employed to detect metal cations, *e.g.*, Cu^{2+} and Zn^{2+}.[89-90]

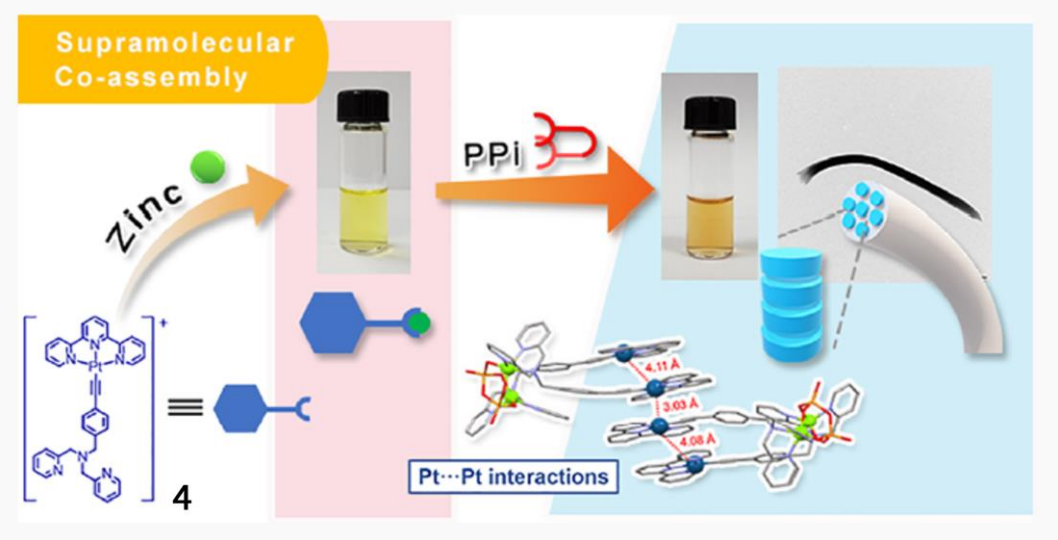

Figure 1.13. Schematic representation of the luminescence sensor **4** enables the detection of Zn^{2+} and PPi through the coordination interaction and the Pt···Pt interaction. Reprinted with permission from ref [89]. © 2021 American Chemical Society.

A dual responsive Pt(II) complex-based luminescence sensor **4** for Zn^{2+} and pyrophosphate (PPi, usually in sodium salt form, $Na_4P_2O_7$) was reported by Yam and coworkers.[89] In their design, a dipicolylamine (DPA) moiety that was conjugated to alkynylplatinum(II) terpyridine functions as the Zn^{2+} captured unit. The newly formed [**4**•Zn^{2+}] complex was used for the detection of PPi.[89] Concretely, Zn^{2+} first binds to the DPA group within the Pt(II) complex through a coordination interaction, resulting in a blue shift of the low-energy absorption band (360-500 nm) and an increase in emission intensity at 615 nm of the sensor **4**. The absorbance and emission studies demonstrated that the binding stoichiometry between **4** and Zn^{2+} is 1:1. Subsequently, upon the addition of PPi, the concentration of [**4**•Zn^{2+}] adduct increases with the absorption band at ~ 650 nm, with a concomitant drop of the higher energy absorption band at ~ 415 nm, accompanied by an isosbestic point at 347 nm. In addition, the emission titration study shows an intensity decrease of the [**4**•Zn^{2+}] adduct emissive bands (~ 600 nm), and a new emission band in the range of 650-850 nm appears.

According to the previous investigation of the Pt(II) terpyridine complexes, these spectroscopic changes were assigned to the newly formed MMLCT transition band caused by the aggregation of the [**4**•Zn^{2+}]-PPi complex. As shown in **Figure 1.13**, these spectroscopic changes can be seen by the naked eyes with color changes, from light yellow to orange. Interestingly, this PPi-induced aggregation of the Pt(II) complex displays a morphological structure change from particles to fibers. Therefore, this work provided new insights into the design of Pt(II) complex-based probes; clearly, not only the direct binding but also the bridging molecules can be utilized as a recognition motif to broaden the range of target analytes.

Apart from the platinum-based transition metal complexes, also palladium complexes are suitable candidates for molecular sensing design because of the d^8 electron configuration and the chemical reactivity of the Pd metal center.[91-92] For instance, a Pd(II) complex-based emission "turn-on" probe **5** was developed by Siddhartha and coworkers, which is applicable for the selective identification and quantification of creatine in buffer solution and biofluids (**Figure 1.14**).[92] In this work, creatinine can coordinate to the Pd center that displays an emission quencher for the naphthylamide core. As a result, the emission of **5** is enhanced after the displacement, which can be used for the detection of creatinine in PBS solution and human blood serum.

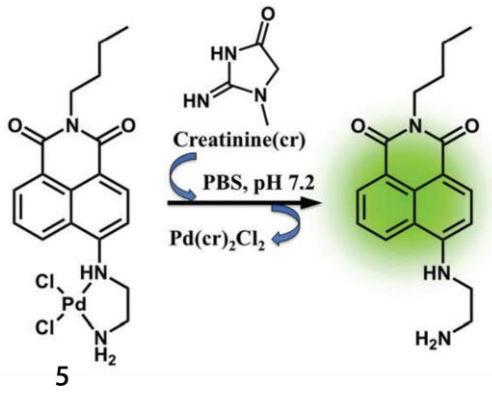

Figure 1.14. Schematic representation of the creatinine detection through the Pd(II) complex-based fluorescent probe **5**. Reprinted with permission from ref.[92]. © 2016 The Royal Society of Chemistry.

Overall, compared to the pure organic molecule probes, d^8 square planar Pt(II) complexes (as well as Pd(II) complex) not only display the tunable spectroscopic properties, *e.g.*, a variety of absorption bands, long-wavelength range emission peaks, and long-lived excited lifetime but also exhibit the analyte-induced self-assembly properties caused by the metal⋯metal interaction and π-π stacking between the adjacent molecules after the aggregation of the metal complexes. Besides, the chemical properties, for instance, the solubility of the metal complex-based probe, can be easily adjusted by changing the ligand moieties owning to the chelating reactivity of the metal center. Therefore, transition metal complexes, especially Pt(II)-based complexes, are attractive for molecular probe design and have been applied for the detection of many analytes, *e.g.*, amino acids, cations and anions, thiols, and amines.[87, 90, 92-94] Furthermore, the high biocompatibility of platinum provides the potential capability for the *in vivo* applications for such Pt(II) complex-based probes.[95-96]

Based on the abovementioned advantages, this thesis proposed and investigated a new molecular sensing concept that relies on a Pt(II) complex bearing a terdentate bis(tetrazolate)-pyridine ligand in **Chapters 3-4**.

1.3 Molecular sensing concepts

Supramolecular chemistry is a highly interdisciplinary field of chemical, biological, and materials science. Nowadays, it has made a significant impact on analytical science development.[97-99] Novel molecular probes, supramolecular binders, and chemosensors combined with innovative assays are leading to a revolution in molecular sensing and medical diagnostics. Although thousands of molecular probes (and chemosensors) have been reported, only a few have reached the clinic requirements and can be further developed for practical applications.[8-9, 100] The reasons are low-binding affinity or low-selectivity or decomposition in the complex media such as biofluids. In other words, the main obstacle in the practical application of molecular probes (or chemosensors) is the difficulty of finding a good balance between the binding affinity and selectivity. For instance, molecular probes usually exhibit high binding affinities to the target analyte owing to the covalent interactions between the probes and analytes of interest.[101-103] However, most molecular probes can not distinguish the analytes with the same reactive functional groups. It is much more challenging to simultaneously achieve high binding affinity and high selectivity by artificial probes and receptors. Therefore, developing new molecular sensing concepts meeting the practical requirements is still one of the frontiers in supramolecular chemistry.

According to the number of the target analytes, the molecular sensing concepts are classified mainly into two categories: single analyte and differential sensing concepts which will be explained in the following. Besides this, chirality sensing and constitutional dynamic chemistry (CDC)-based molecular sensing will be briefly introduced at the end of this subchapter. Before the detailed introduction about the molecular sensing concepts, some ambiguity about the terms is clarified. Following the widely accepted convention and recently published review reports, molecular sensing systems are sorted into two categories according to the different interaction types.[8] Probes refer to those systems forming irreversible covalent bonds with target analytes, and chemosensors refer to those systems that form non-covalent reversible bonds with target analytes.

1.3.1 Single analyte sensing concept

The single analyte sensing concept originated from the "lock-and-key" principle that was firstly proposed by Emil Fisher in 1894.[104] Concretely, the active enzyme has a unique geometric shape that is complementary to the shape of the substrate, which means that the enzyme reacts

explicitly with only one or a very few similar compounds. In general, it is a "one-analyte-one-receptor" paradigm. In a typical design of the single analyte sensing concept, one target analyte can covalently or non-covalently bind to the specifically designed receptor, resulting in signal changes in the chemical properties or photophysical properties of the whole system. The generated signal changes are then employed to identify and quantify the target analyte. In the following, covalent and non-covalent interaction-based single analyte sensing concepts will be generally introduced. As mentioned in **Chapter 1.1**, spectroscopic techniques (absorbance and emission spectrum) are popular in the molecular sensing field owing to their well-understood mechanism and ease of monitoring. Therefore, the following discussion will only concentrate on optical-based molecular sensing systems.

1.3.1.1 The covalent interaction-based single analyte sensing

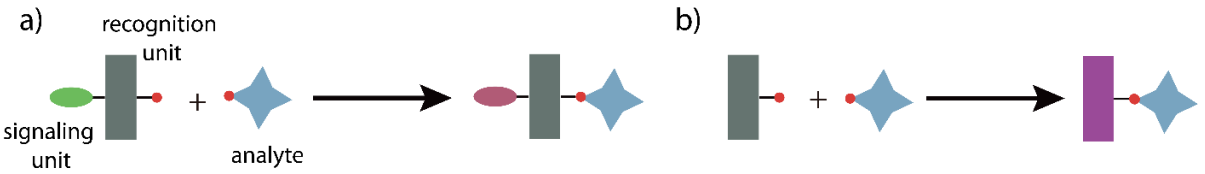

Figure 1.15. Schematic representation of the covalent interaction-based single analyte sensing through a) receptor-spacer-reporter approach, b) the combination of receptor and reporter approach.

Covalent interactions-based single analyte sensing generally refers to the reactive probe systems. As shown in **Figure 1.15**a, a "receptor-spacer-reporter" approach usually is used in the reactive probe design, where a reporter (signaling unit, usually chromophores or fluorophores) is covalently attached to a receptor (target analyte-recognition unit). To achieve the selective distinction of the analyte of interest, the specific-reaction-functional groups need to be included in the design of receptors. Upon the selective covalent binding with the analyte of interest, a signal change, *e.g.*, emission decrease or enhancement, newly formed emission or absorption bands, appears, which can be employed to identify and quantify the analyte. For optical sensing, the photon electron transfer (PET) is a popular mechanism for signal modulation and has been utilized for creating a variety of "turn-on" and "turn-off" fluorescent molecular reactive probes.[97, 102] The PET-based acceptor (electron acceptor)-donor (electron provider) systems can be explained from the perspective of the MOs theory, which was introduced in **Chapter 1.1**. For instance, in a "turn-on" system, after the analyte binding, the HOMO of the donor was lowered, which diminished the electron transferability to the LUMO of the acceptor. As a result, the fluorescence of the donor recovered in the presence of the acceptor. Besides, excited-state intramolecular proton transfer (ESIPT) and intermolecular charge transfer (ICT) are also often-used mechanisms for constructing reactive probes.[105-106]

Since this thesis focuses on the new sensing concept development for small bio-relevant molecules, such as amino acids, biothiols, and amines, several detailed examples for biothiols detection with reactive probes will be introduced in the following.

Biothiols, *e.g.*, L-cysteine (L-Cys), L-homocysteine (L-Hcys), and glutathione (GSH), play critical roles in various physiological functions and pathological conditions because of their chemical reactivities. Moreover, the altered levels of thiols in intra-and extracellular fluids are associated with several human diseases such as leucocyte loss, liver damage, Alzheimer's disease, and HIV.[107] Therefore, biothiols are popular target analytes, and hundreds of different thiol-reactive probes have already been developed.[8, 101-103, 108-110] Typically, the detection of thiols can be achieved by the formation of the covalently linked conjugates between the probes and target analytes. The corresponding covalent reactions include Michael addition, S_N-type, and addition-condensation reactions.

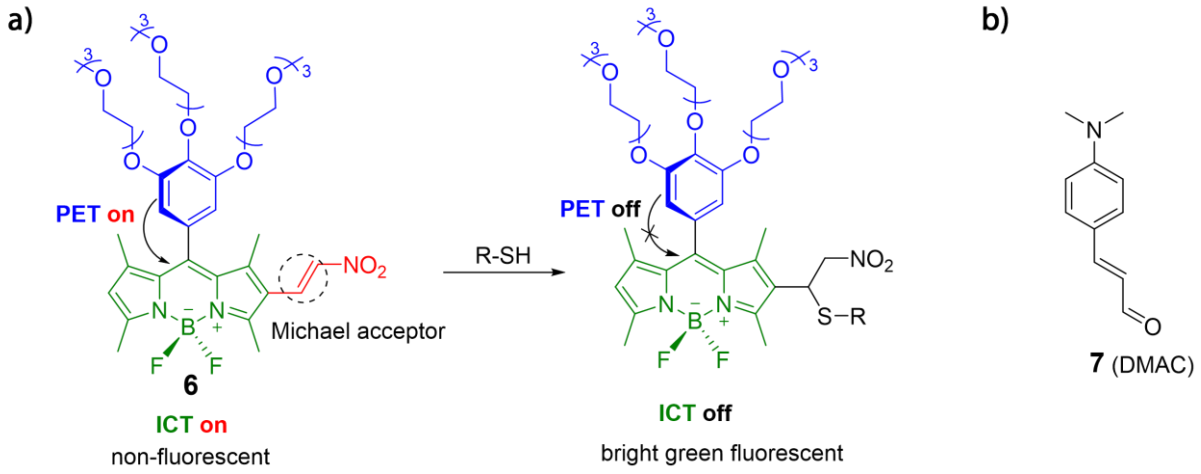

Figure 1.16. a) Schematic representation of the reaction of probe **6** with a thiol-containing analyte. b) Chemical structure of the commercial thiol-reactive probe **7** (DMAC). Figure a) was adapted with permission from ref[111]. © 2012 American Chemical Society.

For instance, Akkaya and coworkers covalently attached a nitroalkene unit to a water-soluble BODIPY dye, obtaining the thiol-reactive probe **6**, which showed a higher emission enhancement upon reacting with L-Cys than with L-Hcys and GSH in aqueous media (**Figure 1.16**a).[111] In this way, L-Cys can be selectively distinguished from other thiols. Besides, the selectivity of the thiol-reactive probes can be achieved by exploiting the distance between two reactive moieties of the analyte, *i.e.*, the -SH and -NH_2 groups.[108, 110] For example, a commercially available chromophore 4-(dimethylamino)cinnamaldehyde (DMAC) with an α,β-unsaturated aldehyde group can form a cyclic addition-condensation product with cysteine, as reported by Strongin, Rusin, and coworkers.[112] In contrast, the adduct is not observed when the probe reacts with L-Hcys because of the far-away distance between -SH and -NH_2 moieties.

As a result, the absorbance of the probe **7** DMAC (**Figure 1.16**b) in the range of 370-450 nm was quenched upon the addition of cysteine, and therefore cysteine can be selectively detected from homocysteine but not cysteinglycine (Cys-Gly) because the distances between -SH and -NH_2 groups in L-Cys and Cys-Gly are the same.

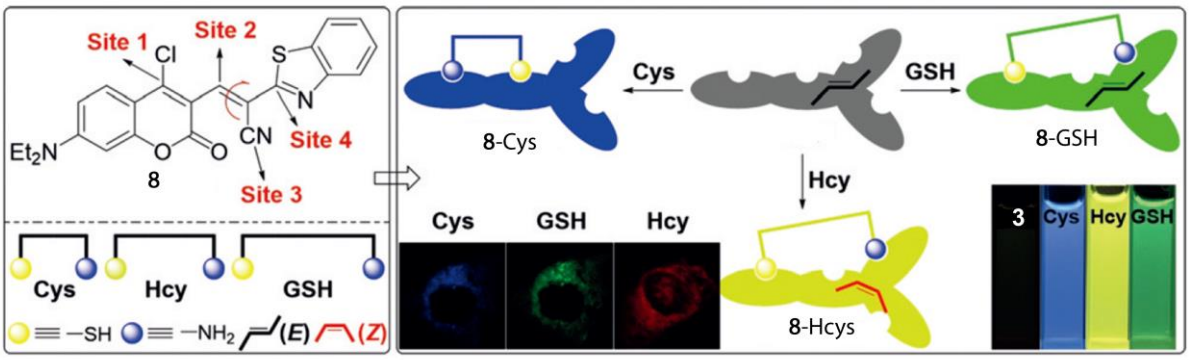

Figure 1.17. Schematic representation of simultaneous sensing of L-Cys, L-Hcys, and GSH using probe **8**. The binding of the probe with different thiols can also be distinguished by the naked eyes through the different colors of the solutions: L-Cys (blue), L-Hcys (yellow), and GSH (green). Reprinted with permission from ref[113]. © 2018 Willey.

In order to improve the selectivity of the reactive probes, multiple reaction binding sites are employed to target the analytes of interest.[113-114] A chlorinated coumarin and benzothiazolylacetonitrile integrated fluorescent probe was demonstrated by Li, Yin, and coworkers.[113] In their study, four binding sites were featured, and different reaction mechanisms were employed to distinguish L-Cys, L-Hcys, and GSH (**Figure 1.17**). In detail, upon binding with different thiols, the probe-analyte conjugates display an emission "turn-on" behavior at different wavelengths at the selected excitation wavelengths. For instance, probe-Cys conjugate shows a strong emission at 457 nm upon the excitation wavelength at 360 nm, while probe-Hcys conjugate displays an emission at 575 nm under the excitation of 480 nm. In this way, L-Cys, L-Hcys, and GSH were successfully distinguished, and the assay was applied for fluorescence imaging in living cells.

Except for the receptor-spacer-reporter approach, the receptor-analyte conjugate can directly as the reporter in some cases (**Figure 1.15**b), mainly seen in the metal-complexes-based reactive probes. In this scenario, not only the metal center as the receptor can target the analyte of interest, but also the generated metal complex-analyte conjugate as the reporter will change its photophysical properties after the analyte coordinating. For instance, the Pt(II) complex probe for aza-heterocyclic drugs and toxins was introduced in detail in **Chapter 1.2.3.2**.[88]

Not limited to the thiol-containing analytes, the reactive probe-based sensing concept has been applied to many other analytes, such as amines, amino acids, carbohydrates, and neurotransmitters, owing to the high binding affinities of the covalent bonding.[8, 100, 102, 115] However, since the specific chemical reactions only work for those analytes with the same reactive functional groups, the selectivity thus becomes a problem. Although multiple binding sites can be included within one probe, it is still challenging for reactive probes to selectively distinguish analytes with a high structural similarity, *e.g.*, L-Cys and Cys-Gly pairs. Besides, elegant molecular design, optimization, and multistep synthesis are generally required, limiting the further practical application of reactive probes.

1.3.1.2 The non-covalent interaction-based single analyte sensing

Continuing with the discussion of the "receptor-spacer-reporter" approach, it can also be applied for the construction of chemosensors, in which the binding interactions between the recognition units and analytes are non-covalent bonds, *e.g.*, host-guest interactions. Therefore, macrocyclic compounds, such as crown and cryptands, cyclodextrins, cucurbit[*n*]urils, and calix[*n*]arenes, become popular receptor units in the design of chemosensors owning to their strong affinities to many target analytes, including amine, amino acids, steroids, and neurotransmitters.[8-9, 97, 116-120]

Following the "receptor-spacer-reporter" pathway, the target analyte can selectively bind to the macrocyclic unit that is usually connected with a chromophore or fluorophore through a linker (spacer), resulting in the changes in photophysical properties of the reporter (chromophore or fluorophore) due to the PET or ICT mechanisms. Many chemosensors have been developed through such design, and some of them were even successfully applied in clinical diagnosis.[121-122]

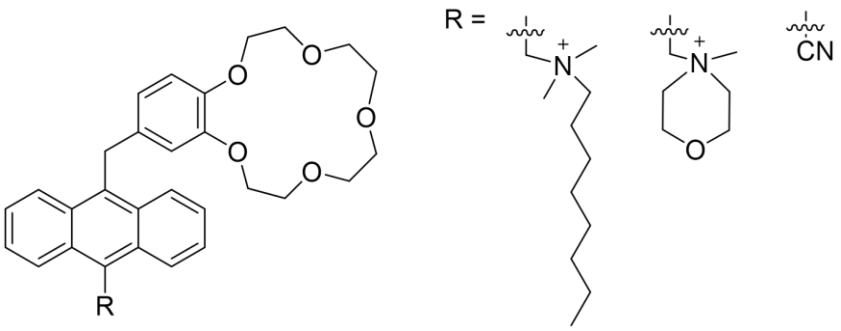

Figure 1.18. Chemical structures of various fluorescent sodium chemosensors.

For instance, the de Silva groups reported a series of such sensing systems.[123-126] In their design, a crown ether was covalently attached to a fluorophore capable of PET (**Figure 1.18**). In the presence of sodium cation, the crown was bound, pulling electron density away from the aromatic ring of the fluorophore, resulting in an interruption of the PET quenching. Thus, a fluorescence "turn-on" sensing for sodium cation was achieved in this way, and based on its emission intensity, the concentration of the present sodium cation was calculated. This system was not limited to sodium cation and can be easily tuned to respond to other cations, such as calcium and potassium. It is now used to monitor cation concentrations in humans and animals in real-time.

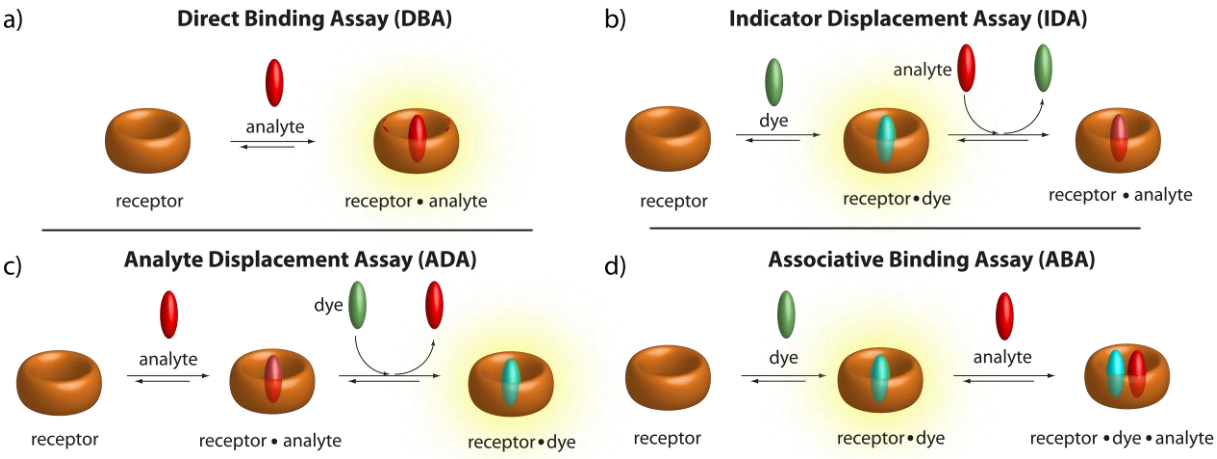

Figure 1.19. Schematic representation of different assay types: a) direct binding assay (DBA), b) indicator displacement assay (IDA), c) analyte displacement assay (ADA), d) associative binding assay (ABA). Reprinted with permission from ref [8]. © 2022 American Chemical Society.

Apart from the "receptor-spacer-reporter" approach, also named the directly sensing pathway, indirectly sensing, *e.g.*, indicator displacement assay (IDA), is another popular design methodology for the chemosensors construction, indicator displacement assay (IDA), see **Figure 1.19**b. Specifically, an indicator dye is first pre-complexed with the receptor molecule and displaced again when a stronger binding or higher concentrated analyte is present. The released dye is thus employed as the indicator for the analyte binding. Such IDA was first popularized by the Anslyn's group and has been further developed by many other groups,[97, 127] for instance, Nau's group,[128-129] Biedermann's group,[130] Anzenbach jr's groups,[131] Hooley's group[132], for a variety of analytes detection, such as amino acids, amines, drugs, and steroids.

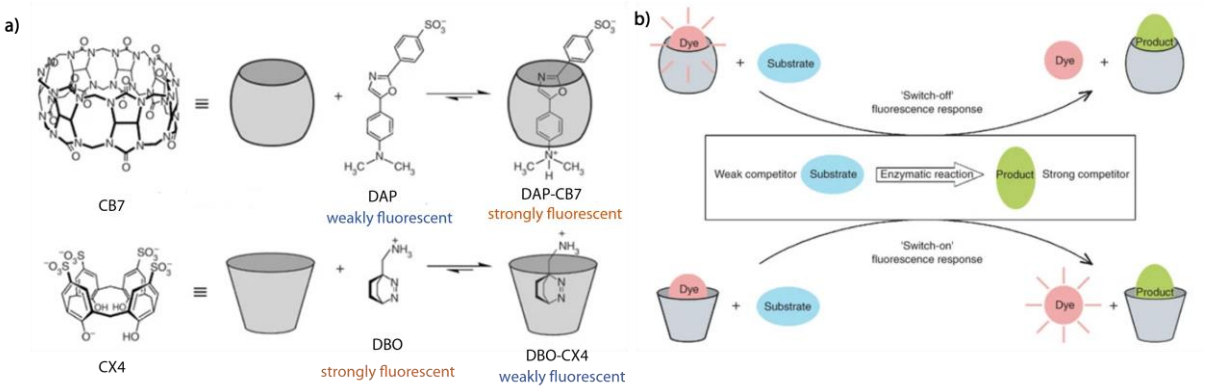

Figure 1.20. a) Chemical structures of the used macrocyclic compounds (CB7 and CX4) and dye molecules (DAP and DBO). b) Schematic representation for monitoring cationic products of an amino acid decarboxylase catalyzed reaction. Adapted with permission from the ref[129]. © 2007 Springer Nature Limited.

For example, an IDA-based competition assay has been demonstrated to monitor cationic products of amino acid decarboxylase catalyzed reaction (**Figure 1.20**).[129] Macrocyclic compounds cucurbit[7]uril (CB7) and *p*-sulfonatocalix[4]arene (CX4) interact with two dye molecules, dapoxyl (DAP) and aminomethyl-substituted 2,3-diazabicyclo[2.2.2]oct-2-ene(DBO), respectively. These two host-dye pairs display different emission properties upon binding to the analytes. The emission of the [DAP-CB7] complex is strongly quenched because of the displacement of DAP, while the weak emission of [CX4-DBO] pair will be enhanced after the binding of the analyte and displacement of DBO. Both CB7 and CX4 have strong binding affinities for the cationic alkylammonium products, and therefore a label-free and real-time monitoring of amino acid decarboxylase activity was achieved through such a sensing system.

Many other indirect analyte sensing formats were proposed (**Figure 1.19**), including analyte displacement assay (ADA)[133] and associative binding assay (ABA).[134] Both direct and indirect sensing assays have impacted molecular sensing and helped push the step from lab design to further clinic applications. However, from the practical application perspective, several disadvantages remain. Firstly, it is still challenging to design and synthesize selective receptors for structurally similar analytes. Secondly, the rational design of the receptors is almost impossible for those complex analytes with unknown identity. Finally, the analysis for complex mixtures, such as biofluids, wines, and perfume, can not be achieved with such sensing systems.

1.3.2 Differential sensing

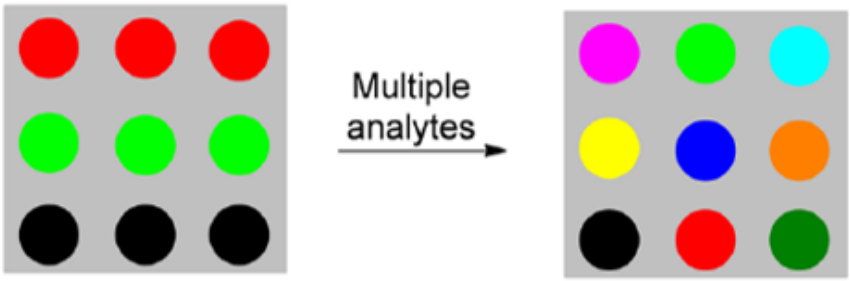

Figure 1.21. Illustration of the sensing scheme of the differential sensing through a sensor array. The underlying idea is to achieve the analyte distinction by exploiting the composite responses of multiple receptors that each is only partially analyte-selective. Reprinted with permission from ref[97]. © 2015 American Chemical Society.

Due to the difficulties in designing synthetic systems that provide both a sufficient affinity and selectivity for the target analyte, the differential sensing approach, which mimics the mammalian nose and tongue for the sense of taste and smell, has been developed.[8-9, 97, 135-136] Rather than sensing one analyte by one specific receptor (one-analyte-one-receptor diagram), the underlying idea is to achieve the analyte distinction by exploiting the composite response of multiple receptors. In this regard, differential sensing is also called sensor array sensing. Each receptor within the sensor array can bind to all the analytes, but the binding affinities are different. In other words, the signal changes caused by each analyte-receptor combination differ. The resulting signal response fingerprints provide the characteristic patterns for the individual analyte or the complex mixtures, and therefore, multiple analytes can be identified by analyzing these characteristic signals.

In principle, the sensor array system can be constructed by either reactive probes or chemosensors. However, chemosensors, especially IDA-based chemosensors, are more suitable for differential sensing since an array could be easily obtained by combining different receptors and indicator dyes without more synthesis efforts. Moreover, compared to the reactive probe, the chemosensor's relatively lower binding affinity and selectivity actually are more beneficial for differential sensing because the cross-reactivities are increased, and thus more information could be observed.

In order to analyze the large amount and complex data set obtained in the array sensing systems, mathematics-based cluster data analysis methods are required. In the perspective of pattern recognition, principal components analysis (PCA) and linear discriminate analysis (LDA) are commonly used. A detailed description of the cluster data analysis principle is out of the scope of this thesis, and more reading materials are provided.[137-139] In short, both PCA and LDA

display the score plots for the tested analytes in two, three, or even higher dimensions. In a good plot, the close clustering of the different repetitions from the same analyte and the separation between different analytes should be generally observed.[137] Furthermore, more complicated but "smart" machine learning-based methodologies were developed for complex data calculation and analysis over recent years. To be noted, an extensive amount of measurement repetitions is the basis of the machine learning-based data analysis in the differential sensing concept.[140-142]

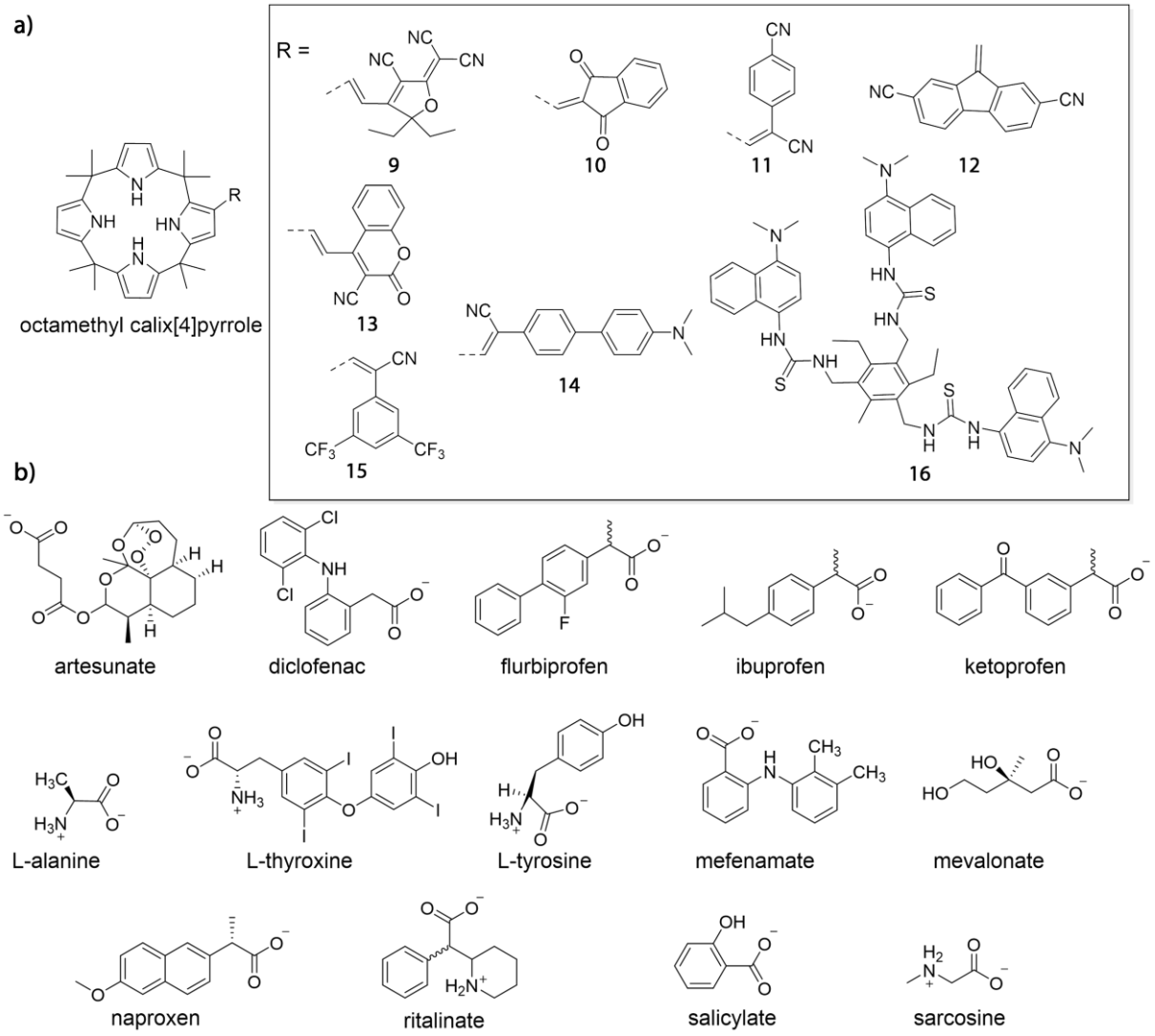

Figure 1.22. Chemical structures of the chemosensors (**9**-**16**), and 14 carboxylate drugs used in this research.[143]

A detailed example is shown in **Figure 1.22** to illustrate the sensor array-based differential sensing concept. The supramolecular sensor array that consists of eight chemosensors embedded in a hydrogel matrix has been reported by Anzenbacher, Jr and coworkers.[143] In their study, 14 carboxylate drugs were accurately identified in water and even in human urine with 100 % classification accuracy by employing this sensor array. Moreover, the sensor is able to differentiate six typical nonsteroidal anti-inflammatory drugs at concentrations of 0.5 - 100 ppm,

which provides the potential utility of the sensor array for diagnostic and environmental monitoring applications.

Compared to using only one probe (chemosensor), the sensor array-based differential sensing concept provides a relatively higher selectivity in molecular sensing. As a result, the distinction and identification of similar structural analytes and even complex mixtures with unknown structures, such as whisky and perfume, are achieved.[135, 144-149] Nevertheless, this approach requires the often cumbersome synthesis of several chemosensor variants. Moreover, array-based sensing schemes that probe the degree of receptor complexation are generally limited in situations where both the identity and the concentration of the analyte are unknown.

1.3.3 Chirality sensing

Chirality is one of the fundamental concepts in chemistry. Most biological relevant molecules are chiral, and the enantiomeric compounds usually show different pharmaceutical activity due to varied interactions with protein receptors. For instance, many R-amino acids are considered diagnostic biomarkers and used for the treatment of schizophrenia, Parkinson's, Huntington's, Alzheimer's, and other neurological diseases.[150-152] Due to the significant importance of the chiral compounds, chirality analysis, *i.e.*, the determination of the chirality, enantiomeric excess (*ee*), and the optical purity, is one of the major research areas in both organic and analytical chemistry. Optical method-based chirality sensing is currently of great interest among many analytical techniques because of its fast-responsive, sensitive, and cost-effective advantages. Chirality sensing is a vast topic and has been reviewed by many chemists from different perspectives.[153-155] According to the binding interaction between the chiral analyte and the receptors, these design strategies can mainly be classified into two categories: (dynamic) covalent reaction-based and non-covalent interaction-based chirality sensing concepts. In the following text, several representative examples will be briefly introduced to gain a general understanding of chirality sensing and provide a short pre-reading material for **Chapter 3**.

Most small chiral molecules are only optical active at the far UV range, and thus, the main goal in the spectroscopic method-based chirality sensing is to generate an easily detectable signal in UV, visible light, and even longer wavelength ranges. To achieve this, a reporter unit, usually a chromophore or a fluorophore, has to be built in the sensor design or created upon the analyte binding. For the colorimetric and fluorescence methods, the key point is that the probe can interact differentially with R or S enantiomers to generate different signal changes; for circular

dichroism (CD) methods, a CD active chromophore has to be introduced or formed after the chiral analyte binding

1.3.3.1 Non-covalent interaction-based chirality sensing

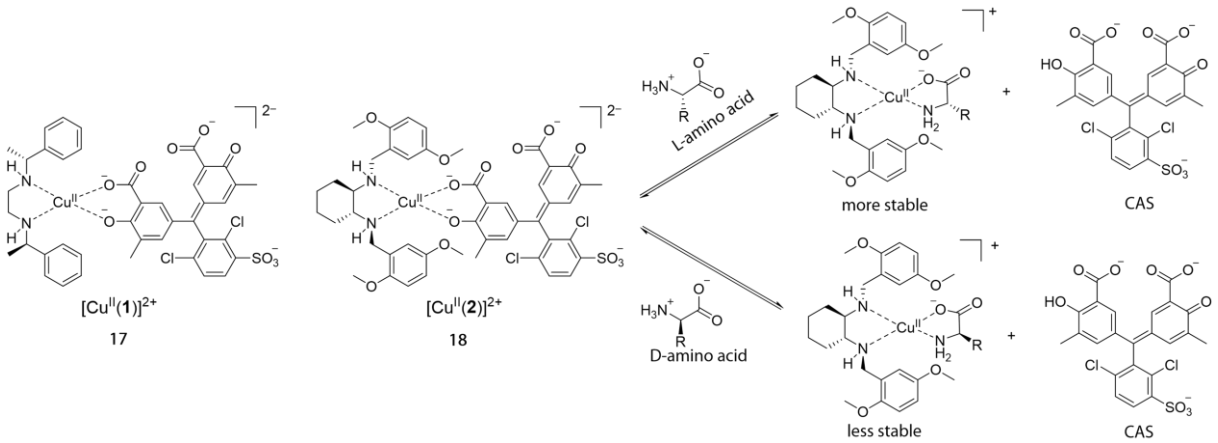

Figure 1.23. Schematic representation of the α-amino acids sensing by a Cu(II) complex-based chiral receptors (**17-18)** through an enantioselective indicator displacement assay (eIDA).

As is the case in single analyte sensing, indicator displacement assay (IDA) can also be applied in chirality sensing, named enantioselective indicator displacement assay (eIDA), which Anslyn and coworkers first proposed.[127, 156] As shown in **Figure 1.23**, two eIDAs implemented by using two chiral receptors **17**, **18** in combination with the indicator dye chrome azurol S (CAS) have been employed to enantioselective discriminate 13 α-amino acids in methanolic buffer mixtures in the low millimolar concentration range. In detail, the Cu metal center within the chiral receptors serves as the recognition unit and displays different binding affinities to α-amino acids because of the differences in steric interactions between the side chain of R or S α-amino acids and the chiral receptors. Therefore, a different extent of the CAS displacement is observed for R or S α-amino acids, which can be utilized as the colorimetric indicator for the binding of the amino acids. In cooperation with the calibration curve and PCA analysis, 13 α-amino acids were distinguished, and the *ee* of the unknown samples was determined.[156] More copper(II) complexes-based eIDA were reported by the same group to identify and determine the *ee* values of α-amino acids.[157-158] To date, eIDA has been successfully employed in chirality sensing for many small bio-relevant molecules, such as carboxylates and vicinal diols.[97, 159-162]

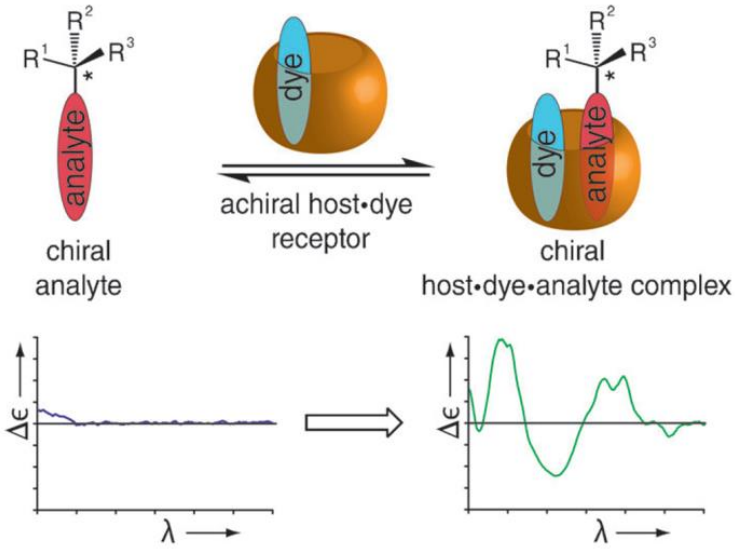

Figure 1.24. Schematic representation of the CB8-dye complex based analyte induced CD method for the chirality sensing. Reprinted with permission from ref[163]. © 2014 Wiley.

Besides the small organic molecular probes, macrocyclic compounds, such as cucurbit[*n*]urils, endo-functionalized molecular tubes, and pillar[*n*]arenes, are introduced in the chiral sensor design.[163-166] Because of the large cavity and hydrophobicity or hydrophilicity, these macrocyclic compounds are able to accommodate multiple guest molecules within the cavity, which is intriguing for chirality sensing in several ways. For instance, Biedermann and Nau reported a CD-based chirality sensing assay that relies on the formation of a ternary complex of CB8, an achiral dye, and a chiral aromatic analyte.[163] As shown in **Figure 1.24**, upon the co-inclusion of a chiral aromatic analyte inside the CB8 cavity, the CD silent CB8-dye complex displays an analyte-induced CD (ICD) signal in the dye absorption range. This assay can be applied for a broad scope of the analyte because this ICD signal's generation relies on the non-covalent interaction between the CB host and the aromatic moieties of the guest molecules. Therefore, it is usable for the detection of many biomolecules and drugs, even for the recognition of peptides.

In essence, both eIDA- and macrocyclic compound-based systems achieve chirality sensing through an indirect approach since the readout of the target analytes depends on the spectroscopic properties of the indicator. It may limit the selectivity of these systems because the characteristic analyte-indicative optical signal could not always be observed. In addition, the selection of a suitable indicator dye may also be a problem when developing a new chiral chemosensor.

1.3.3.2 Covalent interaction-based chirality sensing

Unlike non-covalent interaction-based chirality sensing concepts, chiral analytes directly bind to the probe in covalent interactions-based methodologies. In this way, the generated multiple analyte-indicative spectroscopic signals, for instance, UV/vis combined with CD spectra changes, ensure a higher sensitivity and sometimes also a selectivity of the probe.[167-170]

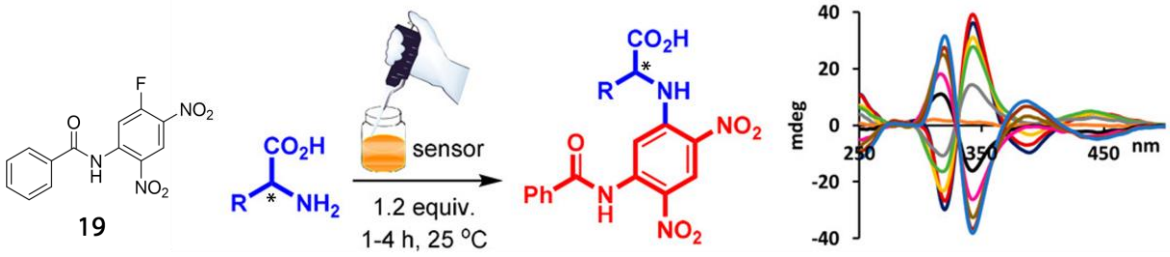

Figure 1.25. Schematic representation of the chirality sensing for amino acids by the aryl fluoride probe **19**. After the conjugation between the analyte and probe, the CD signal in the UV and visible light range was observed. Reprinted with permission from ref[171]. © 2019 American Chemical Society.

An achiral aryl fluoride probe **19** that allows the assignment of the absolute configuration and quantification of the sample concentration and *ee* values for 19 amino acids, biothiols, amines, and amino alcohols, was showcased by Wolf and coworkers (**Figure 1.25**).[171] After the covalent binding, the probe-analyte conjugate displayed characteristic absorption and CD signals in which the absorption corresponds to the total concentration of the analyte, and the CD intensity is dependent on the enantiomeric composition of the analyte. Therefore, even just one small probe achieves the determination of the total concentration, absolute configuration, and *ee* values. This covalent binding and binary response chirality sensing concept can also be applied in IDA format construction. The non-enantioselective information (*i.e.*, absorption or emission) from the displaced indicator served as the concentration ruler, and the chiral analyte-probe conjugate corresponded to the configuration and the *ee* values.[172]

Besides traditional covalent reactions, dynamic covalent reactions, such as imine bonds and boronate easter bonds, have been attractive for the implementation of chirality sensing. Such research includes the single small organic molecule-based probes developed by the Wolf group,[141] and the dynamic multi-component covalent assemblies proposed by Anslyn and coworkers.[173] The introduction of the dynamic covalent interaction enriches the chirality sensing concept and has overcome several problems that a covalent interaction-based approach faces, such as complicated design and synthesis and limited ranges of target analytes.

Compared to the traditional chromatographic techniques-based chirality analysis, which is reliable but usually time-consuming and cost-intensive and requires sophisticated

instrumentation, the optical method is more suitable for practical applications because of ease of monitoring, cost-effectiveness, and high-throughput screening (HTS) ability. Based on the (dynamic) covalent and non-covalent interactions, hundreds of chiroptical probes (and chemosensors) have been developed. However, some shortcomings still remain: *i*) most of the presented chirality probes only work in organic solvents; *ii*) the differential recognition of structural similar chiral analyte can not often be achieved, *e.g.*, Cys and Cys-Gly pairs; *iii*) chiroptical probes require long reaction time (> 10 min). Therefore, the new chirality sensing concepts are still of interest.

1.3.4 Constitutional dynamic chemistry (CDC) based molecular sensing

Supramolecular chemistry is essentially dynamic chemistry in view of the lability of the interactions connecting the molecular components of a supramolecular entity. The introduction of dynamic covalent bonds into such a supramolecular framework leads to the emergence of constitutional dynamic chemistry (CDC) that covers both molecular and supramolecular levels, enabling the system to adapt to internal (or external) environmental changes by modification of their constitution through component exchange or reorganization.[174-177] Constitutional dynamic chemistry bridges supramolecular chemistry to adaptive chemistry and evolution chemistry towards the chemistry of complex matter, *e.g.*, the inclusion of the arrow of time: out-of-equilibrium systems.[70, 174, 178] It provides access to constructing advanced functional materials,[80, 179-185] *e.g.*, temperature/light stimuli-response materials and supramolecular polymers.

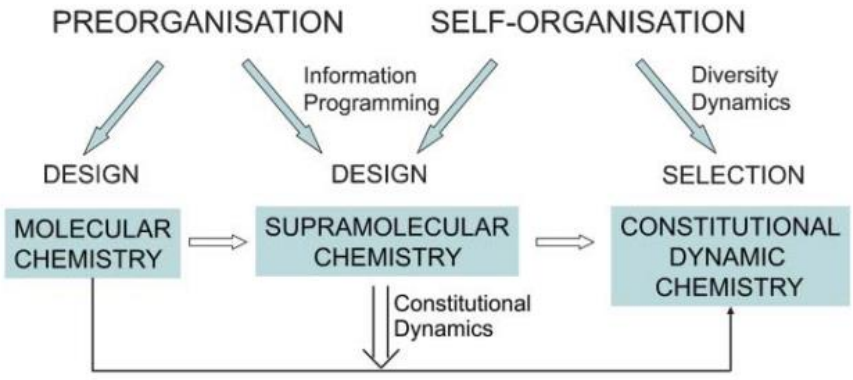

Figure 1.26. From molecular to supramolecular and to constitutional dynamic chemistry under pre-organization and self-organization by design and with selection. Reprinted with permission from ref[174]. © 2007 The Royal Society of Chemistry.

As a matter of fact, the process of molecular sensing is the generation and monitoring of the changes caused by the binding or interactions between the target analytes and molecular sensors. Therefore, the stimuli-responsive nature of the dynamic constitutional chemistry-based

supramolecular system has been playing a significant role in the design of selective receptors.[186-188] The key factor of such a concept is the built-in dynamic covalent bonds, such as disulfide, imine, boronate easter, and Diels-Alder reaction, which commonly serve as the recognition unit in the sensing system. Owning to the specific self-organization character, the molecular components within the CDC system can thus recognize the target analyte and re-organized the molecular components to form the analyte-adaptive constitutional dynamic networks. During the whole dynamic process, the generated information, such as changes in spectroscopic properties and morphology, can be utilized to identify or even quantify the analyte of interest. In principle, the CDC sensing concept could overcome both affinity and selectivity obstacles presented in the typical sensing concepts introduced in the above subchapters. The covalent reaction between the target analyte and the recognition unit provides a high binding affinity. The non-covalent interactions between the molecular components provide analyte-indicative information during the recognition and re-organization process, which ensures the high selectivity of the sensing system.

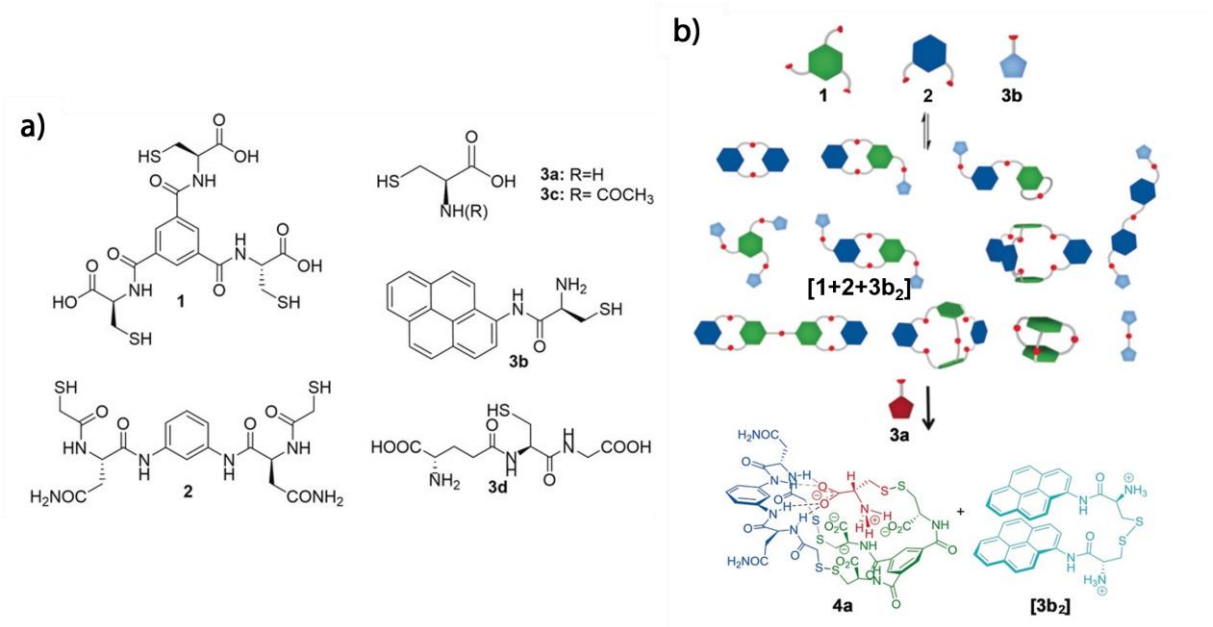

Figure 1.27. a) Chemical structures of the molecular components in the dynamic network. b) Schematic representation of pre-organization of the molecular components and L-Cys detection. Reprinted with permission from ref[187]. © 2018 Wiley.

For instance, a dynamic chemical network for the detection of L-Cys and Cys-Gly was reported by Solà, Alfonso, and coworkers (**Figure 1.27**).[187] In their study, three molecular components first self-organized into a heterotrimer [**1** + **2**+ **3b**$_2$] in aqueous media at a neutral pH value, caused by the disulfide exchange reaction and non-covalent interactions between the different functionalities of the constituents. Upon adding L-Cys, the preformed heterotrimer was dis-

assembled, and new molecular combinations **4a** and **3b**$_2$ were formed due to a stronger interaction between Cys and the components. The emission properties were also changed during the organization-re-organization processes. In detail, in the absence of L-Cys, **3b** presents as the reduced form with a characteristic emission band at 350-450 nm, while the excimer emission band centered at 500 nm caused by the oxidized of **3b** appears upon the addition of L-Cys. Therefore, the identification and quantification of L-Cys can be achieved by monitoring the emission intensities of the monomer and excimer of **3b**. The assay has high selectivity to L-Cys and Cys-Gly, and other biothiols and amino acids did not interfere with the sensing properties. Moreover, the assay showed a potential application for cystinuria diagnosis after evaluating the sensing properties in human urine.

So far, this new CDC-based molecular sensing concept has been successfully applied in single analyte sensing, differential sensing, and chirality sensing.[189-190] Nevertheless, there are still some disadvantages remaining. Except for the difficulty in the selection of proper molecular components, the main problem is that the CDC-based molecular sensing usually needs a long assay time due to the covalent binding and non-covalent interaction-based assembly evolution. For instance, although the previous research showed good sensing properties in aqueous media and human urine, the whole assay time is around 5 hours, limiting its further application in the clinical diagnosis.

2 Discovering of a size-record breaking green-emissive fluorophore HINA

The results described in this chapter have been published as "Discovery of a size-record breaking green-emissive fluorophore: small, smaller, HINA" in Chemical Science, 2021.[191] The cell experimental data and analysis were carried out by co-authors: Dr. Laura Talamini, Dr. Elisa D'Este, and Bianca Martins Estevão. The theoretical computational investigation was carried out by co-author Prof. Wim Klopper. All other experimental data collection and analysis were carried out by me under the supervision of Dr. Frank Biedermann and Prof. Luisa De Cola. Sections in this chapter have been reproduced from the published work[191] with permission from the Royal Society of Chemistry.

2.1 Introduction

Fluorescence is a fundamentally fascinating but also highly practical relevant property of organic molecules. Countless examples of fluorescent aromatic compounds have been described, and hundreds of fluorescent dyes have been found for commercial use.[13, 192-195] Decade-long debates were spurred about the origin of the dual fluorescence of 4-(dimethylamino)benzonitrile (DMABN), which is a small, weak emissive push-pull system.[196-198] For comparison, the GFP chromophore, discounting the surrounding protein pocket, is one of the smallest green-emitting fluorophores of biological origin.[199] However, the emission of synthetic protein-free GFP analogs is always quenched by polar solvents unless protected from the solvent to make them self-aggregated.[199-201] Structurally related polymethine or squarylium fluorescent push-pull dyes consist of at least two aromatic methylene-bridged aromatic moieties.[6-7, 202-204] Nitrobenzoxadiazole and its derivatives (NBDs) are practically widely used green-emitting synthetic fluorophores that display good fluorescence quantum yields (QYs, ~ 10 %) in hydrophobic environments but are not emissive in water, which is a typical phenomenon for almost push-pull chromophores.[205-207] Therefore, poly- or heteroaromatic or substituted compounds consisting of at least two aromatic rings (see **Figure 2.1**), such as rhodamines, fluoresceins, and BODIPYs, are practically used fluorophores in aqueous media with a visible region of the spectroscopic properties.[6, 202, 208-209] The investigation of small green-emitting water-soluble fluorophores is still attractive for chemists due to their wide applications, for instance, as non-disturbing (orthogonal) fluorescent labels.[202, 205, 210] In

addition, luminescent compounds with rich photophysical properties also provide challenging and valuable test cases for theoretical electron dynamics studies.[211-213]

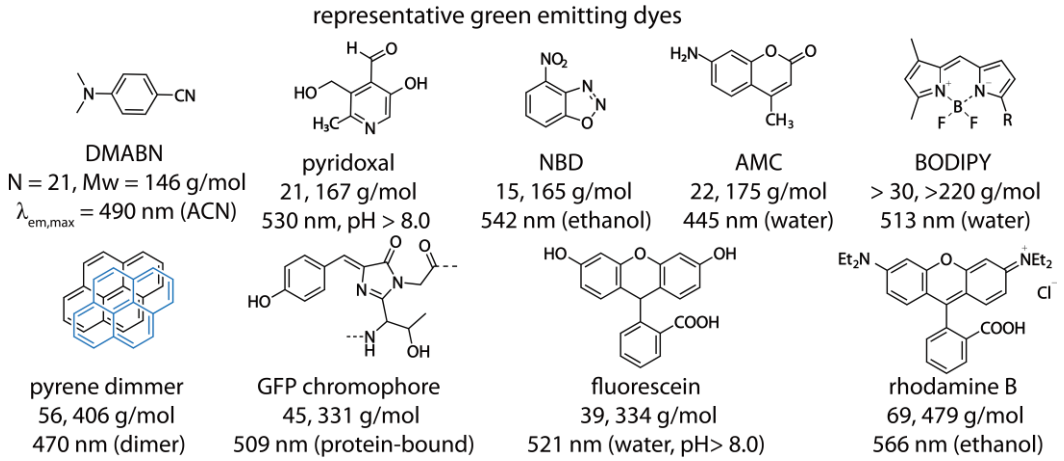

Figure 2.1. Chemical structures, abbreviations, and molecular weights of commonly used green-emitting dyes. The maximum emission peak ($\lambda_{em,\,max}$) is given as well.

Out of serendipity, I surprisingly found the unexpected green emission of 3-hydroxy-isonicotinic aldehyde (HINA) in aqueous media, see **Figure 2.2** for its chemical structure. Although HINA was first reported in 1959 with a detailed UV/Vis study and was commercially available already,[214-216] its fluorescence emission properties were never reported before. After the careful investigation by thin-layer chromatography (TLC), high-performance liquid chromatography (HPLC), and nuclear magnetic resonance (NMR), I excluded that the observed fluorescence stems from any impurity (see additional data at the end of this chapter).

HINA consists of only 14 atoms (123 g/mol); for comparison, naphthalene and azulene (both 128 g/mol) that have a similar size to HINA are both blue emissive ($\lambda_{em,\,max}$ = 327 and 373 nm in methanol, respectively).[217-219] Typical green-emitting dyes are much larger in atom number, molecular weight, and size than HINA, see **Figure 2.1**. For instance, NBD, whose emission maximum (542 nm in ethanol) is similar to that of HINA (535 nm in water, pH > 7.1), is already 35 % larger than HINA in molecular weight.[205]

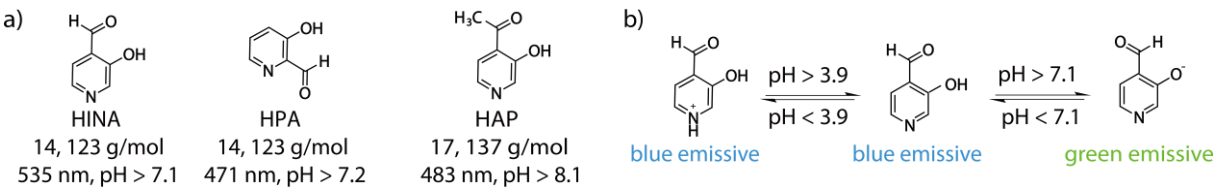

Figure 2.2. a) Chemical structures of investigated small-molecule green-emitting fluorophores and $\lambda_{em,\,max}$ of their anionic form in water. b) Schematic representation of hydration and (de)protonation equilibria of HINA in aqueous media.

This chapter demonstrates a detailed exploration of HINA (and its analogs, see **Figure 2.2**a), ranging from its fundamental photophysical properties to its potential applications, including cell imaging, molecular sensing, and reaction monitoring.

2.2 Results and discussions

2.2.1 pH Dependency of HINA

Systematic photophysical investigations by absorbance and emission spectroscopy were carried out to elucidate the pH-dependent behaviors of HINA. The pH titration experiment was conducted by using standard titrant solutions of NaOH (1 N) and H_2SO_4 (0.5 N), which were drop-wised and added into a solution of HINA (50 µM) in water. After pH recording, the absorbance and emission spectra of the solution were measured, see **Figure 2.3**.

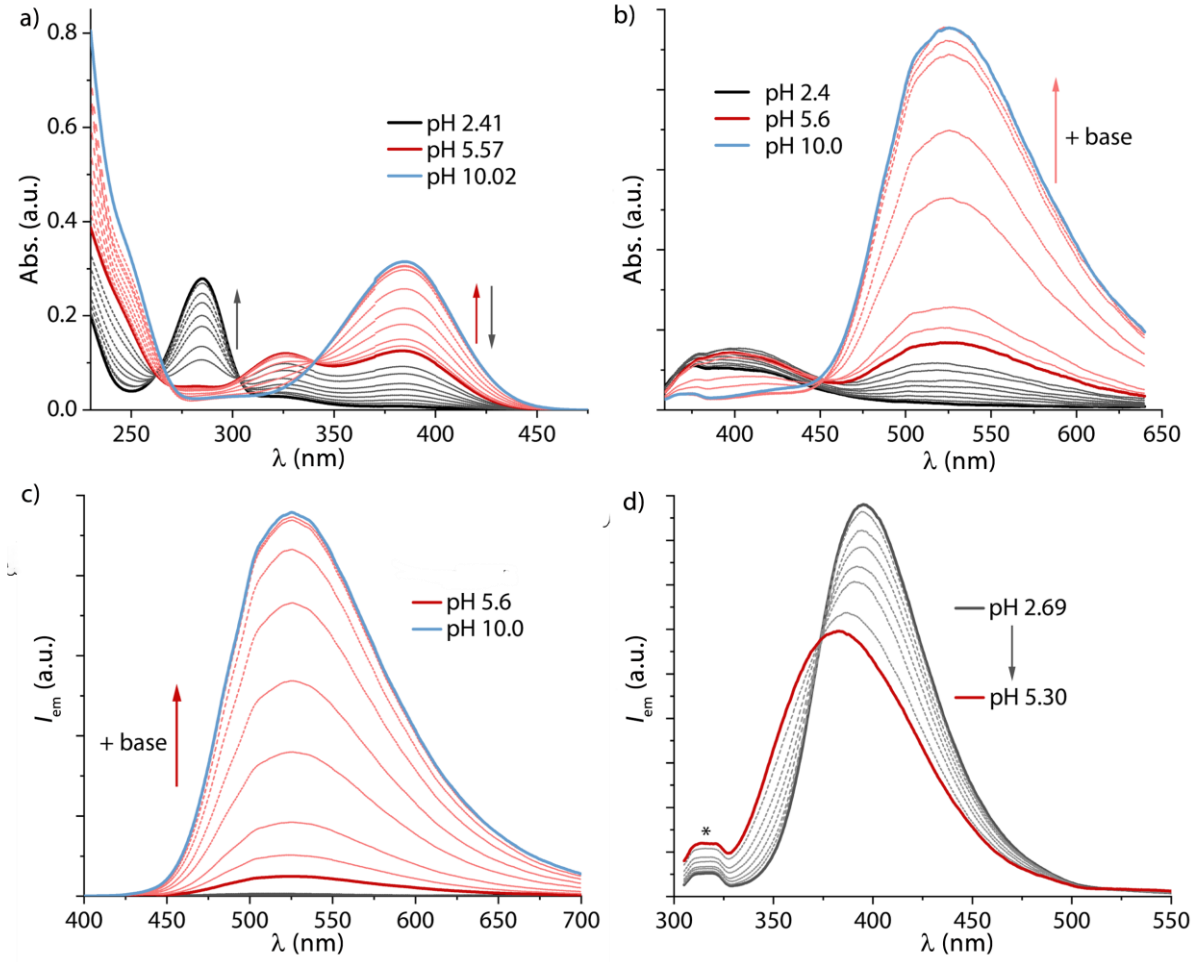

Figure 2.3. Absorbance (a) and emission (b-d) spectra of HINA titrated with a standard solution of H_2SO_4 (0.5 N, a series of black lines) and a standard solution of NaOH (0.1 N, a series of red lines) in MilliQ water at 25 °C. In b), λ_{ex} = 330 nm was used as the excitation wavelength, while excitation was carried out in c) at 380 nm, and d) at 285 nm. The asterisk in the emission spectrum indicates the Raman scattering band of water at the selected excitation wavelength.

At 3.8 < pH < 7.1, HINA is present mainly in its neutral form, which absorbs at a short wavelength range and is blue emissive with a respectable quantum yield of 7 %. With the addition of base NaOH (1 N), the absorbance intensity of HINA at 386 nm increased while simultaneously, the absorbance band centered at 323 nm decreased (**Figure 2.3**a). More intriguingly, the blue emission band of the neutral HINA centered at 382 nm vanishes upon deprotonation, and an even stronger green emission band (λ_{em} = 525 nm) appears. The isoemissive point is found at 450 nm, see **Figure 2.3**b. These changes in both absorbance and emission spectra also caused an apparent color change that can be seen by naked eyes (**Figure 2.4**).

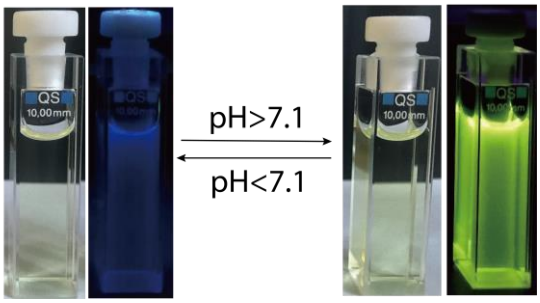

Figure 2.4. Photographic images of HINA dissolved in water, in its neutral form (left) and anion form (right), under ambient light and UV light irradiation.

Beginning with the HINA neutral form, upon the addition of H_2SO_4, a new absorbance band (λ_{abs} = 286 nm) appeared, corresponding to the N-protonated HINA form of HINA (cationic form), while the absorbance band centered at 325 nm decreased. Out of expectation, the cation form of HINA is still blue emissive ($\lambda_{em,\,max}$ = 395 nm, QY = 0.9 %), which is bathochromically shifted from 382 nm compared to its neutral form (**Figure 2.3**a,d). Moreover, the emission lifetimes of the cationic, neutral, and anionic forms of HINA are all in the nanoseconds (ns) ranges (0.2 ns, 0.9 ns, and 1.0 ns, respectively),[3] which identified them as fluorophores (**Table 2.1**). Despite its simple structure, HINA is a fascinating fluorophore that displays three different emissive (de)protonated states (**Figure 2.2**b), and each of them has unique spectral features. To the best of my knowledge, it is the first small fluorophore with such unique features compared to other previous reports.

Besides, I explored the pH-dependent properties of the HINA analogs, *i.e.*, 3-hydroxy-picolin aldehyde (HPA) and 3-hydroxy-4-acetyl pyridine (HAP) as well. Similar to HINA, both chemicals exhibit three distinct (de)protonated states. However, its emission quantum yields are relatively low (~ 1 %), and its anionic forms have emission bands at 484 nm, which is hypochromically shifted compared to the anionic form of HINA. The pH-dependent spectra (absorbance and emission spectra) for HPA and HAP were listed at the end of this chapter, see

Figure 2.24 and **Figure 2.25**. Overall, it is surprising that HINA (and its analogs) display such unexpected pH-dependent photophysical properties. All the photophysical properties measured for HINA (and its analogs) are summarized in **Table 2.1**.

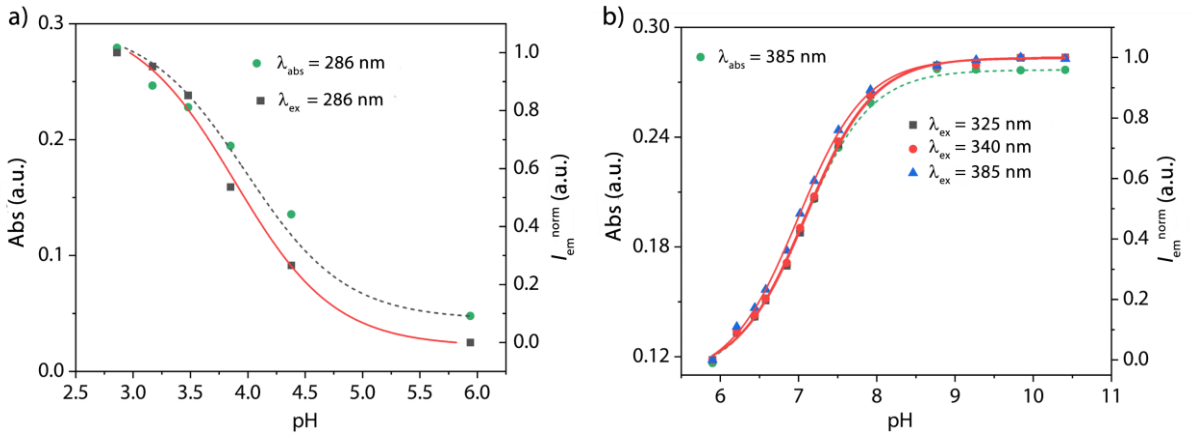

Figure 2.5. a) Plot of absorbance (λ_{abs} = 286 nm, green dots) and [0,1]-normalized emission (λ_{ex} = 286 nm, λ_{em} = 397 nm, black square) intensity change of HINA (50 µM) with pH values in the range of 2.56 - 5.94. b) Plot of absorbance (λ_{abs} = 286 nm, green dots) and [0,1]-normalized emission (λ_{ex} = 325 nm, black squares, λ_{ex} = 340 nm, red dots; λ_{ex} = 385 nm, blue triangles; λ_{em} = 397 nm) intensity changes of HINA with pH values in the range of 5.90-10.41. ***Notes***: the excitation wavelengths used here are characteristic for the neutral form (325 nm), isosbestic point of neutral form and deprotonated form (340 nm), and the deprotonated form (385 nm), respectively. Fits are shown in the dashed black link (absorbance) and the solid red line (emission). All the fitted pK_a values are summarized in **Table 2.2**.

To gain insight into the pH-dependent properties of HINA, the pK_a values were determined by both spectroscopic method and pH titration with a pH meter. The pK_{a1} (ground state) was determined by the absorbance spectra of HINA (HPA and HAP) in the pH range of 2.5-5.5, while the pK_{a2} value was determined in the pH range of 5.5-10. The pK_a values were observed by fitting the plot of the absorption intensity at the characteristic wavelength as a function of pH values (**Figure 2.5**). The fitting equations were given as follows.[220-221]

$$pK_{a1} = p\mathrm{H}_X - \log(A_H^+ - A_X) + \log(A_X - A_N)$$
$$or \quad pK_{a1}^* = p\mathrm{H}_X - \log(I_H^+ - I_X) + \log(I_X - I_N) \qquad \textbf{Eq. 2.1}$$
$$pK_{a2} = p\mathrm{H}_X + \log(A_B^- - A_X) - \log(A_X - A_N)$$
$$or \quad pK_{a2}^* = p\mathrm{H}_X + \log(I_B^- - I_X) - \log(I_X - I_N) \qquad \textbf{Eq.2.2}$$

Where A_H^+, A_X, A_N and A_B^- represent the absorbance of the protonated form at the pH chosen for the neutral form and the deprotonated form, respectively. I_H^+, I_X, I_N and I_B^- represent the emission intensity of protonated form at the pH chosen for the neutral form and the deprotonated form, respectively. The non-linear fitting was conducted with the Origin 2018b software package.

A value of pK_{a2} = 7.05 ± 0.01 was obtained for the anionic HINA form (**Figure 2.6**), which agrees with the value from the pH-meter recording 7.02.[64, 222] Coincidently, the pK_a value lies

perfectly in the biological range, which provides the basis for potential biological chemistry applications of this small green fluorophore. Furthermore, the excited state (de)protonated behavior was determined by the emission-based spectral fitting process, in a similar approach to the ground state pK_a values determination. HINA was excited at an isosbestic point, or at a wavelength where mainly the neutral form of HINA, or at a wavelength where mainly the anionic form of HINA absorbs, and the emission was recorded where only the anionic form emits. Surprisingly, the excited state pK_{a2} values (pK_{a2}*) for the anionic form of HINA were almost the same, pK_{a2}* ~ 7.0, no matter which excitation wavelengths were used.

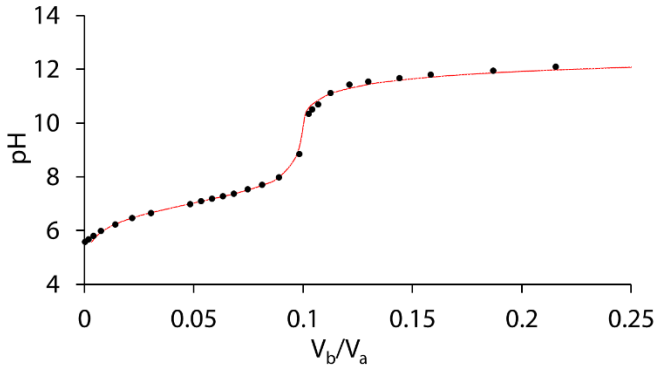

Figure 2.6. The pH titration curve of HINA (10 mM) titrated with a standard solution of NaOH (0.1 N) in MilliQ water, the red dash line is the fitting curve, pK_{a2} = 7.02.

To gain a deep understanding of their excited pK_a values, the excited-state acidities (pK_a*) of HINA, HPA, and HAP were calculated by a Förster cycle analysis (**Eq. 2.3-2.6**).[223] The "thermodynamic" acidity of the excited HINA (HPA and HAP) was estimated from the experimentally available absorbance and emission energies of the protonated and deprotonated species (in cm^{-1} units), and the ground state pK_a values obtained from the pH-meter recording experiments.

$$pK_a^* = pK_a - \frac{h\nu_1 - h\nu_2}{2.3\,RT} \quad \textbf{Eq. 2.3}$$

$$\tilde{\nu}_{00}^{\mathrm{A^-}} = \frac{\tilde{\nu}_{\mathrm{A^-}}^{a} + \tilde{\nu}_{\mathrm{A^-}}^{f}}{2} \quad \textbf{Eq. 2.4}$$

$$\tilde{\nu}_{00}^{\mathrm{HA}} = \frac{\tilde{\nu}_{\mathrm{HA}}^{a} + \tilde{\nu}_{\mathrm{HA}}^{f}}{2} \quad \textbf{Eq. 2.5}$$

$$\Delta pK_a = \frac{\mathrm{Nhc}}{2.3RT}\left(\tilde{\nu}_{00}^{\mathrm{A^-}} - \tilde{\nu}_{00}^{\mathrm{HA}}\right) = \frac{0.625}{T}\left(\tilde{\nu}_{00}^{\mathrm{A^-}} - \tilde{\nu}_{00}^{\mathrm{HA}}\right) \quad \textbf{Eq. 2.6}$$

The parameters $\tilde{\nu}_{\mathrm{A^-}}^{a}$ and $\tilde{\nu}_{\mathrm{A^-}}^{f}$ represent the wavenumbers of the maximum absorbance and emission of the anionic species. Likewise, the $\tilde{\nu}_{\mathrm{HA}}^{a}$ and $\tilde{\nu}_{\mathrm{HA}}^{f}$ represent the wavenumbers of the maximum absorbance and emission of the neutral form of HINA (HPA and HAP). T in the equation is the temperature on the Kelvin. After employing these equations, the excited acidities

of HINA, HPA, and HAP were calculated as -5.5, -3.7, and 1.3, respectively. With such strong excited acidities, the excitation of the neutral form of HINA, HPA, and HAP should be completely deprotonated, and one could expect only to see the emission of the anionic species if the deprotonation occurs within the lifetime of the excited states. However, this is not the case because the absorbance- and emission-based pH titration plots essentially overlay, which indicates that the deprotonation of the fluorophore does not occur when exciting the neutral form of HINA, HPA, and HAP. It is believed that there is a fast intermolecular excited-state intramolecular proton transfer (ESIPT) process between the adjacent HO- and CHO- moieties (see **Chapter 2.2.5**), which intercepts proton transfer to the solvent molecules and thereby prevents the expected fluorescence behavior based on the calculated pK_a* values. Similar deviations between the calculated pK_a* values and the experimental observations have been described in the literature for the systems that do not deprotonate within the lifetime of the excited state.[224] Unlike many other reported hydroxarenes such as phenols and naphthols, HINA does not function as a photoacid.[223-224]

In complementary, the pK_a values determination results for HPA and HAP were listed in the additional data section at the end of this chapter, and all the pK_a values for HINA, HPA, and HAP were summarized in **Table 2.2**.

Table 2.1. Photophysical properties and pK_a values of HINA, HPA, and HAP in aerated water at 25 °C.

	λ_{Abs} (nm) & [log ε][a]	λ_{em} (nm)[b] & QY[c]	τ (ns)[d]	λ_{Abs} (nm) & [log ε][a]	λ_{em} (nm)[e] & [QY][f]	τ (ns)[d]	λ_{Abs} (nm) & [log ε][a]	λ_{em} (nm)[g] & [QY][f]	τ (ns)[d]	pK_{a1}, pK_{a2} in H_2O[h]
	cationic form at pH < pK_{a1}			neutral form at pK_{a1} < pH < pK_{a2}			anionic form at pH > pK_{a2}			
HINA	286 [3.71]	395 [0.9 %]	0.2	325 [3.32]	382 [7.0 %]	0.9	385 [3.74]	525 [15.0 %]	1.0	3.9, 7.1
HPA	285 [3.84]	395 [0.4 %]	0.2	316 [3.63]	376 [1.2 %]	0.4	369 [3.87]	484 [1.4 %]	0.2	3.2, 7.2
HAP	318 [3.64]	n.a.[i]	-	329 [3.53]	410 [0.1 %]	0.2	365 [3.72]	484 [0.8 %]	0.9	2.6, 8.1

[a] Absorbance peak maximum and logarithmic extinction coefficient. [b] Emission peak maximum, λ_{ex} = 285 nm. [c] emission quantum yield, λ_{ex} = 300 nm. [d] Emission lifetime, λ_{ex} = 370 nm. [g] Emission peak maximum, λ_{ex} = 380 nm. [h] From pH titration experiments. Estimated error ± 0.1 from different methods. [i] Very weak emission.

Table 2.2. pK_a (pK_a*) values determined with different methods for HINA, HPA, and HAP.

	pK_{a1} (pK_{a1}*)			pK_{a2} (pK_{a2}*)		
	pH meter	absorbance	emission	pH meter	absorbance	emission
HINA	3.54	3.88 ± 0.03	3.87 ± 0.02	7.02	7.03 ± 0.04	7.08 ± 0.07
HPA	3.11	3.20 ± 0.02	3.62 ± 0.01	7.24	6.98 ± 0.10	7.03 ± 0.19
HAP	2.58	3.07 ± 0.03	-	8.10	7.41 ± 0.09	7.64 ± 0.12

2.2.2 Solvent dependency of HINA

To further understand this unexpected emission of HINA (HPA and HAP), the spectroscopic properties of the fluorophores in different organic solvents were investigated. Anhydrous acetonitrile (ACN), dimethyl sulfoxide (DMSO), methanol (MeOH), and ethylene glycol (EG) were used in the measurements.

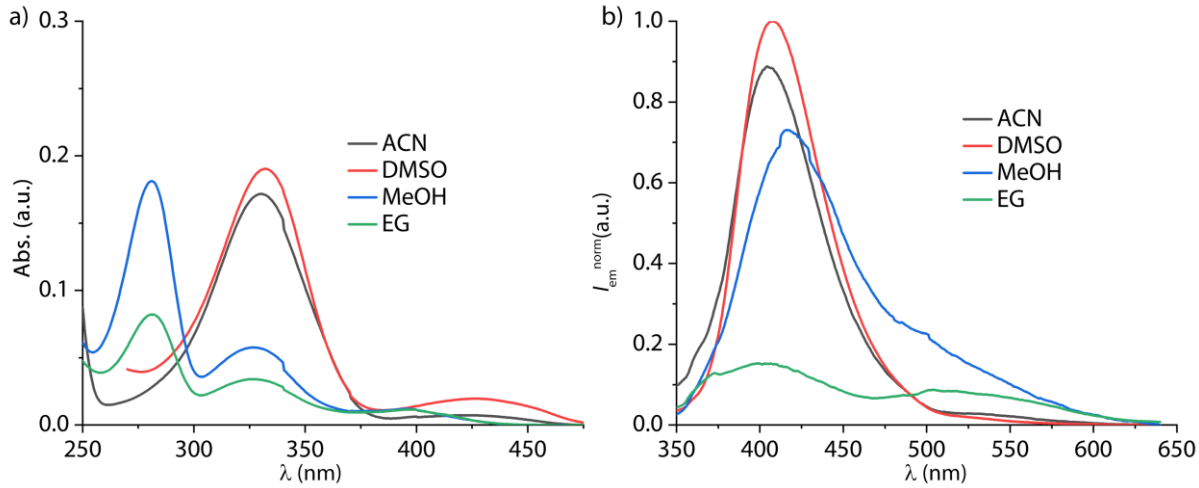

Figure 2.7. Absorbance (a) and [0-1]-normalized emission spectra of HINA (50 μM, λ_{ex} = 330 nm) in different anhydrous organic solvents.

As shown in **Figure 2.7**, HINA presents in its neutral form with a characteristic absorption peak centered at 330 nm, and the emission of HINA is at around 400 nm in these anhydrous organic solvents. With the percentage of water in the water/ACN mixed solvents increased, the absorbance of the neutral HINA (330 nm) decreased while the new absorbance peak belonging to the anionic form (385 nm) appeared. At the same time, the green emission, which corresponds to the anionic form of HINA, was increased (**Figure 2.8**a). Like the ACN/water mixture solvent, HINA exhibits almost the same absorbance and emission behaviors in DMSO/water mixture solvent (**Figure 2.8**b). In fact, in all tested anhydrous polar organic solvents, including ACN, DMSO, MeOH, and EG, the emission of HINA centered at around 400 nm is very weak. However, after the addition of water, its emission shifts to 450-600 nm and becomes much stronger. At first glance, it seems that an aqueous media is necessary for the formation of the green emissive species of HINA.

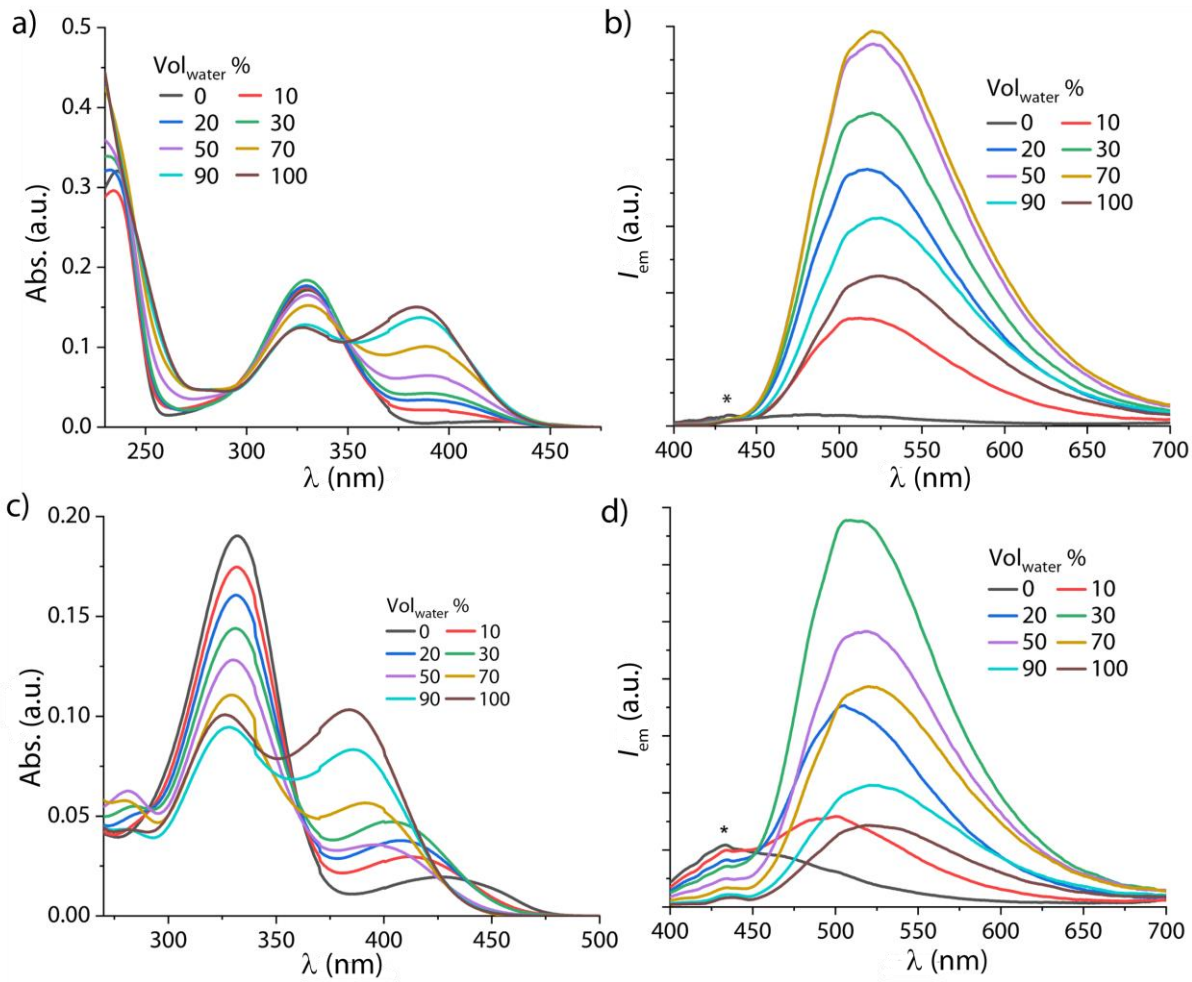

Figure 2.8. (a-b) Absorbance and emissions spectra of HINA in a series of mixture solvents of ACN/water (ACN/water, v/v) at 25 °C. (c-d) The same measurements of HINA were conducted in the mixture solvent of DMSO/water. The asterisk in the emission spectrum indicates the Raman scattering peak of water at the selected excitation wavelength.

However, the emission of HINA in the wavelength range of 450-600 nm also appears with an anhydrous base or anionic-stabilizing urea addition in organic solvent DMSO, see **Figure 2.9** (results in other organic solvents see the additional data). This result confirms again that the green emission comes from the anionic form of HINA and excludes the former hypothesis that water is the necessary condition for the green-emitting species formation. The hydrates of HINA are thus also not the green emissive species. In addition, the emission quantum yield of HINA increases as well upon deprotonation and gets higher in polar protic solvents than that in polar aprotic solvents, for instance, even reaching up to 24 % in basified methanol (see **Table 2.3**).

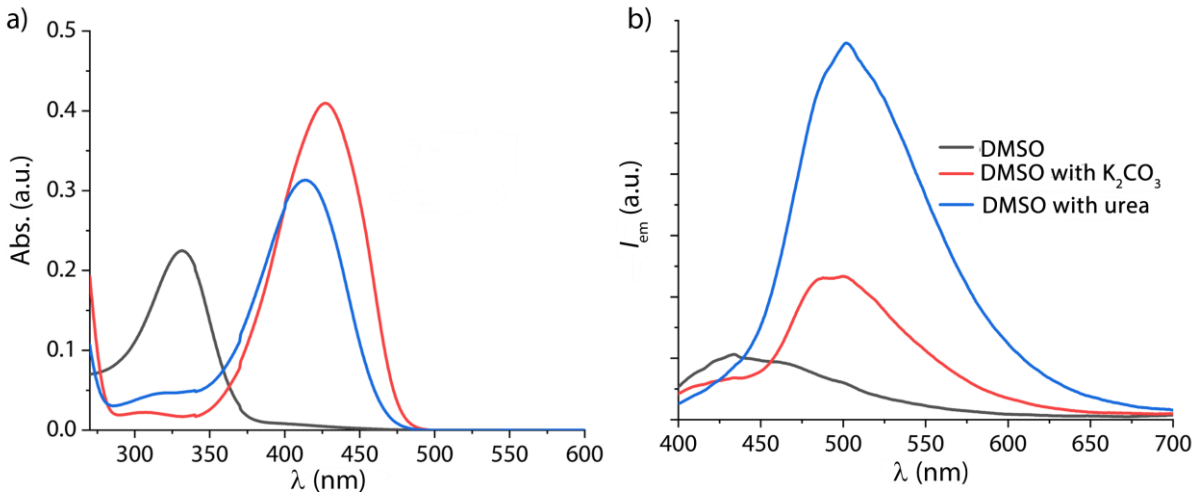

Figure 2.9. Absorbance (a) and emission (b, λ_{ex} = 380 nm) spectra of HINA (50 µM) in DMSO (black), and with K_2CO_3 (red) and urea (blue) addition.

Table 2.3. Emission quantum yield of HINA in the absence and presence of the anhydrous base (K_2CO_3) in the selected organic solvents.

	ACN	DMSO	MeOH
In absence of base	0.2 %	2.1 %	4.7 %
In presence of base	0.3 %	2.9 %	24 %

Besides, aggregation is also a known factor for some emission systems, such as pyrene (**Figure 2.10**) or other aggregation-induced emissive (AIE) systems, [194, 212, 225] but it is not the case for HINA. As shown in the dilution experiments (**Figure 2.10**), a linear relationship was found between the emission intensity and HINA in a concentration range of 0.16 µM - 40 µM, in which the aggregation already starts for pyrene and synthetic GFP chromophores.[226-227]

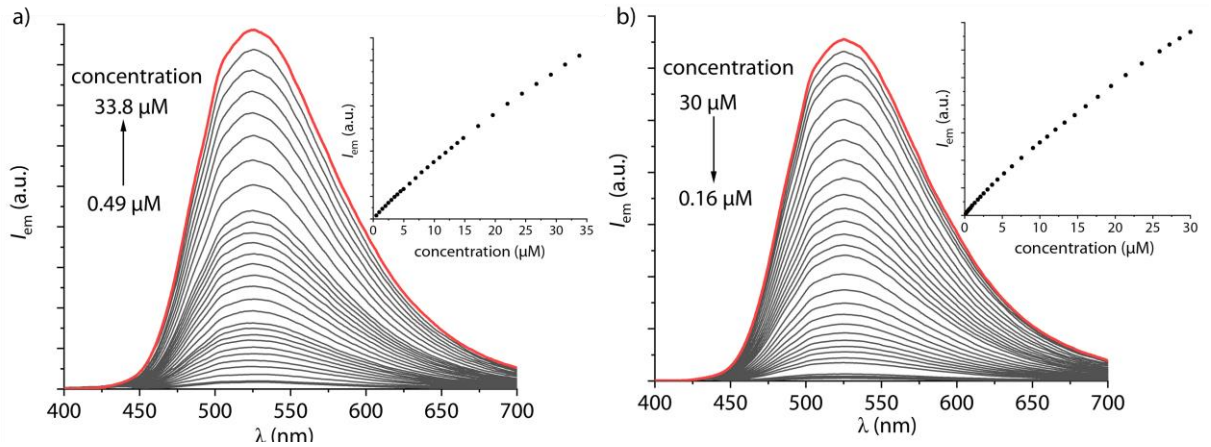

Figure 2.10. Concentration dependency emission spectra of HINA in bicarbonate buffer (25 mM) at pH 9.5. In a) the concentration of HINA was increased from 0.49 µM to 33.8 µM; in b) HINA was diluted from 30 µM to 0.16 µM. Inserts in both emission spectra show the linear relationship between the emission intensity and the concentration of HINA. ***Note***: contrary to HINA, pyrene and synthetic GFP chromophores[226-227] start to aggregate at around 10 µM or even lower.

2.2.3 NMR studies of HINA

In aqueous environments, the aldehyde moiety of HINA equilibrates with its hydrate form, which was confirmed by other researchers decades ago through UV/vis measurements.[228] Therefore, it is a plausible hypothesis that needs to be checked that the formed hydrates contribute to the green emission of HINA. Under this query, a series of NMR studies, including the 1D (^{1}H and ^{13}C NMR) and 2D NMR (COSY, HSQC, and HMBC, see the additional data) measurements, were demonstrated. As shown in **Figure 2.11**, an equilibrium between the HINA and HINA-hydrate is clearly seen in the solution of HINA in D_2O and D_2O/NaOH mixture solvent. According to the previous reports, the hydrate formation constant (K_{hyd}) was calculated for HINA and its anionic form (in D_2O/NaOH mixture solvent) by the following equation.[228-231]

$$K_{hyd} = \frac{\text{peak area integration of HINA–hydrate}}{\text{peak area integration of HINA}} \qquad \textbf{Eq. 2.7}$$

The constant observed for HINA (in pure D_2O) is $K_{hyd} = 8*10^{-3}$ M^{-1}, and it is higher than that for the anionic HINA (HINA in D_2O/NaOH mixture). It indicates that the neutral form of HINA has a higher tendency to form the hydrates than its anionic form, which is reasonable since HINA is more electron-poor in its structure than its anionic form. However, this observation conflicts with the previous hypothesis, ruling out the green emissive contribution from the hydrate form of HINA. It thus proves that water is not necessary for the formation of green emissive species, in agreement with the aforementioned base-addition results (**Figure 2.9**). In addition, no hydrates were found in the ^{1}H NMR spectra of HINA in DMSO-d_6/water systems, while the green emissive occurred in the same system. Again, it indicates that the green

emissive does not come from the hydrates, and water is not necessary for the formation of the green emissive species (see additional data).

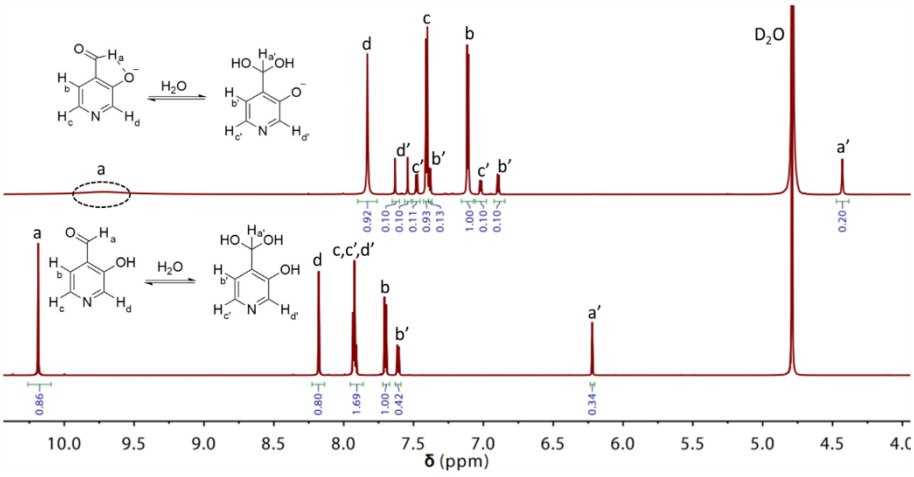

Figure 2.11. ^{1}H NMR spectra of HINA in D_2O (bottom) and NaOH addition (top).

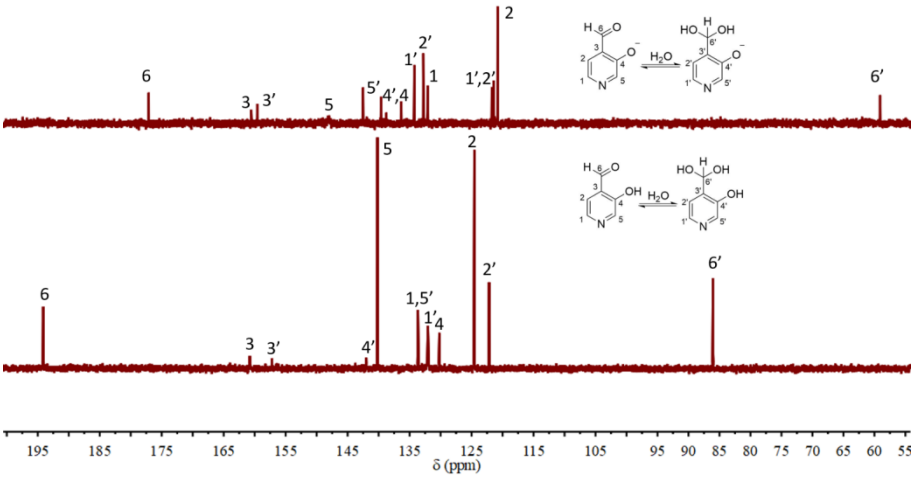

Figure 2.12. ^{13}C NMR spectra of HINA in D_2O (bottom) and NaOH addition (top).

2.2.4 Comparison of HINA with its analogs

To explore the emission mechanism of HINA, in addition to the already aforementioned HPA (an isomer of HINA) and HAP (a ketone analog of HINA), the photophysical properties of the structurally similar molecules (**Figure 2.13**), salicylaldehyde (SA, a phenyl analog of HINA) and pyridoxal (a biological hydroxy-formyl-pyridine), were evaluated as well. As mentioned beforehand (**Table 2.1**), HPA shows similar spectroscopic features as HINA, which also displays three (de)protonate states in aqueous media. However, the absorbance and emission of HPA, both in its neutral and anionic forms, are hypsochromically shifted compared to HINA. Furthermore, the blue and green emissions, corresponding to its neutral and anionic forms,

respectively, are weaker than those of HINA. For instance, the quantum yield of anionic HPA is only 1.4 %.

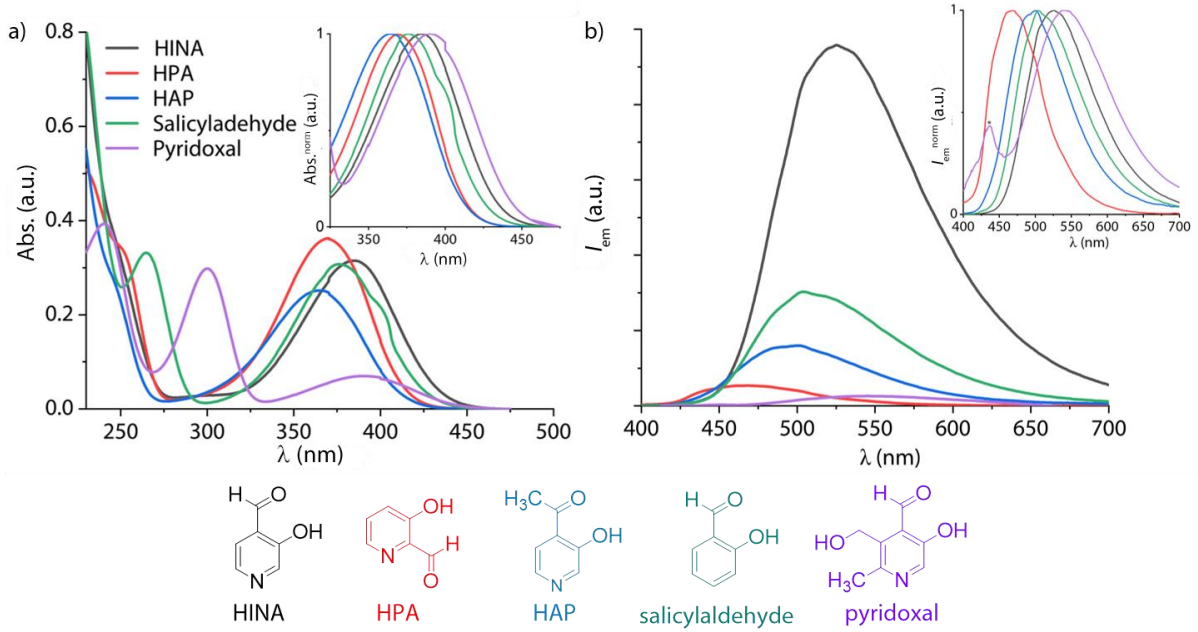

Figure 2.13. Absorbance (a) and emission (b, λ_{ex} = 380 nm) spectra of anionic form of HINA (black line), HPA (red line), HAP (blue line), salicylaldehyde (green line), and pyridoxal (purple line) in water at pH ≥ 9.5. Insets show the normalized spectra at their maximum absorbance and emission wavelength. The chemical structures of these five small molecules are shown below the spectra.

HAP, the ketone analog of HINA, is even poor emissive (QY < 1 %) and requires a higher pH for its deprotonation than HINA or HPA. It is worth mentioning that HAP, as is typical for ketones, does not or only very little form hydrate in water, which can be confirmed by the ^{1}H NMR results (additional data), providing further evidence that the hydrates are not the blue and green emission species for these kinds of fluorophores. Similar to HINA, the pK_a values observed for both HPA and HAP through absorbance- and emission-based titration overlay with the observation from the pH titration experiment (see **Table 2.2** and additional data). Again, the deprotonation of the neutral form of these hydroxyl-pyridines does not occur during the lifetime of their excited states, although they exhibit the strong acidity of the excited states (pK_{a2}*), which was estimated by Förster's cycle analysis (see **Chapter 2.2.1**).

To the best of knowledge, 7-azaindole (7AI, 15 atoms) and salicylaldehyde (SA) are the smallest green-emissive fluorophores that have been reported so far. Compared to HINA, they both require a higher pH of pH > 13.5 and pH > 8.40, respectively, for the deprotonation.[232-234] SA is structurally closely related to HINA (14 atoms), in which the pyridine ring is changed to a phenyl ring, resulting in a more electron-rich structure of SA, but shows an unexpected hypochromic shift in its absorbance and emission spectra (**Figure 2.13**). Compared to HINA,

SA is a poor fluorophore because it is not emissive in its neutral form and weak emissive in its anionic form (QY = 2 % at pH = 10.0). Pyridoxal is significantly large both in atom numbers and molecular weight but is much less emissive than other formyl-hydroxyl-pyridines.

2.2.5 Computational investigation

The theoretical computation in this section is done by Prof. Wim Klopper. Therefore, this thesis will not detail the methodology development. Only the results and the conclusions will be described in the following text.

In order to explore the emission mechanism of these pyridine fluorophores, coupled-cluster (CC) calculations were performed by the Klopper group using the second-order approximate coupled-cluster singles-and-doubles model CC2 with the def2-TZVPPD basis set,[235-236] and using the resolution-of-the-identity (RI) approximation with corresponding auxiliary basis set (cabs).[237-238] As shown in **Table 2.4**, the anionic HINA's predicted absorbance and emission bands agree with the experimental findings. The $n \rightarrow \pi^*$ transition has almost zero oscillator strength (0.0003) while that of the $\pi \rightarrow \pi^*$ is four orders of magnitude larger, which resulted in computed RGB values (additional data) that agrees well with the experimental observed green emission. Besides, the maximum emission wavelength tendency between HINA, HPA, and SA was predicted correctly (**Table 2.4** and **Figure 2.14**). Nevertheless, it is found that the theoretical calculation for HINA and its analogs is not that easy despite their simple chemical structures. In fact, there are very close electronic states in energy and the vibronic effects,[211-212, 239] that are important for describing the photophysical properties because the computed emission maximum wavelength of the neutral form (and pronated form) of HINA observed from the DFT and CC-based methods are primarily deviated from experimental values, even after considering the solvation effects.

Table 2.4. Vertical absorption (VA) energy (in eV) with corresponding oscillator strength (f_{osc}), vertical emission (VE) energy (in eV) with corresponding oscillator strength (f_{osc}), adiabatic electronic energy (in eV), and $0 \rightarrow 0$ transitions (in eV) of the $n \rightarrow \pi^*$ and $\pi \rightarrow \pi^*$ transitions of the anions of HINA, SA, and HPA obtained at the CC2/def2-TZVPPD level. Wavelengths (in nm) are given in parentheses.

		VA	f_{osc}	VE	f_{osc}	Adiab.	0→0
HINA	$\boldsymbol{n \rightarrow \pi^*}$	2.81 (442)	0.0003	1.78 (696)	0.0001	2.38 (521)	2.31 (537)
	$\boldsymbol{\pi \rightarrow \pi^*}$	2.99 (415)	0.1669	2.20 (562)	0.0889	2.66 (466)	2.59 (479)
SA	$\boldsymbol{n \rightarrow \pi^*}$	3.09 (402)	0.0001	1.99 (624)	0.0001	2.60 (476)	2.51 (495)
	$\boldsymbol{\pi \rightarrow \pi^*}$	3.09 (402)	0.1641	2.47 (502)	0.0985	2.28 (440)	2.73 (453)
HPA	$\boldsymbol{n \rightarrow \pi^*}$	2.74 (453)	0.0002	1.84 (674)	0.0001	2.35 (527)	2.27 (547)
	$\boldsymbol{\pi \rightarrow \pi^*}$	3.03 (409)	0.1582	2.36 (525)	0.0844	2.74 (452)	2.67 (464)

For the neutral form of HINA and its analogs, substantial discrepancies with the experiments appeared when computing the emission transition because of the quite different equilibrium structures of ground and excited states, which can be considered an excited-state intramolecular proton-transfer (ESIPT). The ESIPT may also explain the vast differences between the calculated excited acidities (pK_{a2}*) and the experimental observation from experimental findings in pH-titrating experiments. Further, it may also be an explanation for the almost same pK_a values found in absorbance and emission recording measurements. Therefore, advanced theoretical studies and methods are still needed for a deep understanding of the emission mechanisms of HINA and its analogs.

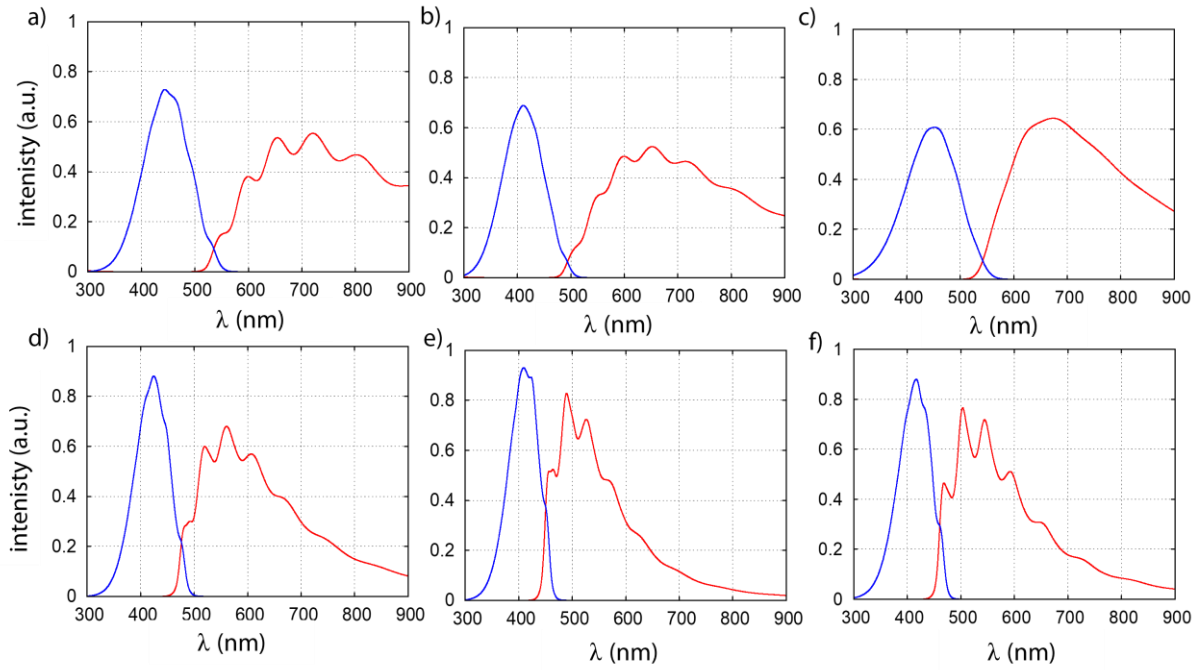

Figure 2.14. Franck-Condon profiles of absorption (blue lines) to and emission (red lines) from the $n \rightarrow \pi^*$ (a-c) and $\pi \rightarrow \pi^*$ (d-f) excited states of the anions of a,d) HINA, b,e) SA, and c,f) HPA. Computed at 298.15 K with Gaussian broadening with full width at half maximum of 500 cm^{-1} from CC2/def2-TZVPPD data using the time-dependent wave-packet approach as implemented in hotFCHT.

2.2.6 Potential applications

Unlike other push-pull fluorophores, HINA shows a good quantum yield in water, making it attractive for further applications. For instance, it may serve as a ratiometric, fluorescent pH indicator due to its distinct differences in absorbance- and emission properties in its protonated, neutral, and deprotonated forms. The following text describes the potential applications of HINA in the molecular sensing and cell imaging field.

2.2.6.1 Application in cell imaging studies

The cell-related experiment in this section is done by Dr. Laura Talamini and Bianca Martins Estevão from the research group of Prof. Luisa De Cola. Therefore, this thesis will not detail the methodology development. Only the results and the conclusions will be described in the following text.

The superior emission range, good quantum yield in water, and the physiological pK_a values make HINA attractive for the application in cell imaging. MC38, MCF10, and HEK293 cells were used for the measurements. The detailed information on the procedure is listed at the end of this chapter. Preliminary results show that these fluorophores are at a low cell toxicity level; for instance, see **Figure 2.15**, the cell viability of MCF10 cells is still around 100 % upon

treatment with 200 µM HINA after 24 hours. Further, the cell imaging experiments show that the fluorophores can permeate through biological membranes[208, 240] and localize in the perinuclear region of the cells (**Figure 2.16**a).

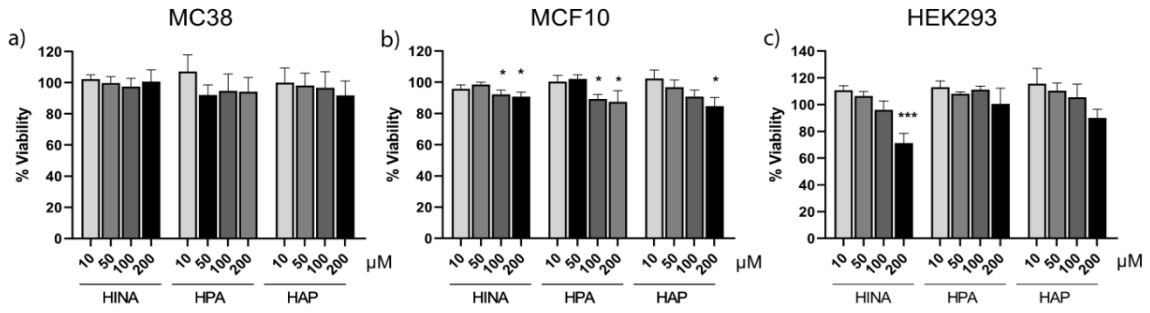

Figure 2.15. Cytotoxicity assay of HINA, HPA, and HAP in a) MC38, b) MCF10, and c) HEK293 cell line after 24 hours of incubation at increasing concertations (10-200 µM). The cytotoxicity is expressed as % of cell viability compared to control. Data are expressed as mean ± standard error. One-way ANOVA and Dunnett's post hoc test *p< 0.05 and ***p<0.0005.

The photoactivation cell experiment in this section is carried out by Dr. Elisa D'Este.

More interestingly, rapid fluorescence photoactivation of HINA-treated cells was found within seconds during the fluorescence imaging experiments (**Figure 2.16**b). Similar behavior was confirmed by irradiation of HINA solution with a strong light source (spectrometer) and in the presence of hydrogen peroxide (additional data). However, the mechanism of this photoactivation of HINA is not clear yet.

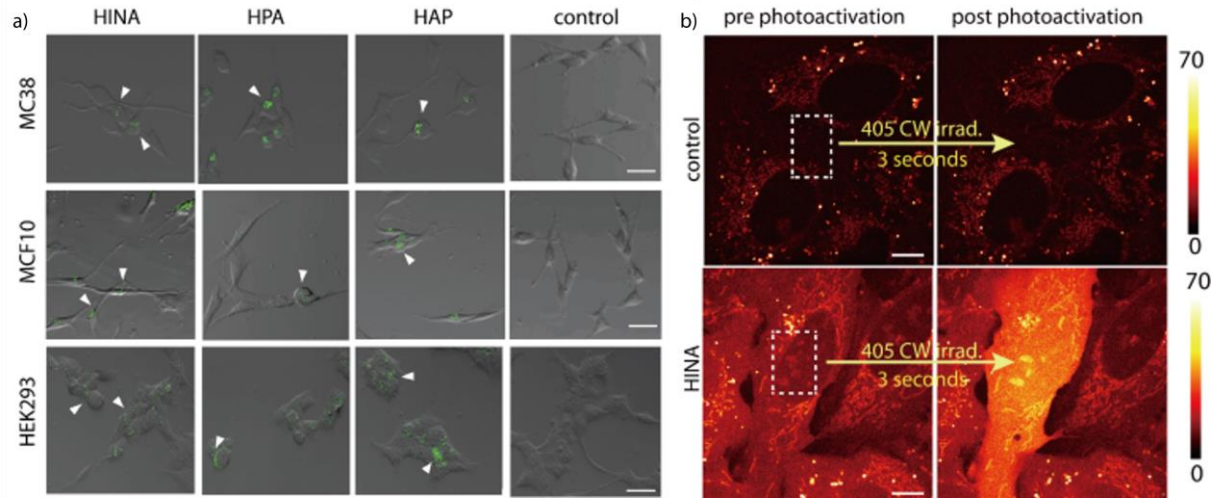

Figure 2.16. a) Microscopy images of the internalization of HINA, HPA, and HAP in MC38 (top row), MCF10 (middle row), and HEK293 (bottom row) cell line after 1 hour of incubation at the concertation of 100 µM. The green signal (white arrowhead) is related to dye molecules, and it is mainly localized in the perinuclear region of cells. The control experiment (untreated with dyes) did not show any specific signal (left panel). Scale bar: 20 µm. b) Confocal images before and after photoactivation of U2OS cells incubated with 2 mM HINA followed by washing (bottom row) and control without dye. Dashed boxes indicate the area irradiated with a CW 405 light source for three seconds. Colour bars and corresponding minimum and the maximum number of counts displayed in the image are on the right. Scale bars: 10 µm.

2.2.6.2 Sensing application of HINA

The initial reason why I chose the HINA molecule was inspired by the commercial available chromophore 4-(dimethylamino)cinnamaldehyde (DMAC) which can react with L-cysteine (L-Cys) by forming a 1,3-thiazolidine ring between the aldehyde group and L-Cys. It is also one of the commonly used design principles for a thiol-reactive probe.[101, 112, 241] Therefore, HINA, as expected, can serve as a thiol-amine probe, see **Figure 2.17** for the structures, and the reaction was also characterized by ^{1}H and ^{13}C NMR measurements (additional data).

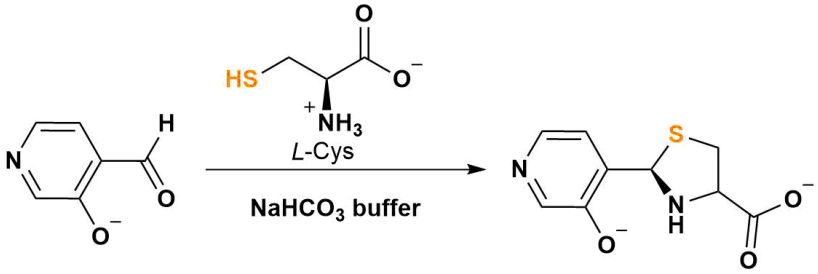

Figure 2.17. Schematic representation of the reaction of L-Cysteine with HINA in $NaHCO_3$ buffer (25 mM) at pH 9.5 and 25 °C.

Unfortunately, according to the absorbance and emission measurements, HINA behaves similar to other reported aldehyde moiety-based probes that only can detect L-Cys in a large excess amount and needs a long reaction time (**Figure 2.18**). Therefore, HINA seems not an ideal probe for L-Cys detection despite its excellent aqueous solubility and sufficiently quantum yield in the aqueous solution.

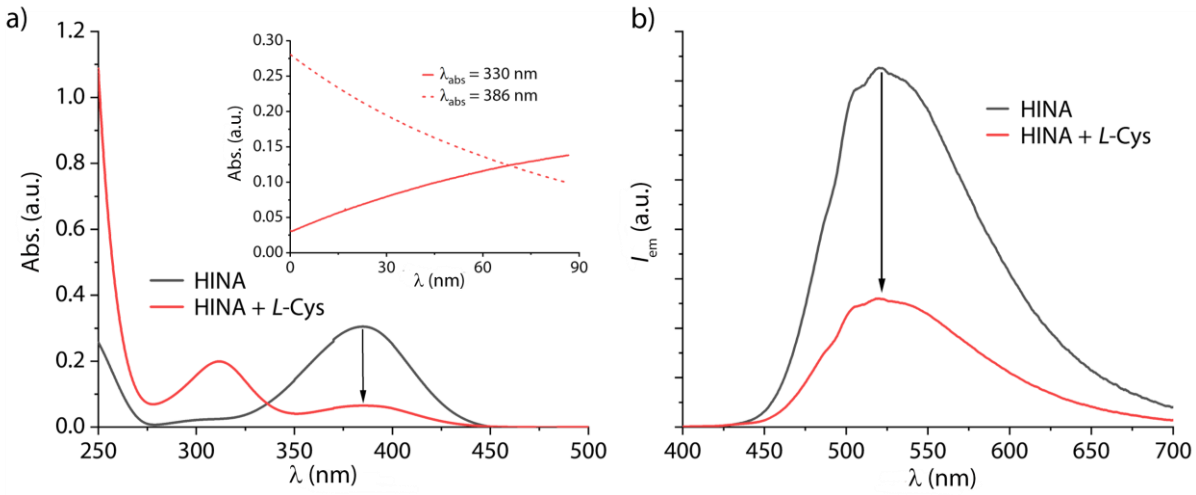

Figure 2.18. Absorbance (a) and emission (b) spectra of HINA (50 µM, black line) upon addition of L-cysteine (1 mM, red line) in $NaHCO_3$ buffer (25 mM) at pH 9.5 and 25 °C. Inset shows the absorbance kinetics trace of the reaction. The absorbance and emission spectra were recorded after 90 minutes of reaction time.

Because of its promising fluorescence, HINA was also considered to serve as an emissive indicator in the supramolecular sensing assay. In addition, the pyridine moiety within the HINA

structure makes it an attractive coordination ligand for many metal complexes, *e.g.*, platinum(II).[242] As shown in **Figure 2.19**a, the emission of HINA was quenched after the Pt-coordination. Then it was displaced by a stronger binding ligand, *e.g.*, thiols, resulting in an emission recovery in organic and aqueous solutions (**Figure 2.19**b). The binding constants for these two steps (HINA to L-Pt-DMSO; L-Cys to L-Pt-HINA) reaction were determined by emission titration measurements (**Figure 2.20**).

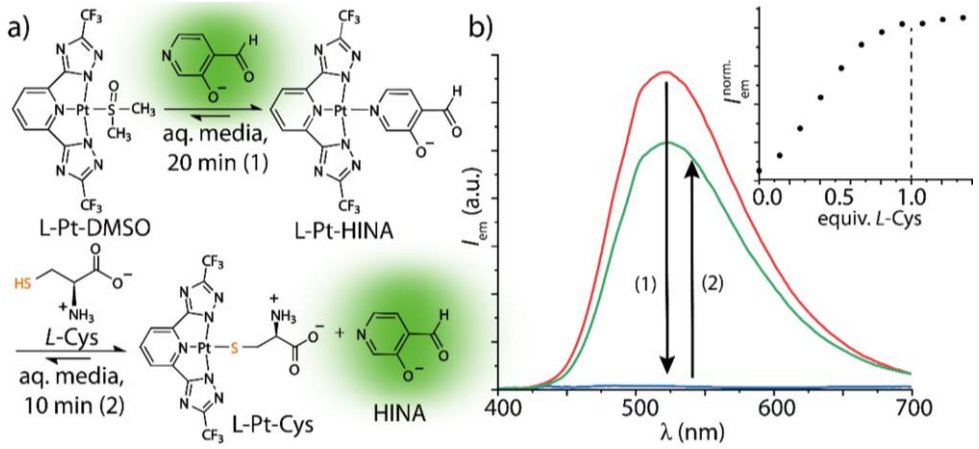

Figure 2.19. a) Schematic representation of the two-step reaction of L-Cys detection: *i*) HINA can react with a Pt(II)-precursor (L-Pt-DMSO) to form a non-emissive L-Pt-HINA complex; *ii*) Upon addition of L-Cys, HINA is displaced and emissive again. b) Emission spectra of HINA (50 µM, red line, λ_{em} = 380 nm) upon addition of L-Pt-DMSO (50 µM, blue line) and subsequent addition of L-Cys (50 µM, green line). The insert shows a titration of L-Pt-HINA (50 µM) with L-Cys in a concentration range of 0 - 73 µM. All the spectra were obtained in 25 mM $NaHCO_3$ buffer (pH 9.5) containing 0.9 mM CTAB.

The binding constants values confirmed that L-Cys is a stronger binder (1.0×10^7 M^{-1}) for Pt(II) complexes compared to HINA (5×10^6 M^{-1}). Moreover, the reaction was also characterized by ESI-MS and ^{1}H NMR measurements. The molecular mass of the L-Pt-HINA and L-Pt-Cys metal complexes can be clearly seen from the ESI-MS spectra of the reaction solution (see additional data). Overall, L-Cys can be detected in a micromolar concentration range within 10 min in organic and aqueous solutions by this Pt-complex-based indicator displacement assay (IDA), where HINA serves as an emissive indicator.

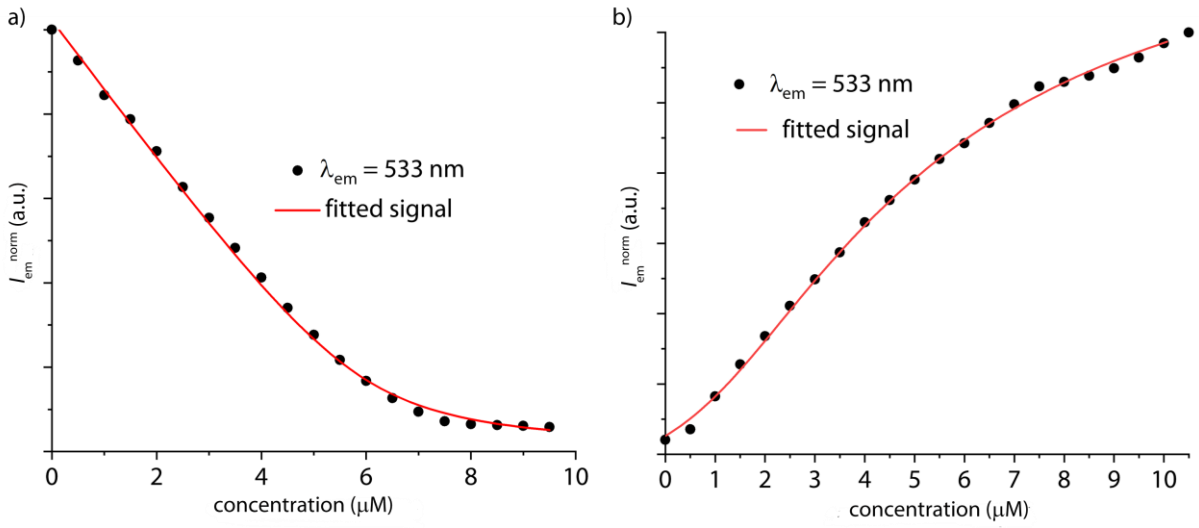

Figure 2.20. a) Binding constant determined by fluorescence intensity (λ_{ex} = 380 nm, λ_{em} = 533 nm) of HINA (5 μM) and L-Pt-DMSO (0-9.5 μM). The binding constant of HINA to L-Pt-DMSO is K_{a1} = 5.0 (± 0.2) 10^6 M^{-1} with a direct binding model. b) Binding constant determined by fluorescence intensity (λ_{ex} = 380 nm, λ_{em} = 533 nm) of L-Pt-HINA (5 μM) and Cys (0-10.5 μM). The binding constant of L-Cys with Pt-DMSO is K_{a2} = 1.0 (± 0.2) 10^7 M^{-1} by using an IDA fitting model. The K_{a1} value was taken from the first step as a K_{HD} value in the fitting process. Acquired data is depicted as black dots and fitted data as the red line.

Analogously, HINA can also be displaced from a Pd(II)-complex by pyridine (**Figure 2.21**-**Figure 2.22**). It is believed that HINA-capped metal-organic building blocks could be reacted on-demand with stronger ligands to form metal-organic cages or -frameworks,[243-245] thereby providing an *in-situ* fluorescence response for monitoring of such reactions in real-time.

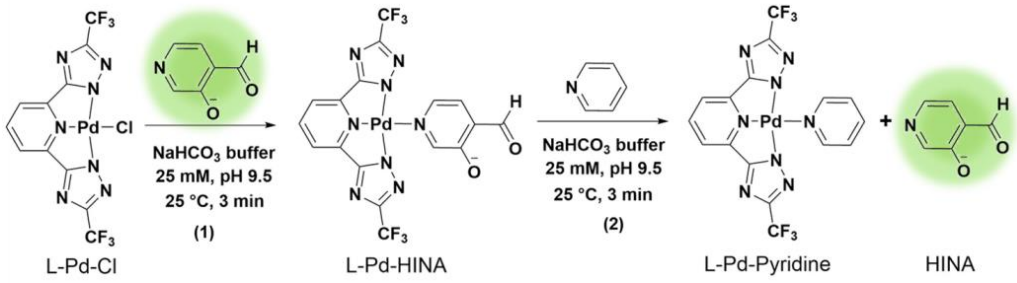

Figure 2.21. Schematic representation of HINA can be reacted with Pd(II) precursor to form a non-emissive L-Pd-HINA complex, and HINA can be released as an emissive indicator upon adding pyridine in $NaHCO_3$ buffer (25 mM) with 0.9 mM CTAB at pH 9.5 and 25 °C.

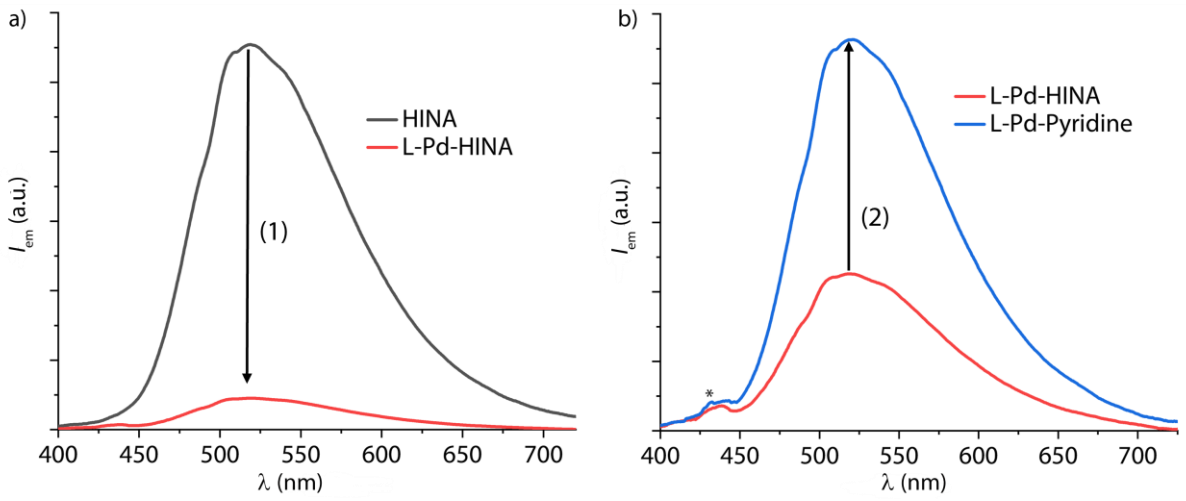

Figure 2.22. Emission spectra of the formation of non-emissive L-Pd-HINA complex (a) and upon addition of pyridine (b) in $NaHCO_3$ buffer (25 mM) with 0.9 mM CTAB at pH 9.5 and 25 °C. The asterisk in the emission spectrum indicates the Raman scattering band of water at the selected excitation wavelength.

The following chapters will introduce a more detailed investigation of the thiol sensing via metal complex-based assay.

2.3 Conclusions and outlook

In conclusion, 3-hydroxyisonicotinealdehyde (HINA) has been identified as the smallest green emissive dye and maybe reach the fundamental size limit. Uniquely, HINA occurs in three different protonation states, and each of them is distinctly fluorescent. Despite being a push-pull chromophore, the QY of HINA in water is surprisingly high. HINA's commercial availability and favorable photophysical properties (large Stokes shift, pH-dependent ratiometric emission properties that are switching in bio-relevant pH 7 regime) will enable future applications, ranging from its use as a fluorescent dye to its function as an indicator in supramolecular assays.

The synthesis and investigation of additional hydroxyl-functional pyridine-aldehydes and -ketones will lead to the discovery of novel green-emissive labels with improved photophysical properties. Like HINA, these dyes will provide excellent test cases to evaluate theoretical predictions of emission spectra using highly advanced computational methods capable of considering both vibrionic effects and excited-state intramolecular proton-transfer process (ESIPT). Therefore, a following-up study will start with a series of fluoro-substituted HINA derivatives. See **Figure 2.23** for their structures.

The synthesis of the fluoro-substituted HINA derivatives was carried out by Hannes Kühner from the research group of Prof. Stefan Bräse.

Figure 2.23. Chemical structures of fluoro-substituted HINA derivatives.

Experimental information

Cell experiments description

Cell imaging experiments

This part of the work was done by Dr. Laura Talamini and Bianca Martins Estevão from the research group of Prof. Luisa De Cola.

Cells were grown as a single layer in adhesion in an appropriate cell culture medium and were maintained at 37 °C and in a 5% CO_2 humidified atmosphere.

MC38 cells were grown in DMEM-Low Glucose (Dulbecco′s Modified Eagle Medium, pyruvate, and L-glutamine, Gibco) with the addition of 10 % fetal bovine serum (FBS, Gibco) 0.1 mM MEM Non-essential Amino Acid Solution (Sigma-Aldrich) 10 mM HEPES buffer (Sigma-Aldrich) 100 U/mL penicillin 0.1 mg/mL streptomycin. MCF10 cells were grown in DMEM-Low Glucose (Dulbecco's Modified Eagle Medium, pyruvate and L-glutamine, Gibco) with the addition of 10 % of fetal bovine serum (FBS) and 1 % L-glutamine (200 mM) 100 U/mL penicillin, 0.1 mg/mL streptomycin, 100 ng/mL cholera toxin (Sigma-Aldrich) and 10 µg/mL human insulin (Sigma-Aldrich). HEK293 cells were grown in DMEM-Low Glucose (Dulbecco′s Modified Eagle Medium, pyruvate, and L-glutamine, Gibco) with the addition of 10% fetal bovine serum (FBS) 100 U/mL penicillin, 0.1 mg/mL streptomycin.

MC38, MCF10, and HEK293 were seeded on a round glass slide in 12-well plates at the 70000 cell/well concentration and left to adhere for 24 hours. Exclusively for HEK293 cells, a round glass slide was pre-coated with 0.01 % poly-lysine solution (Santa Cruz) to optimize the cell attachment.

HINA, HPA, and HAP internalization was carried out by incubating at the concentration of 100 µM for 1 hour. After incubation, cells were washed two times with phosphate-buffered saline (PBS 1x, Gibco) fixed with 4 % paraformaldehyde (PAF) in PBS 1x for 20 minutes and washed two times with PBS 1x. Images were captured with LSM 710 confocal microscopy (Zeiss)

equipped with specific laser λ_{ex} = 405 nm. The images of HEK 298 and MCF cell line were acquired in a 60 % power of the laser gain 873, digital gain 0.89, and offset -285; the image of MC38 cell line was collected in an 18 % power of the laser gain 716, digital gain 1.43 and offset -257.

In order to evaluate the cytotoxicity of HINA and its analogs, the cell viability assay (CellTiter96® Aqueous One solution Cell Proliferation Assay, Promega) was carried out on MCF10 and HEK293 cell lines. Cells were seeded at 20000 cells/well into a 96-well plate. The fresh medium containing serial concentrations of HINA or HPA, or HAP (10 µM - 200 µM) was added 24 hours after the seeding. Cells were incubated with the treatment for 24 hours. CellTiter96® Aqueous reagent (20 µL/well) was added and incubated for 2 hours according to the manufacturer's procedure. At least, plates were placed in a microplate reader (Multiskan GO, Thermo Scientific) to measure the absorbance at 490 nm, and the cytotoxicity was expressed as % of cell viability compared to control.

Photoactive in cell

This part of the work was done by Dr. Elisa D'Este.

U2OS or HeLa cells plated on glass coverslips were incubated with 2 mM HINA for 30 – 60 minutes in DMEM without phenol red (Gibco) supplemented with Pen/Strep (AppliChem) at 37°C, 5 % CO_2, and 95 % humidity. Washing (when applicable) and imaging were performed in the same medium. Imaging was performed at room temperature on an Abberior easy3D STED/RESOLFT QUAD scanning microscope (Abberior Instruments) built on a motorized inverted microscopeIX83 (Olympus) and equipped with a 100x/1.40 UPlanSApo oil immersion objective lens (Olympus). For confocal experiments, cells were imaged and photoactivated with a 405 CW laser set to 3 % of power, which corresponds to ~100 µW before the back focal aperture, and detection was performed with avalanche photodiodes (APD) in spectral window 475-600 nm. For the photoactivation, selected regions were scanned 100 times with 250 nm pixel size, 10 µs dwell time, and 1 line accumulation.

Quantification of the fluorescence intensity before and after photoactivation was performed in ImageJ 1.50b. For each irradiated cell, 5 different regions of interest (ROIs, 3 x 3 µm) in which no obvious cellular structures were visible (*e.g.*, no mitochondria-like labeling) were selected, and mean intensity values were averaged. As a control, 5 ROIs from the same field of view and non-irradiated cells were similarly selected and averaged. All irradiated cells (5/5) showed an increase in fluorescence in no-wash conditions, while 3/5 cells glowed up in case of washing.

Wide-field imaging was performed on the same microscope using a Basler acA4112-20 µm camera, X-Cite 200DC (Excelitas) light source, and a DAPI filter cube.

Computational information

The theoretical computation was carried out by prof. Wim Klopper.

Coupled-cluster calculations were performed using the second-order approximate coupled-cluster singles-and-doubles model CC2 in the def2-TZVPPD basis set, using the resolution-of-the-identity (RI) approximation with corresponding auxiliary basis set (cbas). The 1 s core orbitals were not included in the CC2 calculations (frozen-core approximation). All calculations were performed with version V7.4.0 of the TURBOMOLE program package.[207] Geometry optimizations of ground and excited states were performed with tight thresholds (scfconv=10, denconv=1d-9, jobex -level cc2 -energy 9 -gcart 6), and harmonic vibrational frequencies were obtained from numerical differences of analytical nuclear gradients using the NumForce script (NumForce -level cc2 -central -d 0.001). Franck-Condon profiles were computed using the time-dependent wave-packet approach as implemented in hotFCHT.[246] These computations were performed for a temperature of 298.15 K and included a Gaussian broadening with full width at half maximum of 500 cm^{-1}.

Additional data

pH-dependent properties for HPA and HAP

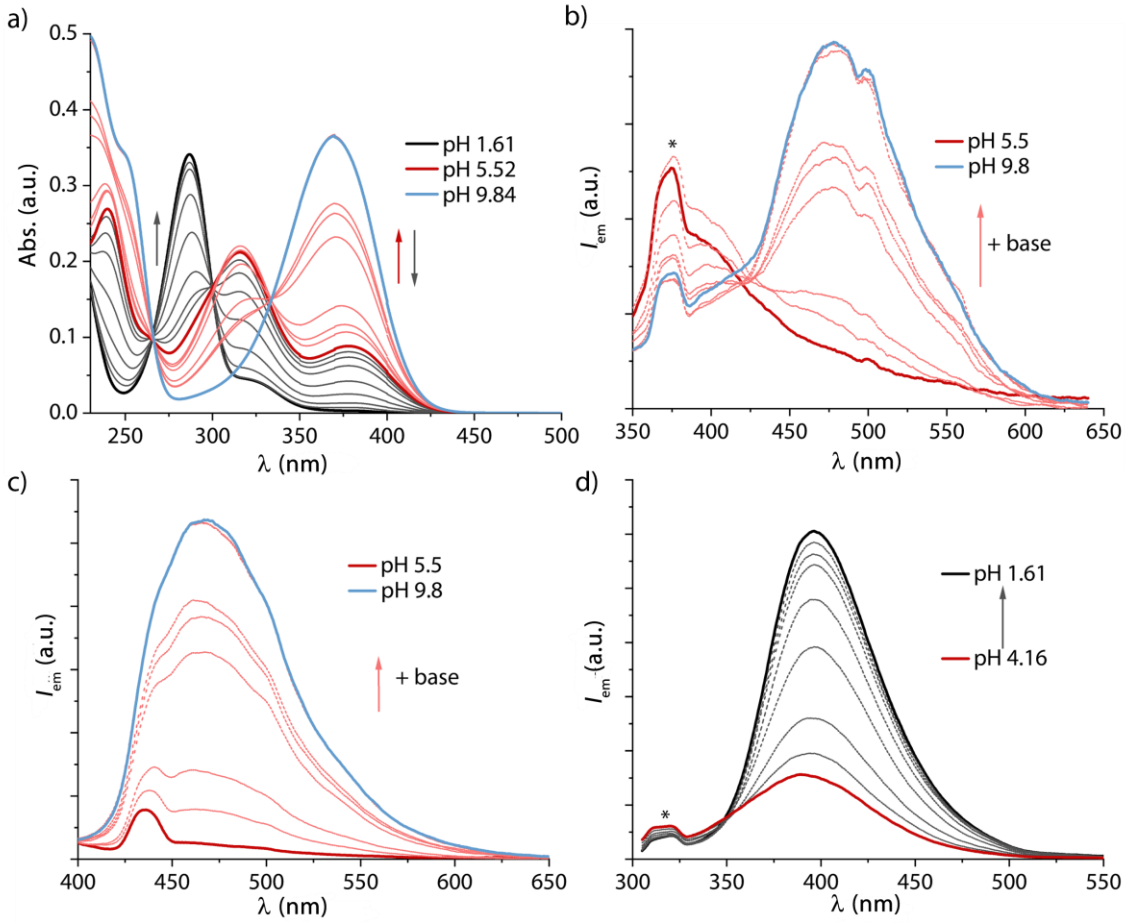

Figure 2.24. Absorbance (a) and emission (b-d) spectra of HPA (50 μM) titrated with a standard solution of H_2SO_4 (0.5 N, a series of black lines) and a standard solution of NaOH (0.1 N, a series of red lines) in MilliQ water at 25 °C. In b) λ_{ex} = 330 nm was used as the excitation wavelength while excitation was carried out in c) at 380 nm, and in d) at 285 nm. The asterisk in the emission spectrum indicates the Raman scattering band of water at the selected excitation wavelength.

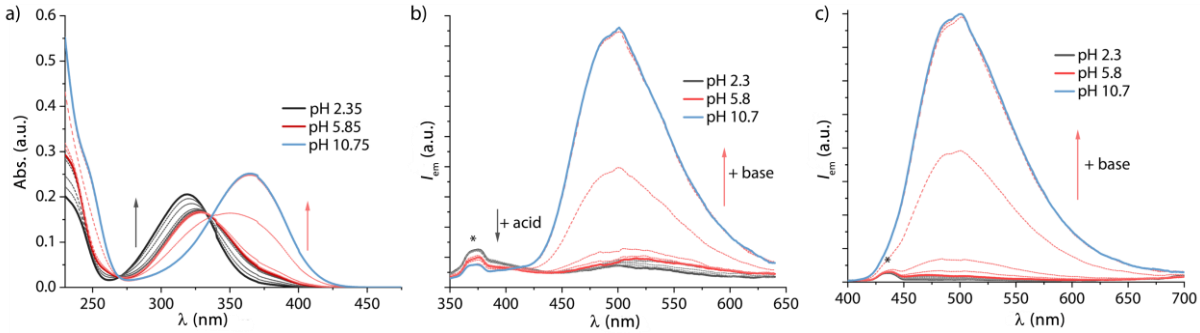

Figure 2.25. Absorbance (a) and emission (b-c) spectra of HAP (50 μM) titrated with a standard solution of H_2SO_4 (0.5 N, a series of black lines) and a standard solution of NaOH (0.1 N, a series of red lines) in MilliQ water at 25 °C. In b) λ_{ex} = 330 nm was used as the excitation wavelength while excitation was carried out in c) at 380 nm. The asterisk in the emission spectrum indicates the Raman scattering band of water at the selected excitation wavelength.

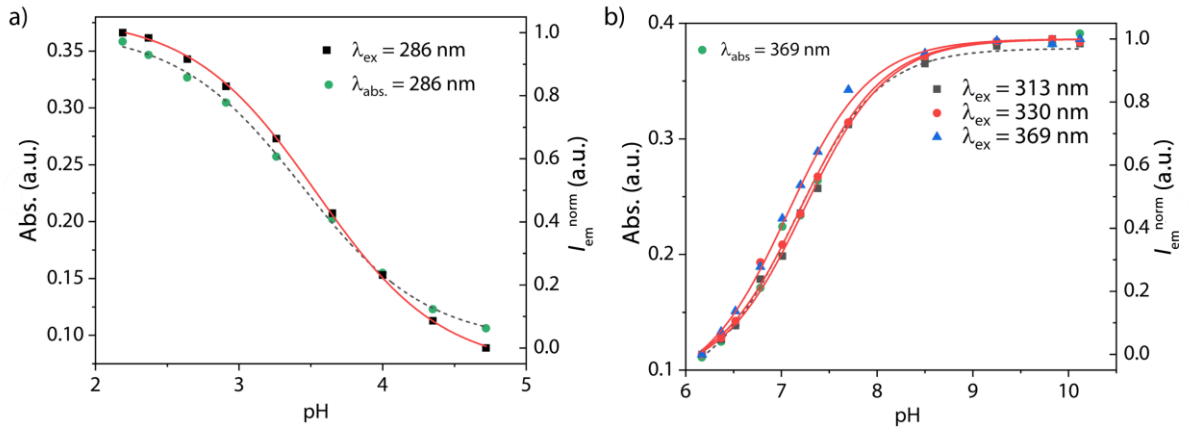

Figure 2.26. a) Plot of absorbance (λ_{abs} = 286 nm, green dots) and [0,1]-normalized emission (λ_{ex} = 286 nm, λ_{em} = 397 nm, black square) intensity change of HPA (50 µM) with pH values in the range of 2.19 - 4.72. b) Plot of absorbance (λ_{abs} = 369 nm, green dots) and [0,1]-normalized emission (λ_{ex} = 313 nm, black squares, λ_{ex} = 330 nm, red dots; λ_{ex} = 369 nm, blue triangles; λ_{em} = 467 nm) intensity changes of HPA with pH values in the range of 6.17 – 10.12. ***Notes***: the excitation wavelengths used here are characteristic for the neutral form (313 nm), isosbestic point of neutral form and deprotonated form (330 nm), and the deprotonated form (369 nm), respectively. Fits are shown in the dashed black link (absorbance) and the solid red line (emission). All the fitted pK_a values are summarized in **Table 2.2**.

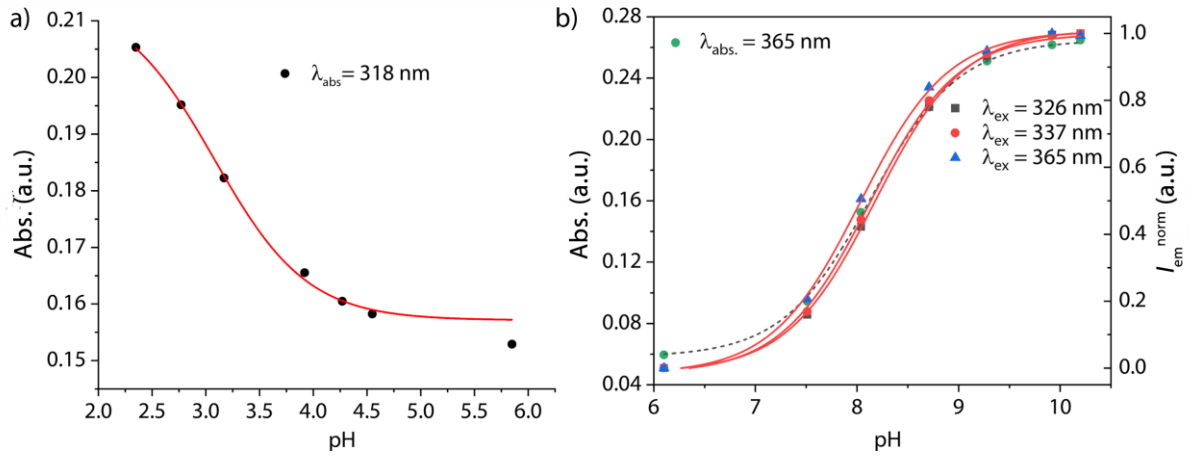

Figure 2.27. a) Plot of absorbance (λ_{abs} = 318 nm, black dots) intensity at the change of HAP (50 µM) with pH values in the range of 6.17 – 10.12. b) Plot of absorbance (λ_{abs} = 365 nm, green dots) and [0,1]-normalized emission (λ_{ex} = 326 nm, black squares, λ_{ex} = 337 nm, red dots; λ_{ex} = 365 nm, blue triangles; λ_{em} = 486 nm) intensity changes of HPA with pH values in the range of 6.10 – 9.92. ***Notes***: the excitation wavelengths used here are characteristic for the neutral form (326 nm), isosbestic point of neutral form and deprotonated form (337 nm), and the deprotonated form (365 nm), respectively. Fits are shown in the dashed black link (absorbance) and the solid red line (emission). All the fitted pK_a values are summarized in **Table 2.2**.

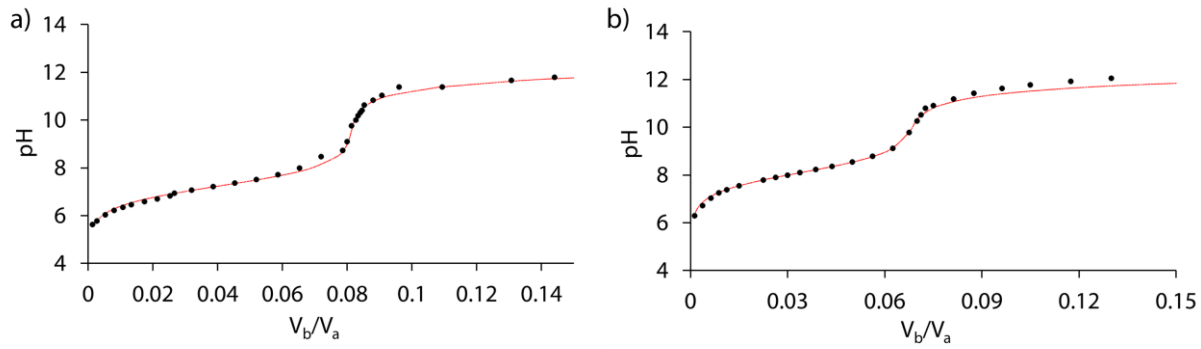

Figure 2.28. pH titration curve of HPA (10 mM, a) and HAP (10 mM, b) that was titrated with a standard solution of NaOH (0.1 N) in MilliQ water, the red dash line is the fitting curve, pK_{a2} = 7.24 (HPA), and pK_{a2} = 8.10 (HAP).

Solvent-dependency properties

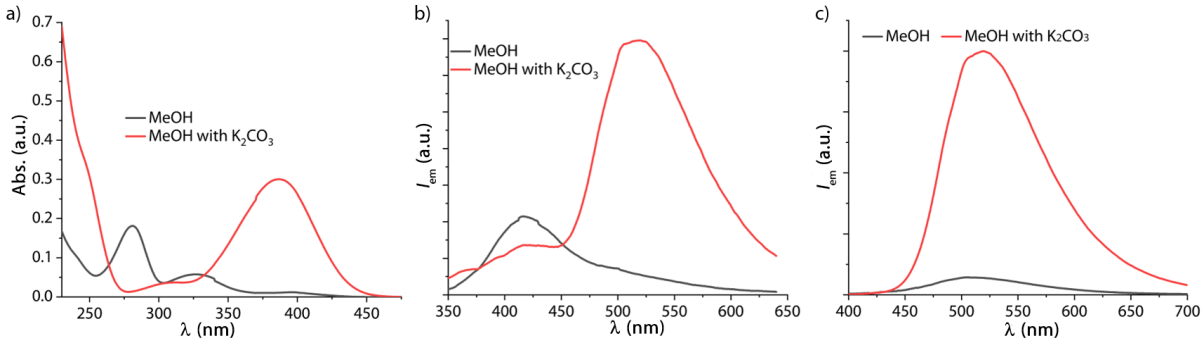

Figure 2.29. Absorbance (a) and emission (b-c) spectra of HINA (50 µM) in MeOH (black) and with anhydrous K_2CO_3 addition (red). In b) λ_{ex} = 330 nm was used as the excitation wavelength while λ_{ex} = 380 was used in c).

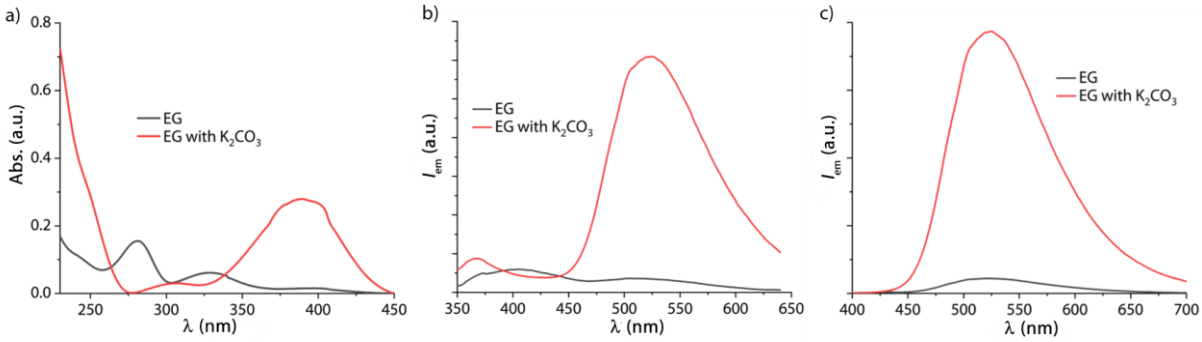

Figure 2.30. Absorbance (a) and emission (b-c) spectra of HINA (50 µM) in ethylene glycol (EG, black) and with anhydrous K_2CO_3 addition (red). In b) λ_{ex} = 330 nm was used as the excitation wavelength while λ_{ex} = 380 nm was used in c).

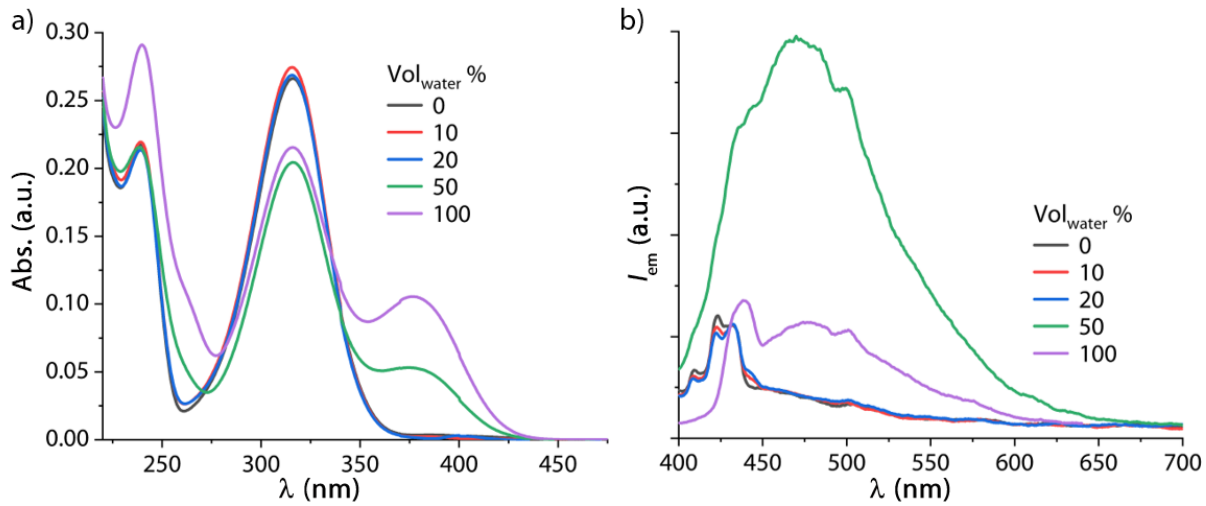

Figure 2.31. Absorbance (a) and emission (b) spectra of HPA (50 µM, λ_{ex} = 380 nm) in the mixture solvent of ACN/water (v/v) at 25 °C.

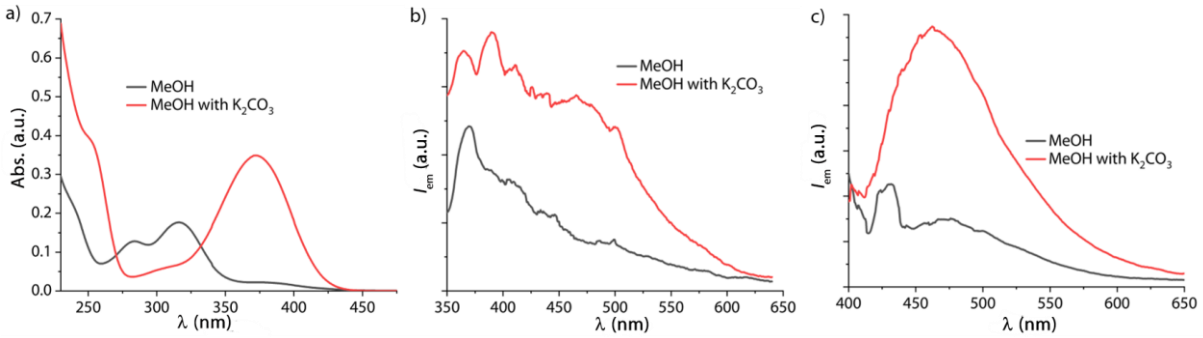

Figure 2.32. Absorbance (a) and emission (b-c) spectra of HPA (50 µM) in MeOH (black) and with anhydrous K_2CO_3 addition (red). In b) λ_{ex} = 330 nm was used as the excitation wavelength while λ_{ex} = 380 was used in c).

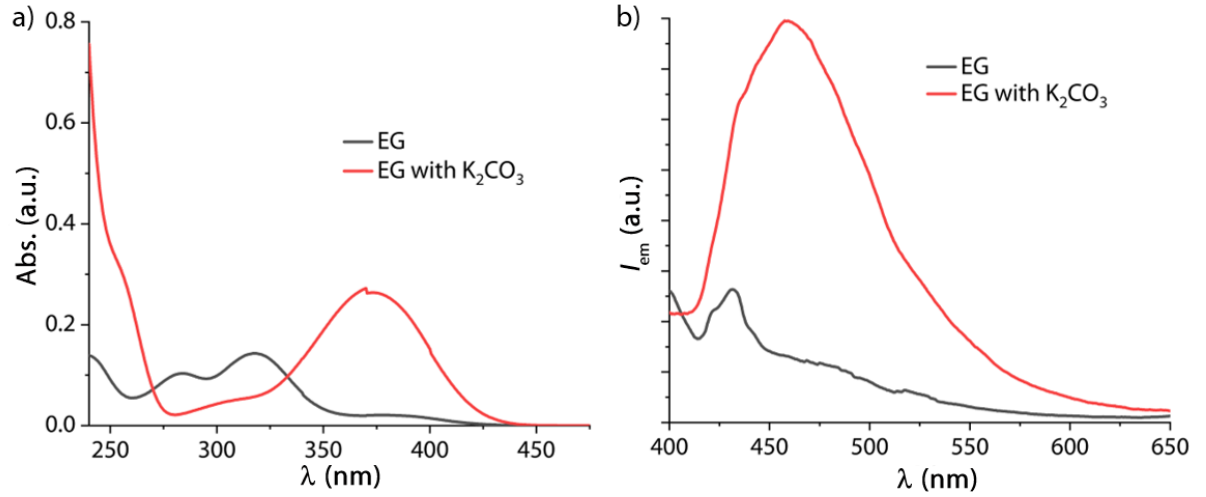

Figure 2.33. Absorbance (a) and emission (b-c) spectra of HPA (50 µM) in EG (black) and with anhydrous K_2CO_3 addition (red). In b) λ_{ex} = 330 nm was used as the excitation wavelength while λ_{ex} = 380 was used in c).

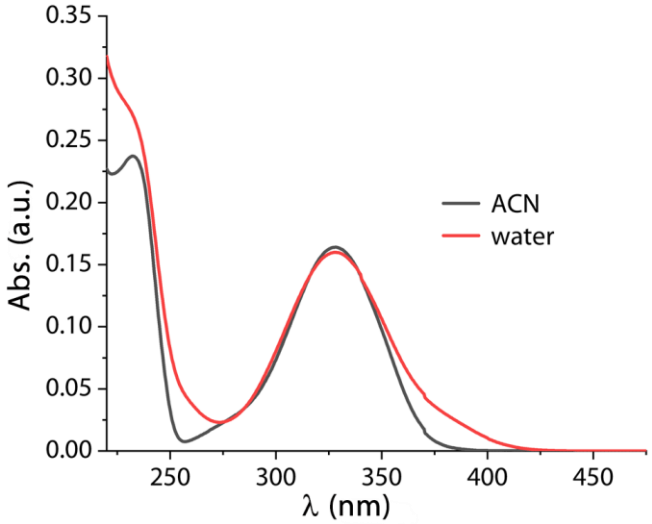

Figure 2.34. Absorbance spectra of HAP (50 μM) in ACN-water mixtures at 25 °C.

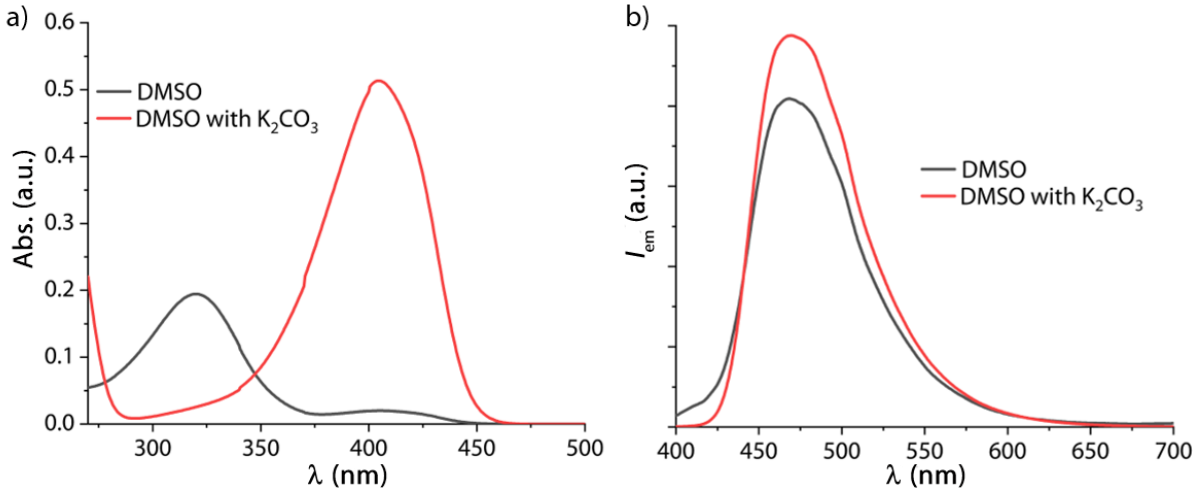

Figure 2.35. Absorbance (a) and emission (b, λ_{ex} = 380 nm) spectra of HAP (50 μM) in DMSO and with K_2CO_3 (0.3 M, red line) at 25 °C.

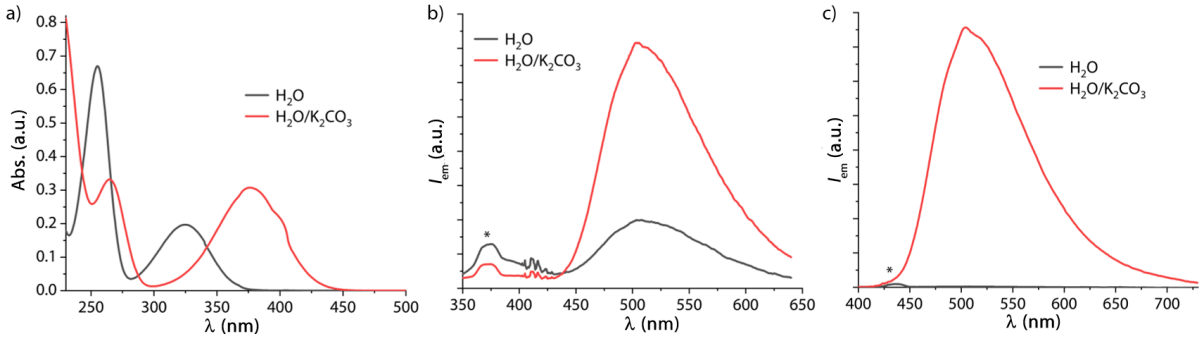

Figure 2.36. Absorbance (a) and emission (b-c) spectra of SA (50 μM) in MilliQ water and with K_2CO_3 (0.3 M) addition at 25 °C. In b) λ_{ex} = 330 nm was used as the excitation wavelength while excitation was carried out in c) at 380 nm. The asterisk in the emission spectrum indicates the Raman scattering band of water at the selected excitation wavelength.

NMR measurements

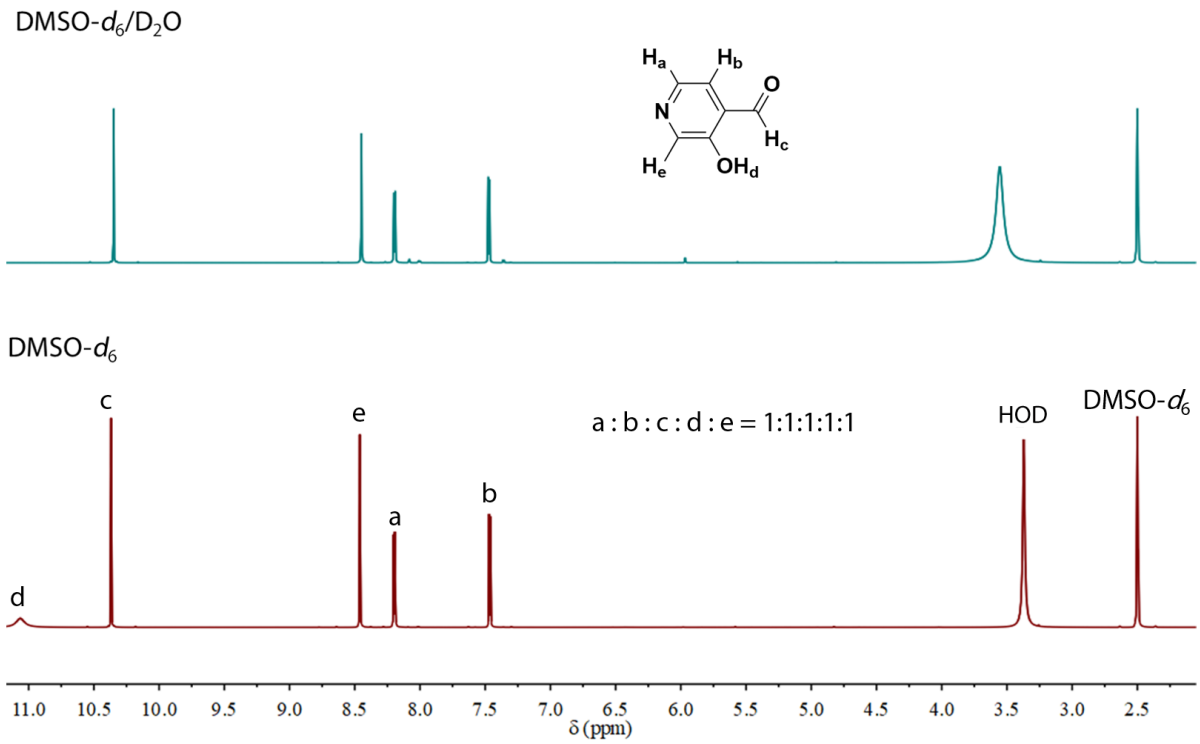

Figure 2.37. ^{1}H NMR comparison of HINA in DMSO-d_6 (bottom, red line) and the mixed solvent of DMSO-d_6/D_2O (top, blue line).

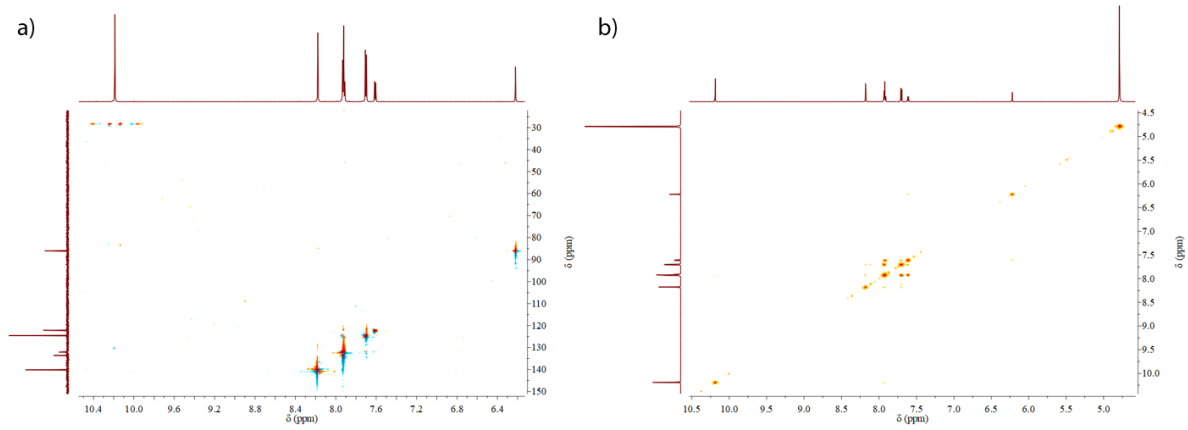

Figure 2.38. HSQC (a) and COSY (b) spectra of HINA in D_2O.

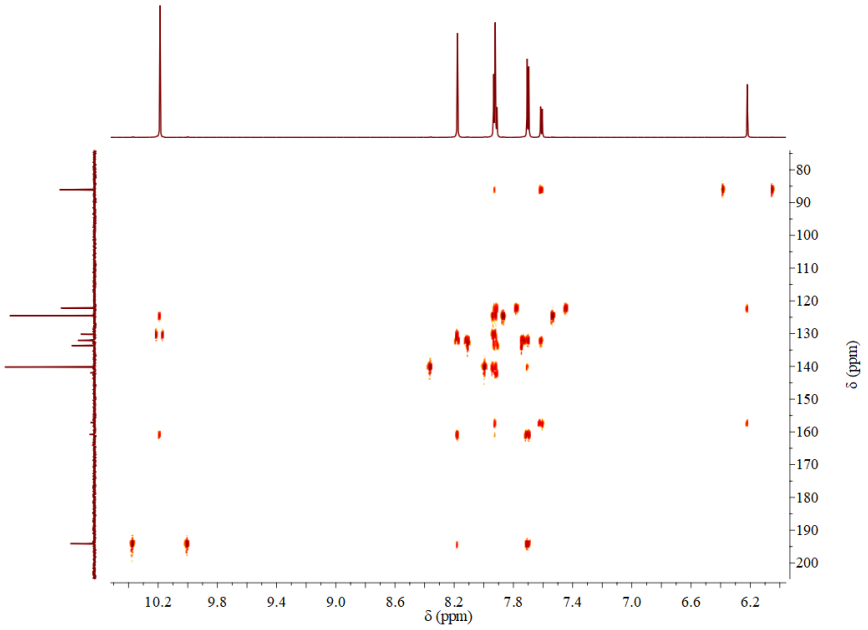

Figure 2.39. HMBC spectra of HINA in D_2O.

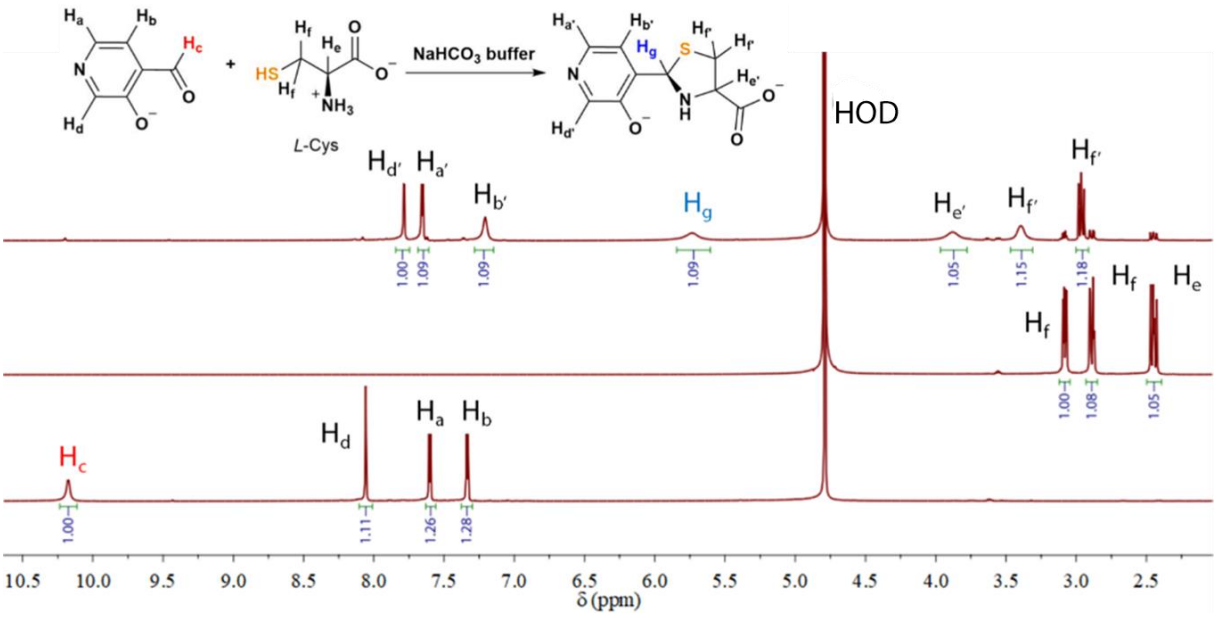

Figure 2.40. ^{1}H NMR spectra of HINA (50 µM, bottom), L-Cys (50 µM, middle), and the mixture solution (top) of HINA and L-Cys after overnight reaction in D_2O under the basic condition.

ESI-MS measurements

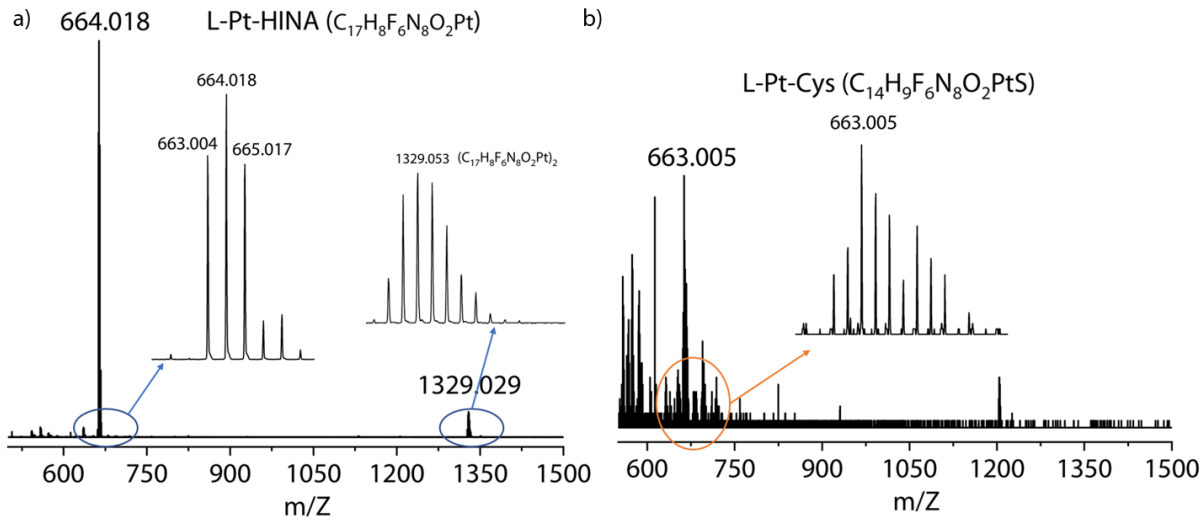

Figure 2.41. a) ESI-MS spectra of the solution of HINA (50 μM) after reacting with L-Pt-DMSO (55 μM) in 25 mM $NaHCO_3$ buffer (pH 9.5) containing 0.9 mM CTAB. Calcd. for $[M]^-$: 664.030; $[2M-H]^-$: 1329.060; found: $[M]^-$: 664.018; $[2M-H]^-$: 1329.029. b) ESI-MS spectra of the solution of L-Cys (50 μM) after reacting with L-Pt-HINA (50 μM) in 25 mM $NaHCO_3$ buffer (pH 9.5) containing 0.9 mM CTAB. Calcd. for $[M]^+$: 663.012; found: $[M]^+$: 663.005.

Photoactivation property of HINA

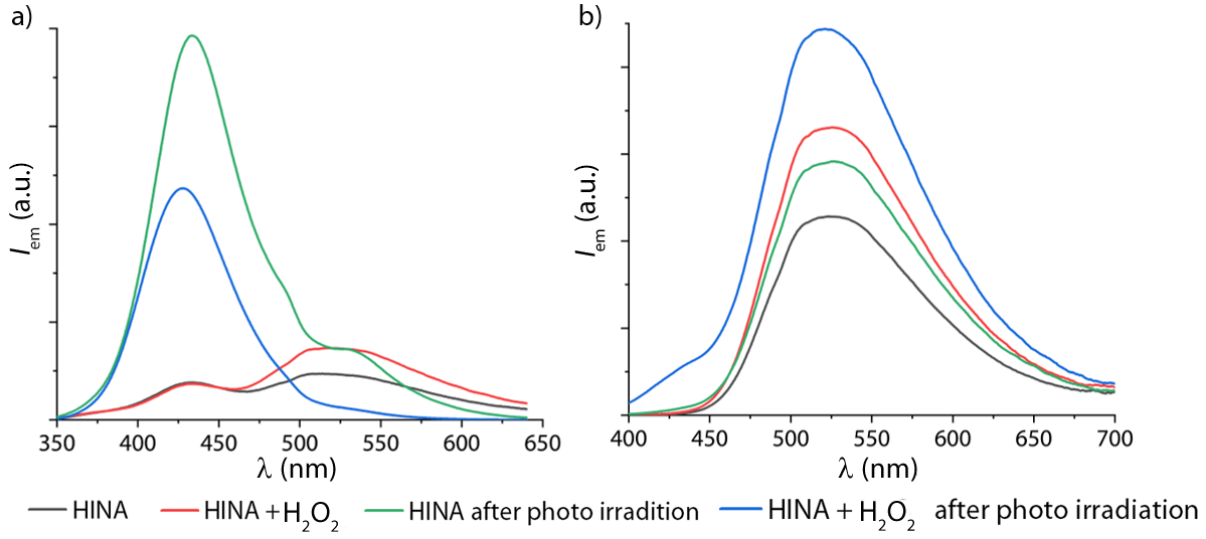

Figure 2.42. Emission spectra of HINA (1 mM, black line), HINA upon addition of H_2O_2 (10 mM, red line), the mixture of HINA and H_2O_2 with photo-irradiation 30 min (blue line), and HINA alone with photo-irradiation 30 min (green line). a) Excitation wavelength is 330 nm; in b) is 380 nm. All the spectra were measured in PBS buffer at pH 6.0.

Computational results

Table 2.5. Leading natural transition orbitals (NTOs) of the $n \rightarrow \pi^*$ and $\pi \rightarrow \pi^*$ transitions of the anions of HINA, SA, and HPA, computed at the equilibrium geometries of the respective excited states. Obtained at the CC2/def2-TZVPPD level and plotted for an isosurface value of $\pm$ 0.05 $a_0^{-3/2}$.

	$n \rightarrow \pi^*$		$\pi \rightarrow \pi^*$	
	Hole state	**Particle state**	**Hole state**	**Particle state**
HINA	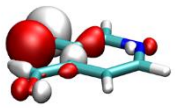	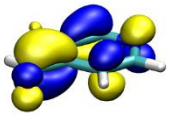	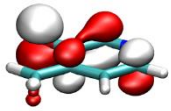	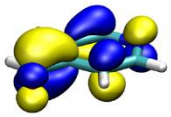
SA	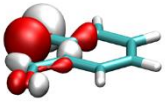	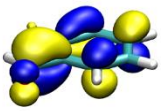	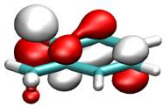	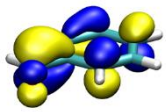
HPA	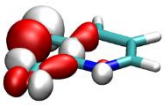	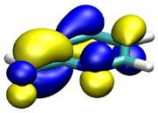	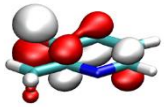	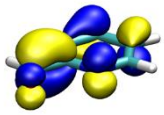

3 The spectral evolution of probe-conjugates enables analyte identification and quantification

*The results described in this chapter have been prepared for submission as "Differential sensing without arrays: The spectral evolution of probe-conjugates enables analyte identification and quantification." The experimental data collection and analysis were carried out by me under the supervision of Dr. Frank Biedermann and Prof. Luisa De Cola. The machine learning-based data analysis was carried out by Thomas Jochmann. The synthesis of SAP **1** was assisted by my former colleagues: Dr. Pronay Kumar Biswas and Alicja Siennicka.*

3.1 Abstract

Selectivity is an important factor in analytical chemistry and molecular diagnostics. Compared to biosensors, almost all known synthetic probes and receptors have suffered from selectivity shortcomings, pointing to fundamental obstacles to creating "protein-like" binding pockets. This chapter showcases a "self-assembling probe (SAP)" molecular sensing concept where the time- and spectra-resolved information are employed to distinguish and quantify target analytes. Concretely, SAP, obtained by merging self-assembling property into reactive probe design responds to biothiols first through an unselectively ligand exchange coordination reaction. Subsequently, information-rich absorption spectra are observed because of the supramolecular structure evolution of the SAP-analyte conjugate. In cooperation with patter-recognition-based machine learning data analysis, the high-throughput screening (HTS) available SAP assays are able to achieve the identification and quantitation of urinary biothiols and drugs both in aqueous media and biofluids. This sensing concept may be applied to develop new sensors for environmental analysis and molecular diagnosis.

3.2 Introduction

Selectivity and binding affinity are two important factors for developing an artificial molecular sensory system. Although thousands of molecular probes (and chemosensors) have been reported, only a few have reached the clinical requirements and can be further developed for practical applications, which indicates the difficulties of devising and synthetically accessing binders that provide both high affinity and high selectivity for a target analyte.[8-9, 100] For instance, molecular-recognition-based macrocyclic systems (**Figure 3.1**a), *e.g.*,

cyclodextrins,[247] cucurbit[*n*]urils,[116] calix[*n*]arenes,[117] pillar[*n*]arenes[118], temple receptors,[119] and naphthotubes[120], have appeared for sensing small bioactive molecules, such as amino acids, neurotransmitters, steroids, and drugs. However, only a few of those systems have reached clinical use, *e.g.*, for metal cation- or glucose monitoring.[121-122]

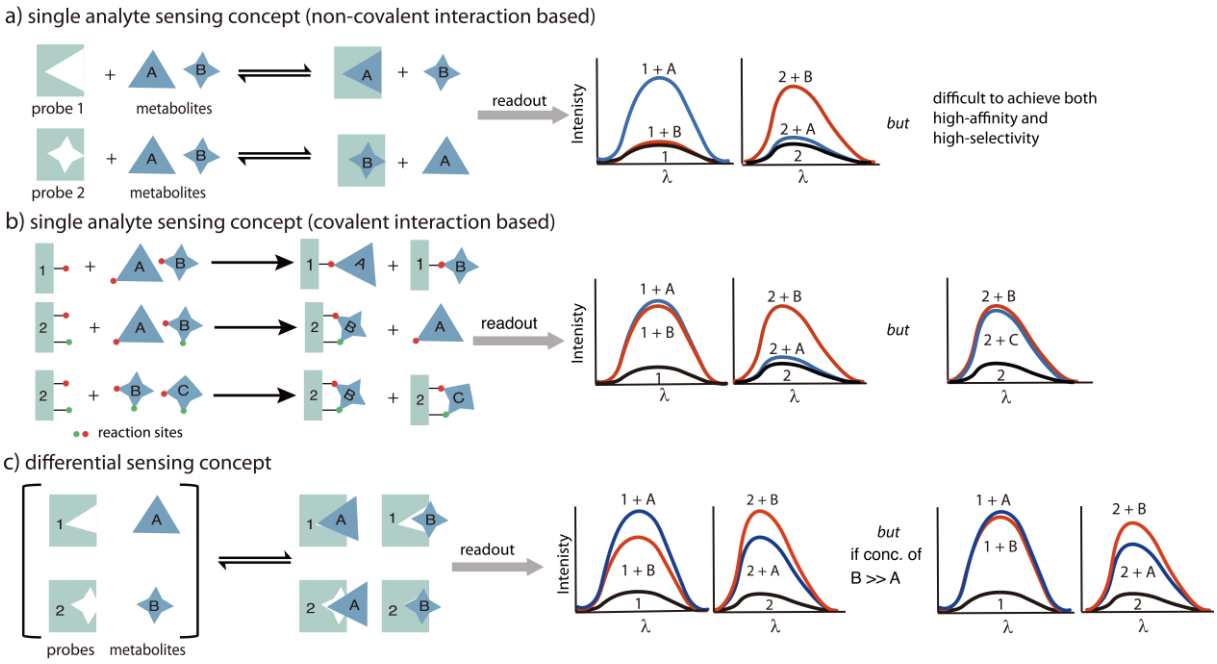

Figure 3.1. Schematic representation of previous molecular sensing concepts. a) Analyte-recognition by selective receptors proceeds through non-covalent binding. b) Covalent-interaction-based reactive molecular probes exploit single or multiple reactive moieties of the analyte. c) Array-based sensing achieves analyte distinction by use of multiple differentially-selective receptors.

In complementary, covalent interactions-based reactive molecular probes (MPs) do not suffer from affinity problems as the high energetic gain from covalent bond formation drives the analyte-probe conjugation more than artificial receptors (**Figure 3.1**b).[8, 100-101, 248] Unfortunately, this feature of MPs complicates the selective detection of analytes even further, *e.g.*, most biothiols with a sterically accessible -SH moiety are targeted by a thiol-reactive probe.[101, 248] Thus, sensing protocols involving simple MPs are often coupled to time-demanding and difficult-to-parallelize chromatographic separation protocols.[249] In recent years, advanced MP designs have been put forward that allow for the selective distinction of, *e.g.*, L-Cys, L-Hcys, and GSH through exploiting the distance between two reactive moieties of the analyte, *i.e.*, the -SH and -NH_2 group or the introduction of multiple reaction sites.[112, 250-251] However, it remains questionable if structurally similar analyte pairs such as L-Cys and Cys-Gly, which both occur in human urine,[249] can also be distinguished by these design strategies. Furthermore, artificial receptor and reactive molecular probe sensing concepts that are essentially a “one-analyte-one-receptor paradigm” inevitably lead to a proportional scaling of

the amounts of receptors that need to be prepared when a multiparameter sensing protocol is desired. For instance, hundreds of small molecules present in human urine, saliva, or blood serum whose relative concentration changes may provide more diagnostically relevant information than the analysis of a single or few biomarkers.[252-253]

Due to the difficulties in designing synthetic systems that provide sufficient affinity and selectivity for the target analyte, the array-based differential sensing concept became an attractive alternative (**Figure 3.1**c). The underlying idea is to evaluate the composite response of multiple receptors that are each only partially analyte-selective. Both gas sensory systems that mimic the mammalian nose and sensor arrays that enable the distinction and classification of complex fluid samples (*e.g.*, whiskeys, wines, perfume, and biofluids) have been reported.[132, 148-149, 254-256] Nevertheless, this approach requires the often cumbersome synthesis of several chemosensor variants. Moreover, array-based sensing schemes that probe the degree of receptor complexation are generally limited in situations where both the identity and the concentration of the analyte are unknown.

Herein, a new probe design and sensing concept is introduced, which enables analyte distinction, notably for structurally similar compounds, by merely using an easy-to-synthesize and unselectively binding probe that provides an information-rich optical signal.

3.3 Result and discussion

3.3.1 Self-assembling probe (SAP) sensing concept design

As shown in **Figure 3.2**, SAPs merge the covalent reaction and non-covalent interaction between the probe and target analyte to ensure both high binding affinity and high selectivity. In detail, SAPs are designed to engage in a fast chemical reaction with a class of target analytes, *e.g.*, thiols, thereby offering the same sensitivity advantage as MPs. Simultaneously, non-covalent interactions between the formed probe-analyte conjugates are employed because subtle structural differences between the supramolecular motifs can lead to significantly different spectroscopic outputs, thereby offering the high selectivity of SAPs. The self-assembly path of SAP-analyte conjugates will be fine-controlled by non-covalent forces between the aggregating building blocks, which in terms depend on the structure of the covalently bonded analytes. In addition, the SAP concept relies on the use of chromophoric entities that provide aggregation-dependent photophysical properties, *e.g.*, absorbance. Finally, the SAP-based assays are monitored by time-resolved spectroscopy, and the resulting

spectrograms are analyzed by machine learning-based clustering analysis processing to achieve analyte identification and quantification.

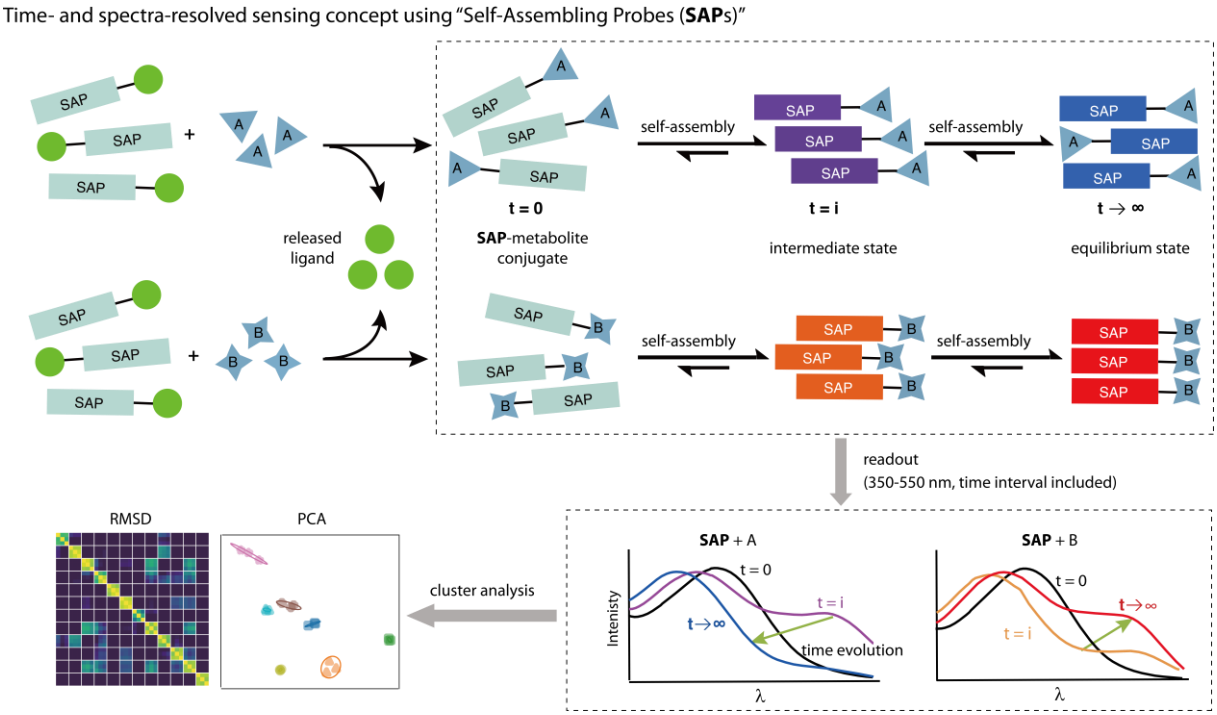

Figure 3.2. Schematic representation of the proposed time- and spectra-resolved molecular sensing concept utilizing SAPs. Firstly, SAPs unselectively bind the analyte through a metal-ligand exchange reaction. Subsequently, the formed SAP-analyte conjugate readjusts its structural assembly, resulting in altered electronic couplings between the chromophores. Thus, yielding an information-rich evolution of the absorbance spectra over time. The analyte is then distinguished and visualized by machine learning-based data analysis.

3.3.2 Selection of SAP candidate

The SAP sensing concept relies on self-aggregating molecular entities that adopt unique supramolecular assemblies controlled by subtle structural differences. For instance, many pure organic chromophores, *e.g.*, perylene-bisdiimides (PDI), naphthalene-diimides (NDIs), and other aromatic and polyaromatic compound classes, came to mind.[69, 257-259] However, most of these purely organic systems show only modest spectroscopic changes upon assembly structure evolution. In contrast, as described in **Chapter 1.2**, square-planar platinum(II) complexes form aggregated structures in solution, and their spectroscopic properties are sensitively affected by the Pt···Pt distance and orientation.[68, 76] Owing to these unique features, chromophoric Pt(II)-systems have been successfully employed for cell imaging, materials design, and sensing applications.[55, 88-89, 260-261] Therefore, the square-planar transition metal complexes are considered an ideal candidate for the construction of SAPs by introducing a labile ligand that can be readily displaced in the presence of the target analyte.

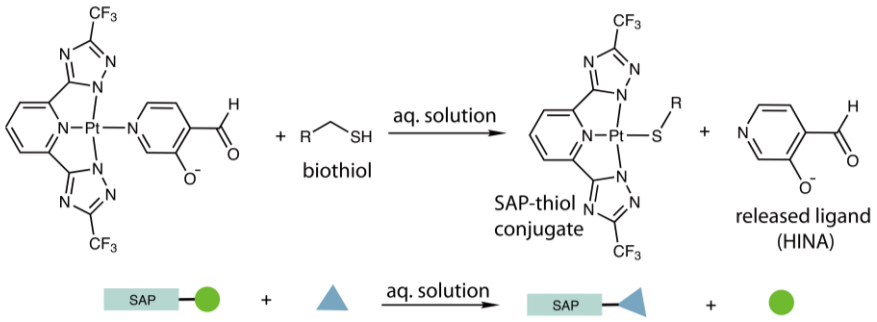

Figure 3.3. Chemical reactions of SAP **1** with biothiols proceeds by releasing the emissive indicator HINA and the formation of SAP-thiol conjugate in $NaHCO_3$ buffer (25 mM, 0.9 mM CTAB) at pH 9.5.

In the previous chapter, a Pt(II)-complex composed of the terdentate N-metallacycling ligand and the electron-rich and labile ancillary ligand-hydroxyisonicotine-aldehyde (HINA) was demonstrated, which reacts with L-Cys through the displacement of HINA (**Figure 3.3**).[191] As the released HINA is highly emissive, this complex could be, in principle, available for emission-based detection of thiols. Moreover, because the analyte is indicated by the released HINA, different thiols-expectedly-caused a very similar emission response after reacting with this probe. Therefore, biothiol selectively distinction is impossible by only monitoring the emission changes during this reaction process (**Figure 3.4**), resembling the commonly-encountered shortcomings of IDA.

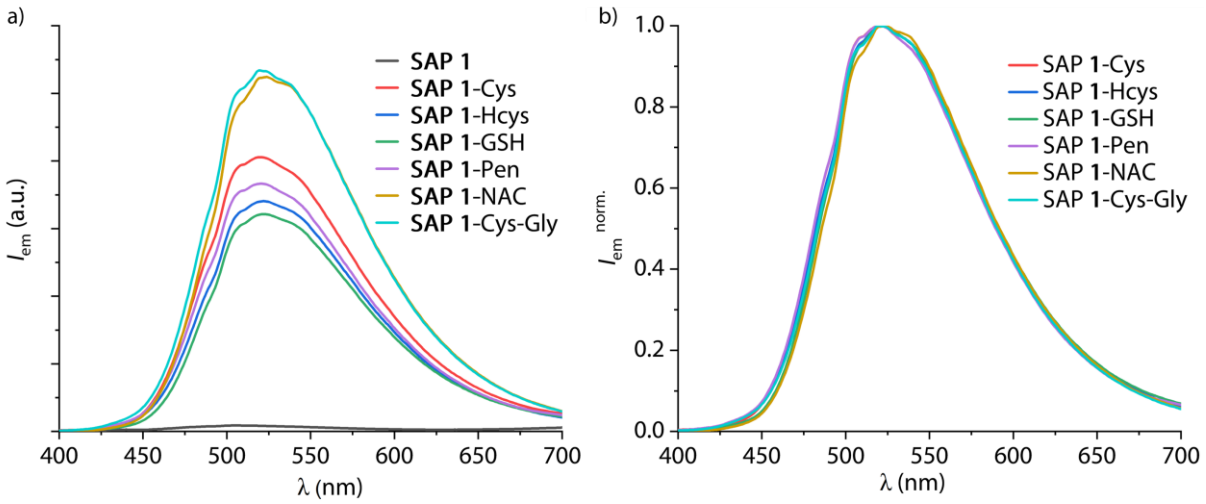

Figure 3.4. a) Emission spectra (λ_{ex} = 380 nm) of SAP **1** (50 µM) upon addition of urinary thiols (50 µM) in $NaHCO_3$ buffer (25 mM) with 0.9 mM CTAB at pH 9.5 and 25 °C. The spectra were recorded after the reaction reached an apparent equilibrium (~ 3 h). b) [0-1] Normalized emission spectra of a).

However, a more information-rich output could be obtained if one monitors the optical properties related to the self-assembling metal-organic complex, not the indicator dye, HINA. Therefore, the aforementioned Pt(II) complex, herein referred to as SAP **1**, was prepared in synthetic isolated and *in-situ* forms. While both forms can be used for the analyte targeting, the

in-situ preparation of the SAPs was recommended by simply mixing a DMSO-ligand containing metal complex precursor and HINA in aqueous media as a convenient path.

3.3.2.1 Formation of SAP **1**

The preparation of the *in-situ* form of SAP **1** will be introduced in the following text, and the synthesis and isolation procedures are given in the additional data section at the end of this chapter. The determination of the binding constants for the formation of SAP **1** and SAP **1**-thiol conjugate can be seen in **Chapter 2.2.6.2**.

*In-situ SAP **1** preparation*

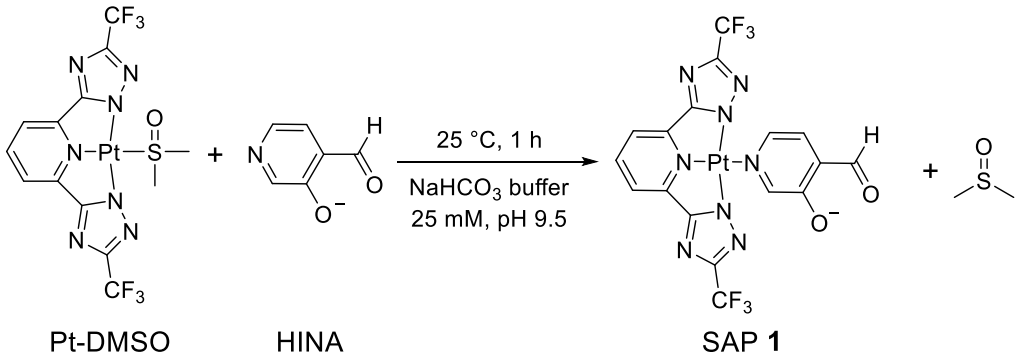

Figure 3.5. Chemical structures of the *in-situ* formation of SAP **1** from Pt-DMSO with HINA.

100 µL (100 µM) of a solution of 5 mM Pt-DMSO (DMSO) and 110 µL (110 µM) of a solution of 5 mM HINA (MilliQ water) were added into a 5 mL centrifuge tube and filled with 4795 µL sodium bicarbonate buffer (25 mM) containing 0.9 mM CTAB at pH 9.5, stirring for 1 hour at 25 °C. A 100 µM stock solution of SAP **1** was obtained, and the probe solution was preferably prepared freshly and used within 8 hours after preparation. The formation of SAP **1** was characterized by ESI-MS, ^{1}H NMR, and absorbance spectroscopy. **Figure 3.6** shows that the normalized absorbance spectra of both SAP **1** forms (*in-situ* and synthesis and isolated) were overlayed perfectly, suggesting that they are the same species. It is worth mentioning that the broad absorbance spectrum and the intense light scattering of the synthetic form of SAP **1** (here referred to as SAP **1s**) indicate that the aggregates of SAP were formed due to the poor solubility of SAP **1s** in aqueous buffer media. All other characterization results can be found in the experimental section at the end of this chapter.

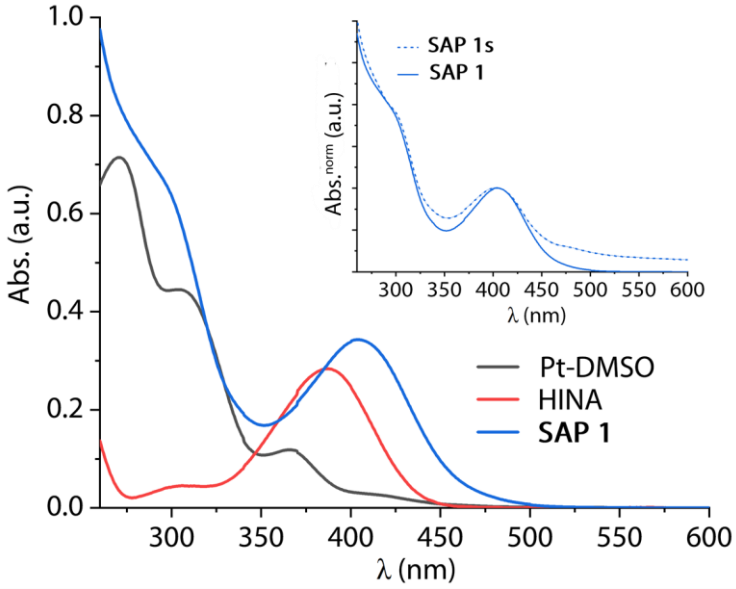

Figure 3.6. Absorbance spectra of Pt-DMSO (50 µM, black curve), of HINA (50 µM, red curve), and of their reaction mixture (blue curve). Inserted graph: normalized absorbance spectrum of the probe observed in cuvette SAP **1** (solid curve) and the synthetic SAP **1** (SAP **1s**) flash injected from a THF stock solution (dashed curve). All the experiments were performed in a solvent of $NaHCO_3$ buffer (25 mM) with 0.9 mM CTAB at pH 9.5 and 25 °C.

3.3.2.2 Influence of the surfactant

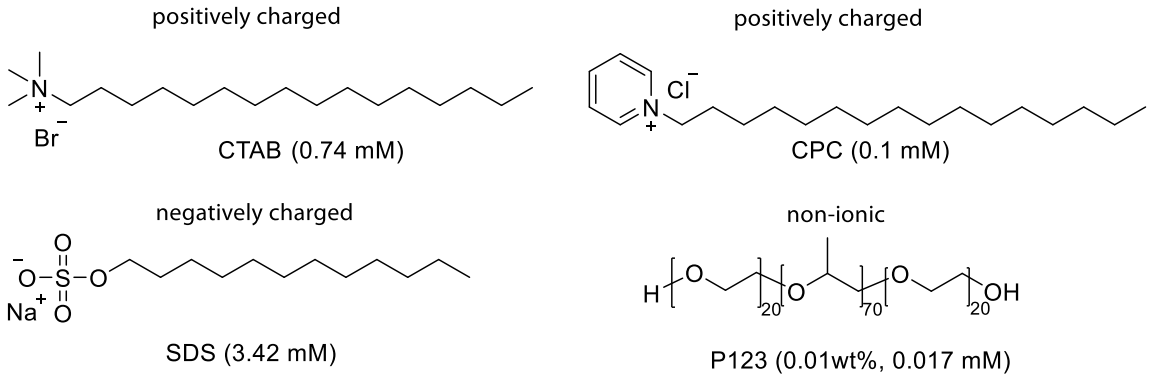

Figure 3.7. Chemical structures of the surfactants tested in this study and their critical micelle concentration (CMC) in aqueous media.

Surfactants can serve as a solubility container in aqueous media for organic molecules.[262] Indeed, the addition of a suitable surfactant ensures the solubility of the SAPs in the aqueous reaction buffer. Therefore, several surfactants, including ionic (positively charged and negatively charged) and non-ionic ones, were tested (**Figure 3.7**), and the used concentration was above their critical micelle concentration (CMC)[262-265] to ensure the formation of the micelles.

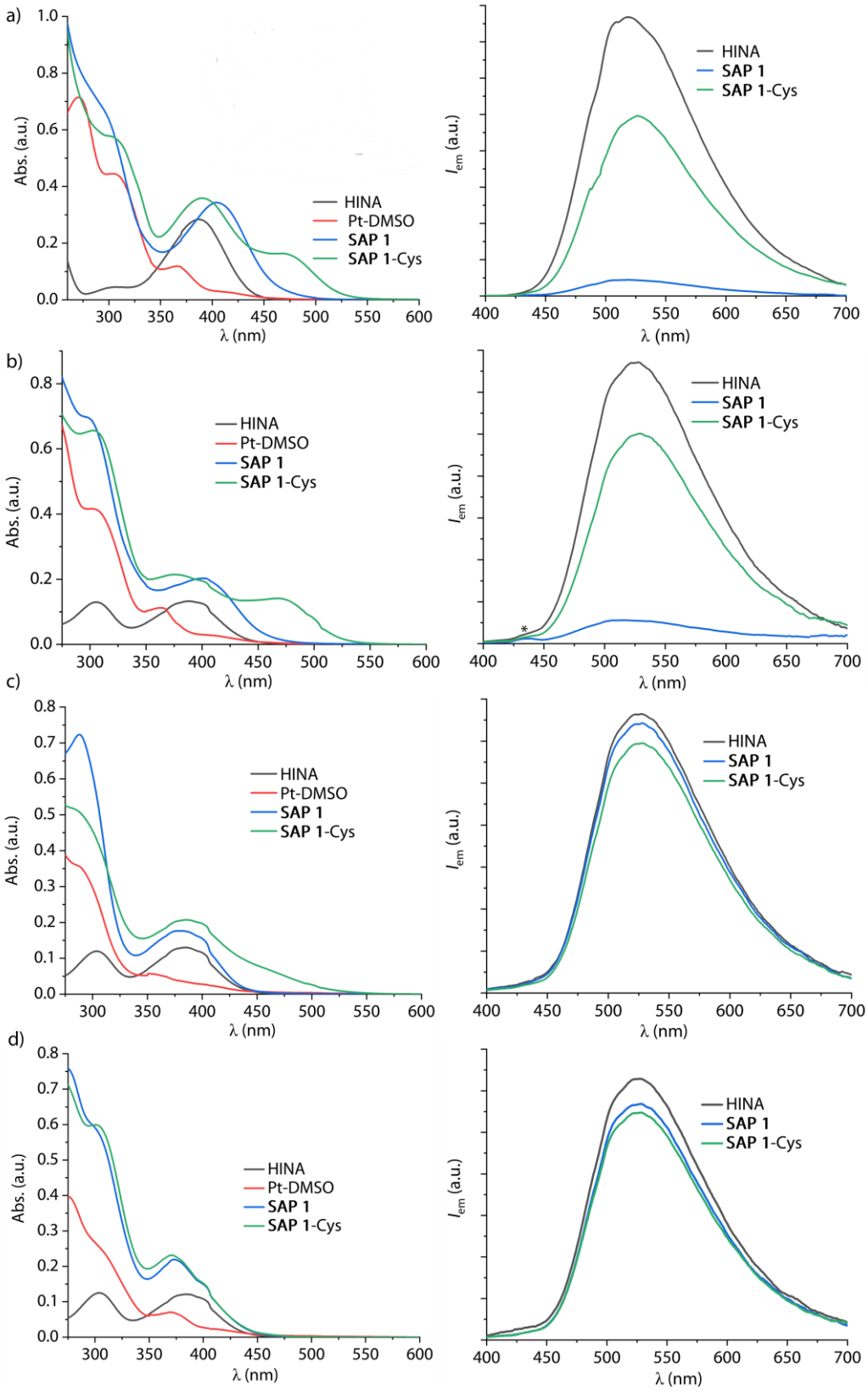

Figure 3.8. Absorbance (top) and emission (bottom, λ_{ex} = 380 nm) spectra of the formation of SAP **1** and upon reaction with L-Cys in $NaHCO_3$ buffer (25 mM) contained different surfactants: a) CTAB (0.9 mM), b) CPC (0.9 mM), c) SDS (43 mM), and d) P123 (0.5 wt%) at pH 9.5. In the graph, the black curve (HINA, 50 µM), the red curve (Pt-DMSO, 50 µM), the blue curve (SAP **1**), and the green curve (upon addition L-Cys, 50 µM). The asterisk in the emission spectrum indicates the Raman scattering band of water at the selected excitation wavelength.

Firstly, all the tested surfactants did enhance the solubility of the SAP system; secondly, the sensing property of the probe was strongly dependent on the charge of the surfactants. As shown in **Figure 3.8**a-b, upon reaction with L-Cys, almost the same fluorescence emission enhancement was observed for the SAP assay conducted in the positively charged surfactants hexadecyltrimethylammonium bromide (CTAB) and cetylpyridinium chloride (CPC). Moreover, both systems displayed an absorption band in the range of 450-550 nm, indicating the formation of stronger Pt···Pt interactions between the metal centers of adjacent SAP-Cys conjugates compared to that in other surfactants. Therefore, the sensing performance studies of the SAP assay were conducted in the positively charged surfactant CTAB. Moreover, SAPs form metastable self-aggregating structures in an aqueous buffer solution in the presence of CTAB, which can be seen from the dynamic light scattering (DLS) and nuclear magnetic resonance (NMR) studies (see additional data section at the end of this chapter).

Besides, the sensing performance of the SAP assay was also explored at different pH values to optimize the sensing condition. As shown in **Figure 3.9**, the SAP formation process is not affected too much by the different pH, while the reaction speed of the conjugation of SAP **1** with L-Cys is accelerated at higher pH values. The pH 9.5 was chosen for the following investigation of the sensing properties for SAP assays.

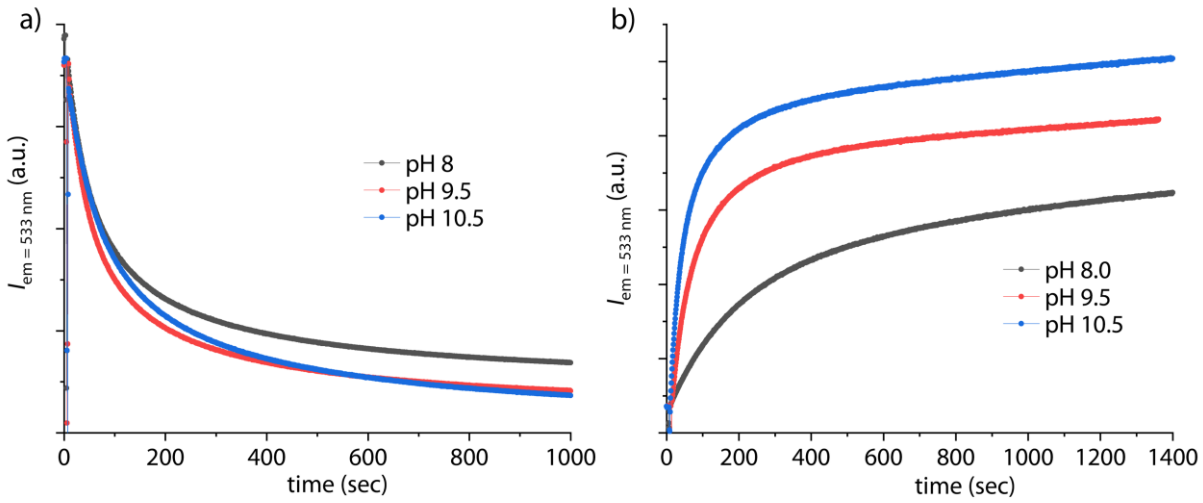

Figure 3.9. a) Emission kinetic traces (λ_{ex} = 380 nm, λ_{em} = 533 nm) for the formation of SAP **1** (50 µM) at different pH values. b) Emission kinetics traces (λ_{ex} = 380 nm, λ_{em} = 533 nm) for the reaction of L-Cys with SAP **1** at different pH values. All measurements were performed in $NaHCO_3$ buffer (25 mM) in the presence of 0.9 mM CTAB at 25 °C.

3.3.3 Selection of target analyte

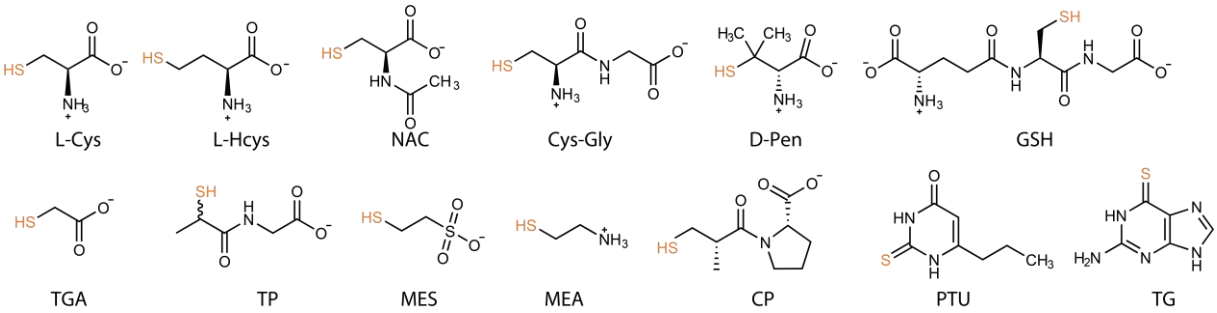

Figure 3.10. Chemical structures of urinary thiols and thiol drugs used in this study.

Biological thiols are popular targets for developing reactive molecular probes[101, 248] and have been suggested to play critical roles in various physiological functions and pathological conditions due to their chemical reactivity and reducing properties.[107] For instance, altered levels of thiols in intra- and extracellular fluids have been associated with several human diseases such as leukocyte loss, liver damage, Alzheimer's disease, and HIV. Several thiol-functional metabolites occur in human urine at micromolar concentrations,[249] *i.e.*, L-cysteine (L-Cys), L-homocysteine (L-Hcys), L-cysteinylglycine (Cys-Gly), *N*-acetyl-L-cysteine (NAC), L-glutathione (GSH) and thioglycolic acid (TGA), see **Figure 3.10**. Moreover, seven common thiol-containing drugs (2-mercaptoethylamine (MEA), D-penicillamine (D-Pen), 2-mercaptoethane sulfonic acid (MES), tiopronin (TP), captopril (CP), 6-propyl-2-thiouracil (PTU), 6-thioguanine (TG)) are excreted in human urine in the micromolar concentration regime (**Table 3.1**). Unlike all other reported molecular probe-based studies for thiol detection, this study aims to discriminate all urinary biothiols and drugs from each other, not only the commonly studied L-Cys, L-Hcys and GSH pairs.

3.3.4 Time-and spectra-resolved SAP interactions with biothiols

3.3.4.1 Reaction mechanism studies

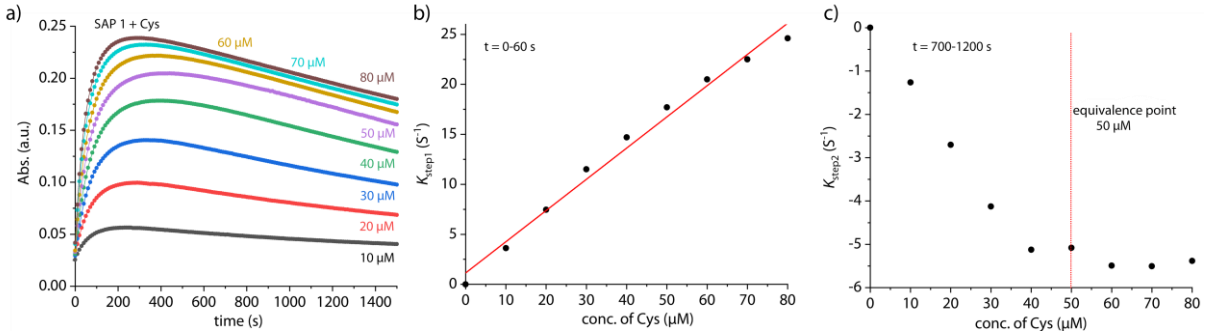

Figure 3.11. a) Absorbance kinetic traces (475 nm) as a function of the concentration of L-Cys (10 – 80 µM) in the presence of SAP **1** (50 µM) in 25 mM $NaHCO_3$ buffer (0.9 mM CTAB) at pH 9.5 and 25 °C. b-c) Concentration-dependent initial reaction rates of step 1 (0 – 60 s) and step 2 (700 – 1200 s). ***Note:*** The initial reaction rates for two steps (K_{step1}/s^{-1} and K_{step2}/s^{-1}) were obtained by plotting the slope of each time-course curve at characteristic time ranges as the function of the L-Cys concentration. The slope values were obtained from a linear fitting function with Origin software.

Upon adding a solution of a biothiol, *e.g.*, L-Cys, to SAP **1** in a 25 mM $NaHCO_3$ (pH 9.5) solution, the absorbance at 475 nm and emission at 525 nm quickly increased within the first 200 s after assay initiation (**Figure 3.11**a), and the initial reaction rate was directly proportional to the thiol concentration. In principle, this feature could be used to quantify thiols in the aqueous solution as the absorption intensity was linear dependent on the concentration of thiols (**Figure 3.11**b). However, the thiol distinction can not be achieved in this way because of the almost similar absorbance (or emission) response for all the target analytes in the first ~ 200 s caused by the unselectively coordination reaction between the Pt center and -SH moiety of the target analyte. Surprisingly, an entirely different observation was made when monitoring the UV/Vis spectra evolution from 200 s onwards. Then, the absorbance at 475 nm steadily decreased again. As shown in **Figure 3.11**c, after the concentration ratio of two molecular components (SAP **1** and L-Cys) reaches 1 to 1, the initial reaction rate constants were kept at a consistent value, and the reaction rate became independent of the thiol concentration.

A possible reaction pathway was proposed based on the observation from the absorbance- and emission-kinetics measurements. As depicted in **Figure 3.2**, the reaction of SAP **1** with a thiol-functional analyte passes through several steps: *i*) After assay initiation, SAP **1** quickly exchanges in a bimolecular reaction mechanism its HINA ligand for the stronger binding biothiol. The observed spectral changes are caused by the Pt-thiol conjugate formation and HINA release. *ii*) In a slower subsequent process, the **SAP**-analyte conjugate readjusts its

supramolecular aggregation structure. As a result, an alteration of the metal-metal-ligand charge transfer (MMLCT) occurs, which is sensitively controlled by the intermolecular distance and orientation between **SAP** metal centers. This process manifests itself by notable changes in the absorbance spectra and passes through intermediate states. *iii*) Finally, a kinetically stable state is reached after several hours.

3.3.4.2 Detection and distinction of different urinary thiols

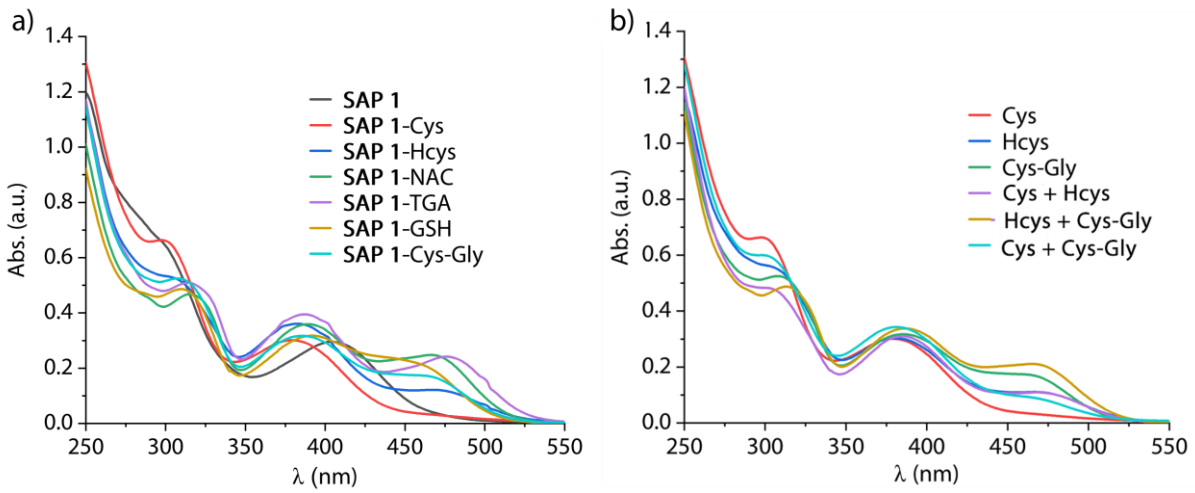

Figure 3.12. Absorbance spectra of SAP **1** upon the addition of single urinary thiols (a) and thiol mixtures (b) in $NaHCO_3$ buffer (25 mM) with 0.9 mM CTAB at pH 9.5 and 25 °C. The spectra were recorded after the reaction reached an apparent equilibrium.

Although the spectroscopic response of the first reaction can be used for the thiol quantification, the following aggregation structure-evolution involved by the Pt···Pt interactions was even more intriguing. By visual inspection of the end-point spectra recorded after an assay time of 90 min, it is immediately evident that all eight urinary biothiols became directly distinguishable upon reaction with SAP **1** (**Figure 3.12**a). Even more surprisingly, the differentiation of the L-Cys/Cys-Gly mixtures was possible using this assay (**Figure 3.12**b), which is typically not achieved by other reported studies.

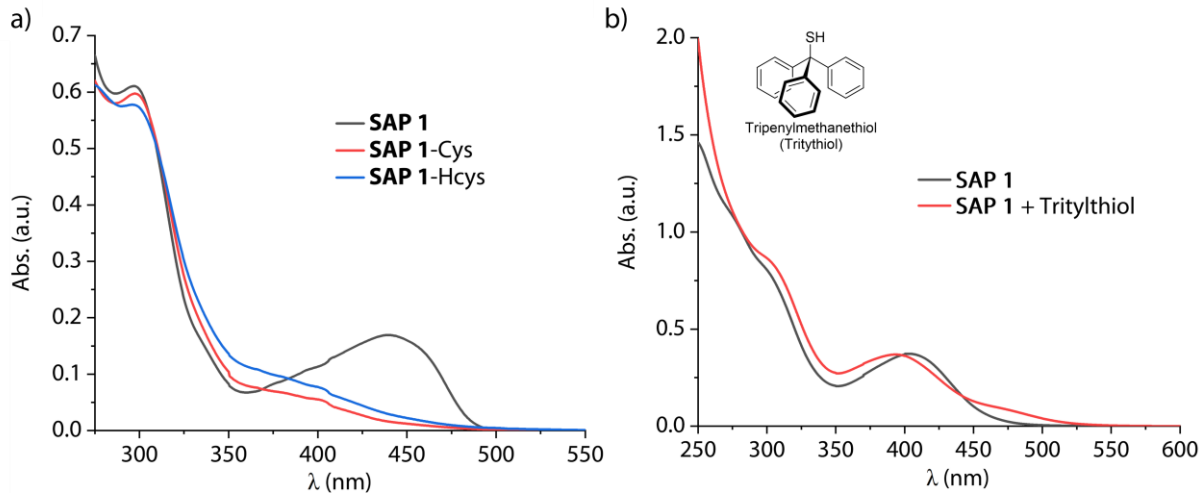

Figure 3.13. a) Absorbance spectra of the reaction mixture of SAP **1** (50 µM) and L-Cys (50 µM) or L-Hcys (50 µM) were recorded after a reaction time of 3 h in DMF. ***Note:*** in this case, SAP **1** was first prepared and isolated following the procedures described in the experimental section at the end of this chapter. b) Absorbance spectra of SAP **1** (50 µM) prior to (black curve) and after (red curve) reacting with tritylthiol (50 µM) for 3 h in $NaHCO_3$ buffer (25 mM, pH 9.5) with 0.9 mM CTAB. Insert shows the chemical structure of the analyte.

As aforementioned, this feature is caused by the supramolecular nature of the system and does not result from the molecular electronic differences between the SAP-thiol conjugates, which can be proved by the following studies. Firstly, almost all the analytes are fully aliphatic and structurally similar (**Figure 3.10**), and they are thus not expected to affect the chromophoric centers sensitively by direct electronic coupling. Secondly, when the SAP assay was carried out in an organic solvent, *e.g.*, DMF, where the self-assembly of SAP **1** does not occur, indistinguishable absorbance spectra were obtained for L-Cys and L-Hcys (**Figure 3.13**a). Thirdly, when using triphenylmethanethiol as the model analyte, the SAP-thiol conjugation still smoothly proceeded. However, the subsequent spectra evolution was not observed because the bulky structure of the analyte prevented the supramolecular polymerization of the SAP-thiol conjugate (**Figure 3.13**b).

By recording the spectra evolution in a broad wavelength range (350 nm-550 nm) at regularly spaced time intervals, even more information was obtained that can be employed for the thiol distinction. As shown in the spectrograms of **Figure 3.14**, all eight structure-similar urinary thiols and three thiol mixtures were clearly distinguished from each other. Individual absorbance kinetics spectra are listed in **Figure 3.15**.

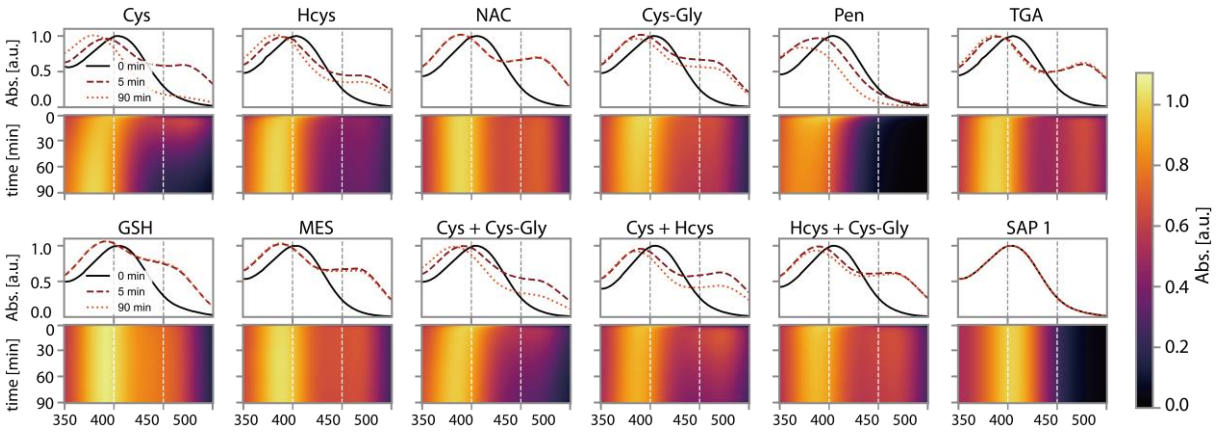

Figure 3.14. Spectrograms for the reaction of SAP **1** with urinary thiols (50 µM) or thiol mixtures (50 µM of each component). The heatmaps of the spectra evolution were recorded in an assay time of 90 min at 180 s spacing.

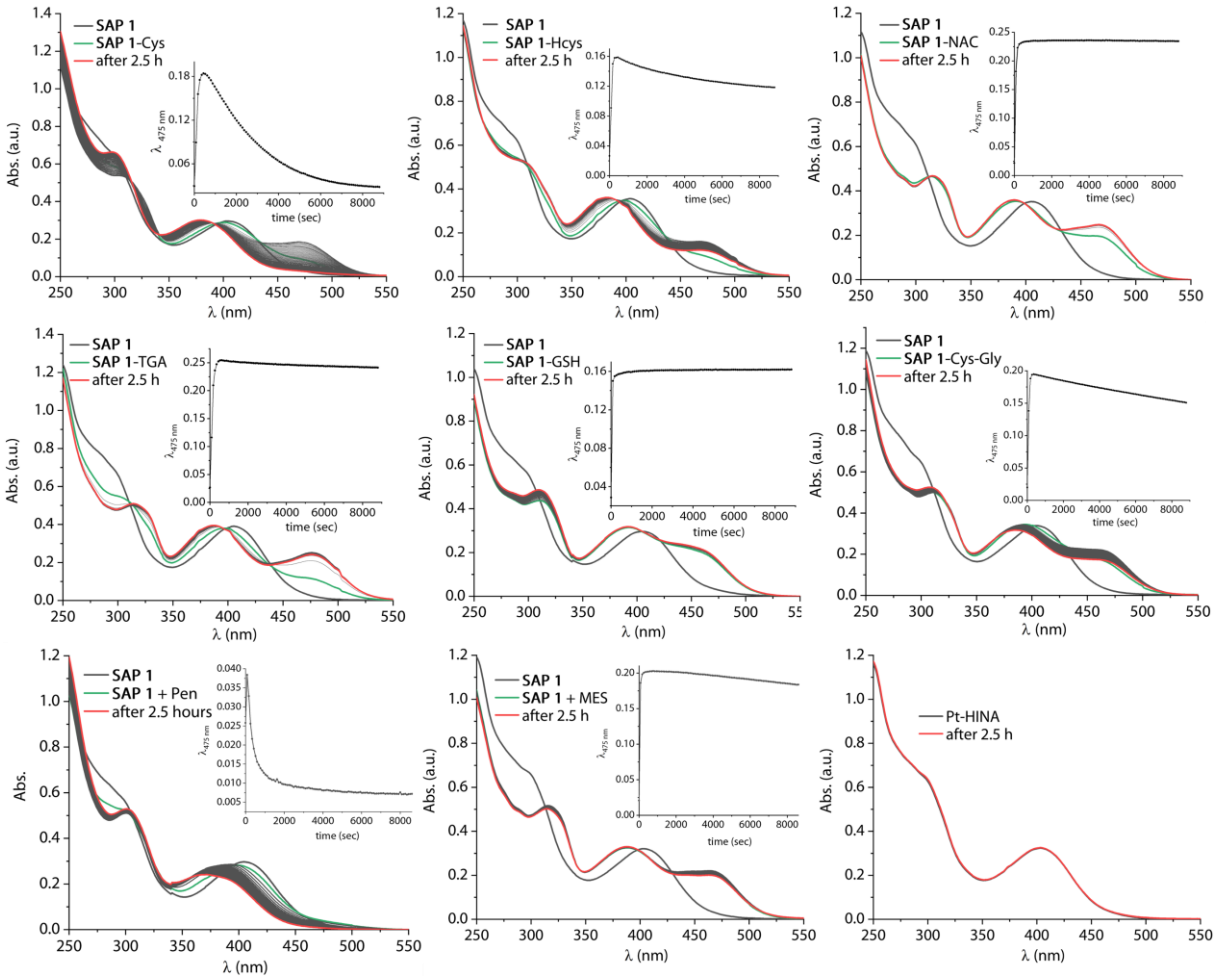

Figure 3.15. Absorbance spectrogram evolution for the reaction of SAP **1** (50 µM) with six urinary thiols (50 µM) and represented two thiol drugs (50 µM) in $NaHCO_3$ (25 mM, pH 9.5) with 0.9 mM CTAB through a cuvette-format. The spectrogram of SAP **1** was shown in the last graph as a blank sample. The interval time between each spectrum is 86 s, and the total measuring time is 2.5 h. The inserts show the changes in the absorbance intensity at 475 nm during the course of the reaction at 25 °C.

3.3.5 Cluster analysis for thiol distinction

The machine learning-based cluster analysis was carried out by Thomas Jochmann. Therefore, this section will not detail the methodology development. Only the results and the conclusions will be described in the following text.

In order to visualize the differential of the target analytes, two different machine learning-based cluster data analysis approaches were employed: *i*) Principal component analysis (PCA)[137] on the spectrogram data to group specimens with similar spectral-kinetic patterns. As shown in **Figure 3.16**a, the PCA score plot from the first two principal components, The similar PCA scores from replicas of the same analytes with non-overlapping 95 % confidence ellipses, suggest an analyte-specific response. *ii*) As previously mentioned, monitoring the full spectra evolution of the SAP assay will bring rich information for the analyte distinction. Therefore, pairwise root mean squared deviation (RMSD)-based cluster analysis from about 10,000 time- and spectra-resolved values were developed. In **Figure 3.16**b, three replicas per analyte were depicted inside the white-boarded blocks as smaller squares. The color bar on the right side shows the similarity between the two samples: yellow represents the small distances (spectrograms are very similar); violet color represents the markable distance, which means the samples are very different. As expected, all eight urinary thiol-analytes and three mixtures were well visually distinguished after processing the cluster data analysis.

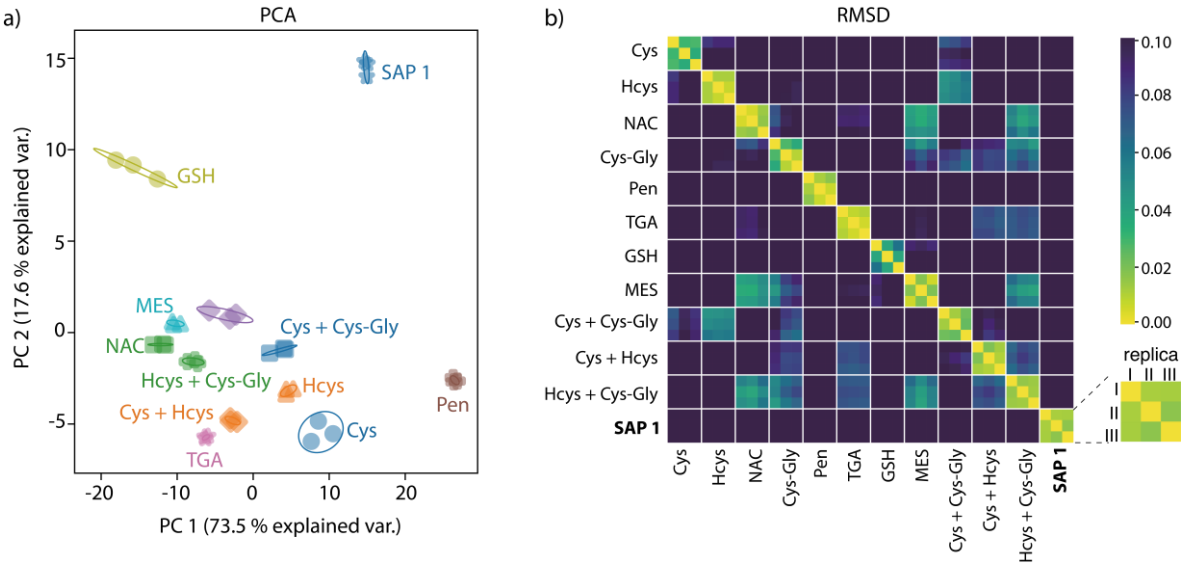

Figure 3.16. Cluster analysis with PCA (a) and RMSD-based specimen-to-specimen similarity assessment of the spectrogram data (b). Three replicas for each sample were measured. Yellow color represents smaller deviations (spectrograms are similar); violet color marks larger deviations (spectrograms are more different).

3.3.6 High-throughput screening (HTS) with SAP **1**

3.3.6.1 Analyte identification by SAP **1** assay

To evaluate the potential high-throughput screening possibility of the **SAP** assay, the measurements were transferred from the cuvette-based protocol to a 96-well plate set up, in which a plate reader equipped with an ultra-fast UV/vis spectrometer and a chemical reaction injector was used. In this way, the spectrograms of the 96 samples were monitored in parallel, which extended the analyte selection to include thiol-containing drugs, and increased the number of the measurements replicas while simultaneously reducing the manual effort. A short description of the workflow for this high-throughput screening SAP assay is given as follows.

All the stock solution of thiol analytes was prepared in MilliQ water (their concentration was determined by the Ellman assay[266]), then diluted to 0.1 mM with $NaHCO_3$ buffer (25 mM, pH 9.5) with 0.9 mM CTAB. The stock solution of SAP **1** was prepared by following the procedure in **Chapter 3.3.2** and directly used. The 96-well black optical plate wells were filled with a 100 µL stock solution of thiol analytes (0.1 mM). The stock solution of SAP **1** (0.1 mM) was loaded into the injector of the plate reader. To initial the assay, 100 µL of SAP solution was injected into the corresponding wells during the second cycle. The solution of $NaHCO_3$ (25 mM, pH 9.5) with 0.9 mM CTAB was measured as a blank sample, and six repetitions were made for each sample. The spectra were recorded from 300-550 nm with a fixed time interval (180 s) and cycle number (35 cycles) between each spectrum. The temperature was kept at 25 °C during the whole measurement process.

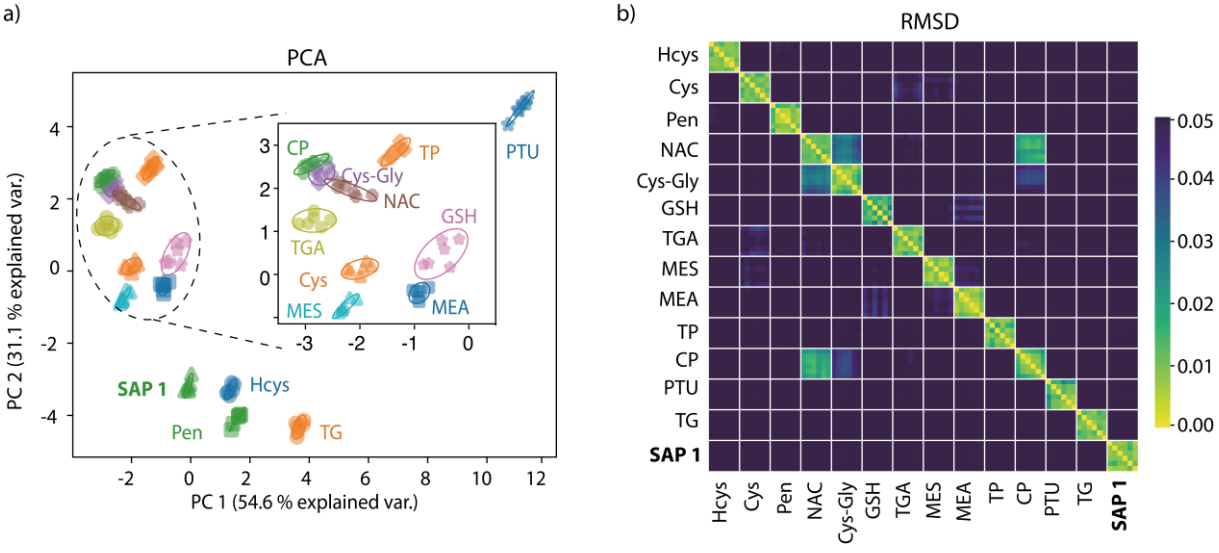

Figure 3.17. PCA scores plots (a) and pairwise RMSD (b) of the absorbance response spectrograms of SAP **1** applied to all urinary thiols and thiol-containing drugs in an assay time of **27** min. Six replicas for each analyte are

depicted inside the white-bordered blocks as smaller squares. Yellow color represents smaller deviations (spectrograms are similar); violet color marks larger deviations (spectrograms are more different).

The PCA and RMSD-based cluster analysis results are shown in **Figure 3.17**. As a result, all 13 thiol-contained metabolites and drugs were clearly distinguishable in the microwell plate format using the SAP **1** assay.

A long assay time is a limitation for further practical applications of the covalent interaction-based reactive molecular probe. For practical use, it may be convenient to reduce the assay time. Therefore, the performance of the SAP assay in a shorter data acquisition time was investigated. Pleasingly, as shown in **Figure 3.17**, 27 min of spectrogram data were sufficient to distinguish all biothiols and drugs from each other with high confidence. For most analyte combinations, even the use of only 6 min of assay data sufficed (**Figure 3.18**). The individual absorbance spectrograms for the reaction of SAP **1** with the representative analytes in an assay time of 1.7 h are shown in **Figure 3.19**.

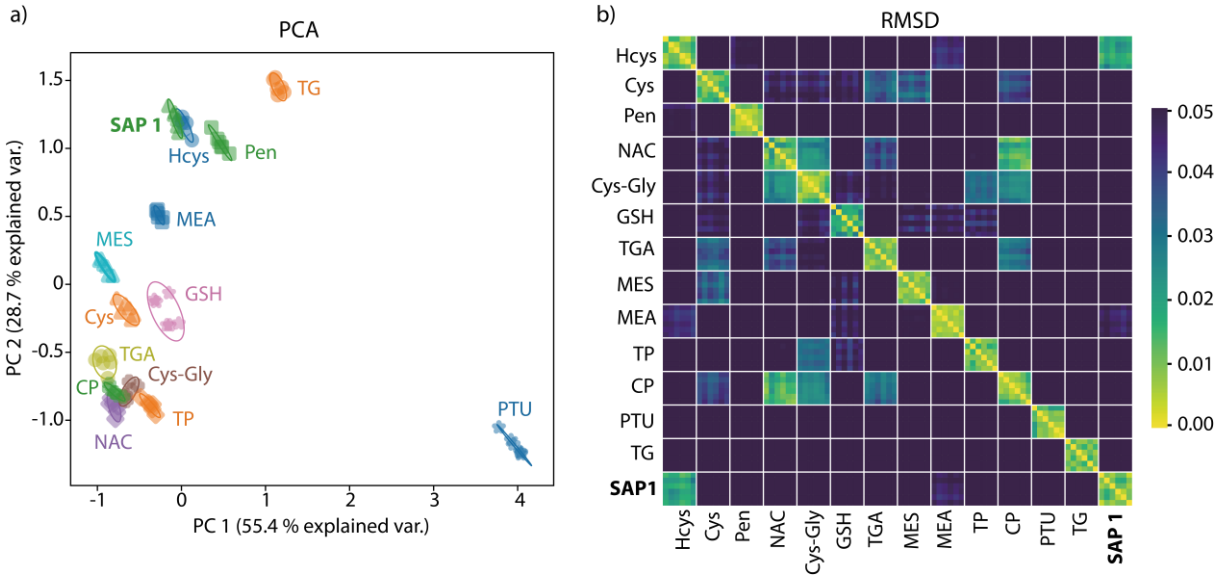

Figure 3.18. PCA scores plots (a) and pairwise RMSD (b) of the absorbance response spectrograms of SAP **1** applied to all urinary thiols and thiol-containing drugs in an assay time of **6** min. Six replicas for each analyte are depicted inside the white-bordered blocks as smaller squares. Yellow color represents smaller deviations (spectrograms are similar); violet color marks larger deviations (spectrograms are more different).

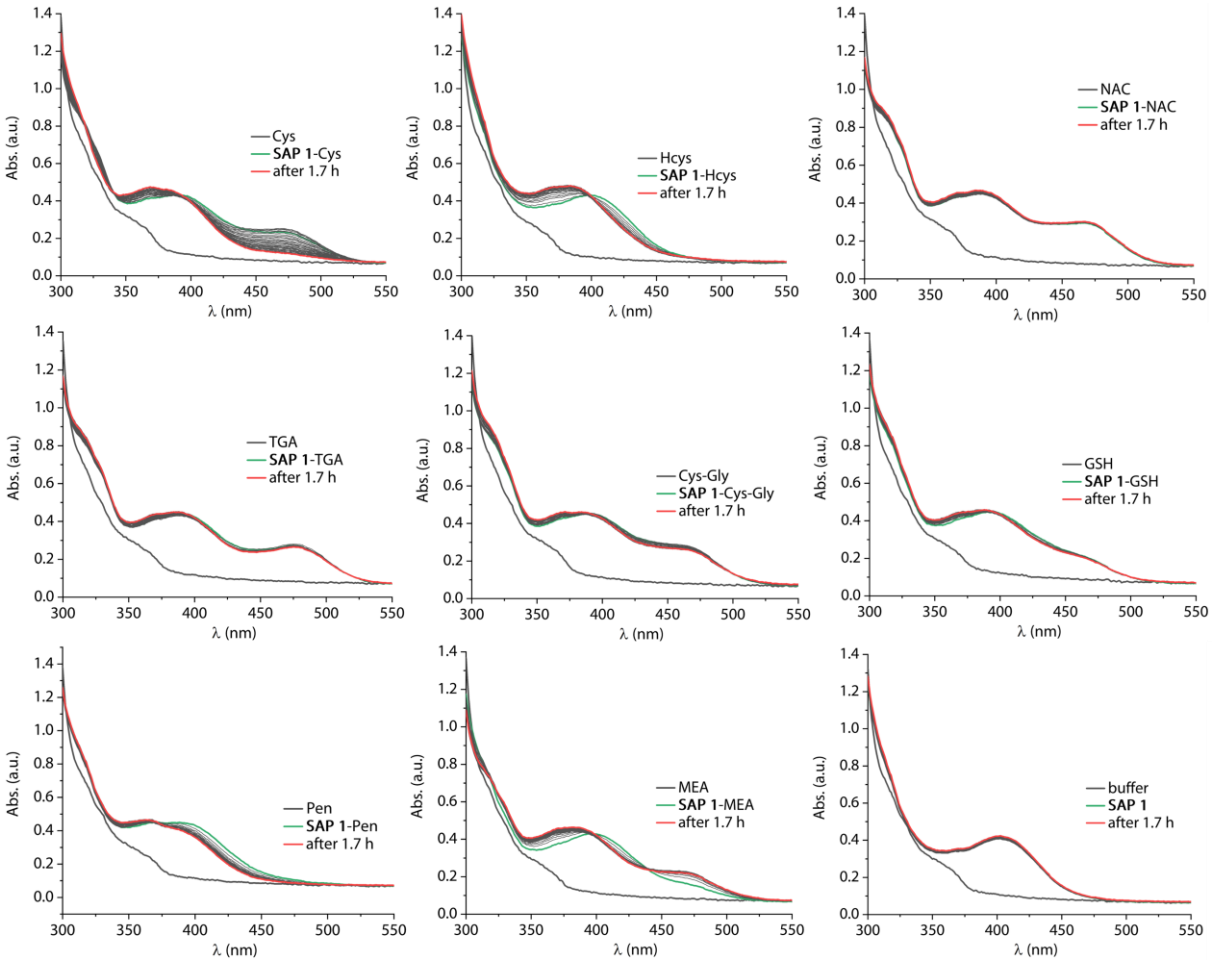

Figure 3.19. Absorbance spectrogram evolution for the reaction of SAP **1** (50 µM) with represented urinary thiols (50 µM) and thiol-containing drugs (50 µM) in $NaHCO_3$ (25 mM, pH 9.5) with 0.9 mM CTAB. The interval time between each spectrum is 86 s, and the total measuring time is 2.5 h. The blank sample of SAP **1** alone was shown in the last graph in this figure.

3.3.6.2 Analyte quantification by SAP **1** assay

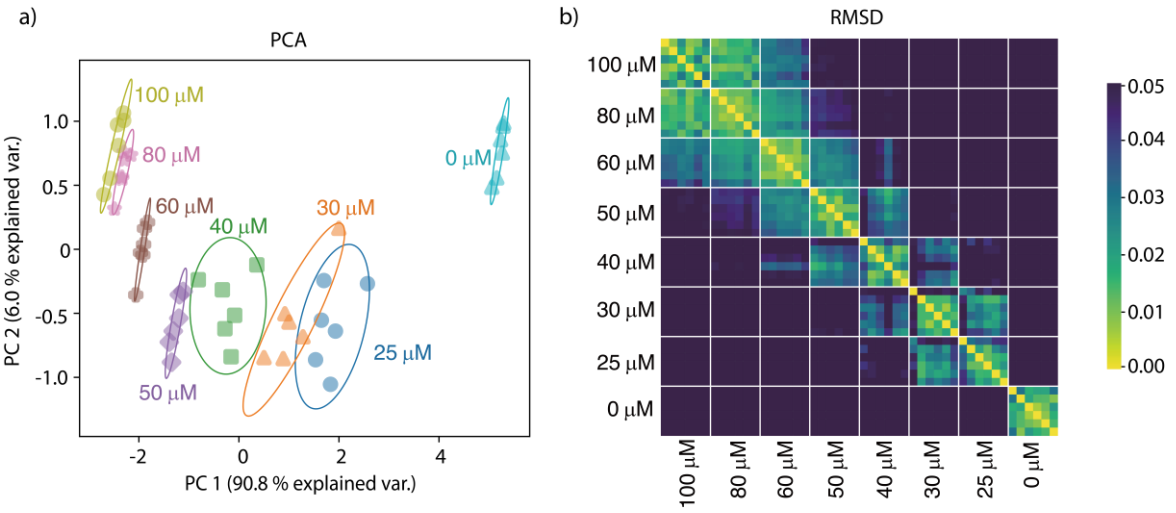

Figure 3.20. PCA scores plots (a) and pairwise RMSD (b) of the absorbance response spectrograms of SAP **1** applied to different concentration L-Cys (0-100 µM) in an assay time of **27** min. Six replicas for each analyte are

depicted inside the white-bordered blocks as smaller squares. Yellow color represents smaller deviations (spectrograms are similar); violet color marks larger deviations (spectrograms are more different).

As mentioned in **Chapter 3.3.4** (**Figure 3.11**a-b), the absorbance intensity is linearly dependent on the concentration of the target analyte, *e.g.*, L-Cys. Therefore, the SAP assay could be potentially used to quantify the analyte besides the identification. **Figure 3.20** shows that different concentration L-Cys (from 25 – 100 µM) were pairwise distinguished after applying the SAP **1** assay and the cluster data analysis method. More data for L-Hcys and NAC can be found in the additional data section at the end of this chapter. In addition, one can further increase the information content and thus thiol-quantification ability by conducting the experiments at different SAP concentrations. Overall, the proposed SAP assay has the potential power to identify and quantify the analyte of interest.

3.3.7 Application of SAP in human biofluids

Encouraged by the promising results in buffered aqueous solution, the performance of the SAP assay in human biofluids, *e.g.*, human serum and urine, was evaluated. Firstly, other nucleophilic substances present in biofluids, *e.g.*, amino acids, biogenic amines, and creatinine, which could be the potential interferents, were applied to evaluate the selectivity of the SAP **1** assay. Fortunately, none of these tested substances caused a noticeable effect on the assay under the typical conditions of pH 9.5 with the addition of CTAB as a surfactant (**Figure 3.21**). It is worth mentioning that amines, *e.g.*, cadaverine, starts to compete with thiols once the pH of the solution is over 10.0.

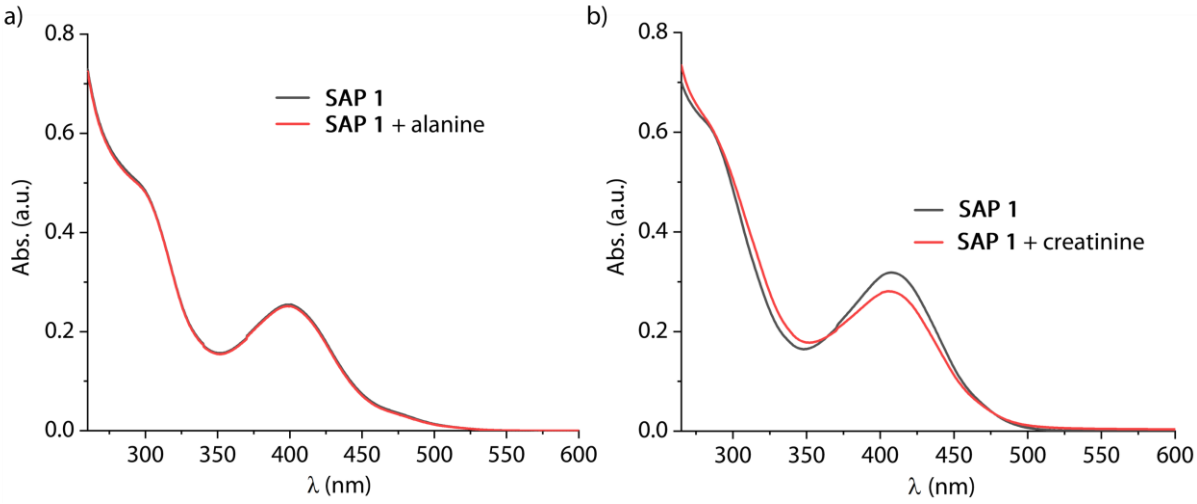

Figure 3.21. Absorbance spectra of SAP **1** (50 µM) prior to (black curve) and after (red curve) reacting with alanine (a) and creatinine (b) in $NaHCO_3$ buffer (25 mM, pH 9.5) with 0.9 mM CTAB. The spectra were recorded after the reaction reached an apparent equilibrium (~ 3 h) at 25 °C.

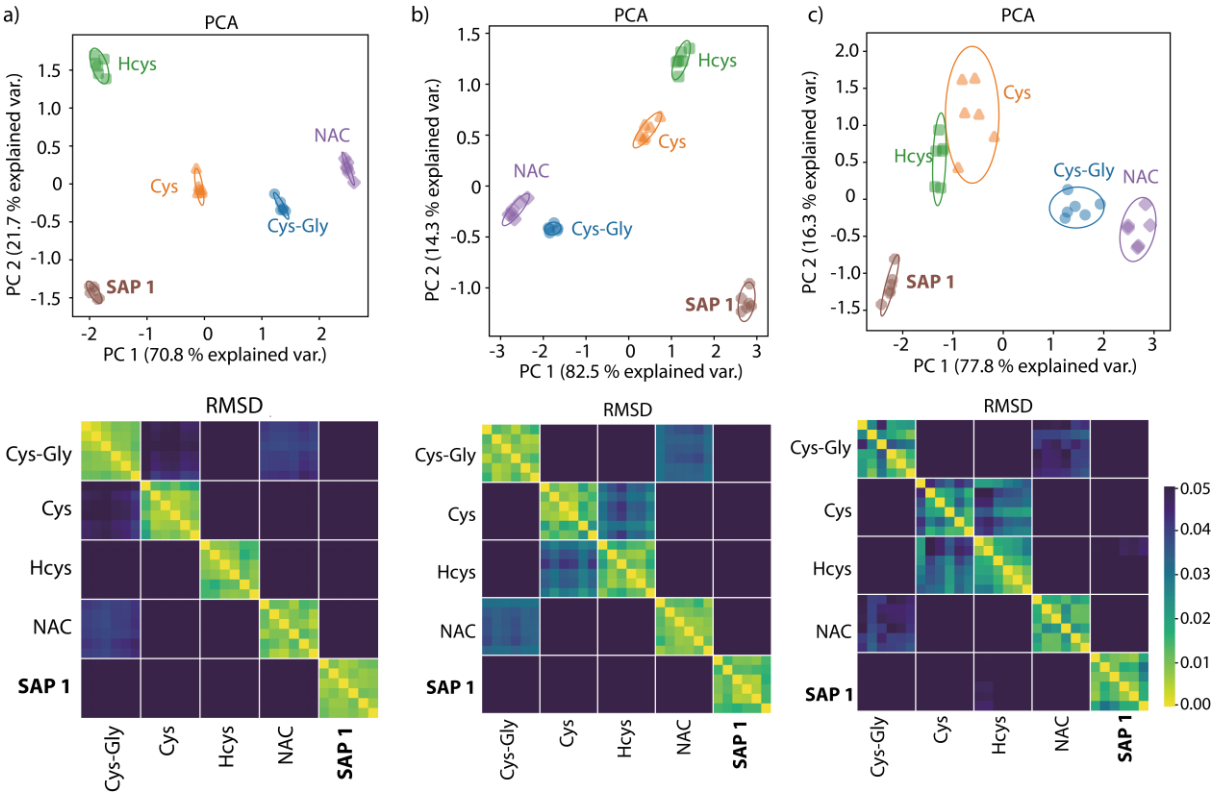

Figure 3.22. PCA score plots (top) and pairwise RMSD (bottom) of the absorbance response spectrograms of SAP 1 applied to biothiol spiked (50 µM): a) human urine, b) deproteinized serum from Seqens company, and c) deproteinized serum from Merck company. Six replicas per analyte are depicted inside the white-bordered blocks as smaller squares. Yellow color represents small deviations (spectrograms are very similar); violet color marks larger deviations (spectrograms are more different).

Then, the sensing performance of the SAP assay was demonstrated in biothiol-spiked human urine and deproteinized serum in an exploratory manner. As shown in **Figure 3.22**, different analytes were well distinguished in either urine or deproteinized serum, suggesting the potential ability of molecular diagnostic in the clinical application of the SAP assay. Based on these results, different urine samples from healthy donors were applied to the SAP **1** assay, resulting in distinct data clusters for the different specimens, which is plausible given the known differences in thiol excretion between individuals due to environmental influences.[249, 253]

3.3.8 Outlook of SAP assays

This thesis explored the performance of the self-assembling Pt(II) complex-based time- and spectra-resolved sensing concept by using thiol-containing metabolites and drugs as the model analytes. In fact, because of the coordinate reactivity of the transition metal center, other chemically reactive entities can also be introduced to the SAP framework to enrich the analyte fields, *e.g.*, amino acids, amines, or carbohydrates. For instance, fructose may be easily targeted when the HINA ligand is replaced by a pyridine boronic acid molecule in the SAP. In addition,

tuning and controlling the spectroscopic and kinetic features is possible by adding auxiliary substances (**Figure 3.8**), changing the reaction pH (**Figure 3.9**), or using co-solvents.[68, 73]

Moreover, other self-aggregating planar metal-organic complexes[55, 94, 267] could also be promising as aggregating building blocks. For example, a Pd(II) complex-based SAP **2** was developed through the same procedure as the SAP **1** for thiol detection. Unfortunately, SAP **2** only showed a rapid emission increase upon reaction with L-Cys but did not display significant absorbance spectra alterations after the thiol conjugation was completed (**Figure 3.23**). Therefore, different thiols distinctions are not achieved by this Pd(II) based SAP **2**. However, this result again highlights the importance of non-covalent Pt···Pt interactions as a spectroscopic reporter during the analyte distinction. Nevertheless, other molecular motifs that feature self-aggregating properties could still be the potential candidates for constructing the proposed sensing concept.

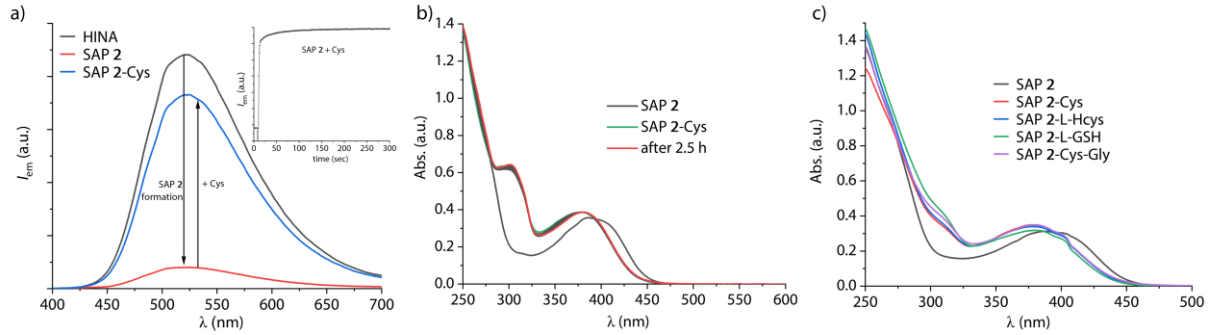

Figure 3.23. a) Emission spectra (λ_{ex} = 380 nm) of the formation of SAP **2** (red curve) by mixing the solution of HINA (50 µM, black curve) and Pd-Cl (50 µM), and upon reacting with L-Cys. Insert shows the changes in the emission intensity at 525 nm during the course of the reaction. ***Note:*** the emission trace of Pd-Cl was omitted in the graph due to its extremely weak intensity. b) Absorbance kinetics of the reaction of SAP **2** with L-Cys. The interval time between each spectrum is 86 s, and the total measuring time is 2.5 h. c) Absorbance spectra of SAP **2** upon addition of urinary thiols, L-Cys, L-Hcys, and Cys-Cys. All the measurements were performed in $NaHCO_3$ buffer (25 mM, pH 9.5) with 0.9 mM CTAB at 25 °C. The concentrations of SAP **2** and thiols in all the measurements were 50 µM.

The SAP assay concept is complementary and combinable with differential sensing approaches but is *not* requiring array-based sensing protocols. It is sufficient to record the spectrogram of one reaction chamber (*e.g.*, microwell or cuvette) to obtain the necessary data for analyte distinction and quantification. Similar to differential sensing, SAP assays require an additional data processing step that can be performed within seconds on standard computers. In the future, the information-rich readout provided by SAPs may enable multiplex classification of biofluid specimens and may assist the development of rapid diagnostics tests (RTD).

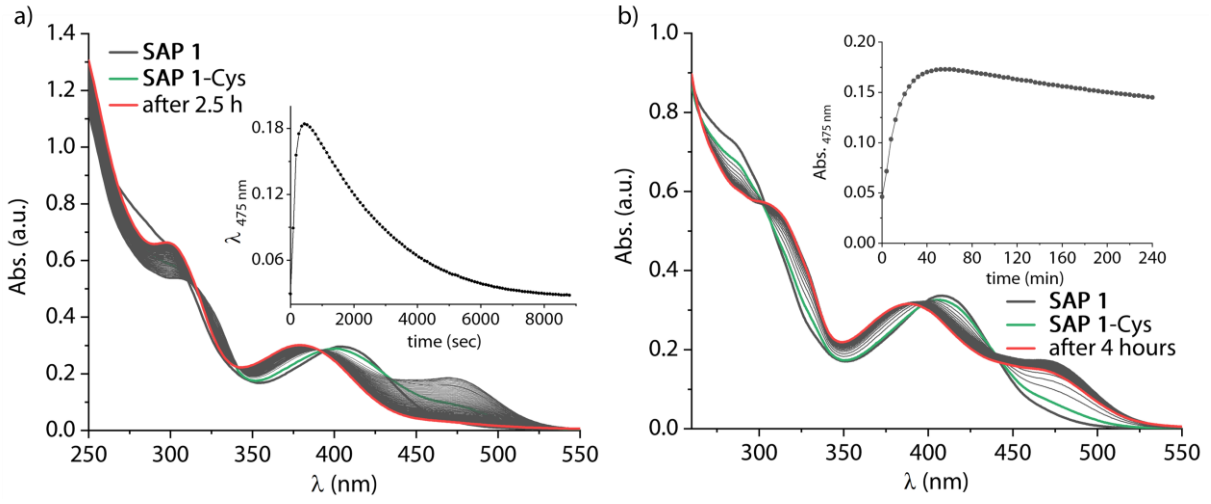

Figure 3.24. Absorbance spectrograms evolution for the reaction of SAP **1** (50 µM) with L-Cys (50 µM) in $NaHCO_3$ buffer (25 mM, pH 9.5) with 0.9 mM CTAB at 25 °C (a) and 10 °C (b). The interval time between each spectrum is 86 s, and the total measuring time for (a) is 2.5 h, while (b) is 4 h. The insets show the changes in the absorbance intensity at 475 nm during the course of the reaction.

In addition to the remarkable sensing performance and the potential application possibility in molecular diagnostics, the SAP concept may also bridge the fundamental research[69-72] on self-

assembly, dynamic constitutional chemistry, structural evolution, and out-of-equilibrium systems to a further application step. In contrast to many of the established self-assembling building blocks, SAPs provide a much more detailed spectroscopic response that will allow for easier comparison of theoretical method predictions and generally enriches the understanding of supramolecular concepts. For instance, simple changes in the reaction temperature can be used to approach metastable aggregates (**Figure 3.24**). Moreover, exploratory chiroptical monitoring of SAP reactions with chiral biothiols already revealed that analyte-dependent chiral assemblies are formed, which switch their chirality during the structural evolution, see the next chapter for the chirality sensing investigation of the SAP assay.

3.4 Conclusions

In conclusion, the novel time- and spectra-resolved sensing concept was developed by merging covalent and non-covalent interactions. In this design, the covalent interaction between the reactive moieties ensures high sensitivity and broads the analyte fields due to the unselectively binding. Subsequently, the non-covalent interactions between the probe-analyte conjugates provide the system with a high selectivity because of the stimuli-responsive nature of the supramolecular chemistry. Therefore, only one SAP is sufficient to distinguish 13 different biothiols and drugs from each other in aqueous media and even in biofluids. This proposed sensing concept provides a strategy alternative to the challenging design of selectively binding receptors and probes.

Experimental information

Synthesis of SAPs

Synthesis and isolation of SAP 1

*The synthesis and isolation of SAP **1** was carried out by my former colleagues Dr. Pronay Kumar Biswas and Alicja Siennicka.*

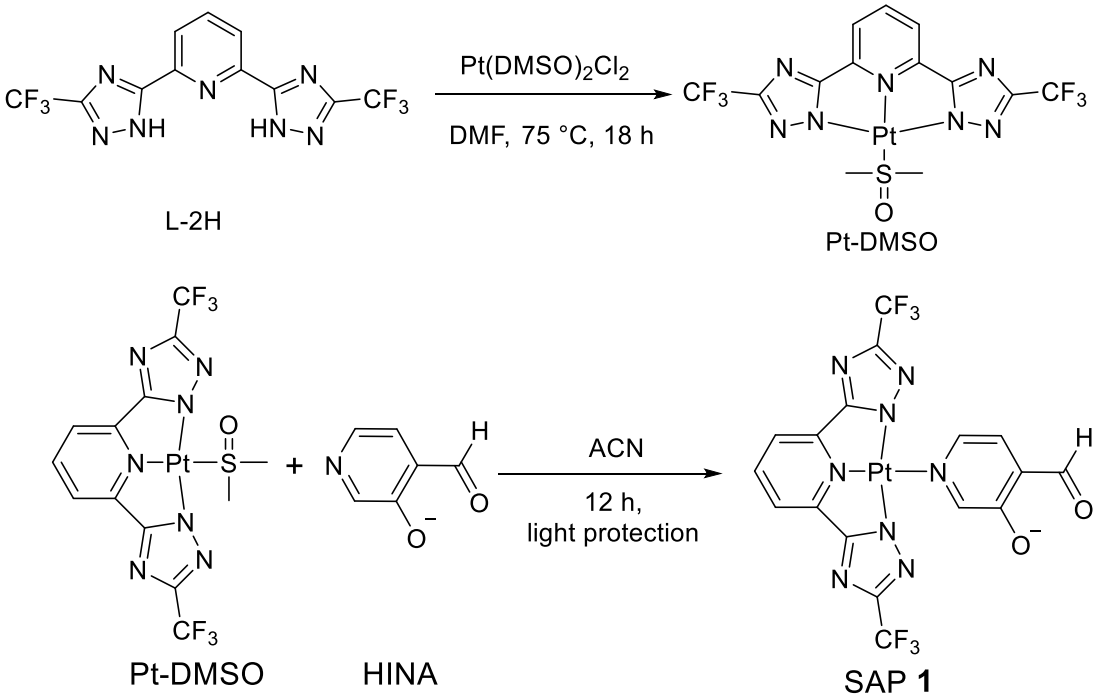

Figure 3.25. Schematic representation of the synthetic route for SAP **1**.

Synthesis of Pt-DMSO

Pt-DMSO was synthesized as described in the literature.[88, 268]

Synthesis of SAP 1

6.2 mg (0.01 mM) of Pt-DMSO and 4.9 mg (0.04 mM) of HINA were dissolved in 1.5 mL ACN. The reaction mixture was stirred overnight in the dark. A pink solid formed, which was collected by centrifugation and washed with acetonitrile (3.0 mL). The washing process was repeated twice with acetonitrile (3.0 mL) and once with water (2.0 mL), ethanol (2.0 mL), and DCM (2.0 mL). The product was obtained as a yellow solid of 4.0 mg in 60 % yield. The compound was stored in the dark at room temperature. ESI-MS (negative scan, m/z): calculated 664.0239, found 664.0087. ^{1}H NMR (500 MHz, THF-d_8) δ = 11.07 (s, 1H) 10.47 (s, 1H) 9.50 (s, 1H) 9.35 (d, *J*=5.8, 1H) 8.32 (t, *J*=7.9, 1H) 8.00 (dd, *J*=6.8, 4.7, 3H) ppm. ^{13}C NMR (126 MHz, THF-d_8) δ = 189.68, 164.25, 156.26, 148.89, 145.56, 145.50, 144.00, 129.00, 123.88, 121.06, 119.09, 118.40, ppm. ^{19}F NMR (471 MHz, THF-d_8) δ = −65.11 (s) ppm.

Synthesis and isolation of SAP 2

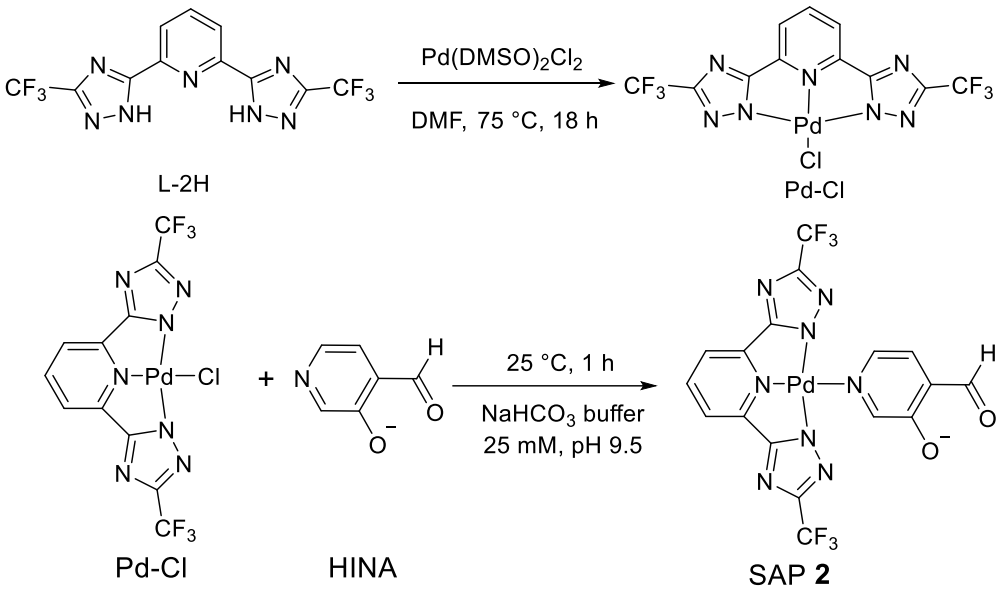

Figure 3.26. Schematic representation of the synthetic route for SAP **2**.

Synthesis of Pd-Cl

cis-Dichlorobis(dimethyl sulfoxide)palladium(II) ($Pd(DMSO)_2Cl_2$) (0.45 g, 0.9 mmol) and 2,6-bis(3-(trifluoromethyl)-1H-1,2,4-triazol-5-yl)pyridine (L-2H)[88] (0.213 g, 0.61 mmol) were dissolved in 5 mL DMF with stirring at 75 °C. After 18 hours, the reaction mixture was cooled to room temperature, and the volatiles was removed by a rotary evaporator. Subsequently, the crude product was dispensed in 5 mL DCM, sonicated, centrifuged, and the supernatant was decanted. This procedure was repeated once with 5 mL DCM and another time with 5 mL MeOH to obtain a yellow solid.[268] ESI-MS (negative scan, m/z): calculated 489.9096, found 489.9074. ^{1}H NMR (500 MHz, DMSO-d_6) δ = 8.24 (t, 1H), 7.87 (d, 2H) ppm. ^{13}C NMR (126 MHz, DMSO-d_6) δ = 163.86, 152.57, 147.59, 143.97, 121.70, 119.70 ppm. ^{19}F NMR (470 MHz, DMSO-d_6) δ = −64.58 ppm.

Preparation of SAP 2 *in-situ*

100 µL (100 µM) of a solution of 5 mM Pd-Cl (DMSO) and 110 µL (110 µM) of a solution of 5 mM HINA (MilliQ water) were added into a 5 mL centrifuge tube and filled with 4795 µL sodium bicarbonate buffer (25 mM) containing 0.9 mM CTAB at pH 9.5, stirring for 1 hour at 25 °C. A 100 µM stock solution of SAP **2** was obtained and used directly. The probe solution was preferably prepared freshly and used within 8 hours after preparation.

Additional data

NMR spectrum

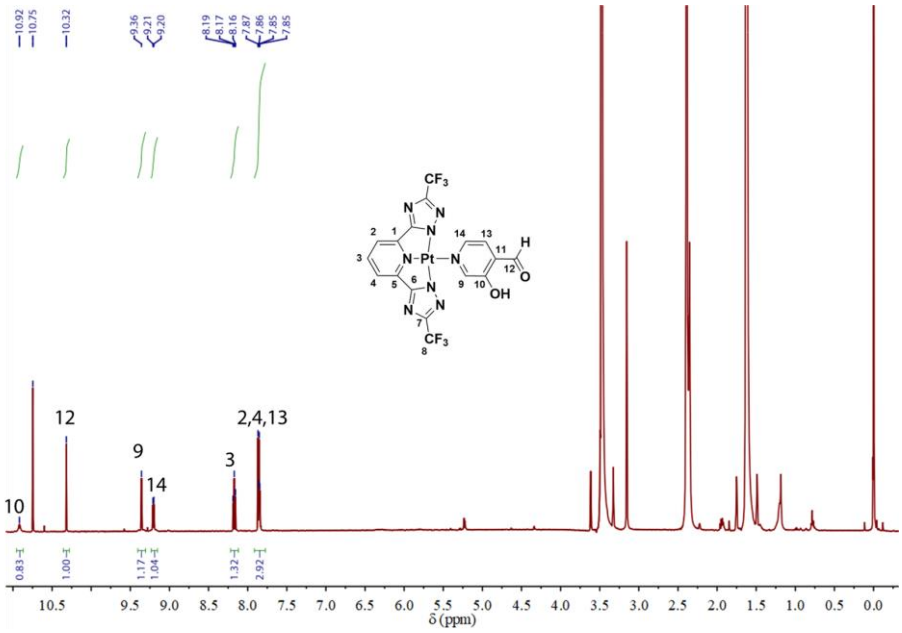

Figure 3.27. ^{1}H NMR spectrum of the isolated form of SAP **1** in THF-d_8. The non-assigned peaks belong to THF-d_8. The ^{1}H NMR of THF-d_8 alone is shown as a reference in **Figure 3.28.**

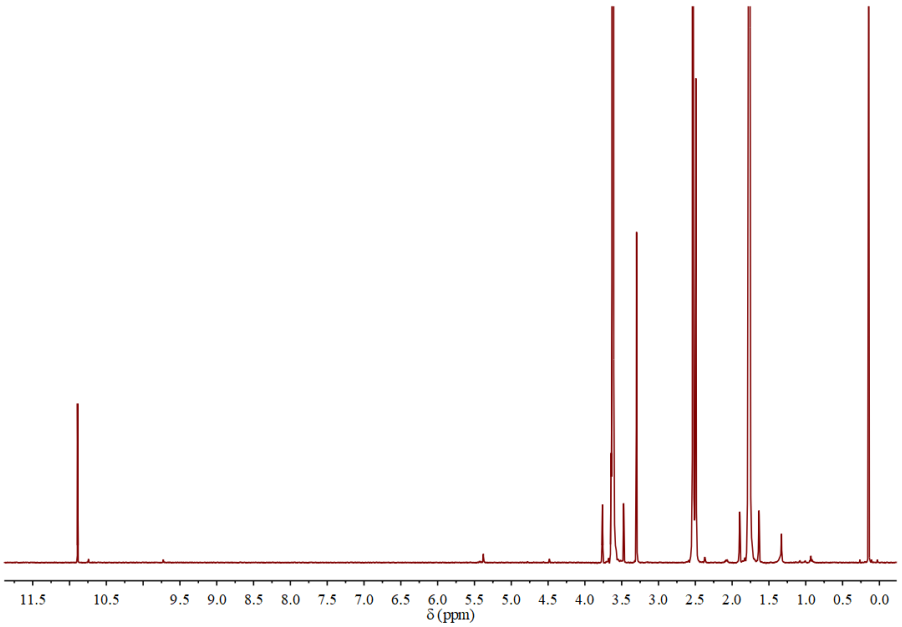

Figure 3.28. ^{1}H NMR spectrum of THF-d_8

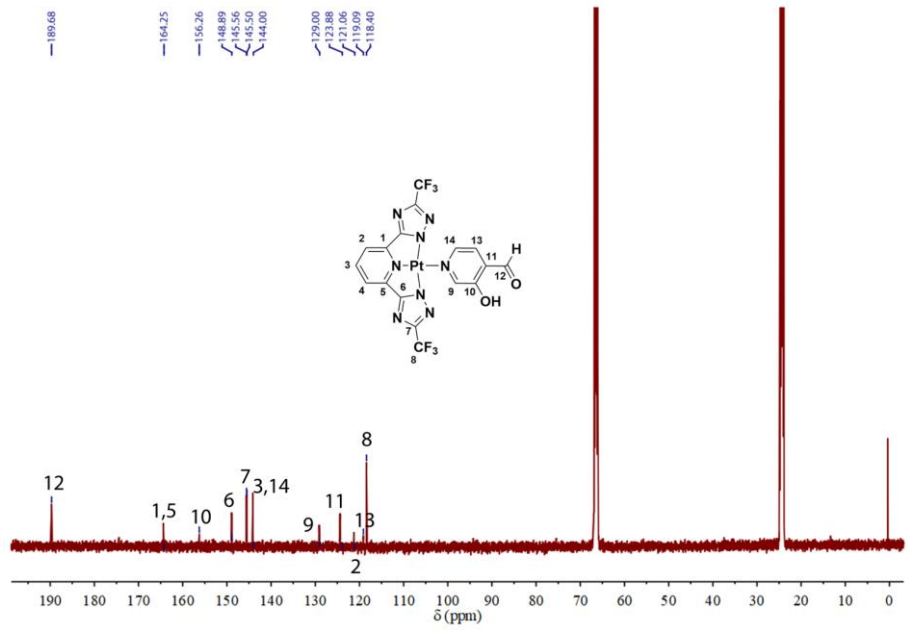

Figure 3.29. ^{13}C NMR spectrum of the isolated form of SAP **1** in THF-d_8.

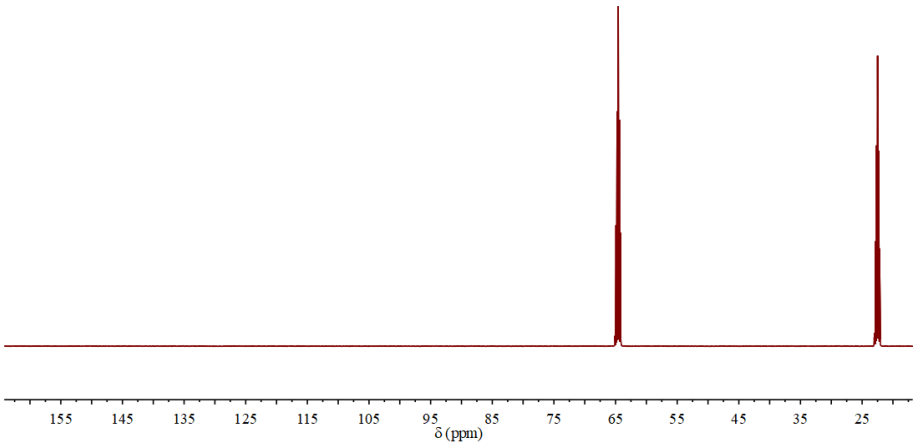

Figure 3.30. ^{13}C NMR spectrum of THF-d_8.

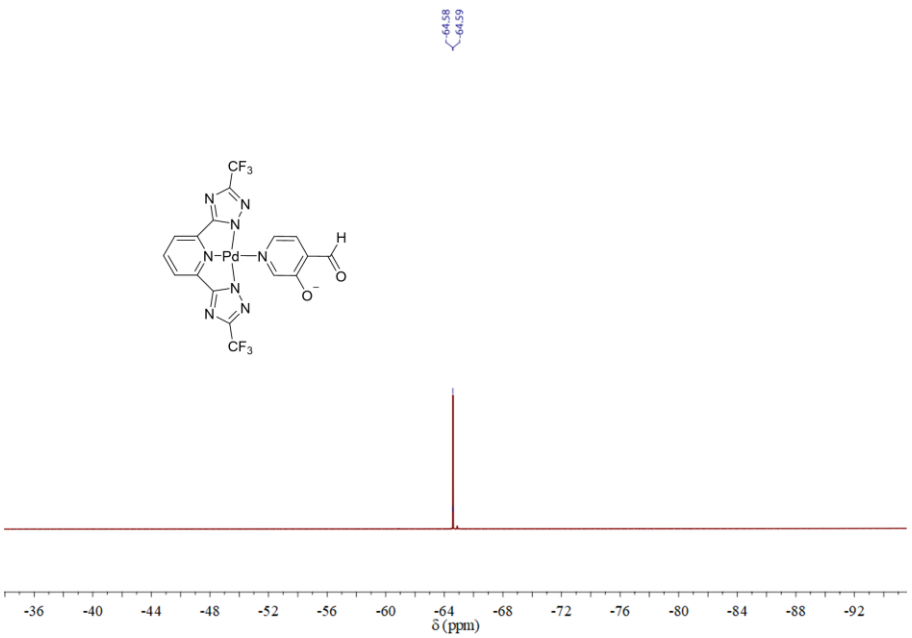

Figure 3.31. ^{19}F NMR spectrum of the isolated form of SAP **1** in THF-d_8.

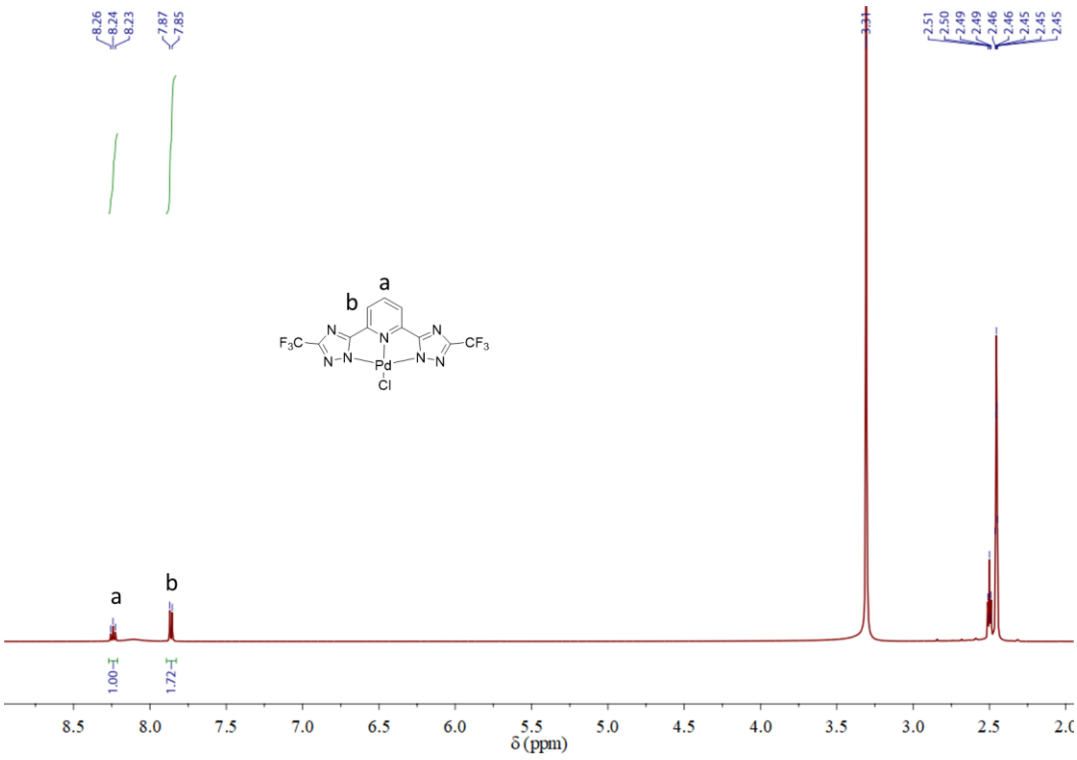

Figure 3.32. ^{1}H NMR spectrum of Pd-Cl in DMSO-d_6

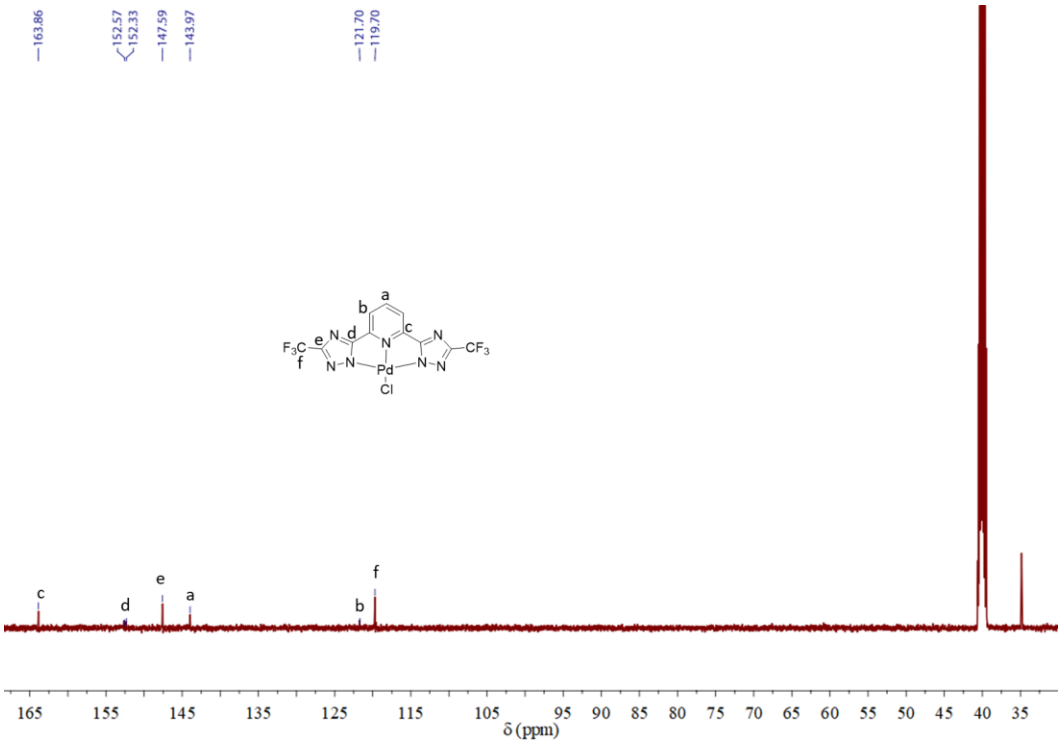

Figure 3.33. ^{13}C NMR spectrum of Pd-Cl in DMSO-d_6.

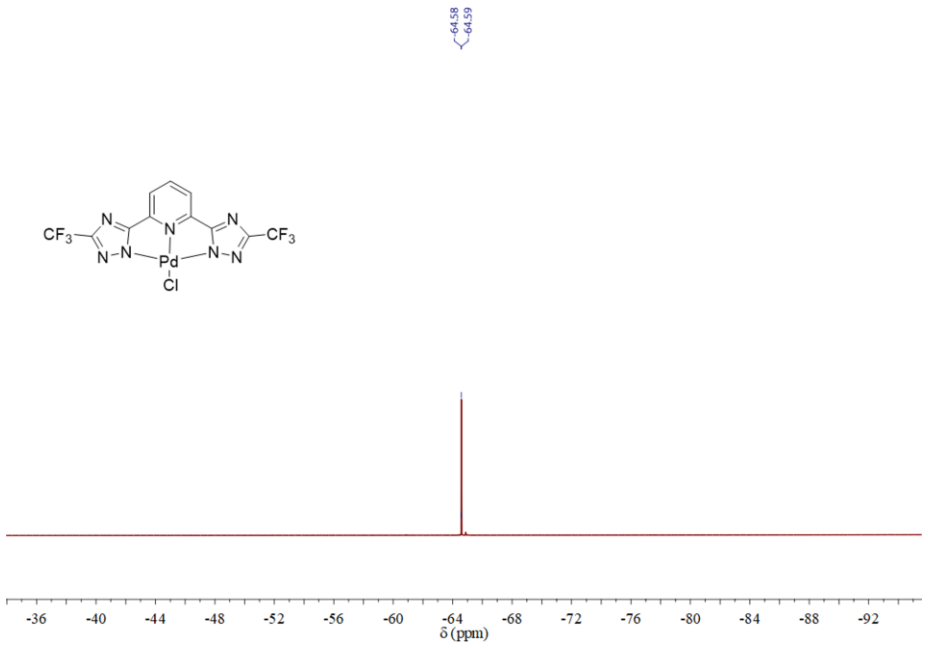

Figure 3.34. ^{19}F NMR spectrum of Pd-Cl in DMSO-d_6.

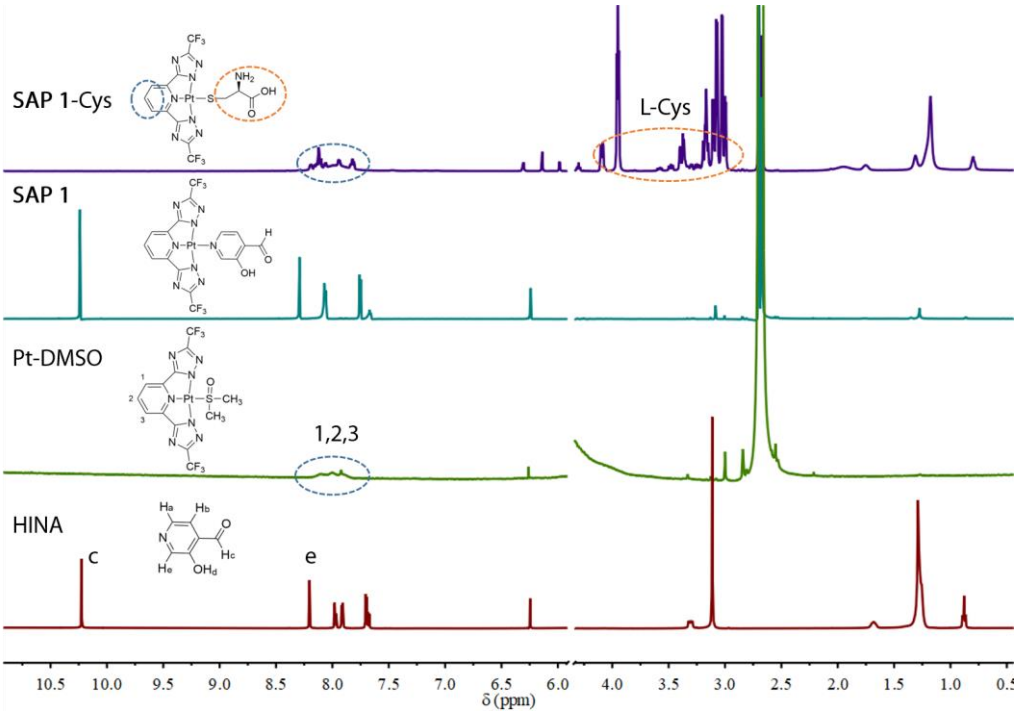

Figure 3.35. ^{1}H NMR characterization of the *in-situ* formation SAP **1** and its reaction with L-Cys. From bottom to top: ^{1}H NMR characterization of HINA (10 mM) and Pt-DMSO (10 mM) and their reaction product SAP **1**. Also shown is the ^{1}H NMR spectrum of the SAP **1** (10 mM) and L-Cys (10 mM) reaction mixture. All spectra were recorded in D_2O with CTAB (9 mM) as a surfactant. Note that at the concentration needed for NMR, the aldehyde moiety of HINA undergoes a reversible chemical reaction with the thiol and amine moieties of L-Cys.

ESI-MS spectrum

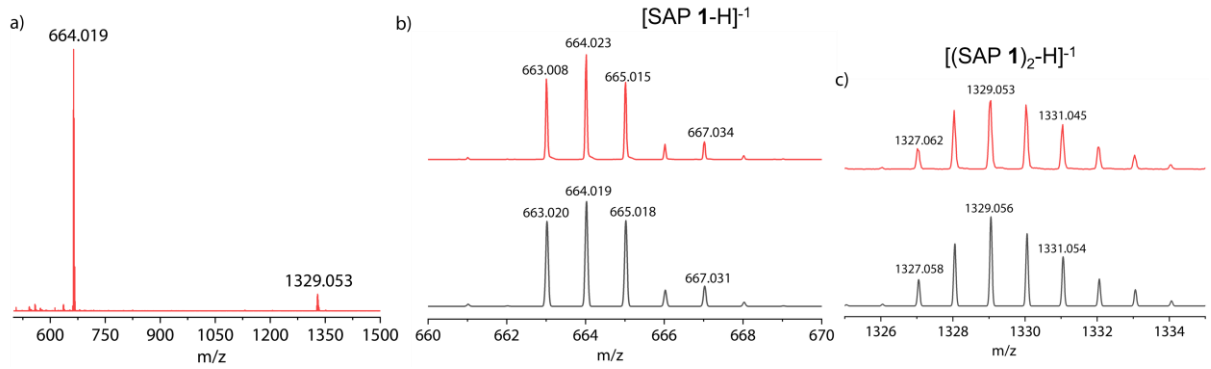

Figure 3.36. a) Full ESI-MS spectrum (negative mode) of the solution of SAP **1.** The MS experiment was conducted starting from a solution of SAP **1** in $NaHCO_3$ buffer (25 mM, pH 9.5) with 0.9 mM CTAB. b-c) Zoom in on the experimental (red) and calculated (black) ESI-MS spectra of [SAP **1**-H]$^{-1}$ (b) and [(SAP **1**)$_2$-H]$^{-1}$ (c).

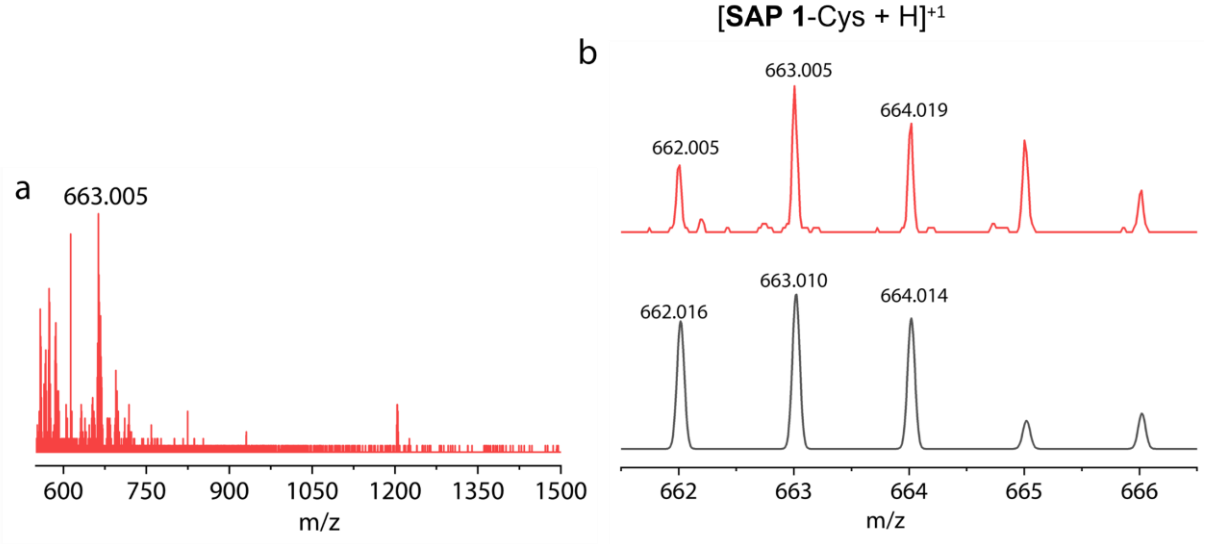

Figure 3.37. a) Full ESI-MS spectrum (positive mode) of the solution of SAP **1**-Cys**.** The MS experiment was conducted starting from a solution of SAP **1**-Cys conjugate in $NaHCO_3$ buffer (25 mM, pH 9.5) with 0.9 mM CTAB. b) Zoom in on the experimental (red) and calculated (black) ESI-MS spectra of [SAP **1**-Cys + H]$^{+1}$.

Emission response of SAP 1 reaction with biothiols

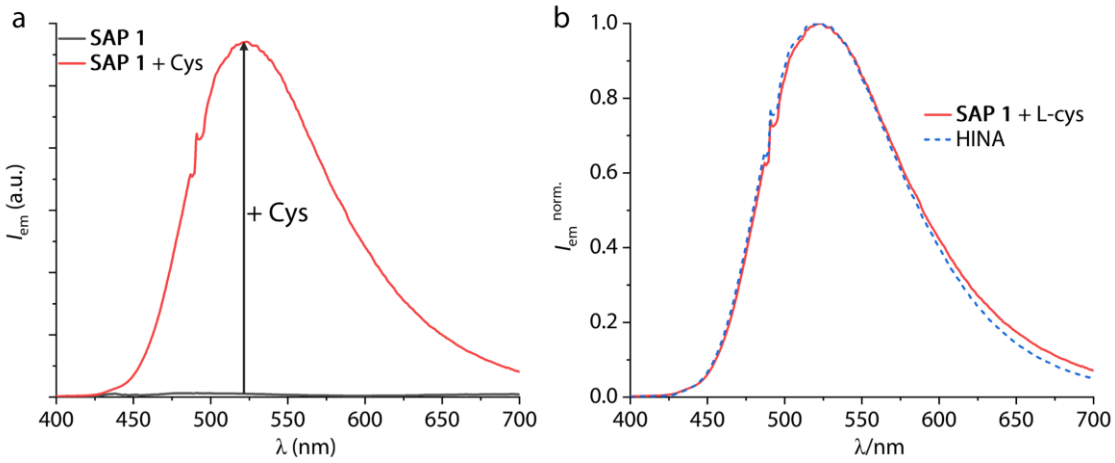

Figure 3.38. a) Emission (λ_{ex} = 380 nm) spectra of **SAP 1** (50 μM) prior to (black curve) and after (red curve) the reaction with L-Cys (50 μM). The spectra were recorded after the reaction reached an apparent equilibrium (~ 3 h) at 25 °C. b) Comparison of the normalized spectra of the reaction mixture with that of a HINA solution. The spectra of HINA (50 μM) are shown as a blue dashed curve. All the spectra were measured in $NaHCO_3$ buffer (25 mM, pH 9.5) with 0.9 mM CTAB at 25 °C.

Spectrogram evolution for SAP 1 assay in a 96-well plate format

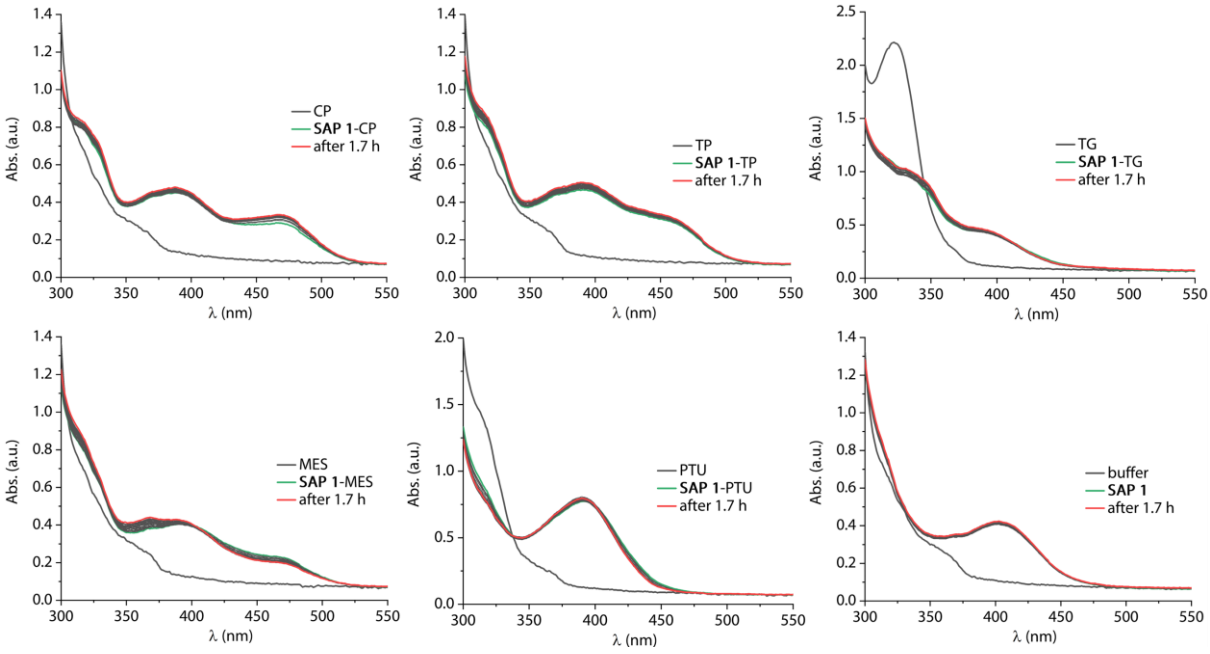

Figure 3.39. Absorbance spectrogram evolution for the reaction of SAP **1** (50 μM) with represented thiol drugs (50 μM) in $NaHCO_3$ (25 mM, pH 9.5) with 0.9 mM CTAB through a 96-well plate format. The spectrogram of SAP **1** is shown in the last graph as a blank sample. The interval time between each spectrum is 180 s, and the total measuring time is 1.7 h.

Table 3.1. Summary of the physiological concentration range of urinary thiols in human urine[a] and blood.

	concentration range	media	ref
L-Cys	20 - 140 µmol/ mmol creatinine = 0.2 - 1.4 mM	urine	253
	200 – 280 µM	serum	269
GSH	5.0-85 nmol/ mmol creatinine = 50-850 nM	urine	8
	4.9-7.3 µM	human serum	269
L-Hcys	0.60-1.70 µmol/ mmol creatinine = 6.00 - 17.0 µM	urine	8
	6.5-11.9 µM	human serum	269
NAC	1.00-2.14 µmol/ mmol creatinine = 10.0 - 21.4 µM	urine	8
Cys-Gly	0.90-2.5 µmol/ mmol creatinine = 9.0 - 25 µM	urine	270
	18.6 - 35.8 µM	serum	269
TGA	0.72-0.84 µmol/ mmol creatinine = 7.2 - 8.4 µM	urine	271
TP	~174 µM	urine[b]	272
	0.0 - 10 µM	plasma[c]	272
MEA	5.0 - 50 µM	plasma[d]	273
D-Pen	6.7 - 43 µM	plasma[e]	274
CP	~58.3 µM	urine[f]	275
	14.7 µM	plasma[g]	275
MES	3.0-30 µM	plasma[h]	276
	0.80 - 4.2 µM	urine[i]	276

[a] Urinary analyte concentrations were converted assuming a representative creatinine level of 10 mmol/L. [b] Cumulative excretion in urine during 48 h after intake of 3 mmol intake. [c] within 30 h after 3 mmol intake. [d] within 6 h after cysteamine dose of 900 mg. [e] within 4 h after 750 mg intake. [f] within 24 h after 100 mg intake. [g] after 1.1 h with 100 mg oral intake. [h] within 2 h after 800 mg oral intake. [i] within 0-8 h after 800 mg oral intake.

4 The spectral evolution of probe-conjugates enables chirality analysis

4.1 Abstract

Thiol-reactive metal-organic complexes readily self-assemble into chiral structures after reaction with chiral biothiols in aqueous media and afford analyte-indicative circular dichroism (CD) signals in the near UV and visible range. The supramolecular polymerization-based modus operandi of self-assembling probes (SAPs) exploits the ultrasensitive susceptibility of self-assembling systems towards minute structural differences for yielding distinct spectroscopic fingerprints that allow for direct identification and differentiation of six structurally similar analytes. Additional spectroscopic information is harvested by the evolution of the supramolecular system over time. The introduced supramolecular concept is likely adaptable in bioanalytical chemistry, especially for the spectroscopic distinction of metabolites, and offers a novel approach for generating information-rich spectral and time-dependent signals that will foster the analysis of complex biofluids, *e.g.*, urine, saliva, and serum, through machine learning.

4.2 Introduction

Chiral molecules play critical roles in many biological processes and are essential building blocks for peptides, proteins, and other natural compounds.[277] The commonly used chirality analysis methodologies rely on chromatographic techniques, which indeed are reliable but usually time- and money-consuming, and sophisticated instrumentation required. In contrast, the optical detection, *i.e.*, absorbance, emission, and circular dichroism (CD) spectroscopic techniques-based method, is more suitable for practical applications due to its ease of monitoring, cost-effectiveness, and high-throughput screening (HTS) properties. The key factor in the spectroscopic method-based chirality sensing is to generate an easily measurable signal in UV, visible light, and even longer wavelength ranges because most small chiral molecules are only optical active in the far UV range. As mentioned in **Chapter 1.3.3**, according to different binding interactions between the receptors (or molecular probes) and the target chiral analytes, the current chirality sensing concepts could be mainly classified into the following categories. They are non-covalent interactions-based eIDA systems[97, 156-162] or macrocyclic molecular systems;[163-166] covalent reaction (coordination interaction included)-based metal

complex systems,[167-170] or pure organic small molecular probes;[171-172] and dynamic covalent reaction-based sensing concepts[141, 173] (**Figure 4.1**a). Based on these concepts, hundreds of chiroptical probes (and chemosensors) have been developed and attempted to reach the practical application requirements in clinical diagnosis fields, although they rarely have succeeded. However, there are still shortcomings remaining: *i*) most of the current chirality probes only work in organic solvents; *ii*) the discrimination of the structural similar chiral analytes, *e.g.*, Cys and Cys-Gly pairs, cannot be achieved (low selectivity); *iii*) the assay typically takes hours. Therefore, the new chirality sensing concept still needs to be considered.

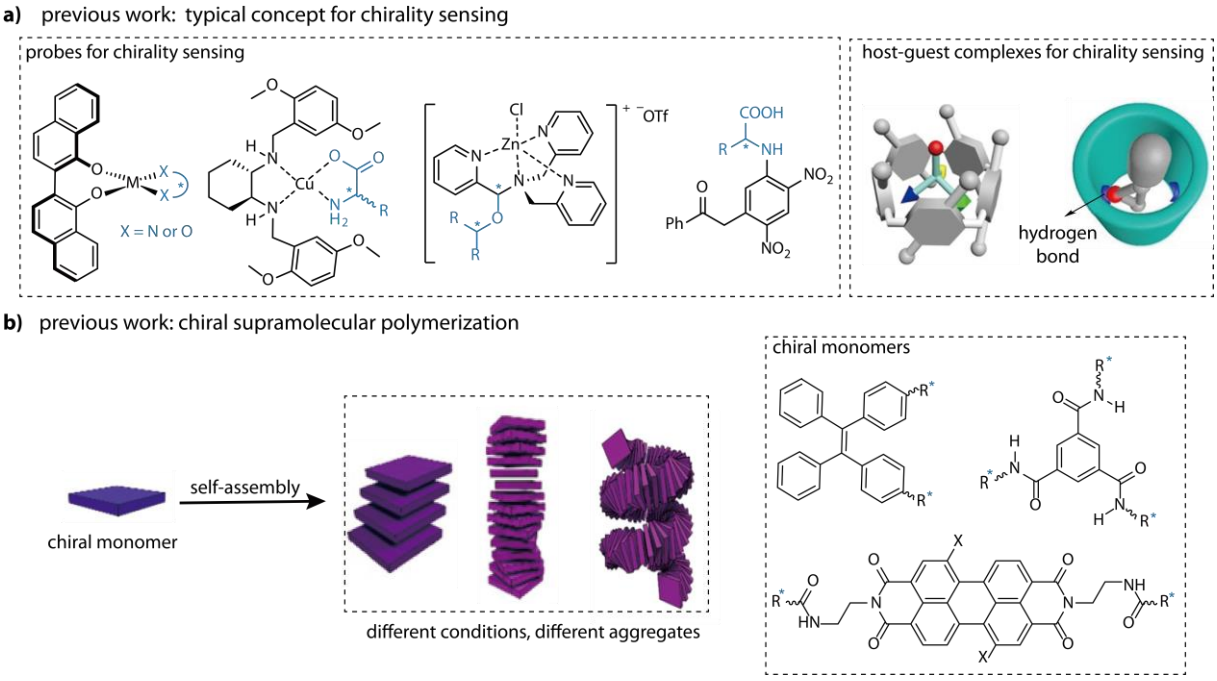

Figure 4.1. a) Schematic representation of the previously reported chirality sensing probes (and receptors) based on the (dynamic) covalent reactions or non-covalent interactions. b) Schematic representation of chiral supramolecular polymerization and the chemical structures of the representative chiral monomers. Part of the figures is adapted with permission from ref [278-279]. © 2017 American Chemical Society and 2020 Willey.

The stimuli-responsive behavior of supramolecular chemistry is the reason why these systems exhibit high sensitivity to the minor structural changes of the building blocks, which has pronounced differences in the shape, size, and properties of the resulting self-assembled structures (**Figure 4.1**b).[68-69, 76, 258, 280-281] Over the decades, many beautiful designed systems have been reported, *e.g.*, foldamers,[282-283] self-aggregating and π-π-stacking systems,[284-287] and supramolecular-polymer systems.[180, 288-290] In these systems, chiroptical signals are enhanced after the self-assembling or polymerization occur only if the molecular components are chiral and optically active. Therefore we could utilize this amplification approach to achieve the small chiral molecules detection.

As discussed already in **Chapter 3**, pronounced difference analyte-dependent aggregation structures were obtained in the "self-assembling probes (SAPs)" systems because of the non-covalent Pt···Pt interaction between the SAP-analyte conjugates. Therefore, it is worth exploring whether this molecular sensing concept could be applied to chirality sensing, with which the chiral target analytes are detected directly by the SAP-analyte aggregated assemblies (**Figure 4.2**).

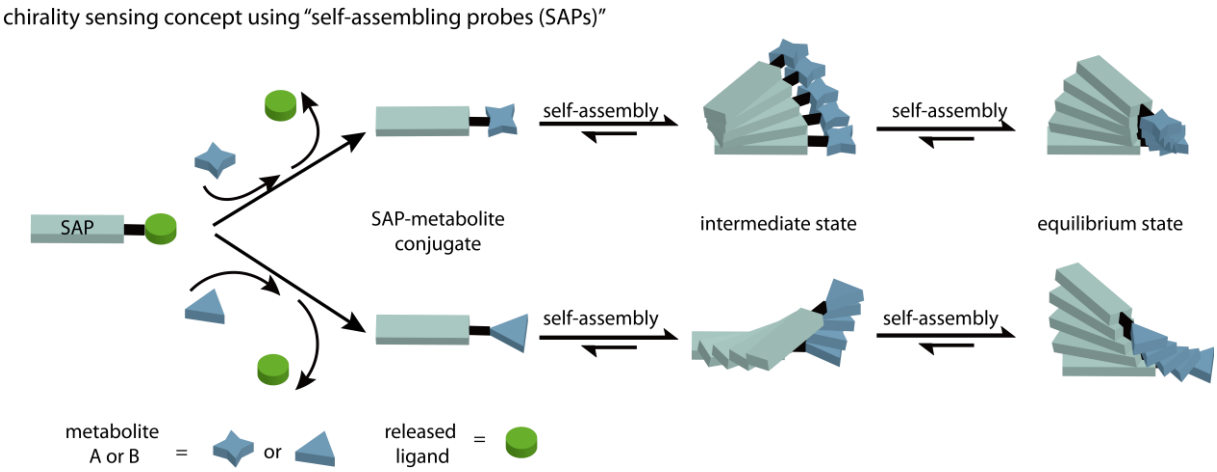

Figure 4.2. Schematic representation of the chirality sensing *via* "self-assembling probes (SAPs)." The SAPs first react with thiols through a fast ligand exchange reaction resulting in an emissive indicator (HINA) releasing. The observed SAP-thiol conjugate is then generally assembled into chiral aggregates over time, providing analyte-indicative UV/vis and CD spectroscopic information for the analyte identification and differentiation.

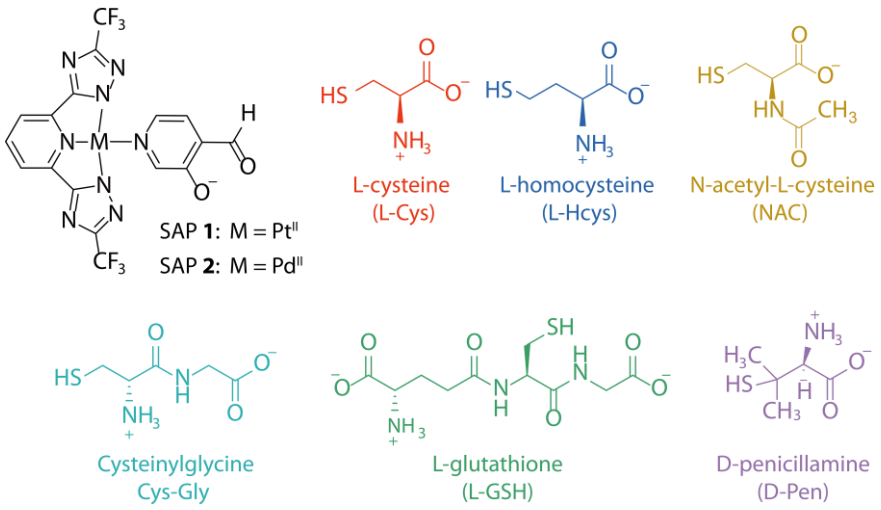

Figure 4.3. Chemical structures of the SAPs (SAP **1**: Pt(II) complex and SAP **2**: Pd(II) complex) and the chiral thiol-containing metabolites were tested in this study.

Similar to the investigation for the absorbance spectrogram-based urinary thiols and thiol-containing drugs sensing, the urinary chiral thiols were employed as the model analyte to evaluate the chirality sensing properties of the SAP concept (**Figure 4.3**). Concretely, the target chiral analytes were first unselectively coordinated to the SAP through a fast ligand exchange

reaction, releasing the emissive indicator HINA. Subsequently, the formed SAP-analyte conjugates evolute to self-assembled analyte-induced chiral structures driven by the non-covalent Pt···Pt interactions (**Figure 4.2**). In this way: *i*) measurable CD signals are generated to indicate the configuration and enantiomeric excess (*ee*) components of the target analytes; *ii*) the achiral signals of the conjugates, *i.e.*, absorbance or emission intensity, can be employed for the determination of the total concentration of the analytes; *iii*) stimuli-responsive nature of the supramolecular system enables the SAP assay differential racemates from their enantiomerically pure compounds by non-chiral techniques, *e.g.*, UV/vis and DLS. In addition, the metastable self-assembled states were captured during the aggregation evolution process, and a chirality conversion of the conjugates was obtained.

4.3 Result and discussion

4.3.1 Chiral single analyte identification

As reported in **Chapter 3**, the reaction of SAP **1** with a thiol-function analyte passes through the following steps: *i*) After the reaction initiation, SAP **1** quickly exchanges its HINA ligand with the stronger coordinating biothols. The observed spectroscopic changes (emission increase at 525 nm and absorbance increase at 471 nm) were caused by the SAP-thiol conjugate formation and emissive indicator HINA release (**Figure 3.38**). *ii*) In a slower subsequent process, the SAP-analyte conjugate readjusts its supramolecular aggregation structure driven by the metallophilic interactions of Pt(II) complexes and π-π stacking, resulting in analyte-indicative absorbance spectrum evolution. *iii*) Finally, a kinetically stable aggregation structure is reached after several hours.

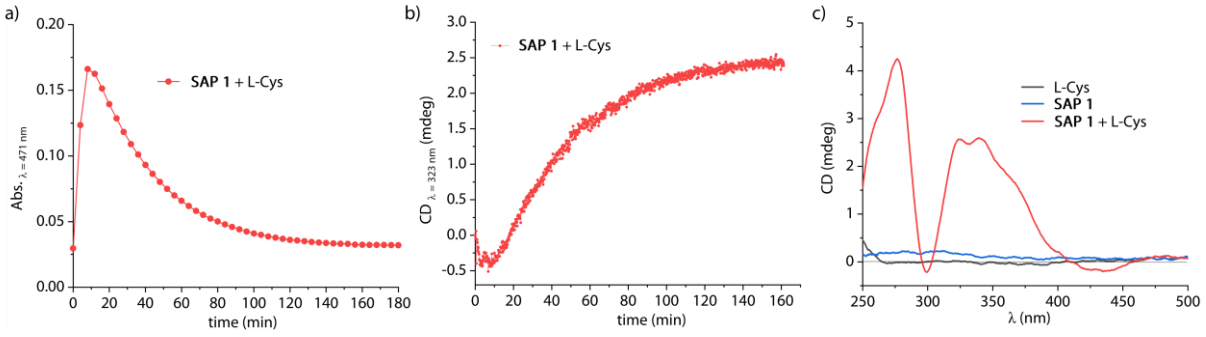

Figure 4.4. Absorbance (a, λ_{abs} = 471 nm) and CD (b, λ_{CD} = 323 nm) kinetics traces of the reaction of SAP **1** (50 µM) with L-Cys (50 µM). c) CD spectra of SAP **1** (50 µM) prior to (blue curve) and after (red curve) the reaction with L-Cys (50 µM, black curve). The spectra were recorded after the reaction reached the apparent equilibrium state (~ 3 h). All the measurements were conducted in $NaHCO_3$ buffer (25 mM, pH 9.5) with 0.9 mM CTAB at 25 °C.

Inspired by the in-depth studies of the formation of supramolecular polymers,[180, 288-290] chiral spectroscopic features are also expected when a chiral analyte is introduced. Indeed, it is the case, as shown in **Figure 4.4**b, the CD intensity at 323 nm gradually increases after L-Cys addition in ~10 min, which was in good agreement with the absorbance kinetic study, where the intensity at 471 nm started to decrease after 10 min of the reaction initiation (**Figure 4.4**a). This observation indicates that the introduced small chiral molecules triggered the chiral polymerization of the SAP-thiol conjugates, which in essence were driven by the non-covalent metallophilic interactions of Pt(II) complexes and π-π stacking between the metal center of the adjacent conjugate molecules. Thus, the resulting spectroscopic changes were analyte-dependent. In other words, different analytes can cause different aggregate structures of the SAP-analyte conjugates, although the first coordination step unselectively occurs. Therefore, the chirality sensing for different analytes was achieved merely using one SAP.

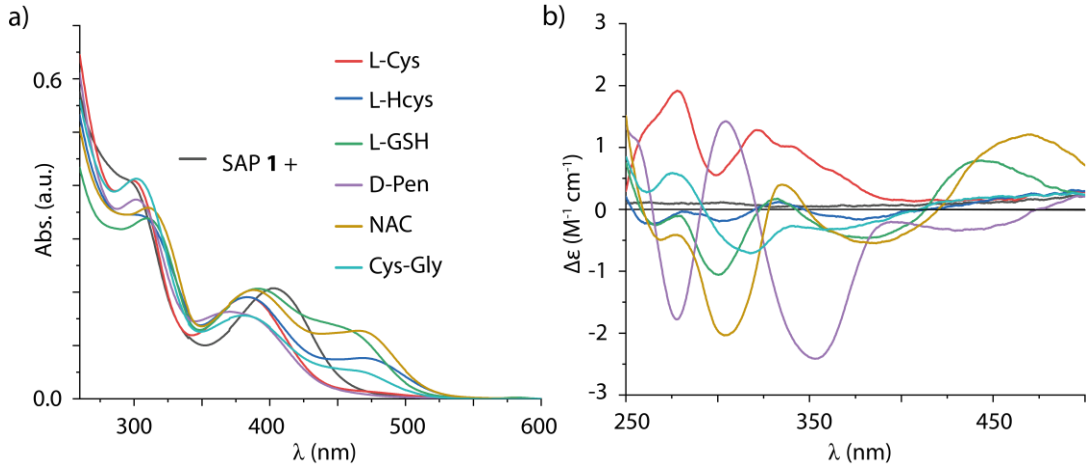

Figure 4.5. Absorbance (a) and CD (b) spectra of SAP **1** (50 μM) upon addition of chiral thiol-containing metabolites (50 μM) in $NaHCO_3$ buffer (25 mM, pH 9.5) with 0.9 mM CTAB. The spectra were recorded after the interaction reached an apparent equilibrium state (~ 3 h) at 25 °C.

Figure 4.5 shows that all six structural similar chiral thiol-containing metabolites were clearly distinguished in the micromolar range after applying the SAP **1** assay, which could not achieve by any previously reported studies that were aware of. Moreover, the analyte identification through SAP assay can be carried out in *in-situ* format, unlike other systems where the pre-chemical reaction and reaction mixture dilution steps were needed.

4.3.2 Analysis of chiral analyte mixtures

4.3.2.1 Enantiomeric excess (*ee*) value determination

After establishing a proof of concept for the proposed SAP chirality sensing concept, a series of non-racemic penicillamine (Pen) mixtures at the same total thiol concentration of 50 μM but with different L/D ratios were applied to evaluate the possibility of the enantiomeric excess (*ee*) value determination of the SAP assay. The spectroscopic results are shown in **Figure 4.6**, and all the spectra were recorded after the reaction reached an apparent equilibrium state (~ 3 h) in $NaHCO_3$ buffer (25 mM, pH 9.5) with 0.9 mM CTAB at 25 °C.

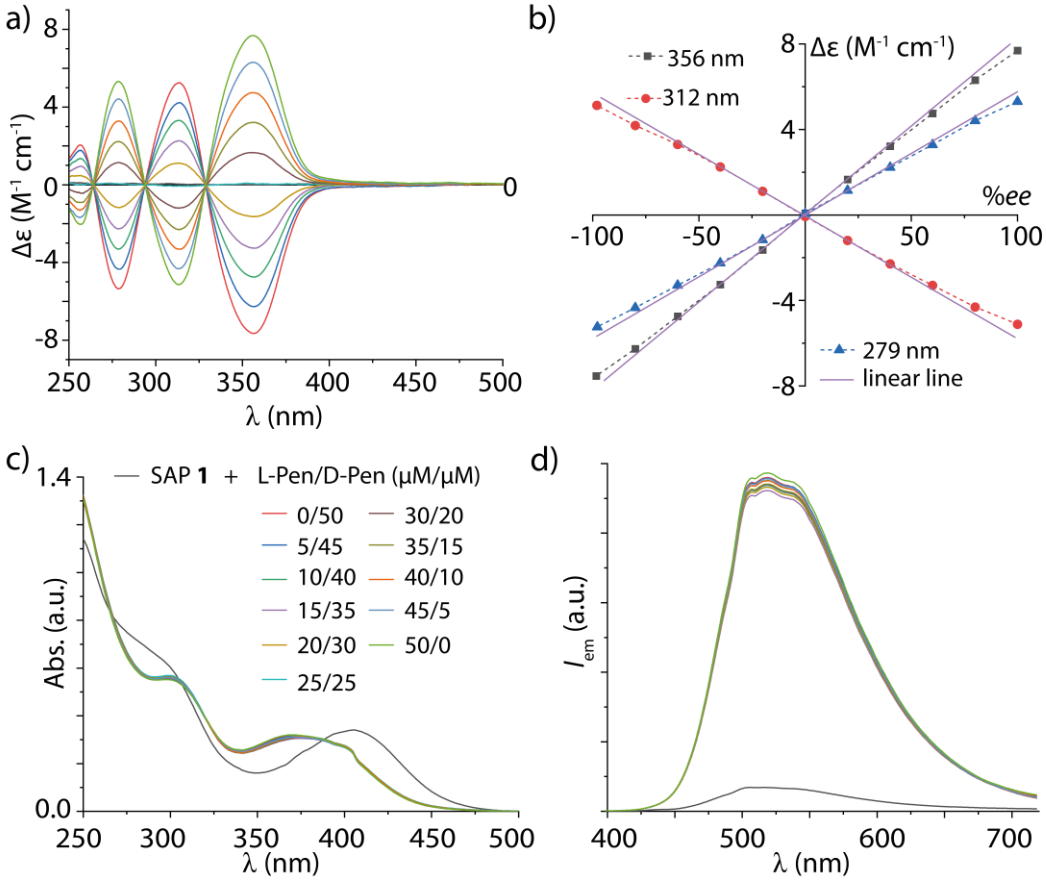

Figure 4.6. a) CD spectra of SAP **1** (50 μM) upon addition of a series of racemic mixtures of Pen (50 μM), the ratio of L-Pen to D-Pen varies from 0/50 to 50/0. ***Note:*** The molar circular dichroism Δε was obtained *via* Δε = θ / (c * l * 32980) with the experimentally recorded ellipticity value θ in mDeg, the pathlength l in cm, and the concentration c of the probe in mol/L. b) Intensity changes of the CD signals at 356 nm (black dashed curve), 312 nm (red dashed curve), and 279 nm (blue dashed curve) with different *ee* values of Pen mixtures. The solid lines in each curve were obtained from the linear fitting function by the Origin software. c-d) The corresponding absorbance (c) and emission (d, λ_{ex} = 380 nm) spectra of the samples in figure a). All the spectra were recorded after the reaction reached an apparent equilibrium state (~ 3 h) in $NaHCO_3$ buffer (25 mM, pH 9.5) with 0.9 mM CTAB at 25 °C.

This result is, at first sight, reminiscent of the behavior of other covalent reactions-based chirality sensing systems, in which the Cotton effect response of the racemic mixture is linear

dependent on the *ee* values because the conjugation of the chiral target molecules brings a chiral environment to the achiral probe moiety.[171-172] Therefore, the *ee* value quantification is available using the SAP **1** assay. Calling back to the discussion in **Chapter 3**, the absorbance intensity at ~ 470 nm was increased as a linear relationship to the concentration of L-Cys once the SAP **1** reaction was initiated. It indicated that the quantitative detection of the target analyte could be achieved by monitoring the absorbance intensity at the corresponding wavelength position. In fact, the results in **Figure 4.6**c-d evidenced that conclusion as well because all the racemic mixtures of Pen showed the same absorbance (and emission) spectra. Combining both information from the CD and absorbance (or emission) spectroscopy, the absolute concentration of each component in the racemic, even non-racemic thiol mixtures, can be determined. The same studies were demonstrated for the other model analyte L-Cys, and the result was shown in the additional data section at the end of this chapter.

4.3.2.2 Enantiomers and racemates differentiation

In the SAP sensing system, the introduction of the chiral analyte triggered the chiral supramolecular aggregation of the SAP-analyte conjugate. The chiroptical spectroscopic signals thus originated from the chiral-analyte-dependent aggregation structures. In essence, this is different from the previously reported covalent reaction-based non-aggregation behavior probes, in which the chiral intensity was only caused by the monomer of the probe-analyte conjugate. Because of the self-assembling nature of the SAP chirality sensing system, one could wonder whether the racemates can be differentiated from their pure enantiomers.

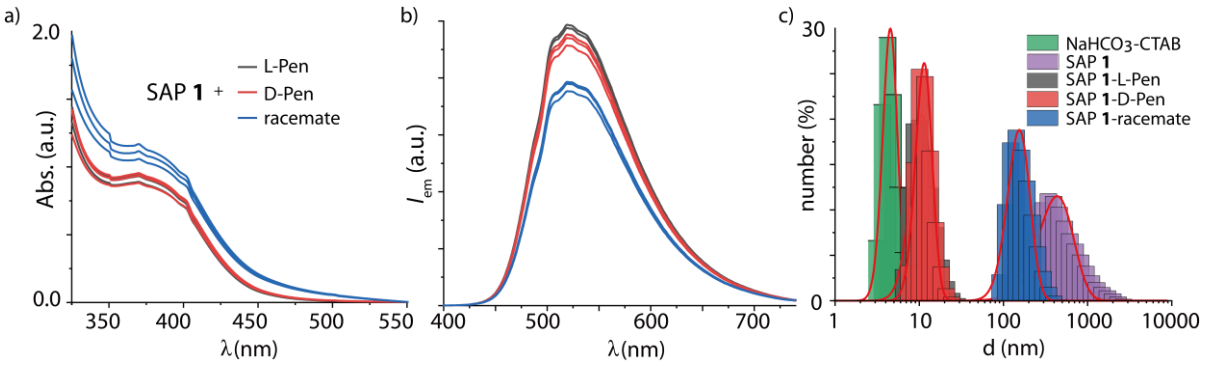

Figure 4.7. Absorbance (a) and emission (b, λ_{ex} = 380 nm) spectra of SAP **1** (200 µM) upon the reaction of L-Pen (200 µM, black curves), D-Pen (200 µM, red curves), and the racemic mixtures of L- and D-Pen (100 µM of each, red curves) in $NaHCO_3$ buffer (25 mM, pH 9.5) with 0.9 mM CTAB. Each sample was prepared in parrel with three replicas. The spectra were recorded after the reaction reached an apparent equilibrium state (~ 3 h) at 25 °C. c) DLS number distribution of SAP **1** (200 µM, purple columns, 535.0 ± 13.4 nm) upon the reaction of L-Pen (200 µM, black columns, 11.7 ± 0.1 nm), D-Pen (200 µM, red columns, 12.0 ± 0.1 nm), and racemic Pen mixtures (200 µM, blue columns, 168.97 ± 1.85 nm). The DLS number distribution of the $NaHCO_3$ buffer (25 mM, pH 9.5, 0.9 mM CTAB) is given in the graph as green columns, 4.7 ± 0.1 nm.

Indeed, it is the case. After applying the SAP **1** assay to the pure enantiomers and the racemic mixtures of penicillamine (200 µM), it was clearly seen that the absorbance intensity at ~ 400 nm of the racemic Pen was more vigorous and showed more light scattering than that of the pure enantiomer L-Pen or D-Pen (**Figure 4.7**a). These fundings suggest the bigger aggregates formed caused by the co-assembly between the SAP-L-Pen and SAP-D-Pen. The same result was also observed from the emission spectra (**Figure 4.7**b), where the emission intensity at ~ 530 nm of the racemic Pen mixtures was much weaker than that of the pure enantiomers. Again, the total concentration of penicillamine was the same in all the measurements.

In addition, the DLS measurements provided direct evidence of the co-assembly of the racemic mixture system. As depicted in **Figure 4.7**c, a much larger (168.9 ± 1.8 nm) aggregate formed in the solution of SAP **1** upon reaction with the racemic mixture, while the aggregate sizes were found in the enantiomer systems were both around 12 nm. As it may well be, this is the first time that the enantiomer of a chiral molecule could be distinguished from its racemic mixture by using the achiral techniques. This differential ability of the SAP assay was also demonstrated with another model analyte, Cys. Unlike the Pen system, not too much difference was seen in the absorbance and emissions spectra between racemic mixtures and the pure enantiomers of Cys samples. However, the DLS still showed that the bigger aggregation structures formed in the racemic mixture system (**Figure 4.8**), indicating that the differential ability is actually analyte-structure dependent and again highlighted the assembly nature of the SAP system.

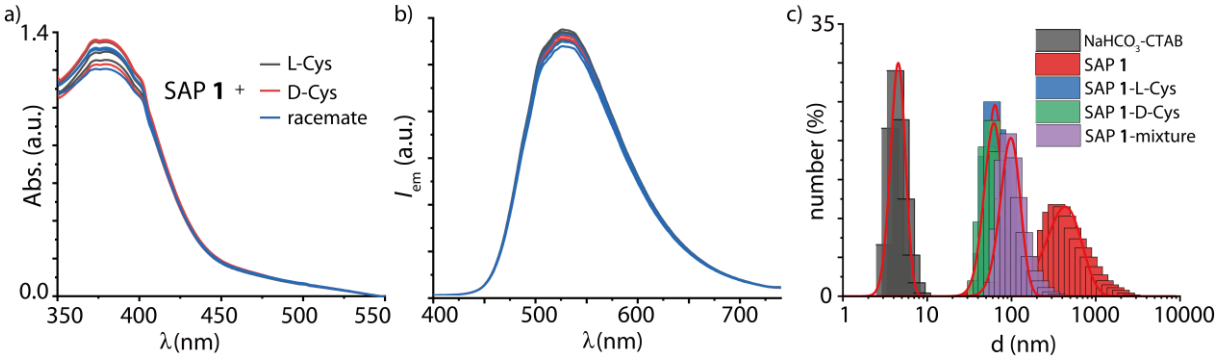

Figure 4.8. Absorbance (a) and emission (b, λ_{ex} = 380 nm) spectra of SAP **1** (200 µM) upon the reaction of L-Cys (200 µM, black curves), D-Cys (200 µM, red curves), and the racemic mixtures of L- and D-Cys (100 µM of each, red curves) in $NaHCO_3$ buffer (25 mM, pH 9.5) with 0.9 mM CTAB. Each sample was prepared in parrel with three replicas. The spectra were recorded after the reaction reached an apparent equilibrium state (~ 3 h) at 25 °C. c) DLS number distribution of SAP **1** (200 µM, red columns, 535.0 ± 13.4 nm) upon the reaction of L-Cys (200 µM, blue columns, 67.1 ± 0.5 nm), D-Cys (200 µM, green columns, 65.8 ± 0.5 nm), and racemic Pen mixtures (200 µM, purple columns, 105.4 ± 1.0 nm). The DLS number distribution of the $NaHCO_3$ buffer (25 mM, pH 9.5, 0.9 mM CTAB) is given in the graph as black columns, 4.7 ± 0.1 nm.

Except for the *ee* value determination and racemate differentiation, the performance of SAP assay in the mixture of different thiols was evaluated. As shown in **Figure 4.9**, upon reaction with a series of L-Cys/Cys-Gly mixture samples with the same total -SH concentration but different ratios of these two components, the non-linearity curve of the Cotton effect response to the concentration of Cys indicated again that the co-assembling between the SAP-Cys and SAP-Cys-Gly conjugates occurred.

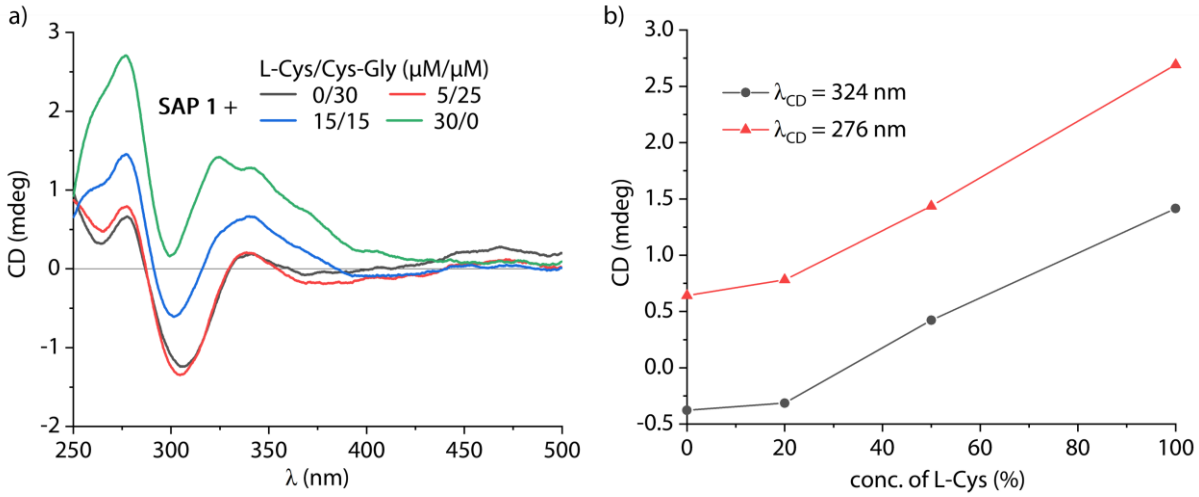

Figure 4.9. a) CD spectra of SAP **1** (30 μM) upon reaction with a series of L-Cys and Cys-Gly mixtures at the same total concentration (30 μM) but with different ratios of two components in $NaHCO_3$ buffer (25 mM, pH 9.5) with 0.9 mM CTAB. The spectra were recorded after the reaction reached an apparent equilibrium state (~ 3 h) at 25 °C. b) Intensity changes of the Cotton effect at 324 nm (black curve) and 276 nm (red curve) with different ratios of Cys in the mixtures.

The chirality sensing performance of the proposed SAP concept is displayed in the following perspectives: *i*) all six different chiral thiol-containing metabolites can be identified; *ii*) the quantitation of the *ee* value and the absolute concentration of each enantiomer component were achieved by employing both absorbance and CD response of the system; *iii*) because of the co-assembly nature of the SAP assay, not only the racemic mixtures could be differentiated from their pure enantiomers, but also the structural similar analytes mixture pairs, *e.g.*, L-Cys and Cys-Gly, could be differential from their corresponding single component. It is worth noting that all the above-mentioned chiral thiol analyses were performed in aqueous media by simply mixing the solution of SAP and target analytes at a micromolar concentration range. It overcame the shortcomings of the previously reported chirality sensing systems: where the reaction of the probe and analyte needed to be conducted in a pure organic solvent first; then, the reaction mixture was diluted to the proper concentration for further spectroscopic characterization.

4.3.3 Out-of-equilibrium features of SAP systems

As discussed in **Chapter 3**, the SAP concept is a time- and spectra-resolved process because both covalent reactions between the probe and target analyte and non-covalent interactions between the adjacent probe-analyte conjugate molecules are involved in the analyte targeting. As a consequence, not only limited to the equilibrium state, more information was expected if monitoring the self-assembly process with spectroscopic techniques. With the help of several kinetics studies, including the CD interval and temperature-dependent kinetics measurements, the out-of-equilibrium feature of the SAP system was clearly seen.

4.3.3.1 Chirality conversion during the self-assembly process

The strong Cotton effect response of the system originated from the chiral self-assembling of the SAP-analyte conjugate, and therefore, the CD spectra interval measurement was employed to explore the whole self-assembly process. The measurement was started to record the CD spectrum of the solution of SAP **1** (50 µM) alone in the $NaHCO_3$ buffer (25 mM, pH 9.5) with 0.9 mM CTAB at 25 °C. After the first spectrum recording, a 50 µM solution of L-Cys was flash injected into the SAP **1** solution to initiate the reaction. 21 spectra were recorded in total, and the time interval between each spectrum was ~ 7 minutes.

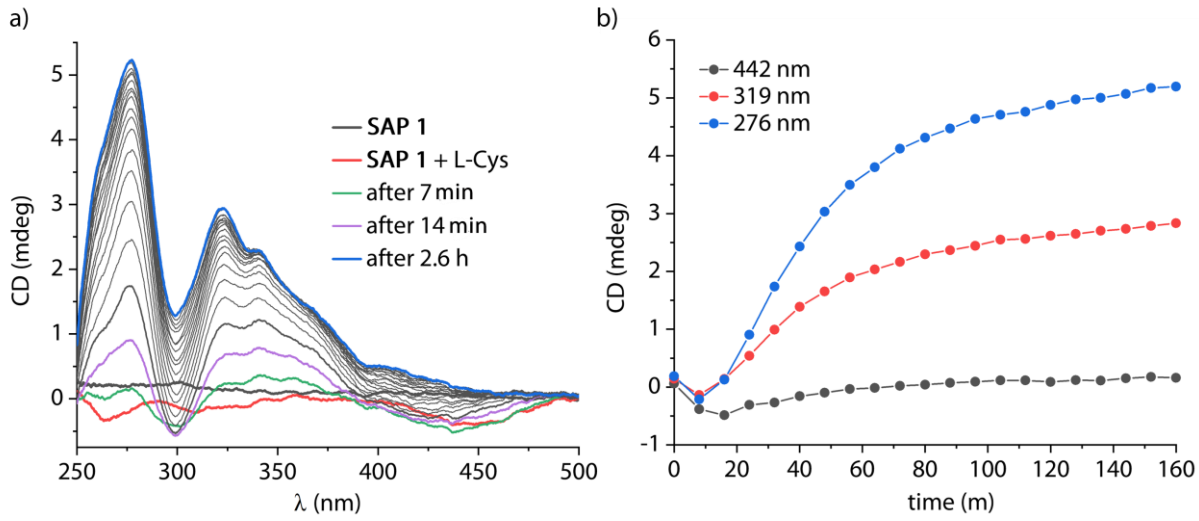

Figure 4.10. a) CD spectrogram evolution for the reaction of SAP **1** (50 µM) with L-Cys (50 µM) in $NaHCO_3$ buffer (25 mM, pH 9.5) with 0.9 mM CTAB. The time interval between each spectrum is 7 min, and the total measuring time is 2.5 h. b) Changes in the CD intensity at 276 nm (blue curve), 319 nm (red curve), and 442 nm (black curve) during the course of the reaction at 25 °C.

As depicted in **Figure 4.10**a, at first glance, it was not surprising that the Cotton effect response gradually appeared to cover the wavelength range of 250-500 nm after the reaction initiation. However, an unexpected behavior was found if one took a closer look at the time-dependent

curves. Upon the flash injection of the L-Cys solution, negative CD signals were firstly observed within an assay time of 7 min (red, green, and purple curves in **Figure 4.10**a), then the CD response changed to positive values over time. This switching behavior between the negative and positive CD values was more obvious by monitoring the CD intensity at the single wavelength, see **Figure 4.10**b. The aggregates of SAP-Cys conjugate showed a negative Cotton effect within the first 20 minutes. Then, the aggregates switched their polymerization to the opposite direction (positive response) and reached an apparent equilibrium at around 160 minutes. It indicated that the chirality of the conjugate aggregates was changed, and the intermediate state existed during the whole polymerization process.

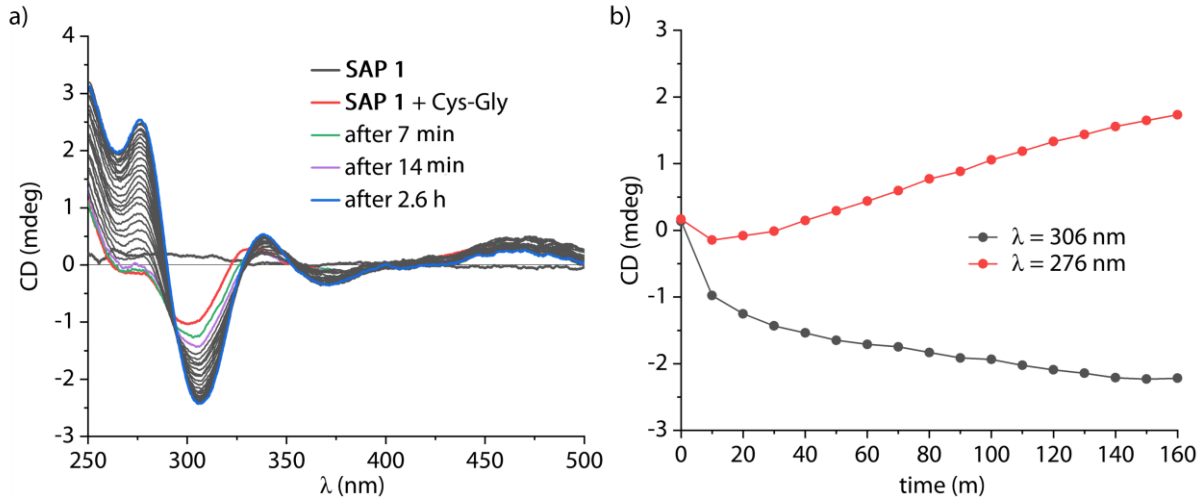

Figure 4.11. a) CD spectrogram evolution for the reaction of SAP **1** (50 µM) with Cys-Gly (50 µM) in $NaHCO_3$ buffer (25 mM, pH 9.5) with 0.9 mM CTAB. The time interval between each spectrum is 7 min, and the total measuring time is 2.5 h. b) Changes in the CD intensity at 306 nm (red curve) and 276 nm (black curve) during the course of the reaction at 25 °C.

Likewise, the same studies were carried out with other representative chiral thiol-containing metabolites, *e.g.*, L-Hcys, Cys-Gly, and D-Pen. Even surprisingly, the aggregation of the SAP-analyte conjugates was strongly dependent on the analyte's structure, which reflected the supramolecular nature of the assay again. As shown in **Figure 4.11**, only the conjugate of SAP-Cys-Gly displays the slight chirality switching behavior same as the L-Cys analyte, while only the CD spectra evolution was seen in the L-Hcys and D-Pen analytes system without the chirality conversion (**Figure 4.12**).

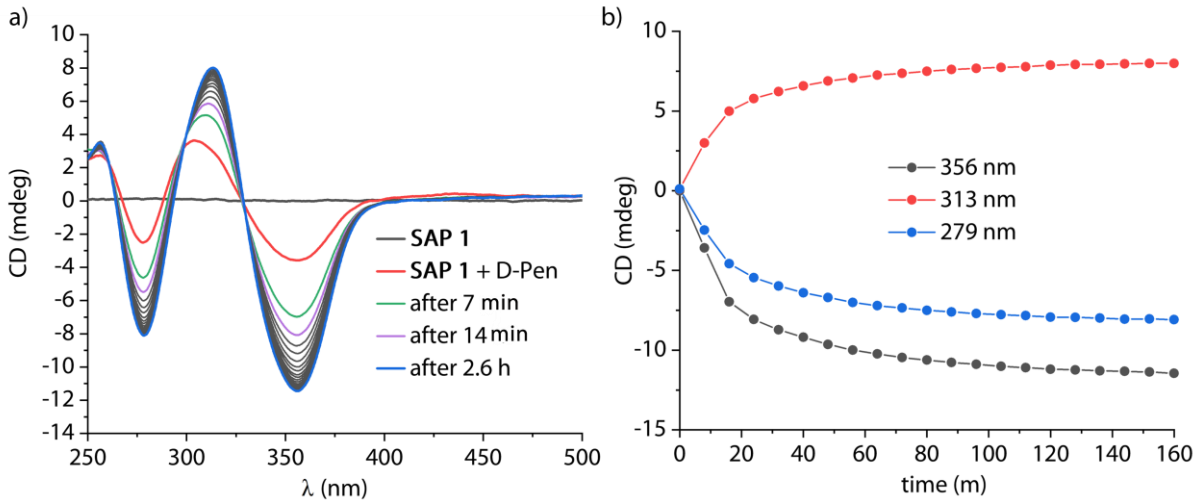

Figure 4.12. a) CD spectrogram evolution for the reaction of SAP **1** (50 µM) with D-Pen (50 µM) in $NaHCO_3$ buffer (25 mM, pH 9.5) with 0.9 mM CTAB. The time interval between each spectrum is 7 min, and the total measuring time is 2.5 h. b) Changes in the CD intensity at 356 nm (black curve), 313 nm (red curve), and 276 nm (blue curve) during the course of the reaction at 25 °C.

4.3.3.2 Temperature dependency study

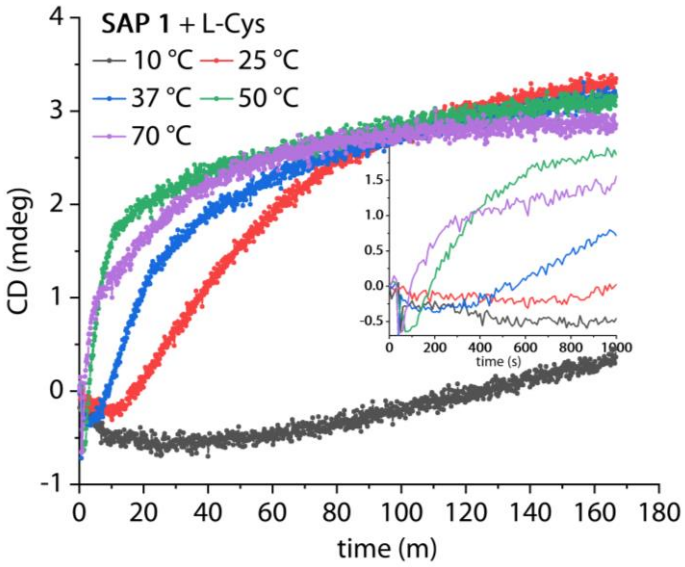

Figure 4.13. CD (λ_{CD} = 280 nm) kinetic traces of the reaction of SAP **1** with L-Cys in $NaHCO_3$ buffer (25 mM, pH 9.5) at different temperatures, 10 °C (black curve), 25 °C (red curve), 37 °C (blue curve), 50 °C (green curve), and 70 °C (purple curve). Insert shows the zoomed graph of the kinetic curves within the first 1000 s.

The behavior of the supramolecular interaction-based system is strongly dependent on the environment changes, *e.g.*, temperature. Therefore, the CD intensity changes at 280 nm of the SAP assay were monitored at different temperatures. As depicted in **Figure 4.13**, firstly, the reaction at above 25 °C, *i.e.*, 25 °C, 37 °C, 50 °C, and 70 °C, took almost the same time to reach the apparent equilibrium state. Secondly, with the temperature increasing, the Cotton effect response of the SAP-L-Cys system rapidly vanished within the first ~ 20 minutes, including the

chirality conversion, but then slowly reached the metastable state. Thirdly, when demonstrating the reaction of SAP **1** with L-Cys at an even lower temperature of 10 °C, the chirality switch process was slowed down, and the intermediate species were captured for a very long time. This low-temperature CD result was in good agreement with the absorbance spectrogram of the conjugation of SAP **1** with L-Cys at 10 °C, in which the conjugate was stabled within ~ 40 min after the reaction initiation (**Figure 4.14**).

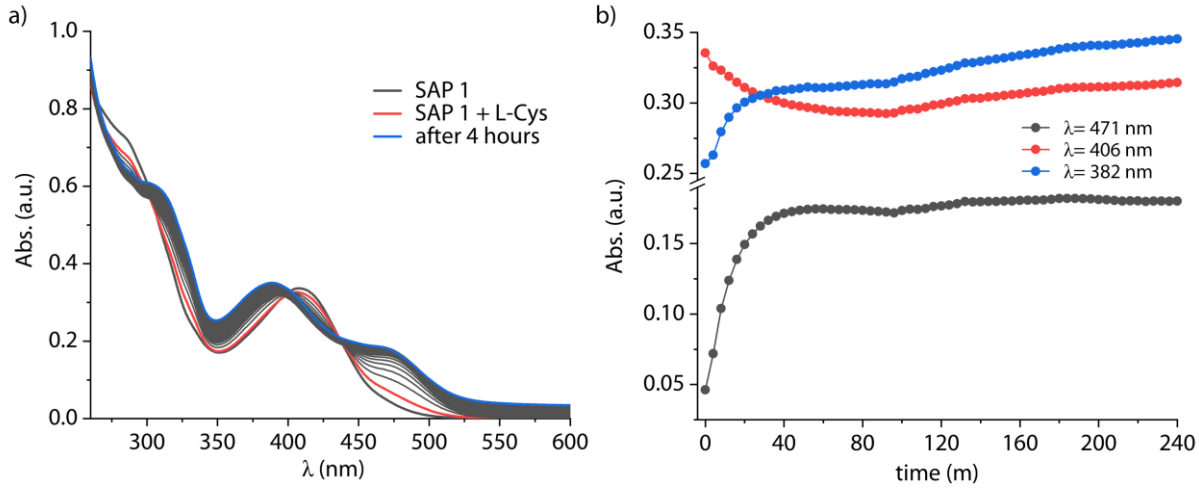

Figure 4.14. a) Absorbance spectra evolution for the reaction of SAP **1** (50 µM) with L-Cys (50 µM) in $NaHCO_3$ buffer (25 mM, pH 9.5) with 0.9 mM CTAB at 10 °C. The interval time between each spectrum is 86 s, and the total measuring time is 4 h. b) The changes in the absorbance intensity at 471 nm (black curve), 406 nm (red curve), and 382 nm (blue curve) during the course of the reaction.

Therefore, the CD kinetics studies provided complimentary proof for the aforementioned reaction mechanism of the SAP assay. Concretely, the thiol-containing analytes first coordinated with the transition metal complexes through the fast ligand exchange reaction. Initially, the formed SAP-analyte conjugates displayed the chiral signal because of the electron coupling between the analyte-metal center and the metal-metal center. Subsqentenly, the SAP-analyte conjugates started to re-organized their structure driven by the non-covalent metal···metal interactions between the neighboring conjugates molecules. Finally, the ordered chiral aggregate structure formed with the opposite handedness of the initial chiral structure.

4.3.3.3 Temperature cycling study

The temperature ramping- and cooling experiments were carried out to gain deep insight into the supramolecular polymerization of the SAP-analyte conjugates. The reaction was conducted at 25 °C by simply mixing a 50 µM solution of SAP **1** with a 50 µM solution of L-Cys in $NaHCO_3$ buffer (25 mM, 0.9 mM CTAB containing, pH 9.5), and the solution of the mixture was kept for 4 h to reach the equilibrium for the conjugates. Then, the CD spectrogram of SAP-

Cys solution was recorded from 25 °C to 90 °C, and to 25 °C, with a temperature step of 5 °C. The solution was kept at each target temperature for 5 min for equilibration.

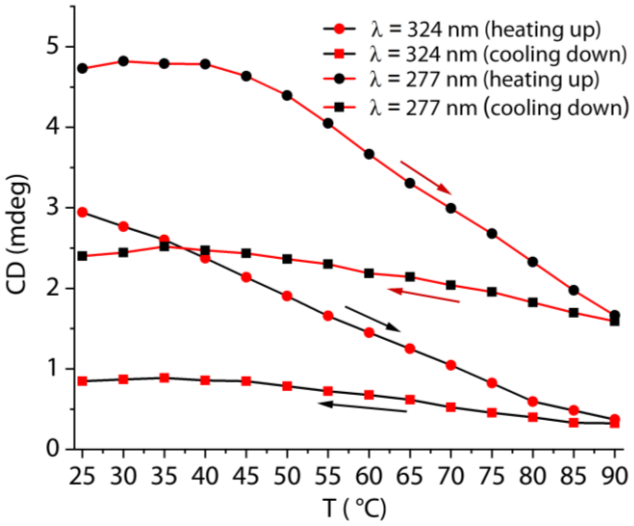

Figure 4.15. The changes in the CD intensity at 324 nm and 277 nm for the reaction of SAP **1** with L-Cys in $NaHCO_3$ buffer (25 mM, pH 9.5) with 0.9 mM CTAB at different temperatures.

As shown in **Figure 4.15**, the CD intensity of the conjugate-aggregates was decreased during the heating up process, which was reasonable since the high temperature speeded up the movement of the molecules within the system, resulting in the disassembly of the chiral aggregates. While in the cooling down process, the CD intensity was just slightly increased, suggesting the re-aggregation occurred but in a different pathway because the CD spectra were completely different from that in the heating up process. Therefore, the CD spectra at 25 °C in the initial and final states are different, although the temperature is the same (**Figure 4.16**). It indicated that the aggregation process of the SAP-analyte conjugates was not a thermodynamic equilibrate system but rather to be considered as an out-of-equilibrium system. The same study was carried out for another model analyte, Cys-Gly, and the result was in the additional data at the end of this chapter.

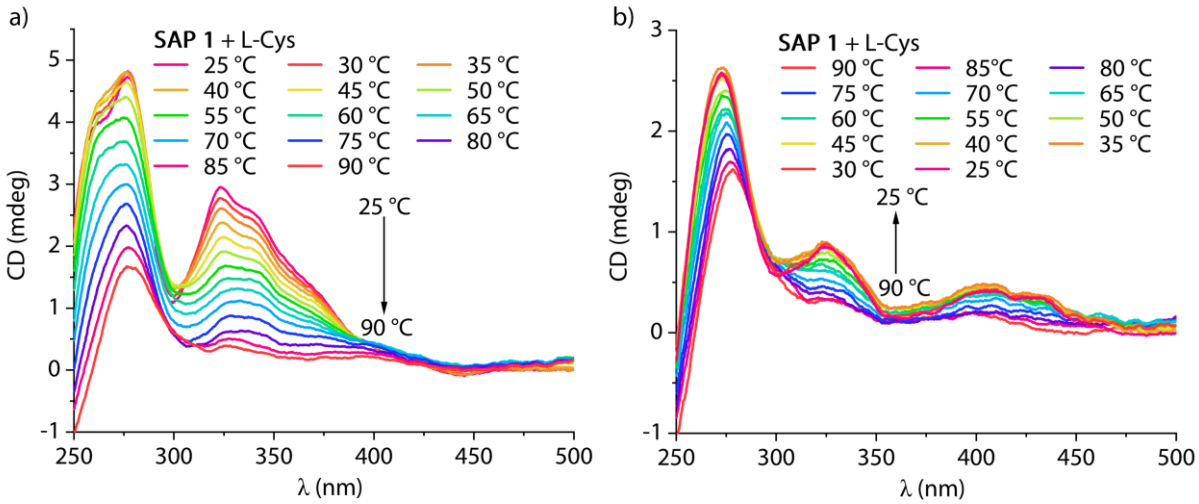

Figure 4.16. CD spectra of the SAP-L-Cys conjugates in $NaHCO_3$ buffer (25 mM, pH 9.5) with 0.9 mM CTAB at different temperatures. a) The temperature was increased from 25 °C to 90 °C, b) the temperature was decreased from 90 °C to 25 °C. The temperature interval between each spectrum was 5 °C. The solution was kept for 5 min at each temperature to reach equilibrium.

4.4 Conclusions

In conclusion, the chirality sensing of the SAP assay was explored in this chapter. Based on metallorganic self-assembling probes (SAPs), micromolar concentrations of water-soluble chiral biothiols, *e.g.*, L-Cys, L-Hcys, Cys-Gly, were targeted through Circular Dichroism (CD) and UV/vis in the preferred near UV or visible range. By using merely one unselective thiol-reactive SAP, six structurally similar thiols (and their enantiomers) are for the first time distinguishable from each other through emerging indicative chiroptical fingerprints. The SAP assay is also adaptable for *ee* value determination of chiral analytes and can be applied to mixtures. Stunningly, racemates can be distinguished from enantiomerically pure compounds even *via* non-chiral spectroscopy, *e.g.*, absorbance, emission, or DLS.

Besides the chirality sensing performance, this chapter is an extension of the previous study. The in-deep exploration of the supramolecular self-assembling process, by employing kinetics and temperature studies, reveals the out-of-equilibrium nature of the system. The chiral-to-chiral switching behavior was clearly observed, and the intermediate species could be captured for several hours by reducing the reaction temperature. This square planar transition metal-based self-assembling probes (SAPs) system provides a simple model for a further and deep understanding of the out-of-equilibrium system. Moreover, this SAP assay-based chirality sensing system bridges the fundamental study to the applicable practical chemistry, which may open a new insight for the practical application of those supramolecular polymerization systems.

Experimental information

Additional data

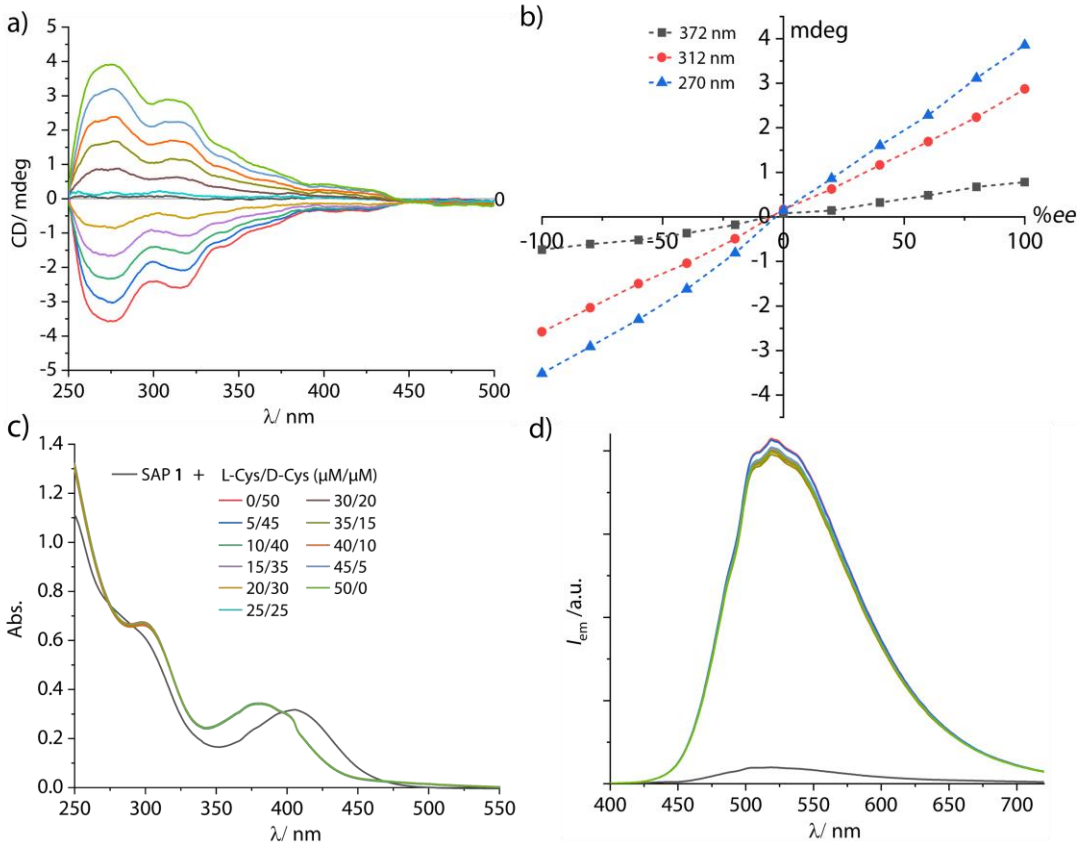

Figure 4.17. a) CD spectra of SAP **1** (50 μM) upon addition of a series of racemic mixtures of L-Cys (50 μM), the ratio of L-Cys to D-Cys varies from 0/50 to 50/0. b) Intensity changes of the CD signals at 372 nm (black dashed curve), 312 nm (red dashed curve), and 270 nm (blue dashed curve) with different *ee* values of L-Cys mixtures. The solid lines in each curve were obtained from the linear fitting function by the Origin software. c-d) The corresponding absorbance (c) and emission (d, λ_{ex} = 380 nm) spectra of the samples in figure a). All the spectra were recorded after the reaction reached an apparent equilibrium state (~ 3 h) in $NaHCO_3$ buffer (25 mM, pH 9.5) with 0.9 mM CTAB at 25 °C.

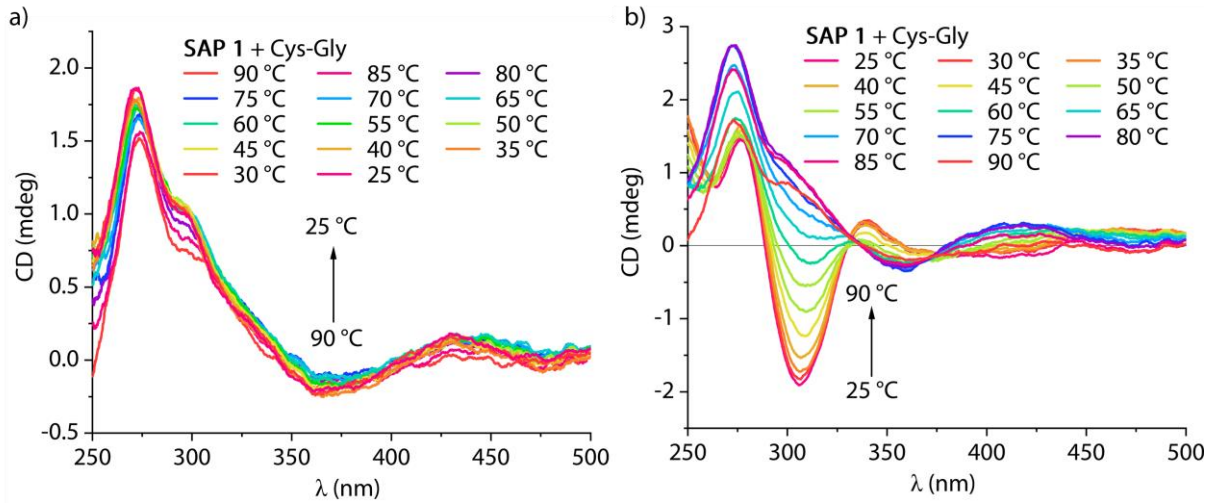

Figure 4.18. CD spectra of the SAP-Cys-Gly conjugates in $NaHCO_3$ buffer (25 mM, pH 9.5) with 0.9 mM CTAB at different temperatures. a) The temperature was increased from 25 °C to 90 °C, b) the temperature was decreased from 90 °C to 25 °C. The temperature interval between each spectrum was 5 °C. The solution was kept for 5 min at each temperature to reach equilibrium.

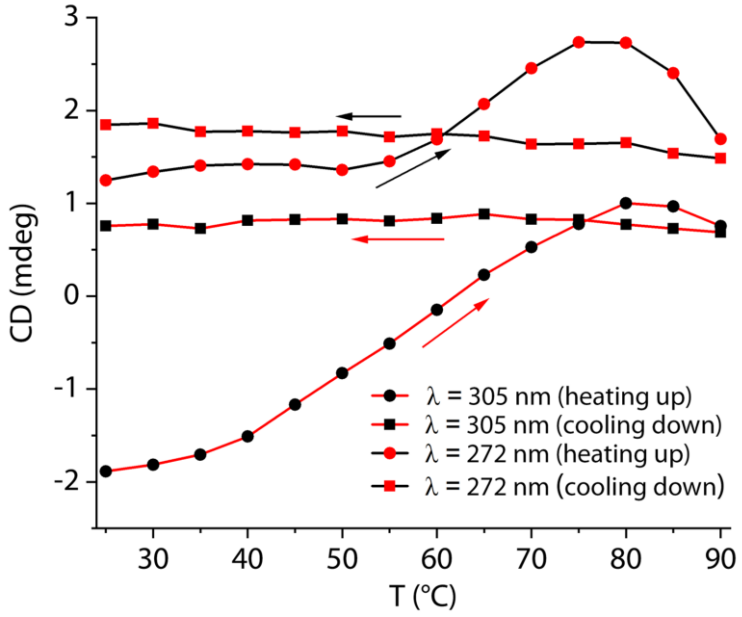

Figure 4.19. The changes in the CD intensity at 324 nm and 277 nm for the reaction of SAP **1** with L-Cys in $NaHCO_3$ buffer (25 mM, pH 9.5) with 0.9 mM CTAB at different temperatures.

5 Concluding remarks and outlook

The main achievement of this thesis is the development of the self-assembling probe (SAP) sensing concept by merging non-covalent metallophilic interactions and covalent molecular reactions. The covalent reaction between SAP and target analyte not only ensures high sensitivity but also enriches the targeting fields. Simultaneously, the analyte-indicative time- and spectra-resolved signals caused by the self-assembly of the SAP-analyte conjugates are observed and used to identify and quantify the analyte. With this novel molecular sensing concept, both high-selectivity and high-binding affinity can be achieved in one probe, and structurally similar biomolecules, *e.g.*, thiols, can be identified and quantified in aqueous media merely using one SAP.

Based on in-depth research work, square-planar Pt(II) complexes are used for the construction of SAPs by introducing a labile ligand that can be readily displaced in the presence of target analytes. Biological thiols are popular targets for developing reactive molecular probes and have been suggested to play critical roles in various physiological functions and pathological conditions due to their chemical reactivity and reducing properties. For instance, altered levels of thiols in intra- and extracellular fluids have been associated with several human diseases, such as leukocyte loss, liver damage, Alzheimer's disease, and HIV. Therefore, the thiol-containing analytes are used to evaluate the sensing performance of SAPs.

After a detailed and careful exploration, the possible sensing mechanism is proposed as follows (**Figure 5.1**): *i*) After assay initiation, SAP quickly exchanges its HINA ligand for the stronger binding biothiol. The observed spectral changes are caused by the Pt-thiol conjugate formation and HINA release. *ii*) In a slower subsequent process, the SAP-analyte conjugate readjusts its supramolecular aggregation structure. As a result, an alteration of the metal-metal-ligand charge transfer (MMLCT) occurs, which is sensitively controlled by the intermolecular distance and orientation between the metal centers of SAP. This process manifests through notable changes in the absorbance spectra and passes through intermediate states. *iii*) Finally, a kinetically stable state is reached after several hours.

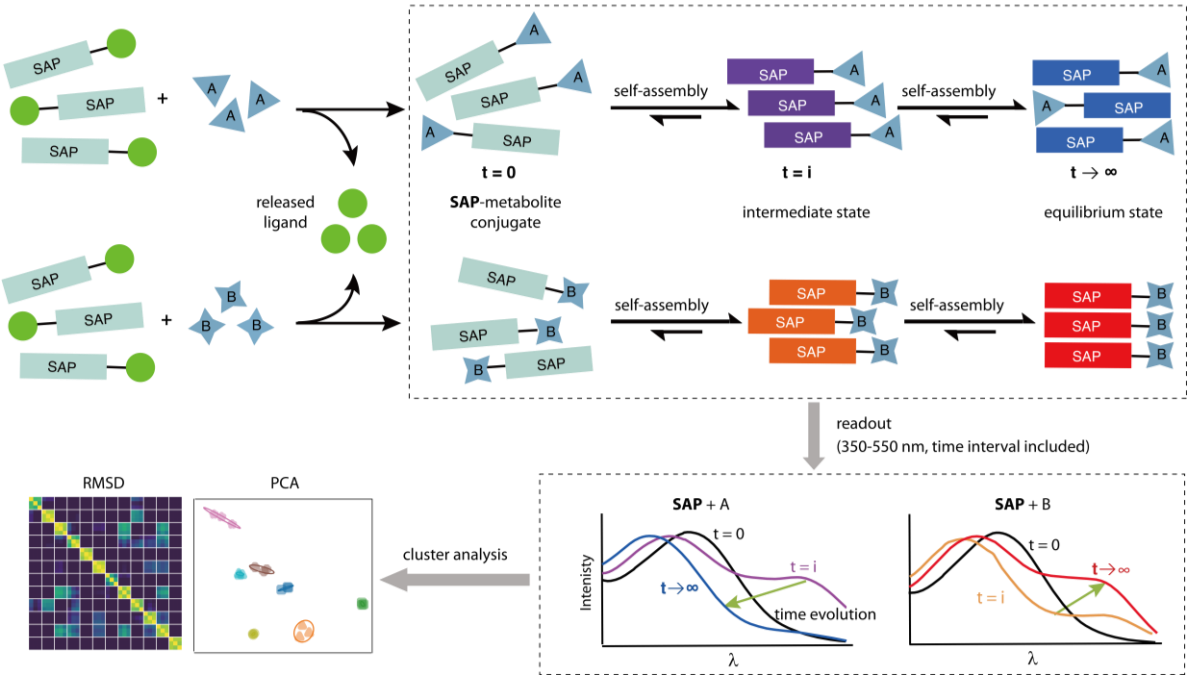

Figure 5.1. Schematic representation of the proposed time- and spectra-resolved molecular sensing concept utilizing SAPs. Firstly, SAPs unselectively bind the analyte through a metal-ligand exchange reaction. Subsequently, the formed SAP-analyte conjugate readjusts its structural assembly, resulting in altered electronic couplings between the chromophores. Thus, yielding an information-rich evolution of the absorbance spectra over time. The analyte is then distinguished and visualized by machine learning-based data analysis.

With this molecular sensing concept, 13 thiol-containing metabolites and drugs, and even thiol mixtures, were successfully distinguished in aqueous media by merely using one SAP. Furthermore, the sensing performance of SAP in human biofluids, *e.g.*, urine and serum, was evaluated in an exploratory manner, and up to five different spiked thiols can be distinguished from each other, which exhibits the substantial potential of SAP for further molecular diagnostics in biofluids.

Additional spectroscopic studies on the reaction mechanism revealed that analyte-indicative information is caused by the supramolecular polymerization of the SAP-analyte conjugate. The SAP can thus be used for chirality sensing, *i.e.*, determination of the absolute configuration, *ee* values, and total concentrations. This is showcased for six structural similar thiol metabolites, which triggered as chiral analytes the chiral supramolecular polymerization of the SAP-analyte conjugates (**Figure 5.2**). Furthermore, the supramolecular self-assembly of the SAP-analyte conjugates is an out-of-equilibrium system. The intermediate transition species are obtained by lowering the reaction temperature, and the chiral-to-chiral switching behavior is observed during the whole polymerization process.

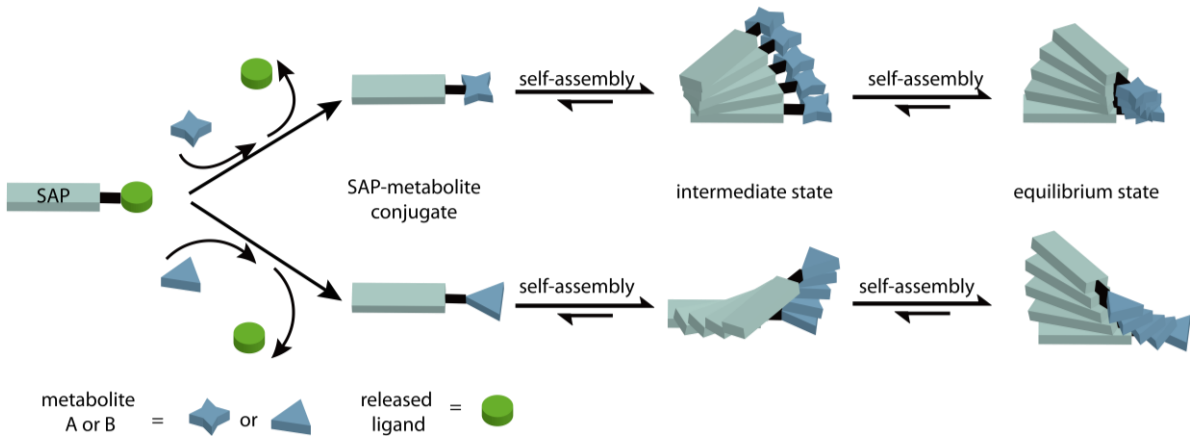

Figure 5.2. Schematic representation of the chirality sensing *via* "self-assembling probes (SAPs)." The SAPs first react with thiols through a fast ligand exchange reaction resulting in an emissive indicator (HINA) releasing. The observed SAP-thiol conjugate is then generally assembled into chiral aggregates over time, providing analyte-indicative UV/vis and CD spectroscopic information for the analyte identification and differentiation.

In fact, because of the coordinate reactivity of the transition metal center, other chemically reactive entities can be introduced to the SAP framework to enrich the analyte fields, *e.g.*, amino acids, amines, or carbohydrates. In addition, the construction of SAP is not only limited to square planar transition metal complexes, *i.e.*, Pt(II) and Pd(II); other chromophores or fluorophores with the self-assembling feature can also be taken into consideration in the SAP design. The remarkable contribution of the SAP concept is to provide a new idea that non-covalent interactions and covalent reactions can cooperate to reach a good balance of high-binding affinity and high-selectivity of the sensing system during the analyte targeting. As complementary, the SAP concept enriches the fundamental research on self-assembly, dynamic constitutional chemistry, structural evolution, and out-of-equilibrium processes, pushing a further step of supramolecular chemistry in practical application fields, *e.g.*, molecular diagnostics. Besides, the SAP system can indicate the supramolecular polymerization process in real-time by monitoring the spectroscopic changes, *i.e.*, absorbance and CD spectra, which provides a simple test case for the in-depth understanding of out-of-equilibrium systems.

In parallel to the SAP molecular sensing concept development, 3-hydroxy-isonicotinic aldehyde (HINA, **Figure 5.3**) is surprisingly found as the smallest green-emissive (128 g/mol, λ_{em} = 525 nm) fluorophore, with excellent water solubility and respectable quantum yield (15 %). Uniquely, HINA occurs in three different protonated states, and each of them is distinctly fluorescent. The commercial availability of HINA and its favorable photophysical properties (large Stokes shift and pH-dependent ratiometric emission properties) enable its application ranging from use as a fluorescent dye to function as an indicator dye in supramolecular assays.

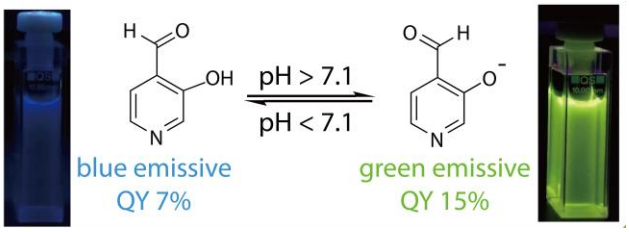

Figure 5.3. Schematic representation of the deprotonation equilibria of HINA in aqueous media and the photo imagings of the corresponding solution.

In the theoretical field, HINA also provides an excellent test case to evaluate theoretical predictions of emission spectra using highly advanced computational methods capable of considering both vibronic effects and excited-state intramolecular proton-transfer process (ESIPT). With the participation of organic chemists, fluoro-substituted HINA derivatives are synthesized. The following study will concentrate on the exploration of the emissive mechanism of these hydroxyl-functional pyridine-aldehydes and pyridine-ketones. Based on these studies, a series of small fluorophores with outstanding photophysical properties such as very high quantum yields will be developed.

6 Instrumentation information

Absorbance spectroscopy

Absorption spectra were measured with a JASCO V730 double-beam UV/Vis spectrometer and baseline-corrected.

Fluorescence spectroscopy

Steady-state emission spectra and time-resolved emission profiles were recorded on a JASCO FP-8300 fluorescence spectrometer equipped with a 450 W xenon arc lamp, double-grating excitation, and emission monochromators. Emission spectra were corrected with source intensity (lamp and grating) and the emission spectral response (detector and grating) by standard correction curves. Time-resolved measurements were recorded with a Horiba Jobin-Yvon IBH FL-322 Fluorolog 3 spectrometer using the time-correlated single-photon counting (TCSPC) electronics FluoroHub. A pulsed laser diode LDH-P-C-373 (λ = 373 nm, pulse duration 1.2 ns, max repetition rate 1 MHz) and LDH-P-C-255 (λ = 255 nm, pulse duration < 1.2 ns, max repetition rate 1 MHz) was used to excite the sample and mounted directly on the sample chamber at 908. The photons were collected using a TBX picosecond photon detection module single-photon-counting detector. The data was acquired using the commercially available software DataStation (Horiba Jobin-Yvon), whereas data analysis was performed using the commercially available software DAS56 (Horiba Jobin-Yvon). Quantum yield measurements were performed with Fluorolog-3 spectrofluorometer with a Quanta-φ integrating sphere as an accessory attached. The data was acquired by the commercially available software FluorEssence^{TM} (Horiba Jobin-Yvon) version 3.5.

Circular Dichroism (CD) spectroscopy

All CD spectra were recorded on a JASCO J-1500 spectrometer equipped with a Peltier-thermostated cell holder and a standard photomultiplier tube (PMT) detector. The HT voltage applied to the PMT detector was kept in auto mode during all the measurements. Blank measurements of MilliQ water or the used buffer solution provided no CD signals in the regions examined. All CD spectra reported are baseline corrected for the corresponding used solvent system.

Plate reader

The high-throughput screening measurements were recorded in CLARIOstar Plus (BMG Labtech) plate reader equipped with an ultra-fast UV-vis spectrometer and a dispenser.

Dynamic light scattering (DLS)

DLS measurements were performed using a Malvern ZetaSizer nano-instrument. The intensity of the scattered light was measured at a fixed angle (173°), while the laser light wavelength for the scattering experiments was 633 nm. Data analysis was performed according to standard procedures using Malvern software. Briefly, the decay rates were determined by the following relationship, where η is the viscosity of the medium (water), D_h is the hydrodynamic diameter, and θ is the scattering angle.

$$\Gamma = D_h \cdot \left(\frac{4\pi\eta}{\lambda} \cdot \sin\left(\frac{\theta}{2}\right)\right)^2$$

To fit the autocorrelation function, the non-negatively constrained least squares (NNLS) algorithm built into the software was used, which allows the determination of the diffusion coefficient (d), from which the hydrodynamic diameter of the particles is calculated using the Stokes-Einstein equation (see below), where k_b is the Boltzmann constant, T is the temperature, and η is the viscosity of the medium (water).

$$D_h = \frac{k_b \cdot T}{6\,\pi \cdot \eta \cdot d}$$

In some cases, the intensity distribution thus derived was recalculated as a volume distribution (or number-weighted distribution) by the Mie theory based-algorithm built into the software.

Cuvettes and microwell plates

All cuvettes used in the aqueous media-based spectroscopic measurements (absorbance and emission spectra) were UV transparent disposable cuvettes from Brand GmhH with a diameter of 10 mm and a wavelength cut off at 220 nm. All CD spectra and organic phase-based spectroscopic measurements were recorded with Suprasil (type 111-QS) quartz emission cuvettes with a light path length of 10 mm, and dimensions of 10x10 mm from Hellma-Analytics.

All microwell-based measurements were performed in black bottom transparent IsoPlate™-96 polystyrene microplates supplied by PerkinElmer.

pH meter

All the pH values of the solutions were recorded with a FiveEasy (Mettler Toledo) pH meter F20 at 25 °C.

Nuclear magnetic resonance (NMR) spectroscopy

NMR spectra were recorded at room temperature in the deuterated solvent with a Bruker Advanced 500 (^{1}H NMR: 500 MHz; ^{13}C NMR: 126 MHz; ^{19}F NMR: 470 MHz). The chemical shift δ is expressed in parts per million (ppm). The multiplicities of the signals were abbreviated as follows: s = singlet, d = doublet, t = triplet, quart = quartet, quin = quintet, m = multiplet. All coupling constants (*J*) are stated as modulus in Hertz (Hz).

Electrospray ionization mass spectrometry (ESI-MS)

ESI-MS measurements were carried out with a Brucker microOTOF-Q (208-320 Vac, 50/60 Hz, 1800 VA) mass spectrometer equipped with an online nanoelectrospray ion source. The spectra were interpreted by molecular peaks $[M]^{n+}$, peaks of deprotonated molecules $[M-H]^{n-}$, peaks of protonated molecules $[M+H]^{n+}$, and characteristic fragment peaks and indicated with their mas-to-charge ratio (m/z).

High-performance liquid chromatography (HPLC)

HPLC experiments were performed on an LC-2000Plus HPLC system equipped with a UV2075 detector and a Kromasil 100 C 18 5 μM LC column (250 × 4.6 mm, Agela) at a flow rate of 0.8 mL/min. The sample was dissolved in water at a concentration of 1.5 mg/mL.

7 List of abbreviations

ACN	acetonitrile
AIE	aggregation-induced emission
ABA	associative binding assay
ADA	analyte displacement assay
CB7	cucurbit[7]uril
CX4	*p*-sulfonatocalix[4]arene
CD	circular dichroism
CDC	constitutional dynamic chemistry
CP	captopril
CTAB	hexadecyltrimethylammonium bromide
CPC	cetylpyridinium chloride
CMC	critical micelle concentration
Cys-Gly	cysteinglycine
DSSCs	dye-sensitized solar cells
DPA	dipicolylamine
DMAC	4-(dimethylamino)cinnamaldehyde
DBA	direct binding assay
DBO	2,3-diazabicyclo[2.2.2]oct-2-ene
DMSO	dimethyl sulfoxide
DMABN	4-(dimethylamino)benzonitrile
DLS	dynamic light scattering
DFT	density functional theory
D_2O	deuterium oxide
D-Pen	D-penicillamine

DCM	dichloromethane
ee	enantiomeric excess
eIDA	enantioselective indicator displacement assay
EG	ethylene glycol
ESI-MS	electrospray ionization mass spectrometry
ESIPT	excited-state intramolecular proton transfer
GSH	glutathione
HOMO	highest occupied molecular orbital
HTS	high-throughput screening
HINA	3-hydroxy-isonicotinic aldehyde
HPA	3-hydroxy-picolin aldehyde
HAP	3-hydroxy-4-acetyl pyridine
HFP	1,1,1,3,3,3-hexafluoro-2-propanol
HPLC	high-performance liquid chromatography
IC	internal conversion
ISC	intersystem crossing
IR	infrared
ICT	intermolecular charge transfer
IDA	indicator displacement assay
ICD	induced circular dichroism
LUMO	lowest unoccupied molecular orbital
LEECs	light-emitting electrochemical cells
LC	ligand-centered
LMCT	ligand-to-metal charge transfer
LMMCT	ligand-metal-metal charge transfer
L-Cys	L-cysteine

L-Hcys	L-homocysteine
L-Pen	L-penicillamine
LDA	linear discriminate analysis
MO	molecular orbital
MC	metal-centered
MLCT	metal-to-ligand charge transfer
MMLCT	metal-metal-to-ligand charge transfer
MeOH	methanol
MES	2-mercaptoethane sulfonic acid
MEA	mercaptoethylamine
MPs	molecular probes
NAC	*N*-acetyl-L-cysteine
NOL	non-linear optical
NBD	nitrobenzoxadiazole
NMR	nuclear magnetic resonance
NDI	naphthalene-diimides
OLEDs	organic light-emitting diodes
P123	PEG-PPG-PEG
PCA	principal components analysis
PET	photon electron transfer
PDI	perylene-bisdiimides
PTU	6-propyl-2-thiouracil
RMSD	root mean squared deviation
S_0	ground state
SOC	spin-orbit coupling
SCO	spin-cross over

SEM	scanning electronic microscopy
SA	salicylaldehyde
SAP	self-assembling probe
SAP 1	Pt-HINA
SAP 2	Pd-HINA
SDS	sodium dodecyl sulfate
TGA	thioglycolic acid
TP	tiopronin
TG	6-thioguanine
THF	tetrahydrofuran
TLC	thin-layer chromatography
T	triplet excited state
TEM	transmission electron microscopy
TMC	transition metal complex
UV	ultraviolet
VR	vibrational relaxation
vis	visible
7AI	7-azaindole
Δε	molar circular dichroism
τ	lifetime
Φ	quantum yield
©	copyright

8 References

1. Braslavsky, S. E., Glossary of Terms Used in Photochemistry, 3rd Edition (Iupac Recommendations 2006). *Pure Appl. Chem.* **2007**, *79* (3), 293-465.

2. Kartik N. Shinde, S. J. D., H. C. Swart, Kyeongsoon Park, Basic Mechanisms of Photoluminescence. In *Basic Mechanisms of Photoluminescence*, Springer Series in Materials Science: Vol. 174.

3. Prof. Dr. Bernard Valeur, P. M. N. B.-S., *Molecular Fluorescence: Principles and Applications*. Second Edition ed.; 2012.

4. Cui, Y.; Yue, Y.; Qian, G.; Chen, B., Luminescent Functional Metal-Organic Frameworks. *Chem. Rev.* **2012**, *112* (2), 1126-1162.

5. Duan, L.; Qiao, J.; Sun, Y.; Qiu, Y., Strategies to Design Bipolar Small Molecules for Oleds: Donor-Acceptor Structure and Non-Donor-Acceptor Structure. *Adv. Mater.* **2011**, *23* (9), 1137-1144.

6. Li, X.; Gao, X.; Shi, W.; Ma, H., Design Strategies for Water-Soluble Small Molecular Chromogenic and Fluorogenic Probes. *Chem. Rev.* **2014**, *114* (1), 590-659.

7. Loudet, A.; Burgess, K., Bodipy Dyes and Their Derivatives: Syntheses and Spectroscopic Properties. *Chem. Rev.* **2007**, *107* (11), 4891-932.

8. Krämer, J.; Kang, R.; Grimm, L. M.; De Cola, L.; Picchetti, P.; Biedermann, F., Molecular Probes, Chemosensors, and Nanosensors for Optical Detection of Biorelevant Molecules and Ions in Aqueous Media and Biofluids. *Chem. Rev.* **2022**, *122* (3), 3459-3636.

9. Mako, T. L.; Racicot, J. M.; Levine, M., Supramolecular Luminescent Sensors. *Chem. Rev.* **2019**, *119* (1), 322-477.

10. Sathyanarayana, D., *Electronic Absorption Spectroscopy and Related Techniques*. Universities Press: 2001.

11. Gispert, J. R., *Coordination Chemistry*. Wiley-VCH Weinheim: 2008; Vol. 483.

12. Mayerhöfer, T. G.; Pahlow, S.; Popp, J., The Bouguer-Beer-Lambert Law: Shining Light on the Obscure. *ChemPhysChem* **2020**, *21* (18), 2029-2046.

13. Lakowicz, J. R., *Principles of Fluorescence Spectroscopy*. Springer Science & Business Media: 2013.

14. Ballhausen, C.; Hansen, A. E., Electronic Spectra. *Annu. Rev. Phys. Chem.* **1972**, *23* (1), 15-38.

15. Bączyński, A.; Radomska, D., Electronic Spectra of Dye Solutions. I. The Mirror Image Rule. *J. Fluoresc.* **1992**, *2* (3), 175-180.

16. Yu, Z.; Hagfeldt, A.; Sun, L., The Application of Transition Metal Complexes in Hole-Transporting Layers for Perovskite Solar Cells: Recent Progress and Future Perspectives. *Coord. Chem. Rev.* **2020**, *406*, 213143.

17. Quintana, C.; Cifuentes, M. P.; Humphrey, M. G., Transition Metal Complex/Gold Nanoparticle Hybrid Materials. *Chem. Soc. Rev.* **2020**, *49* (8), 2316-2341.

18. Demas, J. N.; DeGraff, B. A., Applications of Luminescent Transition Platinum Group Metal Complexes to Sensor Technology and Molecular Probes. *Coord. Chem. Rev.* **2001**, *211* (1), 317-351.

19. Wang, X.-y.; Del Guerzo, A.; Schmehl, R. H., Photophysical Behavior of Transition Metal Complexes Having Interacting Ligand Localized and Metal-to-Ligand Charge Transfer States. *J. Photochem. Photobiol. C: Photochem. Rev.* **2004**, *5* (1), 55-77.

20. Ma, D.-L.; He, H.-Z.; Leung, K.-H.; Chan, D. S.-H.; Leung, C.-H., Bioactive Luminescent Transition-Metal Complexes for Biomedical Applications. *Angew. Chem. Int. Ed.* **2013**, *52* (30), 7666-7682.

21. Yam, V. W.-W.; Lo, K. K.-W., Recent Advances in Utilization of Transition Metal Complexes and Lanthanides as Diagnostic Tools. *Coord. Chem. Rev.* **1999**, *184* (1), 157-240.

22. Collman, J. P.; Boulatov, R., Heterodinuclear Transition-Metal Complexes with Multiple Metal-Metal Bonds. *Angew. Chem. Int. Ed.* **2002**, *41* (21), 3948-3961.

23. Yam, V. W.-W., Molecular Design of Transition Metal Alkynyl Complexes as Building Blocks for Luminescent Metal-Based Materials: Structural and Photophysical Aspects. *Acc. Chem. Res.* **2002**, *35* (7), 555-563.

24. Demas, J.; DeGraff, B., Design and Applications of Highly Luminescent Transition Metal Complexes. *Anal. Chem.* **1991**, *63* (17), 829A-837A.

25. Yam, V. W.-W.; Wong, K. M.-C., Luminescent Metal Complexes of d6, d8 and d10 Transition Metal Centres. *Chem. Commun.* **2011**, *47* (42), 11579-11592.

26. Daniel, C., Electronic Spectroscopy and Photoreactivity in Transition Metal Complexes. *Coord. Chem. Rev.* **2003**, *238-239*, 143-166.

27. Kirk, M. L.; Shultz, D. A., Transition Metal Complexes of Donor–Acceptor Biradicals. *Coord. Chem. Rev.* **2013**, *257* (1), 218-233.

28. Kalyanasundaram, K.; Grätzel, M., Applications of Functionalized Transition Metal Complexes in Photonic and Optoelectronic Devices. *Coord. Chem. Rev.* **1998**, *177* (1), 347-414.

29. Bizzarri, C.; Spuling, E.; Knoll, D. M.; Volz, D.; Bräse, S., Sustainable Metal Complexes for Organic Light-Emitting Diodes (Oleds). *Coord. Chem. Rev.* **2018**, *373*, 49-82.

30. Zhang, Q.-C.; Xiao, H.; Zhang, X.; Xu, L.-J.; Chen, Z.-N., Luminescent Oligonuclear Metal Complexes and the Use in Organic Light-Emitting Diodes. *Coord. Chem. Rev.* **2019**, *378*, 121-133.

31. Tang, M.-C.; Chan, M.-Y.; Yam, V. W.-W., Molecular Design of Luminescent Gold(III) Emitters as Thermally Evaporable and Solution-Processable Organic Light-Emitting Device (Oled) Materials. *Chem. Rev.* **2021**, *121* (13), 7249-7279.

32. Gong, J.; Sumathy, K.; Qiao, Q.; Zhou, Z., Review on Dye-Sensitized Solar Cells (Dsscs): Advanced Techniques and Research Trends. *Renew. Sust. Energ. Rev.* **2017**, *68*, 234-246.

33. Pashaei, B.; Shahroosvand, H.; Abbasi, P., Transition Metal Complex Redox Shuttles for Dye-Sensitized Solar Cells. *RSC Adv.* **2015**, *5* (115), 94814-94848.

34. Bignozzi, C. A.; Argazzi, R.; Boaretto, R.; Busatto, E.; Carli, S.; Ronconi, F.; Caramori, S., The Role of Transition Metal Complexes in Dye Sensitized Solar Devices. *Coord. Chem. Rev.* **2013**, *257* (9), 1472-1492.

35. Costa, R. D., *Light-Emitting Electrochemical Cells*. Springer Nature: 2017.

36. Costa, R. D.; Ortí, E.; Bolink, H. J., Recent Advances in Light-Emitting Electrochemical Cells. *Pure Appl. Chem.* **2011**, *83* (12), 2115-2128.

37. Costa, R. D.; Tordera, D.; Ortí, E.; Bolink, H. J.; Schönle, J.; Graber, S.; Housecroft, C. E.; Constable, E. C.; Zampese, J. A., Copper(I) Complexes for Sustainable Light-Emitting Electrochemical Cells. *J. Mater. Chem.* **2011**, *21* (40), 16108-16118.

38. Su, H.-C.; Hsu, J.-H., Improving the Carrier Balance of Light-Emitting Electrochemical Cells Based on Ionic Transition Metal Complexes. *Dalton Trans.* **2015**, *44* (18), 8330-8345.

39. Zhang, T.; Lin, W., Metal-Organic Frameworks for Artificial Photosynthesis and Photocatalysis. *Chem. Soc. Rev.* **2014**, *43* (16), 5982-5993.

40. Huo, J.; Zhang, Y.-B.; Zou, W.-Y.; Hu, X.; Deng, Q.; Chen, D., Mini-Review on an Engineering Approach Towards the Selection of Transition Metal Complex-Based Catalysts for Photocatalytic H2 Production. *Catal. Sci. Technol.* **2019**, *9* (11), 2716-2727.

41. McConnell, A. J.; Wood, C. S.; Neelakandan, P. P.; Nitschke, J. R., Stimuli-Responsive Metal-Ligand Assemblies. *Chem. Rev.* **2015**, *115* (15), 7729-7793.

42. Guo, Q.; Zhang, X., A Review of Mechanochromic Polymers and Composites: From Material Design Strategy to Advanced Electronics Application. *Compos. B. Eng.* **2021**, *227*, 109434.

43. Gounden, D.; Nombona, N.; van Zyl, W. E., Recent Advances in Phthalocyanines for Chemical Sensor, Non-Linear Optics (NLO) and Energy Storage Applications. *Coord. Chem. Rev.* **2020**, *420*, 213359.

44. Bodenthin, Y.; Schwarz, G.; Tomkowicz, Z.; Lommel, M.; Geue, T.; Haase, W.; Möhwald, H.; Pietsch, U.; Kurth, D. G., Spin-Crossover Phenomena in Extended Multi-Component Metallo-Supramolecular Assemblies. *Coord. Chem. Rev.* **2009**, *253* (19), 2414-2422.

45. Senthil Kumar, K.; Ruben, M., Emerging Trends in Spin Crossover (SCO) Based Functional Materials and Devices. *Coord. Chem. Rev.* **2017**, *346*, 176-205.

46. Higgins, B.; DeGraff, B. A.; Demas, J. N., Luminescent Transition Metal Complexes as Sensors: Structural Effects on Ph Response. *Inorg. Chem.* **2005**, *44* (19), 6662-6669.

47. Lo, K. K.-W.; Li, S. P.-Y., Utilization of the Photophysical and Photochemical Properties of Phosphorescent Transition Metal Complexes in the Development of Photofunctional Cellular Sensors, Imaging Reagents, and Cytotoxic Agents. *RSC Adv.* **2014**, *4* (21), 10560-10585.

48. Ko, C.-N.; Li, G.; Leung, C.-H.; Ma, D.-L., Dual Function Luminescent Transition Metal Complexes for Cancer Theranostics: The Combination of Diagnosis and Therapy. *Coord. Chem. Rev.* **2019**, *381*, 79-103.

49. Babu, E.; Bhuvaneswari, J.; Muthu Mareeswaran, P.; Thanasekaran, P.; Lee, H.-M.; Rajagopal, S., Transition Metal Complexes Based Aptamers as Optical Diagnostic Tools for Disease Proteins and Biomolecules. *Coord. Chem. Rev.* **2019**, *380*, 519-549.

50. HOUSECROFT, C. E.; SHARPE, A. A. G., *Inorganic Chemistry*. the fourth edition ed.; Pearson Education Limited: 2012.

51. Balzani, V.; Bergamini, G.; Campagna, S.; Puntoriero, F., Photochemistry and Photophysics of Coordination Compounds: Overview and General Concepts. In *Photochemistry and Photophysics of Coordination Compounds I*, Balzani, V.; Campagna, S., Eds. Springer Berlin Heidelberg: Berlin, Heidelberg, 2007; pp 1-36.

52. Sinn, S.; Schulze, B.; Friebe, C.; Brown, D. G.; Jäger, M.; Altuntaş, E.; Kübel, J.; Guntner, O.; Berlinguette, C. P.; Dietzek, B.; Schubert, U. S., Physicochemical Analysis of

Ruthenium(II) Sensitizers of 1,2,3-Triazole-Derived Mesoionic Carbene and Cyclometalating Ligands. *Inorg. Chem.* **2014**, *53* (4), 2083-2095.

53. Williams, J. A. G., Photochemistry and Photophysics of Coordination Compounds: Platinum. In *Photochemistry and Photophysics of Coordination Compounds II*, Balzani, V.; Campagna, S., Eds. Springer Berlin Heidelberg: Berlin, Heidelberg, 2007; pp 205-268.

54. Aliprandi, A.; Genovese, D.; Mauro, M.; Cola, L. D., Recent Advances in Phosphorescent Pt(II) Complexes Featuring Metallophilic Interactions: Properties and Applications. *Chem. Lett.* **2015**, *44* (9), 1152-1169.

55. Yam, V. W.-W.; Au, V. K.-M.; Leung, S. Y.-L., Light-Emitting Self-Assembled Materials Based on D8 and D10 Transition Metal Complexes. *Chem. Rev.* **2015**, *115* (15), 7589-7728.

56. Chaaban, M.; Zhou, C.; Lin, H.; Chyi, B.; Ma, B., Platinum(II) Binuclear Complexes: Molecular Structures, Photophysical Properties, and Applications. *J. Mater. Chem. C* **2019**, *7* (20), 5910-5924.

57. Fu, H. L.-K.; Yam, V. W.-W., Supramolecular Metallogels of Platinum(II) and Gold(Iii) Complexes. *Chem. Lett.* **2018**, *47* (5), 605-610.

58. Haque, A.; Xu, L.; Al-Balushi, R. A.; Al-Suti, M. K.; Ilmi, R.; Guo, Z.; Khan, M. S.; Wong, W.-Y.; Raithby, P. R., Cyclometallated Tridentate Platinum(II) Arylacetylide Complexes: Old Wine in New Bottles. *Chem. Soc. Rev.* **2019**, *48* (23), 5547-5563.

59. Li, K.; Ming Tong, G. S.; Wan, Q.; Cheng, G.; Tong, W.-Y.; Ang, W.-H.; Kwong, W.-L.; Che, C.-M., Highly Phosphorescent Platinum(II) Emitters: Photophysics, Materials and Biological Applications. *Chem. Sci.* **2016**, *7* (3), 1653-1673.

60. Yam, V. W.-W.; Law, A. S.-Y., Luminescent D8 Metal Complexes of Platinum(II) and Gold(III): From Photophysics to Photofunctional Materials and Probes. *Coord. Chem. Rev.* **2020**, *414*, 213298.

61. Po, C.; Tam, A. Y.; Wong, K. M.; Yam, V. W., Supramolecular Self-Assembly of Amphiphilic Anionic Platinum(II) Complexes: A Correlation between Spectroscopic and Morphological Properties. *J. Am. Chem. Soc.* **2011**, *133* (31), 12136-43.

62. Mauro, M.; Aliprandi, A.; Septiadi, D.; Kehr, N. S.; De Cola, L., When Self-Assembly Meets Biology: Luminescent Platinum Complexes for Imaging Applications. *Chem. Soc. Rev.* **2014**, *43* (12), 4144-4166.

63. Li, B.; Li, Y.; Chan, M. H.-Y.; Yam, V. W.-W., Phosphorescent Cyclometalated Platinum(II) Enantiomers with Circularly Polarized Luminescence Properties and Their Assembly Behaviors. *J. Am. Chem. Soc.* **2021**, *143* (51), 21676-21684.

64. Yam, V. W.-W.; Wong, K. M.-C.; Zhu, N., Solvent-Induced Aggregation through Metal···Metal/Π···Π Interactions: Large Solvatochromism of Luminescent Organoplatinum(II) Terpyridyl Complexes. *J. Am. Chem. Soc.* **2002**, *124* (23), 6506-6507.

65. Po, C.; Wing-Wah Yam, V., A Metallo-Amphiphile with Unusual Memory Behaviour: Effect of Temperature and Structure on the Self-Assembly of Triethylene Glycol (TEG)-Pendant Platinum(II) Bzimpy Complexes. *Chem. Sci.* **2014**, *5* (12), 4868-4872.

66. Au-Yeung, H.-L.; Leung, S. Y.-L.; Tam, A. Y.-Y.; Yam, V. W.-W., Transformable Nanostructures of Platinum-Containing Organosilane Hybrids: Non-Covalent Self-Assembly of Polyhedral Oligomeric Silsesquioxanes Assisted by Pt···Pt and Π–Π Stacking Interactions of Alkynylplatinum(II) Terpyridine Moieties. *J. Am. Chem. Soc.* **2014**, *136* (52), 17910-17913.

67. Gunnlaugsson, T., Accessible Self-Assembly. *Nat. Chem.* **2016**, *8* (1), 6-7.

68. Aliprandi, A.; Mauro, M.; De Cola, L., Controlling and Imaging Biomimetic Self-Assembly. *Nat. Chem.* **2016**, *8* (1), 10-15.

69. Korevaar, P. A.; George, S. J.; Markvoort, A. J.; Smulders, M. M. J.; Hilbers, P. A. J.; Schenning, A. P. H. J.; De Greef, T. F. A.; Meijer, E. W., Pathway Complexity in Supramolecular Polymerization. *Nature* **2012**, *481* (7382), 492-496.

70. Mattia, E.; Otto, S., Supramolecular Systems Chemistry. *Nat. Nanotechnol.* **2015**, *10* (2), 111-119.

71. Sorrenti, A.; Leira-Iglesias, J.; Markvoort, A. J.; de Greef, T. F. A.; Hermans, T. M., Non-Equilibrium Supramolecular Polymerization. *Chem. Soc. Rev.* **2017**, *46* (18), 5476-5490.

72. Sawczyk, M.; Klajn, R., Out-of-Equilibrium Aggregates and Coatings During Seeded Growth of Metallic Nanoparticles. *J. Am. Chem. Soc.* **2017**, *139* (49), 17973-17978.

73. Moreno-Alcántar, G.; Aliprandi, A.; Rouquette, R.; Pesce, L.; Wurst, K.; Perego, C.; Brüggeller, P.; Pavan, G. M.; De Cola, L., Solvent-Driven Supramolecular Wrapping of Self-Assembled Structures. *Angew. Chem. Int. Ed.* **2021**, *60* (10), 5407-5413.

74. Ghosh, G.; Ghosh, T.; Fernández, G., Controlled Supramolecular Polymerization of D8 Metal Complexes through Pathway Complexity and Seeded Growth. *ChemPlusChem* **2020**, *85* (5), 1022-1033.

75. Langenstroer, A.; Kartha, K. K.; Dorca, Y.; Droste, J.; Stepanenko, V.; Albuquerque, R. Q.; Hansen, M. R.; Sánchez, L.; Fernández, G., Unraveling Concomitant Packing Polymorphism in Metallosupramolecular Polymers. *J. Am. Chem. Soc.* **2019**, *141* (13), 5192-5200.

76. Herkert, L.; Droste, J.; Kartha, K. K.; Korevaar, P. A.; de Greef, T. F. A.; Hansen, M. R.; Fernández, G., Pathway Control in Cooperative Vs. Anti-Cooperative Supramolecular Polymers. *Angew. Chem. Int. Ed.* **2019**, *58* (33), 11344-11349.

77. Bäumer, N.; Matern, J.; Fernández, G., Recent Progress and Future Challenges in the Supramolecular Polymerization of Metal-Containing Monomers. *Chem. Sci.* **2021**, *12* (37), 12248-12265.

78. Gao, Z.; Han, Y.; Wang, F., Cooperative Supramolecular Polymers with Anthracene-Endoperoxide Photo-Switching for Fluorescent Anti-Counterfeiting. *Nat. Commun.* **2018**, *9* (1), 3977.

79. Wan, Q.; To, W.-P.; Yang, C.; Che, C.-M., The Metal–Metal-to-Ligand Charge Transfer Excited State and Supramolecular Polymerization of Luminescent Pincer Pd(II)–Isocyanide Complexes. *Angew. Chem. Int. Ed.* **2018**, *57* (12), 3089-3093.

80. Wehner, M.; Würthner, F., Supramolecular Polymerization through Kinetic Pathway Control and Living Chain Growth. *Nat. Rev. Chem.* **2020**, *4* (1), 38-53.

81. Park, J.; Hwang, M.; Ok, M.; Li, C.; Choi, H.; Seo, M. L.; Jung, J. H., Supramolecular Polymerization of Pt(II) Complex with Terpyridine-Based Ligand Possessing Alanine Moiety in Nonpolar Solvent. *Inorg. Chem. Commun.* **2021**, *129*, 108650.

82. Zhang, K.; Yeung, M. C.-L.; Leung, S. Y.-L.; Yam, V. W.-W., Energy Landscape in Supramolecular Coassembly of Platinum(II) Complexes and Polymers: Morphological Diversity, Transformation, and Dilution Stability of Nanostructures. *J. Am. Chem. Soc.* **2018**, *140* (30), 9594-9605.

83. Kumar, A.; Saha, R.; Mukherjee, P. S., Self-Assembled Metallasupramolecular Cages Towards Light Harvesting Systems for Oxidative Cyclization. *Chem. Sci.* **2021**, *12* (14), 5319-5329.

84. Li, G.; Zhou, Z.; Yuan, C.; Guo, Z.; Liu, Y.; Zhao, D.; Liu, K.; Zhao, J.; Tan, H.; Yan, X., Trackable Supramolecular Fusion: Cage to Cage Transformation of Tetraphenylethylene-Based Metalloassemblies. *Angew. Chem. Int. Ed.* **2020**, *59* (25), 10013-10017.

85. Clever, G. H.; Punt, P., Cation–Anion Arrangement Patterns in Self-Assembled Pd2l4 and Pd4l8 Coordination Cages. *Acc. Chem. Res.* **2017**, *50* (9), 2233-2243.

86. Mukherjee, S.; Mukherjee, P. S., Template-Free Multicomponent Coordination-Driven Self-Assembly of Pd(II)/Pt(II) Molecular Cages. *Chem. Commun.* **2014**, *50* (18), 2239-2248.

87. Zhang, M.; Saha, M. L.; Wang, M.; Zhou, Z.; Song, B.; Lu, C.; Yan, X.; Li, X.; Huang, F.; Yin, S.; Stang, P. J., Multicomponent Platinum(II) Pages with Tunable Emission and Amino Acid Sensing. *J. Am. Chem. Soc.* **2017**, *139* (14), 5067-5074.

88. Sinn, S.; Biedermann, F.; De Cola, L., Platinum Complex Assemblies as Luminescent Probes and Tags for Drugs and Toxins in Water. *Chem. Eur. J.* **2017**, *23* (8), 1965-1971.

89. Wong, Y.-S.; Ng, M.; Yeung, M. C.-L.; Yam, V. W.-W., Platinum(II)-Based Host–Guest Coordination-Driven Supramolecular Co-Assembly Assisted by Pt···Pt and Π–Π Stacking Interactions: A Dual-Selective Luminescence Sensor for Cations and Anions. *J. Am. Chem. Soc.* **2021**, *143* (2), 973-982.

90. Guerchais, V.; Fillaut, J.-L., Sensory Luminescent Iridium(III) and Platinum(II) Complexes for Cation Recognition. *Coord. Chem. Rev.* **2011**, *255* (21), 2448-2457.

91. Hashem, S. G.; Elsaady, M. M.; Afify, H. G.; Omer, W. E.; Youssef, A. O.; El-Kemary, M.; Attia, M. S., Determination of Uric Acid in Serum Using an Optical Sensor Based on Binuclear Pd(II) 2-Pyrazinecarboxamide-Bipyridine Doped in a Sol Gel Matrix. *Talanta* **2019**, *199*, 89-96.

92. Pal, S.; Lohar, S.; Mukherjee, M.; Chattopadhyay, P.; Dhara, K., A Fluorescent Probe for the Selective Detection of Creatinine in Aqueous Buffer Applicable to Human Blood Serum. *Chem. Commun.* **2016**, *52* (94), 13706-13709.

93. Keefe, M. H.; Benkstein, K. D.; Hupp, J. T., Luminescent Sensor Molecules Based on Coordinated Metals: A Review of Recent Developments. *Coord. Chem. Rev.* **2000**, *205* (1), 201-228.

94. Eryazici, I.; Moorefield, C. N.; Newkome, G. R., Square-Planar Pd(II), Pt(II), and Au(III) Terpyridine Complexes: Their Syntheses, Physical Properties, Supramolecular Constructs, and Biomedical Activities. *Chem. Rev.* **2008**, *108* (6), 1834-1895.

95. Cowley, A., A Healthy Future: Platinum in Medical Applications. *Platinum Met. Rev.* **2011**, *55* (2), 98-107.

96. Loye, A. M.; Kwon, H.-K.; Dellal, D.; Ojeda, R.; Lee, S.; Davis, R.; Nagle, N.; Doukas, P. G.; Schroers, J.; Lee, F. Y.; Kyriakides, T. R., Biocompatibility of Platinum-Based Bulk Metallic Glass in Orthopedic Applications. *Biomed. Mater.* **2021**, *16* (4), 045018.

97. You, L.; Zha, D.; Anslyn, E. V., Recent Advances in Supramolecular Analytical Chemistry Using Optical Sensing. *Chem. Rev.* **2015**, *115* (15), 7840-7892.

98. Meadows, M. K.; Anslyn, E. V., *Three Tales of Supramolecular Analytical Chemistry*. Wiley: 2016; p 92-126.

99. Anslyn, E. V., Supramolecular Analytical Chemistry. *J. Org. Chem.* **2007**, *72* (3), 687-699.

100. Li, X.; Gao, X.; Shi, W.; Ma, H., Design Strategies for Water-Soluble Small Molecular Chromogenic and Fluorogenic Probes. *Chem. Rev.* **2014**, *114* (1), 590-659.

101. Peng, H.; Chen, W.; Cheng, Y.; Hakuna, L.; Strongin, R.; Wang, B., Thiol Reactive Probes and Chemosensors. *Sensors* **2012**, *12* (11), 15907-15946.

102. Eun Jun, M.; Roy, B.; Han Ahn, K., "Turn-on" Fluorescent Sensing with "Reactive" Probes. *Chem. Commun.* **2011**, *47* (27), 7583-7601.

103. Jones, L. H., Reactive Chemical Probes: Beyond the Kinase Cysteinome. *Angew. Chem. Int. Ed.* **2018**, *57* (30), 9220-9223.

104. *Perspectives in Supramolecular Chemistry: The Lock-and-Key Principle*. John Wiley & Sons, Ltd.: 1994.

105. Zhang, H.; Zhang, C.; Liu, R.; Yi, L.; Sun, H., A Highly Selective and Sensitive Fluorescent Thiol Probe through Dual-Reactive and Dual-Quenching Groups. *Chem. Commun.* **2015**, *51* (11), 2029-2032.

106. Chen, C.-L.; Chen, Y.-T.; Demchenko, A. P.; Chou, P.-T., Amino Proton Donors in Excited-State Intramolecular Proton-Transfer Reactions. *Nat. Rev. Chem.* **2018**, *2* (7), 131-143.

107. Townsend, D. M.; Tew, K. D.; Tapiero, H., Sulfur-Containing Amino Acids and Human Disease. *Biomed. Pharmacother.* **2004**, *58* (1), 47-55.

108. Yin, C.-X.; Xiong, K.-M.; Huo, F.-J.; Salamanca, J. C.; Strongin, R. M., Fluorescent Probes with Multiple Binding Sites for the Discrimination of Cys, Hcy, and GSH. *Angew. Chem. Int. Ed.* **2017**, *56* (43), 13188-13198.

109. Lin, V. S.; Chen, W.; Xian, M.; Chang, C. J., Chemical Probes for Molecular Imaging and Detection of Hydrogen Sulfide and Reactive Sulfur Species in Biological Systems. *Chem. Soc. Rev.* **2015**, *44* (14), 4596-4618.

110. Yue, Y.; Huo, F.; Cheng, F.; Zhu, X.; Mafireyi, T.; Strongin, R. M.; Yin, C., Functional Synthetic Probes for Selective Targeting and Multi-Analyte Detection and Imaging. *Chem. Soc. Rev.* **2019**, *48* (15), 4155-4177.

111. Isik, M.; Ozdemir, T.; Turan, I. S.; Kolemen, S.; Akkaya, E. U., Chromogenic and Fluorogenic Sensing of Biological Thiols in Aqueous Solutions Using Bodipy-Based Reagents. *Org. Lett.* **2013**, *15* (1), 216-219.

112. Wang, W.; Rusin, O.; Xu, X.; Kim, K. K.; Escobedo, J. O.; Fakayode, S. O.; Fletcher, K. A.; Lowry, M.; Schowalter, C. M.; Lawrence, C. M.; Fronczek, F. R.; Warner, I. M.; Strongin, R. M., Detection of Homocysteine and Cysteine. *J. Am. Chem. Soc.* **2005**, *127* (45), 15949-15958.

113. Yin, G.-x.; Niu, T.-t.; Gan, Y.-b.; Yu, T.; Yin, P.; Chen, H.-m.; Zhang, Y.-y.; Li, H.-t.; Yao, S.-z., A Multi-Signal Fluorescent Probe with Multiple Binding Sites for Simultaneous Sensing of Cysteine, Homocysteine, and Glutathione. *Angew. Chem. Int. Ed.* **2018**, *57* (18), 4991-4994.

114. Liu, J.; Sun, Y.-Q.; Huo, Y.; Zhang, H.; Wang, L.; Zhang, P.; Song, D.; Shi, Y.; Guo, W., Simultaneous Fluorescence Sensing of Cys and Gsh from Different Emission Channels. *J. Am. Chem. Soc.* **2014**, *136* (2), 574-577.

115. Fu, Y.; Finney, N. S., Small-Molecule Fluorescent Probes and Their Design. *RSC Adv.* **2018**, *8* (51), 29051-29061.

116. Sinn, S.; Biedermann, F., Chemical Sensors Based on Cucurbit[n]Uril Macrocycles. *Isr. J. Chem.* **2018**, *58* (3-4), 357-412.

117. Kumar, R.; Sharma, A.; Singh, H.; Suating, P.; Kim, H. S.; Sunwoo, K.; Shim, I.; Gibb, B. C.; Kim, J. S., Revisiting Fluorescent Calixarenes: From Molecular Sensors to Smart Materials. *Chem. Rev.* **2019**, *119* (16), 9657-9721.

118. Kakuta, T.; Yamagishi, T.-a.; Ogoshi, T., Stimuli-Responsive Supramolecular Assemblies Constructed from Pillar[n]Arenes. *Acc. Chem. Res.* **2018**, *51* (7), 1656-1666.

119. Davis, A. P., Biomimetic Carbohydrate Recognition. *Chem. Soc. Rev.* **2020**, *49* (9), 2531-2545.

120. Yang, L. P.; Wang, X.; Yao, H.; Jiang, W., Naphthotubes: Macrocyclic Hosts with a Biomimetic Cavity Feature. *Acc. Chem. Res.* **2020**, *53* (1), 198-208.

121. Crane, B. C.; Barwell, N. P.; Gopal, P.; Gopichand, M.; Higgs, T.; James, T. D.; Jones, C. M.; Mackenzie, A.; Mulavisala, K. P.; Paterson, W., The Development of a Continuous Intravascular Glucose Monitoring Sensor. *J. diabetes Sci. Technol.* **2015**, *9* (4), 751-761.

122. de Silva, A. P.; Vance, T. P.; West, M. E. S.; Wright, G. D., Bright Molecules with Sense, Logic, Numeracy and Utility. *Org. Biomol. Chem.* **2008**, *6* (14), 2468-2480.

123. de Silva, A. P.; Sandanayake, K. R. A. S., Fluorescent Pet (Photo-Induced Electron Transfer) Sensors for Alkali Metal Ions with Improved Selectivity against Protons and with Predictable Binding Constants. *J. Chem. Soc., Chem. Commun.* **1989**, (16), 1183-1185.

124. de Silva, A. P.; Gunaratne, H. Q. N.; Gunnlaugsson, T.; Nieuwenhuizen, M., Fluorescent Switches with High Selectivity Towards Sodium Ions: Correlation of Ion-Induced Conformation Switching with Fluorescence Function. *Chem. Commun.* **1996**, (16), 1967-1968.

125. de Silva, A. P.; Gunaratne, H. Q. N.; McCoy, C. P., Molecular Photoionic and Logic Gates with Bright Fluorescence and "Off−on" Digital Action. *J. Am. Chem. Soc.* **1997**, *119* (33), 7891-7892.

126. Uchiyama, S.; Fukatsu, E.; McClean, G. D.; de Silva, A. P., Measurement of Local Sodium Ion Levels near Micelle Surfaces with Fluorescent Photoinduced-Electron-Transfer Sensors. *Angew. Chem. Int. Ed.* **2016**, *55* (2), 768-771.

127. Sedgwick, A. C.; Brewster, J. T.; Wu, T.; Feng, X.; Bull, S. D.; Qian, X.; Sessler, J. L.; James, T. D.; Anslyn, E. V.; Sun, X., Indicator Displacement Assays (IDAs): The Past, Present and Future. *Chem. Soc. Rev.* **2021**, *50* (1), 9-38.

128. Hennig, A.; Nau, W. M., Chapter 6 Cucurbituril-Based Sensors and Assays. In *Cucurbiturils and Related Macrocycles*, The Royal Society of Chemistry: 2020; pp 121-149.

129. Hennig, A.; Bakirci, H.; Nau, W. M., Label-Free Continuous Enzyme Assays with Macrocycle-Fluorescent Dye Complexes. *Nat. Methods* **2007**, *4* (8), 629-632.

130. Sinn, S.; Spuling, E.; Bräse, S.; Biedermann, F., Rational Design and Implementation of a Cucurbit[8]Uril-Based Indicator-Displacement Assay for Application in Blood Serum. *Chem. Sci.* **2019**, *10* (27), 6584-6593.

131. Minami, T.; Esipenko, N. A.; Akdeniz, A.; Zhang, B.; Isaacs, L.; Anzenbacher, P., Multianalyte Sensing of Addictive over-the-Counter (OTC) Drugs. *J. Am. Chem. Soc.* **2013**, *135* (40), 15238-15243.

132. Chen, J.; Hickey, B. L.; Wang, L.; Lee, J.; Gill, A. D.; Favero, A.; Pinalli, R.; Dalcanale, E.; Hooley, R. J.; Zhong, W., Selective Discrimination and Classification of G-Quadruplex Structures with a Host-Guest Sensing Array. *Nat. Chem.* **2021**, *13* (5), 488-495.

133. Sinn, S.; Krämer, J.; Biedermann, F., Teaching Old Indicators Even More Tricks: Binding Affinity Measurements with the Guest-Displacement Assay (GDA). *Chem. Commun.* **2020**, *56* (49), 6620-6623.

134. Barba-Bon, A.; Pan, Y.-C.; Biedermann, F.; Guo, D.-S.; Nau, W. M.; Hennig, A., Fluorescence Monitoring of Peptide Transport Pathways into Large and Giant Vesicles by Supramolecular Host–Dye Reporter Pairs. *J. Am. Chem. Soc.* **2019**, *141* (51), 20137-20145.

135. Lavigne, J. J.; Anslyn, E. V., Sensing a Paradigm Shift in the Field of Molecular Recognition: From Selective to Differential Receptors. *Angew. Chem. Int. Ed.* **2001**, *40* (17), 3118-3130.

136. Rakow, N. A.; Suslick, K. S., A Colorimetric Sensor Array for Odour Visualization. *Nature* **2000**, *406* (6797), 710-3.

137. Stewart, S.; Ivy, M. A.; Anslyn, E. V., The Use of Principal Component Analysis and Discriminant Analysis in Differential Sensing Routines. *Chem. Soc. Rev.* **2014**, *43* (1), 70-84.

138. Barreira, J. C. M.; Casal, S.; Ferreira, I. C. F. R.; Peres, A. M.; Pereira, J. A.; Oliveira, M. B. P. P., Supervised Chemical Pattern Recognition in Almond (Prunus Dulcis) Portuguese Pdo Cultivars: Pca- and Lda-Based Triennial Study. *J. Agric. Food. Chem.* **2012**, *60* (38), 9697-9704.

139. Sharma, A.; Paliwal, K. K.; Onwubolu, G. C., Class-Dependent PCA, MDC and LDA: A Combined Classifier for Pattern Classification. *Pattern Recognit.* **2006**, *39* (7), 1215-1229.

140. Ma, C.; Xin, M.; Feldmann, K. A.; Wang, X., Machine Learning–Based Differential Network Analysis: A Study of Stress-Responsive Transcriptomes in Arabidopsis *The Plant Cell* **2014**, *26* (2), 520-537.

141. Hassan, D. S.; Wolf, C., Optical Deciphering of Multinary Chiral Compound Mixtures through Organic Reaction Based Chemometric Chirality Sensing. *Nat. Commun.* **2021**, *12* (1), 6451.

142. Huang, X.; Jeon, H.; Liu, J.; Yao, J.; Wei, M.; Han, W.; Chen, J.; Sun, L.; Han, J., Deep-Learning Based Label-Free Classification of Activated and Inactivated Neutrophils for Rapid Immune State Monitoring. *Sensors* **2021**, *21* (2), 512.

143. Liu, Y.; Minami, T.; Nishiyabu, R.; Wang, Z.; Anzenbacher, P., Sensing of Carboxylate Drugs in Urine by a Supramolecular Sensor Array. *J. Am. Chem. Soc.* **2013**, *135* (20), 7705-7712.

144. Diehl, K. L.; Anslyn, E. V., Array Sensing Using Optical Methods for Detection of Chemical and Biological Hazards. *Chem. Soc. Rev.* **2013**, *42* (22), 8596-8611.

145. Wright, A. T.; Anslyn, E. V., Differential Receptor Arrays and Assays for Solution-Based Molecular Recognition. *Chem. Soc. Rev.* **2006**, *35* (1), 14-28.

146. Musto, C. J.; Suslick, K. S., Differential Sensing of Sugars by Colorimetric Arrays. *Curr. Opin. Chem. Biol.* **2010**, *14* (6), 758-766.

147. Wong, S.-F.; Khor, S. M., State-of-the-Art of Differential Sensing Techniques in Analytical Sciences. *TrAC, Trends Anal. Chem.* **2019**, *114*, 108-125.

148. Beatty, M. A.; Selinger, A. J.; Li, Y.; Hof, F., Parallel Synthesis and Screening of Supramolecular Chemosensors That Achieve Fluorescent Turn-on Detection of Drugs in Saliva. *J. Am. Chem. Soc.* **2019**, *141* (42), 16763-16771.

149. Shcherbakova, E. G.; Zhang, B.; Gozem, S.; Minami, T.; Zavalij, P. Y.; Pushina, M.; Isaacs, L. D.; Anzenbacher, P., Jr., Supramolecular Sensors for Opiates and Their Metabolites. *J. Am. Chem. Soc.* **2017**, *139* (42), 14954-14960.

150. Weatherly, C. A.; Du, S.; Parpia, C.; Santos, P. T.; Hartman, A. L.; Armstrong, D. W., D-Amino Acid Levels in Perfused Mouse Brain Tissue and Blood: A Comparative Study. *ACS Chem. Neurosci.* **2017**, *8* (6), 1251-1261.

151. Visser, W. F.; Verhoeven-Duif, N. M.; Ophoff, R.; Bakker, S.; Klomp, L. W.; Berger, R.; de Koning, T. J., A Sensitive and Simple Ultra-High-Performance-Liquid Chromatography–Tandem Mass Spectrometry Based Method for the Quantification of D-Amino Acids in Body Fluids. *J. Chromatogr. A* **2011**, *1218* (40), 7130-7136.

152. Fuchs, S. A.; Berger, R.; Klomp, L. W. J.; de Koning, T. J., D-Amino Acids in the Central Nervous System in Health and Disease. *Mol. Genet. Metab.* **2005**, *85* (3), 168-180.

153. Zhou, Y.; Zhang, J. F.; Yoon, J., Fluorescence and Colorimetric Chemosensors for Fluoride-Ion Detection. *Chem. Rev.* **2014**, *114* (10), 5511-5571.

154. Wolf, C.; Bentley, K. W., Chirality Sensing Using Stereodynamic Probes with Distinct Electronic Circular Dichroism Output. *Chem. Soc. Rev.* **2013**, *42* (12), 5408-5424.

155. Leung, D.; Kang, S. O.; Anslyn, E. V., Rapid Determination of Enantiomeric Excess: A Focus on Optical Approaches. *Chem. Soc. Rev.* **2012**, *41* (1), 448-479.

156. Leung, D.; Folmer-Andersen, J. F.; Lynch, V. M.; Anslyn, E. V., Using Enantioselective Indicator Displacement Assays to Determine the Enantiomeric Excess of A-Amino Acids. *J. Am. Chem. Soc.* **2008**, *130* (37), 12318-12327.

157. Leung, D.; Anslyn, E. V., Transitioning Enantioselective Indicator Displacement Assays for A-Amino Acids to Protocols Amenable to High-Throughput Screening. *J. Am. Chem. Soc.* **2008**, *130* (37), 12328-12333.

158. Folmer-Andersen, J. F.; Kitamura, M.; Anslyn, E. V., Pattern-Based Discrimination of Enantiomeric and Structurally Similar Amino Acids: An Optical Mimic of the Mammalian Taste Response. *J. Am. Chem. Soc.* **2006**, *128* (17), 5652-5653.

159. Zhu, L.; Anslyn, E. V., Facile Quantification of Enantiomeric Excess and Concentration with Indicator-Displacement Assays: An Example in the Analyses of A-Hydroxyacids. *J. Am. Chem. Soc.* **2004**, *126* (12), 3676-3677.

160. Zhu, L.; Zhong, Z.; Anslyn, E. V., Guidelines in Implementing Enantioselective Indicator-Displacement Assays for A-Hydroxycarboxylates and Diols. *J. Am. Chem. Soc.* **2005**, *127* (12), 4260-4269.

161. Shabbir, S. H.; Joyce, L. A.; da Cruz, G. M.; Lynch, V. M.; Sorey, S.; Anslyn, E. V., Pattern-Based Recognition for the Rapid Determination of Identity, Concentration, and Enantiomeric Excess of Subtly Different Threo Diols. *J. Am. Chem. Soc.* **2009**, *131* (36), 13125-13131.

162. Shabbir, S. H.; Regan, C. J.; Anslyn, E. V., A General Protocol for Creating High-Throughput Screening Assays for Reaction Yield and Enantiomeric Excess Applied to Hydrobenzoin. *Proc. Natl. Acad. Sci.* **2009**, *106* (26), 10487-10492.

163. Biedermann, F.; Nau, W. M., Noncovalent Chirality Sensing Ensembles for the Detection and Reaction Monitoring of Amino Acids, Peptides, Proteins, and Aromatic Drugs. *Angew. Chem. Int. Ed.* **2014**, *53* (22), 5694-5699.

164. Prabodh, A.; Bauer, D.; Kubik, S.; Rebmann, P.; Klarner, F. G.; Schrader, T.; Delarue Bizzini, L.; Mayor, M.; Biedermann, F., Chirality Sensing of Terpenes, Steroids, Amino Acids, Peptides and Drugs with Acyclic Cucurbit[n]Urils and Molecular Tweezers. *Chem. Commun.* **2020**, *56* (34), 4652-4655.

165. Wang, L. L.; Chen, Z.; Liu, W. E.; Ke, H.; Wang, S. H.; Jiang, W., Molecular Recognition and Chirality Sensing of Epoxides in Water Using Endo-Functionalized Molecular Tubes. *J. Am. Chem. Soc.* **2017**, *139* (25), 8436-8439.

166. Zhu, H.; Li, Q.; Gao, Z.; Wang, H.; Shi, B.; Wu, Y.; Shangguan, L.; Hong, X.; Wang, F.; Huang, F., Pillararene Host-Guest Complexation Induced Chirality Amplification: A New Way to Detect Cryptochiral Compounds. *Angew. Chem. Int. Ed.* **2020**, *59* (27), 10868-10872.

167. De los Santos, Z. A.; Ding, R.; Wolf, C., Quantitative Chirality Sensing of Amines and Amino Alcohols Via Schiff Base Formation with a Stereodynamic Uv/Cd Probe. *Org. Biomol. Chem.* **2016**, *14* (6), 1934-1939.

168. Thanzeel, F. Y.; Balaraman, K.; Wolf, C., Click Chemistry Enables Quantitative Chiroptical Sensing of Chiral Compounds in Protic Media and Complex Mixtures. *Nat. Commun.* **2018**, *9* (1), 5323.

169. Formen, J. S. S. K.; Wolf, C., Chiroptical Switching and Quantitative Chirality Sensing with (Pseudo)Halogenated Quinones. *Angew. Chem. Int. Ed.* **2021**, *60* (52), 27031-27038.

170. Thanzeel, F. Y.; Wolf, C., Substrate-Specific Amino Acid Sensing Using a Molecular D/ L-Cysteine Probe for Comprehensive Stereochemical Analysis in Aqueous Solution. *Angew. Chem. Int. Ed.* **2017**, *56* (25), 7276-7281.

171. Thanzeel, F. Y.; Sripada, A.; Wolf, C., Quantitative Chiroptical Sensing of Free Amino Acids, Biothiols, Amines, and Amino Alcohols with an Aryl Fluoride Probe. *J. Am. Chem. Soc.* **2019**, *141* (41), 16382-16387.

172. Pilicer, S. L.; Bakhshi, P. R.; Bentley, K. W.; Wolf, C., Biomimetic Chirality Sensing with Pyridoxal-5'-Phosphate. *J. Am. Chem. Soc.* **2017**, *139* (5), 1758-1761.

173. You, L.; Berman, J. S.; Anslyn, E. V., Dynamic Multi-Component Covalent Assembly for the Reversible Binding of Secondary Alcohols and Chirality Sensing. *Nat. Chem.* **2011**, *3* (12), 943-948.

174. Lehn, J.-M., From Supramolecular Chemistry Towards Constitutional Dynamic Chemistry and Adaptive Chemistry. *Chem. Soc. Rev.* **2007**, *36* (2), 151-160.

175. Lehn, J.-M., Towards Complex Matter: Supramolecular Chemistry and Self-Organization. *Eur. Rev.* **2009**, *17* (2), 263-280.

176. Lehn, J.-M., Supramolecular Chemistry. *Science* **1993**, *260* (5115), 1762-1764.

177. Lehn, J.-M., Toward Self-Organization and Complex Matter. *Science* **2002**, *295* (5564), 2400-2403.

178. Lehn, J. M., Constitutional Dynamic Chemistry: Bridge from Supramolecular Chemistry to Adaptive Chemistry. *Top. Curr. Chem.* **2012**, *322*, 1-32.

179. Webber, M. J.; Appel, E. A.; Meijer, E. W.; Langer, R., Supramolecular Biomaterials. *Nat. Mater.* **2016**, *15* (1), 13-26.

180. Sorrenti, A.; Leira-Iglesias, J.; Sato, A.; Hermans, T. M., Non-Equilibrium Steady States in Supramolecular Polymerization. *Nat. Commun.* **2017**, *8* (1), 1-8.

181. Stuart, M. A.; Huck, W. T.; Genzer, J.; Muller, M.; Ober, C.; Stamm, M.; Sukhorukov, G. B.; Szleifer, I.; Tsukruk, V. V.; Urban, M.; Winnik, F.; Zauscher, S.; Luzinov, I.; Minko, S., Emerging Applications of Stimuli-Responsive Polymer Materials. *Nat. Mater.* **2010**, *9* (2), 101-13.

182. Yan, X.; Wang, F.; Zheng, B.; Huang, F., Stimuli-Responsive Supramolecular Polymeric Materials. *Chem. Soc. Rev.* **2012**, *41* (18), 6042-65.

183. Chen, Z.; Suzuki, Y.; Imayoshi, A.; Ji, X.; Rao, K. V.; Omata, Y.; Miyajima, D.; Sato, E.; Nihonyanagi, A.; Aida, T., Solvent-Free Autocatalytic Supramolecular Polymerization. *Nat. Mater.* **2022**, *21* (2), 253-261.

184. Komáromy, D. v.; Stuart, M. C.; Monreal Santiago, G.; Tezcan, M.; Krasnikov, V. V.; Otto, S., Self-Assembly Can Direct Dynamic Covalent Bond Formation toward Diversity or Specificity. *J. Am. Chem. Soc.* **2017**, *139* (17), 6234-6241.

185. Wang, Y.; Wu, H.; Hu, W.; Stoddart, J. F., Color-Tunable Supramolecular Luminescent Materials. *Adv. Mater.* **2021**, e2105405.

186. Harrison, E. E.; Carpenter, B. A.; St. Louis, L. E.; Mullins, A. G.; Waters, M. L., Development of "Imprint-and-Report" Dynamic Combinatorial Libraries for Differential Sensing Applications. *J. Am. Chem. Soc.* **2021**, *143* (36), 14845-14854.

187. Lafuente, M.; Solà, J.; Alfonso, I., A Dynamic Chemical Network for Cystinuria Diagnosis. *Angew. Chem. Int. Ed.* **2018**, *57* (28), 8421-8424.

188. Liu, W.; Tan, Y.; Jones, L. O.; Song, B.; Guo, Q. H.; Zhang, L.; Qiu, Y.; Feng, Y.; Chen, X. Y.; Schatz, G. C.; Stoddart, J. F., Pcage: Fluorescent Molecular Temples for Binding Sugars in Water. *J. Am. Chem. Soc.* **2021**, *143* (38), 15688-15700.

189. Giuseppone, N.; Lehn, J.-M., Constitutional Dynamic Self-Sensing in a Zincii/Polyiminofluorenes System. *J. Am. Chem. Soc.* **2004**, *126* (37), 11448-11449.

190. Chang, X.; Yu, C.; Wang, G.; Fan, J.; Zhang, J.; Qi, Y.; Liu, K.; Fang, Y., Constitutional Dynamic Chemistry-Based New Concept of Molecular Beacons for High Efficient Development of Fluorescent Probes. *J. Phys. Chem. B* **2015**, *119* (22), 6721-6729.

191. Kang, R.; Talamini, L.; D'Este, E.; Estevão, B. M.; De Cola, L.; Klopper, W.; Biedermann, F., Discovery of a Size-Record Breaking Green-Emissive Fluorophore: Small, Smaller, Hina. *Chem. Sci.* **2021**, *12* (4), 1392-1397.

192. Lavis, L. D., Teaching Old Dyes New Tricks: Biological Probes Built from Fluoresceins and Rhodamines. *Annu. Rev. Biochem* **2017**, *86*, 825-843.

193. Liu, J.; Sun, Y. Q.; Zhang, H.; Shi, H.; Shi, Y.; Guo, W., Sulfone-Rhodamines: A New Class of near-Infrared Fluorescent Dyes for Bioimaging. *ACS Appl. Mater. Interfaces* **2016**, *8* (35), 22953-62.

194. Hong, Y.; Lam, J. W.; Tang, B. Z., Aggregation-Induced Emission. *Chem. Soc. Rev.* **2011**, *40* (11), 5361-88.

195. Pina, F.; Melo, M. J.; Laia, C. A.; Parola, A. J.; Lima, J. C., Chemistry and Applications of Flavylium Compounds: A Handful of Colours. *Chem. Soc. Rev.* **2012**, *41* (2), 869-908.

196. Demeter, A.; Druzhinin, S.; George, M.; Haselbach, E.; Roulin, J. L.; Zachariasse, K. A., Dual Fluorescence and Fast Intramolecular Charge Transfer with 4-(Diisopropylamino) Benzonitrile in Alkane Solvents. *Chem. Phys. Lett.* **2000**, *323* (3-4), 351-360.

197. Sayed, M.; Biedermann, F.; Uzunova, V. D.; Assaf, K. I.; Bhasikuttan, A. C.; Pal, H.; Nau, W. M.; Mohanty, J., Triple Emission from P-Dimethylaminobenzonitrile-Cucurbit[8]Uril Triggers the Elusive Excimer Emission. *Chem. Eur. J.* **2015**, *21* (2), 691-696.

198. Catalán, J., On the Dual Emission of P-Dimethylaminobenzonitrile and Its Photophysical Implications. *Phys. Chem. Chem. Phys.* **2013**, *15* (22), 8811-8820.

199. Dong, J.; Solntsev, K. M.; Tolbert, L. M., Solvatochromism of the Green Fluorescence Protein Chromophore and Its Derivatives. *J. Am. Chem. Soc.* **2006**, *128* (37), 12038-12039.

200. Lin, C. Y.; Romei, M. G.; Oltrogge, L. M.; Mathews, II; Boxer, S. G., Unified Model for Photophysical and Electro-Optical Properties of Green Fluorescent Proteins. *J. Am. Chem. Soc.* **2019**, *141* (38), 15250-15265.

201. Deng, H.; Yu, C.; Yan, D.; Zhu, X., Dual-Self-Restricted Gfp Chromophore Analogues with Significantly Enhanced Emission. *J. Phys. Chem. B* **2020**, *124* (5), 871-880.

202. Dsouza, R. N.; Pischel, U.; Nau, W. M., Fluorescent Dyes and Their Supramolecular Host/Guest Complexes with Macrocycles in Aqueous Solution. *Chem. Rev.* **2011**, *111* (12), 7941-7980.

203. Tatikolov, A. S., Polymethine Dyes as Spectral-Fluorescent Probes for Biomacromolecules. *J. Photochem. Photobiol. C: Photochem. Rev.* **2012**, *13* (1), 55-90.

204. Tang, B.; Xing, Y.; Li, P.; Zhang, N.; Yu, F.; Yang, G., A Rhodamine-Based Fluorescent Probe Containing a Se-N Bond for Detecting Thiols and Its Application in Living Cells. *J. Am. Chem. Soc.* **2007**, *129* (38), 11666-7.

205. Benson, S.; Fernandez, A.; Barth, N. D.; de Moliner, F.; Horrocks, M. H.; Herrington, C. S.; Abad, J. L.; Delgado, A.; Kelly, L.; Chang, Z.; Feng, Y.; Nishiura, M.; Hori, Y.; Kikuchi, K.; Vendrell, M., Scotfluors: Small, Conjugatable, Orthogonal, and Tunable Fluorophores for in Vivo Imaging of Cell Metabolism. *Angew. Chem. Int. Ed.* **2019**, *58* (21), 6911-6915.

206. Liu, X.; Qiao, Q.; Tian, W.; Liu, W.; Chen, J.; Lang, M. J.; Xu, Z., Aziridinyl Fluorophores Demonstrate Bright Fluorescence and Superior Photostability by Effectively Inhibiting Twisted Intramolecular Charge Transfer. *J. Am. Chem. Soc.* **2016**, *138* (22), 6960-6963.

207. Saha, S.; Samanta, A., Photophysical and Dynamic Nmr Studies on 4-Amino-7-Nitrobenz-2-Oxa-1,3-Diazole Derivatives: Elucidation of the Nonradiative Deactivation Pathway. *J. Phys. Chem. A* **1998**, *102* (41), 7903-7912.

208. Wang, L.; Tran, M.; D'Este, E.; Roberti, J.; Koch, B.; Xue, L.; Johnsson, K., A General Strategy to Develop Cell Permeable and Fluorogenic Probes for Multicolour Nanoscopy. *Nat. Chem.* **2020**, *12* (2), 165-172.

209. Zamojc, K.; Wiczk, W.; Zaborowski, B.; Jacewicz, D.; Chmurzynski, L., Fluorescence Quenching of 7-Amino-4-Methylcoumarin by Different Tempo Derivatives. *Spectrochim. Acta A Mol. Biomol. Spectrosc.* **2015**, *136*, 1875-80.

210. Toseland, C. P., Fluorescent Labeling and Modification of Proteins. *J. Chem. Biol.* **2013**, *6* (3), 85-95.

211. Mai, S.; Gonzalez, L., Molecular Photochemistry: Recent Developments in Theory. *Angew. Chem. Int. Ed.* **2020**, *59*, 16832 –16846.

212. Tu, Y.; Liu, J.; Zhang, H.; Peng, Q.; Lam, J. W. Y.; Tang, B. Z., Restriction of Access to the Dark State: A New Mechanistic Model for Heteroatom-Containing Aie Systems. *Angew. Chem. Int. Ed.* **2019**, *58* (42), 14911-14914.

213. Chmela, J.; Greisch, J. F.; Harding, M. E.; Klopper, W.; Kappes, M. M.; Schooss, D., Vibronic Coupling Analysis of the Ligand-Centered Phosphorescence of Gas-Phase Gd(III) and Lu(III) 9-Oxophenalen-1-One Complexes. *J. Phys. Chem. A* **2018**, *122* (9), 2461-2467.

214. Harris, C. M.; Johnson, R. J.; Metzler, D. E., Band-Shape Analysis and Resolution of Electronic Spectra of Pyridoxal Phosphate and Other 3-Hydroxypyridine-4-Aldehydes. *Biochim. Biophys. Acta* **1976**, *421* (2), 181-94.

215. Nakamoto, K.; Martell, A., Pyridoxine and Pyridoxal Analogs. Iv. Ultraviolet Spectra and Solution Equilibria of 3-Methoxypyridine-2 (and 4-)-Aldehydes and of 3-Hydroxypyridine-2 (and 4-)-Aldehydes1, 2. *J. Am. Chem. Soc.* **1959**, *81* (22), 5863-5869.

216. Sanz, D.; Perona, A.; Claramunt, R. M.; Elguero, J., Synthesis and Spectroscopic Properties of Schiff Bases Derived from 3-Hydroxy-4-Pyridinecarboxaldehyde. *Tetrahedron* **2005**, *61* (1), 145-154.

217. Weinberger, R.; Love, L. J. C., Luminescence Properties of Polycyclic Aromatic-Hydrocarbons in Colloidal or Microcrystalline Suspensions. *Spectrochim. Acta A Mol. Biomol. Spectrosc.* **1984**, *40* (1), 49-55.

218. Yamaguchi, T.; Kimura, Y.; Hirota, N., Vibrational Energy Relaxation of Azulene in the S-2 State. I. Solvent Species Dependence. *J. Chem. Phys.* **2000**, *113* (7), 2772-2783.

219. Lamberto, M.; Pagba, C.; Piotrowiak, P.; Galoppini, E., Synthesis of Novel Rigid-Rod and Tripodal Azulene Chromophores. *Tetrahedron Lett.* **2005**, *46* (29), 4895-4899.

220. Zhou, J.; Liu, H.; Jin, B.; Liu, X.; Fu, H.; Shangguan, D., A Guanidine Derivative of Naphthalimide with Excited-State Deprotonation Coupled Intramolecular Charge Transfer Properties and Its Application. *J. Mater. Chem. C* **2013**, *1* (29), 4427-4436.

221. Reijenga, J.; van Hoof, A.; van Loon, A.; Teunissen, B., Development of Methods for the Determination of Pka Values. *Anal. Chem. Insights* **2013**, *8* (8), 53-71.

222. de Levie, R., Titration Vs. Tradition. *Chem. Educ.* **1996**, *1* (3), 1-18.

223. Szczepanik, B., Protolytic Dissociation of Cyano Derivatives of Naphthol, Biphenyl and Phenol in the Excited State: A Review. *J. Mol. Struct.* **2015**, *1099*, 209-214.

224. Tolbert, L. M.; Solntsev, K. M., Excited-State Proton Transfer: From Constrained Systems to "Super" Photoacids to Superfast Proton Transfer. *Acc. Chem. Res.* **2002**, *35* (1), 19-27.

225. Meher, N.; Panda, S.; Kumar, S.; Iyer, P. K., Aldehyde Group Driven Aggregation-Induced Enhanced Emission in Naphthalimides and Its Application for Ultradetection of Hydrazine on Multiple Platforms. *Chem. Sci.* **2018**, *9* (16), 3978-3985.

226. Islam, A. S. M.; Sasmal, M.; Maiti, D.; Dutta, A.; Show, B.; Ali, M., Design of a Pyrene Scaffold Multifunctional Material: Real-Time Turn-on Chemosensor for Nitric Oxide, Aiee Behavior, and Detection of TNP Explosive. *ACS omega* **2018**, *3* (8), 10306-10316.

227. Krasowska, J.; Olasek, M.; Bzowska, A.; Clark, P. L.; Wielgus-Kutrowska, B., The Comparison of Aggregation and Folding of Enhanced Green Fluorescent Protein (GFP) by Spectroscopic Studies. *J. Spectrosc. (Hindawi)* **2010**, *24* (3-4), 343-348.

228. Sander, E. G.; Jencks, W. P., Equilibria for Additions to the Carbonyl Group. *J. Am. Chem. Soc.* **1968**, *90* (22), 6154-6162.

229. Cortijo, M.; Llor, J.; Sanchezruiz, J. M., Thermodynamic Constants for Tautomerism, Hydration, and Ionization of Vitamin-B6 Compounds in Water Dioxane. *J. Biol. Chem.* **1988**, *263* (34), 17960-17969.

230. Hilal, S. H.; Bornander, L. L.; Carreira, L. A., Hydration Equilibrium Constants of Aldehydes, Ketones and Quinazolines. *QSAR & Combinatorial Science* **2005**, *24* (5), 631-638.

231. Abe, K.; Endo, H.; Hirota, M., Hydration of Aza-Aromatic Aldehydes. II . Solvent Effect on the Equilibriun Constants of the Hydration. *Bull. Chem. Soc. Jpn.* **1981**, (54), 466-469.

232. Santos, F. M. F.; Dominguez, Z.; Fernandes, J. P. L.; Parente Carvalho, C.; Collado, D.; Perez-Inestrosa, E.; Pinto, M. V.; Fernandes, A.; Arteaga, J. F.; Pischel, U.; Gois, P. M. P., Cyanine-Like Boronic Acid-Derived Salicylidenehydrazone Complexes (Cy-Bashy) for Bioimaging Applications. *Chem. Eur. J.* **2020**, *26* (62), 14064-14069.

233. Wampler, J. E.; Churchich, J. E., Phosphorescence of Pyridoxal. *J. Biol. Chem.* **1969**, *244* (6), 1477-80.

234. Wu, Y. S.; Huang, H. C.; Shen, J. Y.; Tseng, H. W.; Ho, J. W.; Chen, Y. H.; Chou, P. T., Water-Catalyzed Excited-State Proton-Transfer Reactions in 7-Azaindole and Its Analogues. *J. Phys. Chem. B* **2015**, *119* (6), 2302-9.

235. Christiansen, O.; Koch, H.; Jørgensen, P., The Second-Order Approximate Coupled Cluster Singles and Doubles Model Cc2. *Chem. Phys. Lett.* **1995**, *243* (5-6), 409-418.

236. Rappoport, D.; Furche, F., Property-Optimized Gaussian Basis Sets for Molecular Response Calculations. *J. Chem. Phys.* **2010**, *133* (13), 134105.

237. Hellweg, A.; Rappoport, D., Development of New Auxiliary Basis Functions of the Karlsruhe Segmented Contracted Basis Sets Including Diffuse Basis Functions (Def2-Svpd, Def2-Tzvppd, and Def2-Qvppd) for Ri-Mp2 and Ri-Cc Calculations. *Phys. Chem. Chem. Phys.* **2015**, *17* (2), 1010-7.

238. Hättig, C.; Weigend, F., Cc2 Excitation Energy Calculations on Large Molecules Using the Resolution of the Identity Approximation. *J. Chem. Phys.* **2000**, *113* (13), 5154-5161.

239. Baiardi, A.; Bloino, J.; Barone, V., General Time Dependent Approach to Vibronic Spectroscopy Including Franck-Condon, Herzberg-Teller, and Duschinsky Effects. *J. Chem. Theory Comput.* **2013**, *9* (9), 4097-115.

240. Biedermann, F.; Ghale, G.; Hennig, A.; Nau, W. M., Fluorescent Artificial Receptor-Based Membrane Assay (Farma) for Spatiotemporally Resolved Monitoring of Biomembrane Permeability. *Commun. Biol.* **2020**, *3* (1), 383.

241. Zhou, Y.; Yoon, J., Recent Progress in Fluorescent and Colorimetric Chemosensors for Detection of Amino Acids. *Chem. Soc. Rev.* **2012**, *41* (1), 52-67.

242. Pal, S., Pyridine: A Useful Ligand in Transition Metal Complexes. *Pyridine* **2018**, *57*.

243. Samanta, D.; Gemen, J.; Chu, Z.; Diskin-Posner, Y.; Shimon, L. J. W.; Klajn, R., Reversible Photoswitching of Encapsulated Azobenzenes in Water. *Proc. Natl. Acad. Sci.* **2018**, *115* (38), 9379-9384.

244. Pullen, S.; Clever, G. H., Mixed-Ligand Metal-Organic Frameworks and Heteroleptic Coordination Cages as Multifunctional Scaffolds-a Comparison. *Acc. Chem. Res.* **2018**, *51* (12), 3052-3064.

245. McConnell, A. J.; Wood, C. S.; Neelakandan, P. P.; Nitschke, J. R., Stimuli-Responsive Metal-Ligand Assemblies. *Chem. Rev.* **2015**, *115* (15), 7729-93.

246. Jankowiak, H. C.; Stuber, J. L.; Berger, R., Vibronic Transitions in Large Molecular Systems: Rigorous Prescreening Conditions for Franck-Condon Factors. *J. Chem. Phys.* **2007**, *127* (23), 234101.

247. Xu, Z.; Jia, S.; Wang, W.; Yuan, Z.; Jan Ravoo, B.; Guo, D.-S., Heteromultivalent Peptide Recognition by Co-Assembly of Cyclodextrin and Calixarene Amphiphiles Enables Inhibition of Amyloid Fibrillation. *Nat. Chem.* **2019**, *11* (1), 86-93.

248. Chen, X.; Zhou, Y.; Peng, X.; Yoon, J., Fluorescent and Colorimetric Probes for Detection of Thiols. *Chem. Soc. Rev.* **2010**, *39* (6), 2120-2135.

249. Kuśmierek, K.; Chwatko, G.; Głowacki, R.; Bald, E., Determination of Endogenous Thiols and Thiol Drugs in Urine by Hplc with Ultraviolet Detection. *J. Chromatogr. B* **2009**, *877* (28), 3300-3308.

250. McMahon, B. K.; Gunnlaugsson, T., Selective Detection of the Reduced Form of Glutathione (GSH) over the Oxidized (GSSG) Form Using a Combination of Glutathione Reductase and a Tb(III)-Cyclen Maleimide Based Lanthanide Luminescent 'Switch on' Assay. *J. Am. Chem. Soc.* **2012**, *134* (26), 10725-8.

251. Yin, G. X.; Niu, T. T.; Gan, Y. B.; Yu, T.; Yin, P.; Chen, H. M.; Zhang, Y. Y.; Li, H. T.; Yao, S. Z., A Multi-Signal Fluorescent Probe with Multiple Binding Sites for Simultaneous Sensing of Cysteine, Homocysteine, and Glutathione. *Angew. Chem. Int. Ed.* **2018**, *57* (18), 4991-4994.

252. Dame, Z. T.; Aziat, F.; Mandal, R.; Krishnamurthy, R.; Bouatra, S.; Borzouie, S.; Guo, A. C.; Sajed, T.; Deng, L.; Lin, H.; Liu, P.; Dong, E.; Wishart, D. S., The Human Saliva Metabolome. *Metabolomics* **2015**, *11* (6), 1864-1883.

253. Bouatra, S.; Aziat, F.; Mandal, R.; Guo, A. C.; Wilson, M. R.; Knox, C.; Bjorndahl, T. C.; Krishnamurthy, R.; Saleem, F.; Liu, P.; Dame, Z. T.; Poelzer, J.; Huynh, J.; Yallou, F. S.; Psychogios, N.; Dong, E.; Bogumil, R.; Roehring, C.; Wishart, D. S., The Human Urine Metabolome. *PLOS ONE* **2013**, *8* (9), e73076.

254. Han, J.; Ma, C.; Wang, B.; Bender, M.; Bojanowski, M.; Hergert, M.; Seehafer, K.; Herrmann, A.; Bunz, U. H. F., A Hypothesis-Free Sensor Array Discriminates Whiskies for Brand, Age, and Taste. *Chem* **2017**, *2* (6), 817-824.

255. De, M.; Rana, S.; Akpinar, H.; Miranda, O. R.; Arvizo, R. R.; Bunz, U. H.; Rotello, V. M., Sensing of Proteins in Human Serum Using Conjugates of Nanoparticles and Green Fluorescent Protein. *Nat. Chem.* **2009**, *1* (6), 461-5.

256. Rakow, N. A.; Suslick, K. S., A Colorimetric Sensor Array for Odour Visualization. *Nature* **2000**, *406* (6797), 710-713.

257. Würthner, F.; Saha-Möller, C. R.; Fimmel, B.; Ogi, S.; Leowanawat, P.; Schmidt, D., Perylene Bisimide Dye Assemblies as Archetype Functional Supramolecular Materials. *Chem. Rev.* **2016**, *116* (3), 962-1052.

258. Yano, K.; Itoh, Y.; Araoka, F.; Watanabe, G.; Hikima, T.; Aida, T., Nematic-to-Columnar Mesophase Transition by in situ Supramolecular Polymerization. *Science* **2019**, *363* (6423), 161-165.

259. Bhosale, S. V.; Jani, C. H.; Langford, S. J., Chemistry of Naphthalene Diimides. *Chem. Soc. Rev.* **2008**, *37* (2), 331-342.

260. Gao, Z.; Han, Y.; Gao, Z.; Wang, F., Multicomponent Assembled Systems Based on Platinum(II) Terpyridine Complexes. *Acc. Chem. Res.* **2018**, *51* (11), 2719-2729.

261. Chakrabarty, R.; Mukherjee, P. S.; Stang, P. J., Supramolecular Coordination: Self-Assembly of Finite Two- and Three-Dimensional Ensembles. *Chem. Rev.* **2011**, *111* (11), 6810-6918.

262. Techen, A.; Hille, C.; Dosche, C.; Kumke, M. U., Fluorescence Study of Drug–Carrier Interactions in Ctab/Pbs Buffer Model Systems. *J. Colloid Interface Sci.* **2012**, *377* (1), 251-261.

263. Karayil, J.; Kumar, S.; Talmon, Y.; Hassan, P. A.; Tata, B. V. R.; Sreejith, L., Micellar Growth in Cetylpyridinium Chloride/Alcohol System: Role of Long Chain Alcohol, Electrolyte and Surfactant Head Group. *J. Surfactants Deterg.* **2016**, *19* (4), 849-860.

264. Kabanov, A. V.; Batrakova, E. V.; Alakhov, V. Y., Pluronic® Block Copolymers as Novel Polymer Therapeutics for Drug and Gene Delivery. *J. Controlled Release* **2002**, *82* (2), 189-212.

265. Fuguet, E.; Rafols, C.; Roses, M.; Bosch, E., Critical Micelle Concentration of Surfactants in Aqueous Buffered and Unbuffered Systems. *Anal. Chim. Acta* **2005**, *548* (1-2), 95-100.

266. Ellman, G. L., Tissue Sulfhydryl Groups. *Arch. Biochem. Biophys.* **1959**, *82* (1), 70-77.

267. Hecht, M.; Würthner, F., Supramolecularly Engineered J-Aggregates Based on Perylene Bisimide Dyes. *Acc. Chem. Res.* **2021**, *54* (3), 642-653.

268. Price, J. H.; Williamson, A. N.; Schramm, R. F.; Wayland, B. B., Palladium (II) and Platinum (II) Alkyl Sulfoxide Complexes. Examples of Sulfur-Bonded, Mixed Sulfur-and Oxygen-Bonded, and Totally Oxygen-Bonded Complexes. *Inorg. Chem.* **1972**, *11* (6), 1280-1284.

269. Turell, L.; Radi, R.; Alvarez, B., The Thiol Pool in Human Plasma: The Central Contribution of Albumin to Redox Processes. *Free Radical Biol. Med.* **2013**, *65*, 244-253.

270. Chwatko, G.; Bald, E., Determination of Thiosulfate in Human Urine by High Performance Liquid Chromatography. *Talanta* **2009**, *79* (2), 229-234.

271. Hannestad, U.; Mårtensson, J.; Sjödahl, R.; Sörbo, B., 3-Mercaptolactate Cysteine Disulfiduria: Biochemical Studies on Affected and Unaffected Members of a Family. *Biochem. Med.* **1981**, *26* (1), 106-114.

272. Carlsson, M. S.; Denneberg, T.; Emanuelsson, B. M.; K»gedal, B.; Lindgren, S., Pharmacokinetics of Oral Tiopronin. *Eur. J. Clin. Pharmacol.* **1993**, *45* (1), 79-84.

273. Bouazza, N.; Tréluyer, J.-M.; Ottolenghi, C.; Urien, S.; Deschenes, G.; Ricquier, D.; Niaudet, P.; Chadefaux-Vekemans, B., Population Pharmacokinetics and Pharmacodynamics of Cysteamine in Nephropathic Cystinosis Patients. *Orphanet J. Rare Dis.* **2011**, *6*, 86-86.

274. Netter, P.; Bannwarth, B.; Péré, P.; Nicolas, A., Clinical Pharmacokinetics of D-Penicillamine. *Clin. Pharmacokinet.* **1987**, *13* (5), 317-333.

275. Duchin, K. L.; McKinstry, D. N.; Cohen, A. I.; Migdalof, B. H., Pharmacokinetics of Captopril in Healthy Subjects and in Patients with Cardiovascular Diseases. *Clin. Pharmacokinet.* **1988**, *14* (4), 241-259.

276. James, C. A.; Mant, T. G.; Rogers, H. J., Pharmacokinetics of Intravenous and Oral Sodium 2-Mercaptoethane Sulphonate (Mesna) in Normal Subjects. *Br. J. Clin. Pharmacol.* **1987**, *23* (5), 561-568.

277. Karabencheva, T.; Christov, C., Chapter 3 - Mechanisms of Protein Circular Dichroism: Insights from Computational Modeling. In *Advances in Protein Chemistry and Structural Biology*, Donev, R., Ed. Academic Press: 2010; Vol. 80, pp 85-115.

278. Wang, L.-L.; Chen, Z.; Liu, W.-E.; Ke, H.; Wang, S.-H.; Jiang, W., Molecular Recognition and Chirality Sensing of Epoxides in Water Using Endo-Functionalized Molecular Tubes. *J. Am. Chem. Soc.* **2017**, *139* (25), 8436-8439.

279. Zhu, H.; Li, Q.; Gao, Z.; Wang, H.; Shi, B.; Wu, Y.; Shangguan, L.; Hong, X.; Wang, F.; Huang, F., Pillararene Host–Guest Complexation Induced Chirality Amplification: A New Way to Detect Cryptochiral Compounds. *Angew. Chem. Int. Ed.* **2020**, *59* (27), 10868-10872.

280. Lutz, J.-F.; Lehn, J.-M.; Meijer, E.; Matyjaszewski, K., From Precision Polymers to Complex Materials and Systems. *Nat. Rev. Mater.* **2016**, *1* (5), 1-14.

281. Kartha, K. K.; Allampally, N. K.; Politi, A. T.; Prabhu, D. D.; Ouchi, H.; Albuquerque, R. Q.; Yagai, S.; Fernandez, G., Influence of Metal Coordination and Light Irradiation on Hierarchical Self-Assembly Processes. *Chem Sci* **2019**, *10* (3), 752-760.

282. Helmich, F.; Lee, C. C.; Schenning, A. P.; Meijer, E., Chiral Memory via Chiral Amplification and Selective Depolymerization of Porphyrin Aggregates. *J. Am. Chem. Soc.* **2010**, *132* (47), 16753-16755.

283. Mabesoone, M. F.; Markvoort, A. J.; Banno, M.; Yamaguchi, T.; Helmich, F.; Naito, Y.; Yashima, E.; Palmans, A. R.; Meijer, E., Competing Interactions in Hierarchical Porphyrin Self-Assembly Introduce Robustness in Pathway Complexity. *J. Am. Chem. Soc.* **2018**, *140* (25), 7810-7819.

284. Li, J.; Li, Y.; Chan, C. Y.; Kwok, R. T.; Li, H.; Zrazhevskiy, P.; Gao, X.; Sun, J. Z.; Qin, A.; Tang, B. Z., An Aggregation-Induced-Emission Platform for Direct Visualization of Interfacial Dynamic Self-Assembly. *Angew. Chem. Int. Ed.* **2014**, *126* (49), 13736-13740.

285. Zhang, H.; Zheng, X.; Kwok, R. T.; Wang, J.; Leung, N. L.; Shi, L.; Sun, J. Z.; Tang, Z.; Lam, J. W.; Qin, A., In Situ Monitoring of Molecular Aggregation Using Circular Dichroism. *Nat. Commun.* **2018**, *9* (1), 1-9.

286. Hecht, M.; Leowanawat, P.; Gerlach, T.; Stepanenko, V.; Stolte, M.; Lehmann, M.; Wurthner, F., Self-Sorting Supramolecular Polymerization: Helical and Lamellar Aggregates of Tetra-Bay-Acyloxy Perylene Bisimide. *Angew. Chem. Int. Ed.* **2020**, *59* (39), 17084-17090.

287. Martinez, C. R.; Iverson, B. L., Rethinking the Term "Pi-Stacking". *Chem. Sci.* **2012**, *3* (7), 2191-2201.

288. Aida, T.; Meijer, E. W., Supramolecular Polymers – We've Come Full Circle. *Isr. J. Chem.* **2020**, *60* (1-2), 33-47.

289. Korevaar, P. A.; George, S. J.; Markvoort, A. J.; Smulders, M. M.; Hilbers, P. A.; Schenning, A. P.; De Greef, T. F.; Meijer, E., Pathway Complexity in Supramolecular Polymerization. *Nature* **2012**, *481* (7382), 492-496.

290. Markvoort, A. J.; Ten Eikelder, H. M.; Hilbers, P. A.; De Greef, T. F.; Meijer, E., Theoretical Models of Nonlinear Effects in Two-Component Cooperative Supramolecular Copolymerizations. *Nat. Commun.* **2011**, *2* (1), 1-9.

9 Appendix

9.1 List of publications

Scientific publications

R. Kang, T. Jochmann, L. De Cola, F. Biedermann, Differential sensing without arrays: The spectral evolution of probe-conjugates enable analyte identification and quantification. *Manuscript in preparation.*

R. Kang[‡], J. Krämer[‡], L. Grimm[‡], L. De Cola, P. Picchetti, F. Biedermann. Molecular Probes, Chemosensors, and Nanosensors for Optical Detection of Biorelevant Molecules and Ions in Aqueous Media and Biofluids. *Chem. Rev.*, **3**, 3459-3636 (2022).

[‡] These authors contributed equally

R. Kang, L. Talamini, E. D'Este,. B. Martins Estevão, L. De Cola, W. Klopper, F. Biedermann. Discovery of a size-record breaking green-emissive fluorophore: small, smaller, HINA. *Chem. Sci.*, **12**, 1392-1397 (2021).

R. Kang, R. Miao, Y. Qi, X. Chang, C. Shang, L. Wang. Y. Fang. Tuning the Formation of Reductive Species of Perylene-Bisimide Derivatives in DMF *via* Aggregation Matter. *Chem. Commun.*, **53**, 10018-10021 (2017).

Y. Qi, R. Kang, J. Huang, W. Zhang, G. He, S. Yin, Y. Fang. Reunderstanding the Fluorescent Behavior of Four-Coordinate-Monoboron Complexes Containing Monoanionic Bidentate Ligands. *J. Phys. Chem. B*, **121**, 6189-6199 (2017).

Y. Qi, W. Xu, R. Kang, N. Ding, Y. Wang, G. He, Y. Fang. Discrimination of saturated alkanes and relevant volatile compounds *via* the utilization of a conceptual fluorescent sensor array based on organoboron-containing polymers. *Chem. Sci.*, **9**, 1892-1901 (2018).

Poster presentations

R. Kang, T. Jochmann, F. Biedermann, L. De Cola. Self-Assembly Probes (SAPs) Solve the Selectivity Problem of Artificial Chemosensors. Women In Supramolecular Chemistry (WISC), Cagliari, Italy (2021).

R. Kang, S. Sinn, F. Biedermann, L. De Cola. Luminescent Pt(II) complexes for analyte-induced-aggregation sensing of bioactive thiols. European-Winter School on Physical Organic Chemistry (E-WISPOC), Bressanone, Italy (2019).

9.2 Acknowledgments

In this section, I would like to express my sincere appreciation to all the people who helped and supported me during my Ph.D. journey.

First of all, I would like to thank my supervisors, Prof. Luisa De Cola and Dr. Frank Biedermann. I am thankful to Dr. Frank Biedermann for giving me the chance to do my Ph.D. in his research group. I got enormous inspiration and motivation from his enthusiasm for science and meticulous work attitude. I appreciate his patient guidance, kind support, and encouragement. I am thankful to Prof. Luisa De Cola, who made the China Scholarship Council (CSC) funding application with me, and for the valuable discussions and suggestions for my projects. Also, she always offered me opportunities for workshops and conferences to enrich my views not only limited to the research but also outside of the lab. It is really a great and unforgettable experience to work with both of them, which inspires and motivates me a lot toward scientific research. Besides, I would like to thank Prof. Anne S. Ulrich for accepting my doctorate in her group and offering me the freedom of scientific work and support, giving me valuable suggestions for the defense.

I would like to thank all the former and present colleagues I worked with in the Biedermann group. In particular, I am grateful to Dr. Stephan Sinn for showing me all the instruments and teaching me from fundamental knowledge when I started working in the lab. I really appreciated his patient guidance, valuable discussions and suggestions, and kind support. I would like to thank Dr. Laura Grimm, who always helped and supported me when I had problems not only limited to research but also in my daily life. Thanks for the help of the DLS instrument and liposome-related discussions from Dr. Pierre Picchetti. Thanks for the synthesis help from Dr. Pronay Kumar Biswas, Alicja Siennicka, and Changming Hu. I thank Joana Krämer, Amrutha Prabodh, Wenjing Wang, Chunting Zhong, Nilima Kumar Manoj, Yichuan Wang, and Patrick Gruhs for their help, support, and kindness.

I also would like to thank my collaborators. I want to thank Prof. Wim Klopper for his hard work on the computational calculation regarding the HINA project. Thanks for the cell-related contribution from Dr. Elisa D'Este and Dr. Laura Talamini. I want to thank Hannes Kühner for providing me with the chemicals in the HINA project. I also want to say thank you to Thomas Jochmann for his hard work on cluster data analysis and manuscript preparation. Without all of you, I could not be able to finish my Ph.D. Thank you!

I would like to express my gratitude to my former master's supervisor Prof. Yu Fang. He was and remains an excellent scientist and mentor. He inspired me to go to pursue a career in research. His enthusiasm, persistence, and love for research are contagious.

Gratitude goes to my friends. I want to say thank you to Meixia and Shaofei first. Thanks for always taking care of me, not only as friends but rather as a sister and a brother. I am still missing the time you both were in Strasbourg. Thank many other friends, Tingting, Liang, Yimin, Jiayun, Yanyu, Jianfei, Li, and Xingmao, for their kindness.

Last but not least, a big thank you to my family. I want to thank my grandparents and parents for supporting me and believing in me all the time. Also, I need to thank my brother and sister for accompanying my parents and supporting me.

Finally, I would like to acknowledge the China Scholarship Council (CSC) for the financial support of my Ph.D. study. Without this, I could not have been here to pursue my research.

Rui Kang

康 蕊